Sponsor:	CureSPG50, a non-profit entity
IND #:	To Be Assigned
Product:	Recombinant adeno-associated virus (serotype 9) encoding a codon-optimized human AP4M1 transgene (hAP4M1opt); single, one-time intrathecal route of administration
	Product Name: Melpida
Indication:	Treatment of patients with Spastic Paraplegia Type 50 (SPG50) caused by the AP4M1 gene mutation
Meeting Type:	Type B: PreIND
Meeting Date:	Written responses Friday 14 May 2021
Meeting ID#	13219
PTS#	PS006503

TABLE OF CONTENTS

LIST OF TABLES

LIST OF FIGURES

4

1   PRODUCT NAME

Product Name/Sponsor Code: Melpida

Generic and tradenames have not yet been requested for this product.

2   APPLICATION NUMBER

Application number: TBD

3   CHEMICAL NAME AND STRUCTURE

Melpida is a recombinant serotype 9 adeno-associated virus encoding a codon-optimized human *AP4M1* transgene (hAp4m1opt). The final product consists of AAV9 capsids that are packaged with the self-complementary AAV genome. The full sequence of the plasmid will be provided in the IND application. Due to confidentiality (with contributing authors), additional information on the product is not provided in this document. Additionally, no CMC questions are being asked as the CDMO will be Viralgen Vector Core (VVC), Spain, who has had multiple interactions with the agency and has a Master File submitted for cross reference to support some drug substance and drug product aspects of the future IND (MF#19559). Sufficient material will be generated to dose 3 patients when the IND is submitted. Generation of additional future lots will depend on the results from the initial patients dosed and the availability of funding for the drug product.

4   PROPOSED REGULATORY PATHWAY

A Biologics License Application (BLA) for Melpida will be submitted under section 351(a) of the Public Health Service Act if Melpida is efficacious, safe and successfully partnered with a commercial entity.

5   PROPOSED INDICATION

The proposed indication is for the treatment of pediatric patients with Spastic Paraplegia Type 50 (SPG50) caused by biallelic pathogenic variation of the AP4M1 gene.

6   DOSAGE FORM, ROUTE OF ADMINISTRATION AND DOSING REGIMEN

- Route of administration: intrathecal (IT) infusion delivery
- Dosage form: sterile liquid for injection
- Dosing regimen: one-time administration

7   PEDIATRIC STUDY PLANS

A pediatric study plan is not applicable for this ultra-rare Orphan disease. Rare Pediatric Disease designation was granted to Melpida September 2020 (#RPD-2020-441); although orphan designation was requested at the same time, there were no in vivo studies to support the application. An orphan designation will be resubmitted before the 1-year deadline requested in the ODD response (#DRU-2020-7740). Pediatric subjects will be the focus of the clinical program.

8   HUMAN FACTORS ENGINEERING PLANS

Not applicable.

9   COMBINATION PRODUCT INFORMATION

Whole exome sequencing or whole genome sequencing will be used to identify patients. If a non-commercial next generation sequencing is used and a BLA is progressed, a companion diagnostic may be needed for approval.

10   ATTENDEES, AFFILIATIONS AND TITLES (SPONSOR)

Sponsor

Collaborating Institution	Collaborating Investigator	Role/contribution
CureSPG50	Terry Pirovolakis	Founder of CureSPG50 and IND sponsor
Charles River Laboratories (CRL)	Dr Lauren Black Dr Julie Douville Stefania Cinquino	Distinguished Scientist Nonclinical program lead Nonclinical operations
University of Texas Southwestern (UTSW)	Dr Steven Gray Dr Xin Chen	Melpida development and nonclinical studies to support safety and efficacy
National Institutes of Health	Dr Carsten Bonnemann Dr Dimah Saade	Immunosuppression regimen
Hospital for Sick Children, Canada	Dr James J Dowling	Principal investigator,
National Institutes of Health (NIH)	Dr Juan Bonifacino Dr Raffaella De Pace	Patient cell line studies to support mechanism of action of Melpida
Boston Children's Hospital (BCH)	Dr Darius Ebrahimi-Fakhari Dr Mustafa Sahin	Patient cell line studies to support mechanism of action of Melpida Potential clinical site
Regulatory Innovation LLC	Diane Balderson, PhD	Regulatory Affairs Consultant

11   BACKGROUND

A table of abbreviations is included in .

11.1   History of the Development Program

The goal of this PreIND meeting is to receive guidance on the proposed nonclinical development plan for moving Melpida into the clinic for the treatment of subjects with SPG50, an ultra-rare disease.

The sponsor is the founder of CureSPG50, the nonprofit company behind this technology.

Various nonclinical studies have provided data to support the potential benefit of Melpida to pediatric patients with SPG50.

11.2   Status of Development Program

The development program is currently at the IND enabling stage and the 3-month GLP toxicology and biodistribution study in Sprague Dawley rats **is ongoing with a completion date of 23rd May 2021**. A PreIND meeting is being requested to confirm alignment on the nonclinical and clinical aspects outlined in the additional sections below.

The IND is planned for submission in 2H2021.

12   PURPOSE OF THE MEETING

The sponsor is requesting this PreIND meeting to discuss the adequacy of the nonclinical package to support clinical dosing with Melpida for the treatment of pediatric patients with SPG50, an ultra-rare disease.

Spastic Paraplegia Type 50 (SPG50) is one of a group of 4 genetic disorders (SPG47, SPG50, SPG51 and SPG52) involving a pathologic variation that results in the production of an abnormal adaptor protein complex 4 (AP-4); all 4 subtypes present with the same clinical phenotype (Behne et al, 2020; Ebrahimi-Fakhari et al, 2020; Ebrahimi-Fakhari et al, 2018).

AP-4-associated hereditary spastic paraplegia (AP-4-HSP) is caused by bi-allelic loss-of-function variants in one of the 4 subunits that make up AP-4. AP-4-HSP is an ultra-rare autosomal recessive disease with ~156 patients identified worldwide and 59 identified with SPG50. **There are ~9 patients with SPG50 in North America** (AP4M1, OMIM #612936) (source: Ebrahimi-Fakhari et al, unpublished, Registry and Natural History Study for AP-4 Associated Hereditary Spastic Paraplegia (AP-4-HSP) (AP-4-HSP), ClinicalTrials.gov Identifier: NCT04712812).

Symptoms of AP-4-HSP begin in infancy, though patients are often not correctly identified and diagnosed until age 5 to 10 years (Table 8). Patients are usually paralyzed by spastic paraplegia within their first decade and tetraplegic and severely mentally delayed by

adolescence or adulthood; epilepsy is also a key symptom (Ebrahimi-Fakhari et al, 2018). Only a few patients are identified over the age of 30 years due in part to recent advances in genetic diagnostics and also to life limitation associated with the disease (Table 8) (Ebrahimi-Fakhari et al, 2020).

There are no approved treatments for SPG50, leaving an unmet medical need for this serious and quality-of-life limiting disease affecting pediatric patients.

The sponsor has outlined a nonclinical plan to support an IND (Section 14.3.1, Question 2) that includes various studies (Table 3) providing the following conclusions for those that have completed:

- Fibroblasts from a patient with SPG50 (AP4M1(NM_004722.4):c.916C>T / (p.Arg306Ter) / c.694dupG (p.Glu232GlyfsTer21)) transduced with Melpida (*using an AAV2 capsid*) restored autophagy related 9A (ATG9A) trafficking and hence AP-4 function, at MOIs of 1E4 and 1E5 vg/cell with a suggestion of possible toxicity in the higher Multiplicity of Infection (MOI) group (Study #01) (Figure 4). Reducing the MOI to 1E2 and 1E3 vg/cell improved the phenotypes without noticeable toxicity in the same fibroblasts (Figure 5) as well as two other fibroblast cell lines (Figure 6 and Figure 7). Independent studies were duplicated in 2 additional patient lines at MOI 1E2, 1E3, 1E4 & 1E5 vg/cell and showed a dose-dependent reduction in ATG9A staining at the TGN, AP4E1 localization to the TGN and unchanged staining for TGN46 with phenotypic rescue in up to 77% of fibroblasts and no associated toxicity (Study #02) (Figure 8).
- In C57BL/6J mice, Melpida (AAV9) led to dose-dependent hAP4M1opt mRNA expression in all brain regions at 4 weeks post IT injection, with expression sustained up to at least 5 months post infusion. This confirmed that Melpida reached and achieved transgene expression at the targeted site of action (Study #05, Figure 9).
- No severe toxicity has been observed in the in-life portion of a 12 month non-GLP toxicology study of Melpida administered IT at doses of 1.25E11 or 5E11 vg in 5 µL in C57BL/6J mice (Study #05; Figure 10, Figure 11, Figure 12, Figure 13).

Ongoing studies include:
- **A 12-week GLP toxicology and biodistribution study in Sprague Dawley (SD) rats with the clinical product, Melpida, to support the safety of the proposed clinical dose (Study CRL-5550008). Dosing commenced on February 16th and will complete May 23rd. Intrathecal doses of 0 (vehicle), 0.36E12, 1.1E12, or 3.3E12 vg/mouse was administered in a volume of 20 or 60uL.**
- In vivo efficacy study in Ap4m1 knock out (KO) mice dosed at post-natal day (PND) 7 to 10 or PND 90, and assessed for potential phenotypic rescue (study 2020-06).

The proposed clinical synopsis for the first in human study is outlined in Question 3 and provided in Section 17.2.

No CMC questions are being asked as the CDMO will be VVC, Spain, who has had multiple interactions with the agency and has a Master File submitted for cross reference to support some drug substance and drug product aspects of the future IND; information not in the Master File will be provided in the IND. Sufficient material will be generated to dose 3 patients when the IND is submitted. Generation of additional future lots will be dependent on the results from the initial patients dosed and the availability of funding for the drug product.

13   PROPOSED AGENDA

There will be no agenda as the agency is providing written responses only.

14   QUESTIONS FOR DISCUSSION

14.1   Regulatory

14.1.1   Question 1:

> **Does the agency agree that this non-profit charitable sponsor could be granted an exemption by OTAT from eCTD rules and submit their future IND as non eCTD (PDFs with CTD structure) for the first in human study for this ultra-rare disease, with electronic filing requirements after the first in human study?**

14.1.2   Sponsor Position:

The IND will be held by the non-profit charitable organization, CureSPG50, which is a Canadian Charity organization, dedicated to treating patients with SPG50. Financial support for this development program come from donations only. As such, the sponsor would like to understand if an exemption from eCTD requirements per FDA's guidance "Providing regulatory submissions in electronic format – certain human pharmaceutical product applications and related submissions using the eCTD specifications", February 2020, would be granted/supported by this division. If yes, the IND would utilize the alternate electronic format (without xml backbone) per FDA's guidance "Providing regulatory submissions in alternate electronic format", March 2020, and "The comprehensive table of contents headings and hierarchy", Version 2.3.2, and eliminate costs associated with commercial publishing, which typically amount to ~$35,000 for an IND. Hyperlinks between modules will not be available; hyperlinks within modules of the same PDF will be active. Each module will be provided as a single PDF, unless size limits apply, in which case, PDFs will be split as necessary. There is a future opportunity to out license/sell this product to a commercial organization, at which point the eCTD requirements will be met; eCTD will be adopted after the first in human study regardless of out licensing/selling.

The proposed IND components are outlined in Table 1.

Table 1   Proposed IND original and cross-reference components

Module	#PDFs	Comment
1	1	Fully compliant with FDA's guidance
2.3	1	This will list what is available in M3. Hyperlinks to those locations in M3 will not be active.
2.4	1	Hyperlinks within the document will be active. There will be no active hyperlinks to the supporting module 4 reports.
2.6	1	Hyperlinks within the document will be active. There will be no active hyperlinks to the supporting module 4 reports.
3.2.S	1 or 2	Cross-reference will be made to a Master File (MF#19559) for much of the drug substance information originating from VVC, Spain. Original information will be supplied for generation of transgene from Aldevron.
3.2.P	1 or 2	Cross-reference will be made to a Master File (MF#19559) for much of the drug product information originating from VVC, Spain. Original information will be supplied for generation of transgene from Aldevron.
4	5 or 6	Original reports which will include: • Fibroblast and iPSC proof of concept studies from all institutions [Study #01, Study #02] • In vivo data showing transduction of the brain of wildtype mice when administered by intrathecal injection [Study #05] • A dose-range-finding (DRF) non-GLP pharmacology study with Melpida in Ap4m1-KO mice that provides evidence of tolerability and improvements in hindlimb clasping, motor coordination and grip strength over 12 months [ongoing, Study #2020-06], • 12-week GLP toxicology and biodistribution study in SD rats [CRL-5550008]. Hyperlinks within each PDF will be active for navigation.
5	1	Full clinical protocol and Informed consent document. CV, 1752, pharmacy manual. Hyperlinks within the PDFs will be active.

14.2   CMC

Full details of the manufacturing and release specifications/protocols will be provided in the IND.

14.3 Preclinical

14.3.1 Question 2:

Does the Agency agree that the GLP toxicology study in Sprague Dawley rats, coupled with the ex vivo and in vivo data from various studies, supports the intrathecal dosing of Melpida in patients with SPG50?

14.3.2 Sponsor Position:

General Plan

The sponsor proposes to provide a nonclinical IND package that includes the following data obtained with Melpida. The differences between the various lots of Melpida used for each study are outlined in Table 2:

a. Ex-vivo data confirming expression and functionality in patient fibroblasts (Complete, Study #01 and Study #02),
b. In vivo data confirming the pharmacological activity of Melpida in AP4M1-knock out mice (Ongoing, Study 2020-06) and
c. In vivo data confirming the safety and gene expression of Melpida when administered intrathecally to C57BL/6J mice (Complete, Study #05)
d. **An ongoing 12-week GLP toxicology and biodistribution study with the clinical product, Melpida, in Sprague Dawley (SD) rats that confirms the safety of the proposed clinical dose (Ongoing, Study CRL-5550008). This study commenced on 16th February and will complete 23rd May**.

The status of these studies is provided in Table 3.

Table 2   Differences between Lots used in Melpida studies

Vector Lot#	Manufacturer	Material grade	Used in Studies	Titer (vg/mL); assay method	Differences to cGMP material
8829	UNC VC	Research	01, 02,	2.8E12 qPCR	AAV2 capsid; all remaining components the same
LAV112-conc	UNC VC	Research	03, 04, 05, 2020-06, 07	1.03E14 qPCR	Identical to clinical material but manufactured at a different site with a modified process
T-GEMINIS-033	Viralgen	GLP-like	CRL-5550008	5.43E13 ddPCR	Identical to clinical material
TBD	Viralgen	cGMP	Clinical	TBD	

Key: UNC VC, University of North Carolina Chapel Hill, Vector Core; TBD, to be determined

For the IND, the same titering method (ddPCR) will be used for the research, GLP-like and GMP batches to confirm titer used in each nonclinical study.

Table 3   Status of Nonclinical Studies conducted with Melpida/other

Study # GLP Status	Description	Model Doses (total vg) Route	Source	Section
Ex vivo studies				
#01 non-GLP Complete	Ex-vivo efficacy study using patient-derived fibroblasts	AAV2/Fibroblasts (3x Patient Cells) MOI 1E2, 1E3, 1E4 or 1E5 vg/cell	BCH	15.3.2
#02 non-GLP Complete	Ex-vivo efficacy study using patient-derived fibroblasts	AAV2/Fibroblasts (2x Patient Cells) MOI 1E4 or 1E5 vg/cell	NIH	15.3.3
In vivo: Efficacy				
2020-06 non-GLP Ongoing	In-Vivo efficacy study in *Ap4m1* KO mice dosed at PND 7 to 10 or 90 days; terminated at 12 months of age	AAV9/KO Mouse Model (N=154) Veh, 1.25E11 or 5E11 vg/mouse in 5uL IT	UTSW	15.3.4
In vivo Toxicology and biodistribution				
#05 non-GLP Complete	A 12 month in-vivo toxicology and biodistribution study	C57BL/6J mice (N=60) Veh, 1.25E11 or 5E11 vg/mouse in 5uL IT	UTSW	15.3.1
CRL-5550008 GLP Ongoing	**A 90 day in-vivo toxicology and biodistribution study; dosed 7 to 8 WoA;**	**Sprague Dawley Rat (N=132) Veh, 0.36E12, 1.1E12, or 3.3E12 vg/mouse in 20 or 60uL IT**	**CRL**	17.5
Key: GLP, good laboratory practice; vg, vector genomes; KO, knock out; Veh, vehicle; WoA, weeks of age; IT, intrathecal; PND, post-natal day; MOI, Multiplicity of Infection.				

The data obtained from the completed studies confirmed the activity of Melpida and supported the progression of Melpida into a GLP-toxicology study with the prospect of future clinical dosing (details of the studies are provided in Section 15.3.1).

Proposed Toxicology and Biodistribution study (Study CRL-5550008) to support clinical dosing. NOTE this study commenced 16th February and will complete 23rd May.

Title: A single-dose toxicity study of Melpida by intrathecal injection in rats.

This GLP 12-week toxicology and biodistribution study in SD rats with Melpida is described in Table 4. The full protocol is provided in Section 17.5.

Table 4   Single-dose GLP toxicology and biodistribution study in Sprague Dawley rats

Group No.	Test Material	Dose Level (vg)	Dose Volume (µL)	Dose Concentration (vg/µL)	No. of Animals					
					Main Study		Recovery Study			
					Day 8 Necropsy[a]		Day 29 Necropsy[b]		Day 91 Necropsy[c]	
					M	F	M	F	M	F
1	Reference Item	0	60	0	5	5	5	5	5	5
2	Melpida	0.36E12	20	0.18E11	5	5	5	5	5	5
3	Melpida	1.1E12	20	0.55E11	5	5	5	5	5	5
4	Melpida	3.3E12	60	0.55E11	5	5	5	5	5	5

M = Males; F = Females

[a]Animals scheduled for Necropsy on Day 8. Biodistribution will also be assessed.

[b]Animals scheduled for Necropsy on Day 29. Biodistribution will also be assessed.

[c]Animals scheduled for Necropsy on Day 91. Biodistribution will also be assessed.

Justification for the Proposed Animal Model for Toxicology:

The SD rat was selected as the toxicology species based on the following rationale:

- At this time, studies in laboratory animals provide the best available basis for extrapolation to humans and are required to support regulatory submissions. Acceptable models that do not use live animals currently do not exist. The SD rat was chosen as the animal model for this study as it is an accepted rodent species for nonclinical toxicity testing to model the biodistribution of AAV9 expected in larger mammals. The AP4M1 gene is 93% conserved between rodents and humans, justifying the use of the rat to model toxicity from expression of the exogenously delivered human transgene.


```
Range 1: 1 to 453 GenPept  Graphics                    ▼ Next Match  ▲ Previous Match

Score              Expect  Method                      Identities    Positives    Gaps
739 bits(1908)  0.0        Compositional matrix adjust. 421/453(93%) 431/453(95%) 0/453(0%)

Query  1    MISQFFILSSKGDPLIYKDFRGDSGGRDVAELFYRKLTGLPGDESPVVMhhhgrhfihir  60
            MISQFFILSSKGDPLIYKDFRGDSGGRDVAELFYRKLTGLPG ESPVVM+H  RHFIHIR
Sbjct  1    MISQFFILSSKGDPLIYKDFRGDSGGRDVAELFYRKLTGLPGGESPVVMYHDDRHFIHIR  60

Query  61   hSGLYLVVTTSENVSPFSllellsrlatllGDYCGSLGEGTISRNVALVYELLDEVLDYG  120
            HSGLYLV TTSENVSPFSLLELLSRLATLLGDYCGSL EGTISRNVALVYELLDEVLDYG
Sbjct  61   HSGLYLVATTSENVSPFSLLELLSRLATLLGDYCGSLNEGTISRNVALVYELLDEVLDYG  120

Query  121  YVQTTSTEMLRNFIQTEAVVSKPFSLFDLSSVGLFGAETQQSKVAPSSAASRPVLSSRSD  180
            YVQTTST+MLRNFIQTEA VSKPFSLFDLSSVGLFGAETQQ++VAPSSAASRPVLSSRSD
Sbjct  121  YVQTTSTDMLRNFIQTEAAVSKPFSLFDLSSVGLFGAETQQNRVAPSSAASRPVLSSRSD  180

Query  181  QSQKNEVFLDVVERLSVLIASNGSLLKVDVQGEIRLKSFLPSGSEMRIGLTEEFCVGKSE  240
            QSQKNEVFLDVVERLSVLIASNGSLLKVDVQGEIRLKSFLPS SE+ IGLTEEFCVGKSE
Sbjct  181  QSQKNEVFLDVVERLSVLIASNGSLLKVDVQGEIRLKSFLPSSSEICIGLTEEFCVGKSE  240

Query  241  LRGYGPGIRVDEVSFHSSVNLDEFESHRILRLQPPQGELTVMRYQlsddlpsplpfrlfp  300
            LRGYGPGIRVDEVSFHSSVNLDEFESHRIL LQPPQGELTVMRYQLSDDLPSPLPFRLFP
Sbjct  241  LRGYGPGIRVDEVSFHSSVNLDEFESHRILHLQPPQGELTVMRYQLSDDLPSPLPFRLFP  300

Query  301  sVQWDRGSGRLQVYLKLRCDLLSKSQALNVRLHLPLPRGVVSLSQELSSPEQKAELAEGA  360
            SVQWD+GSGRLQVYLKLRCDL  KSQALN+ LHLPLPRGVVSLSQELSSP+QKAEL EGA
Sbjct  301  SVQWDQGSGRLQVYLKLRCDLPPKSQALNIHLHLPLPRGVVSLSQELSSPDQKAELGEGA  360

Query  361  LRWDLPRVQGGSQLSGLFQMDVpgppgppSHGLSTSASPLGLGPASLSFELPRHTCSGLQ  420
            L WDLPRVQGGSQLSGLFQMDVPG  GPPS G S SA PLGLGPASLSFELPRHTCSGLQ
Sbjct  361  LHWDLPRVQGGSQLSGLFQMDVPGLQGPPSRGPSPSAPPLGLGPASLSFELPRHTCSGLQ  420

Query  421  VRFLRLAFRPCGNANPHKWVRHLSHSDAYVIRI  453
            VRFLRL+F  CGNANPHKWVRHLSHS+AYVIRI
Sbjct  421  VRFLRLSFSACGNANPHKWVRHLSHSNAYVIRI  453
```

14

Justification for the Toxicology doses:

Doses administered are scaled on the volume of CSF per species (Table 5).

Table 5   Relationship between preclinical study doses and proposed human intrathecal dose

Species	Injection Volume (mL)	Weight (kg)	CSF Volume (mL)	Dose as % of CSF Volume	Min. Total Dose (vg)	Min. Dose per CSF Volume (vg/mL)	Max. Total Dose (vg)	Max. Dose per CSF Volume (vg/mL)
Mouse (PD)	0.005	~0.025	0.035	14	1.25E11	3.6E12	5.0E11	**1.42E13**
Rat (Tox)	0.02	0.25	0.25	8.0	3.6E11	1.44E12	3.3E12	**1.32E13**
Human (≥4 years)*	**10**	**~40**	**140**	**7.1**			**1E15**	**7E12**

For CSF Volumes, we used the following references: Morgan et al, 2004; Sullivan et al, 1979; Pardridge, 2011; Pardridge, 1991.

* For human subjects <4 years old, a dosing strategy is outlined in Table 6

The toxicology study utilized doses of 3.6E11 to 3.3E12 vg administered by the IT route in rats which encompasses the high dose (5E11 vg) used in the KO mouse study (2020-06) with almost a one-log overage, and are at least one-half log higher than the planned human dose of 1E15 vg when adjusted for CSF volume (1.32E13 vs 7E12 vg/mL; Table 5). When adjusted for CSF volume, the low dose of 1.25E11 vg in the AP4M1 KO mouse is marginally lower than the dose proposed in the clinic (3.6E12 compared to 7E12 vg/mL).

The sponsor considers a maximum feasible dose (MFD) intrathecally of AAV9 in humans to be approximately 10 mL of Melpida at a concentration of 1E14 vg/mL (that is 1E15 vg total). This assumes the use of a standard 10 mL volume for an IT drug and a maximum safe concentration of AAV9 at 1E14 vg/mL; this has been accepted in a recent clinical study for another scAAV9 for the treatment of CLN7 (NCT04737460; Table 16). Even at this MFD, the target tissue (brain) will not be saturated with all target cells transduced. Thus, it is expected that the highest dose that is feasible and tolerated should be used to maximize the number of cells transduced to achieve the greatest therapeutic benefit. Doses greater than the MFD are achieved in mice and rats by using dosing volumes greater than the equivalent of 10 mL in humans.

Justification for Day 8, Day 21 and Day 91 timepoints

Sacrifice at Day 8 is to assess acute toxicity, Day 29 to assess toxicity at peak transgene expression levels (Chen et al, 2021), and Day 91 to assess long-term toxicity.

Results

The main study and associated endpoints will be run by Charles River Laboratories under GLP. The biodistribution (BD) endpoints will be run by the sponsor using qPCR or ddPCR, with a qualified assay that conforms to FDA guidelines **but not in adherence with GLP**.

14.4   Clinical

14.4.1   Question 3:

Does the Agency agree:

  a. with the general design and enrollment criteria of the Phase I/II trial, the dose strategy and route of administration as summarized in Section 14.4.2**?**

  b. that since the ratio of central nervous system mass to whole body mass changes with age, the dose will be scaled by age correlated to brain mass and not body weight based. Does OTAT agree with both the rationale for dosing based on age (≥ 4 years old), or by approximate brain size for subjects < 4 years old (Table 6**)?**

  c. that SPG50 is an infant onset progressive disease, associated with severe morbidities and caused by biallelic mutations in AP4M1. The primary outcome for the proposed clinical study is safety, however, exploratory efficacy outcomes will be collected. Does the Agency agree with the proposed safety and exploratory efficacy outcome measures, based on the known cause and natural history of the disease (Section 14.4.2**)?**

14.4.2   Sponsor Position:

The proposed time and events schedule is outlined in the concept protocol provided in Section 17.2.

- **Title**

Phase I/II gene transfer clinical trial of scAAV9/AP4M1 for treatment of subjects with genetically confirmed hereditary spastic paraplegia Type 50 (SPG50) disease

- **Study Objectives**

The objectives of this study are to determine the safety and tolerability and explore efficacy of a single dose of Melpida delivered intrathecally at a dose of 1E15 vg in a 10mL volume, infused at 1 mL/min.

- **Study Design**

A time and events schedule is provided in the concept protocol in Section 17.2.

Thirty (30) days prior to dosing, subjects will undergo a screening visit. In the week prior to treatment, subjects will undergo clinical safety tests. On the day of dosing, subjects will begin a regimen of immunosuppression (see section below "Immune response to the AAV9 capsid").

Subjects will be admitted to the Pediatric Intensive Care Unit (PICU) the day of treatment (Day 1) at which time blood panels will be taken, and a physical exam with vital signs will be performed. Dosing will occur on Day 1 by IT injection (via lumbar puncture) under anesthesia. The dose of Melpida is proposed to be 1E15 vg (justification below).

16

The subjects will be discharged on the morning of Day 2 (24 h post Melpida administration, assuming appropriate clinical stability), and will return on Day 7, 14 and 28, Month 3, 6 and 12, then every 6 months thereafter for a total duration of 2 years. Annual visits will be required for an additional 3 years, for a total of 5 years follow-up post dosing.

- **Number of Subjects being treated**

The proposal is to treat 3 subjects. This is felt sufficient to establish safety and preliminary efficacy before considering a study focused on efficacy to support a future registration strategy.

- **Intrathecal route of administration for Melpida**

Melpida will be administered via a single lumbar intrathecal (IT) injection to broadly treat the central nervous system as well as peripheral organs. Choice of IT dose administration is based on the following rationale. In comparison to the intravenous route, the IT route achieves the maximum possible transduction of the CNS, the organ system severely afflicted by the condition. Further, IT minimizes the exposure of the immune system to scAAV9 vector limiting the virus mostly to the CNS space. The proposed single dose of 1E15 vg is not expected to completely rescue the disease. This is because the AP4M1 protein is widely expressed and Melpida will not transduce 100% of cells across the CNS, and there is no known mechanism for non-cell-autonomous benefits of AP4M1 gene expression. Thus, the objective is to use the highest safe dose possible to achieve the maximum number of cells transduced.

If the subject appears inadequately hydrated in the judgment of the Principal Investigator, bolus(es) of 10 to 20 mL/kg normal saline may be given during the time between subject check-in and gene transfer. The lowest level of sedation required will be used, and sedation will occur at least 48 hours after Screening/Baseline MRI. Subjects will be continued on their usual diet until eight hours prior to gene transfer, after which they will have no solid food; clear liquids will be allowed up until NPO as per institutional guidelines for sedation, based on age. They will resume their usual diet after they have returned to pre-sedation baseline.

The intrathecal injection will be delivered in a constant volume (scaled with age and/or brain volume according to Table 6). A needle will be inserted percutaneously at the lumbar level into the IT space of the spinal column; Xray verification will be used prior to and after administration of Melpida. A volume of CSF approximately equal to the infusion volume will be withdrawn from the lumbar thecal sac and sent for standard evaluation (CSF cell count and differential, glucose, protein, culture and AAV9 neutralizing antibodies). The vector solution will then be infused at a rate of 1 mL per minute. Subject will remain 15-degree Trendelenburg (head down) for 1 hour following vector administration and while still sedated to promote distribution throughout the CSF space.

Subjects will be closely monitored for side effects during the infusion: Heart rate, respiratory rate, pulse oximetry, temperature, and blood pressure will be measured before the infusion, every five minutes during the infusion, immediately after the infusion, and repeated at 15 minutes post-infusion for 1 hour, then hourly for the next 4 hours, then 4 hours thereafter until discharge. Neurology checks and continuous telemetry will be taken for at least 24 hours after dosing.

17

- **Device for Melpida administration**

For IT administration, a Pajunk Atraumatic Sprotte Needle will be inserted percutaneously at the lumbar level into the intrathecal space of the spinal column. A volume of CSF approximately equal to the infusion volume is withdrawn from the lumbar thecal sac. Melpida solution will be loaded into a 20 mL BD syringe, connected to the needle with a 60" Marquette Medical IV extension tubing and Braun Discofix 4-way stopcock. The vector solution will be infused at a rate of 1 mL per minute, using a suitable infusion pump. Subject will remain in a 15-degree Trendelenburg (head down) position for 1 hour following vector administration and changing side every 15 minutes.

- **Rationale for brain size dependent dose calculation:**

The dose of Melpida will be scaled from animals to humans based on the CSF volume to account for the different brain size and subject's age. For subjects 4 years and older, a 10 mL infusion volume will be used. For subjects < 4 years old, the dose will be scaled lower according to approximate brain size based on their baseline MRI (Table 6).

Table 6   Dose extrapolation based on age and brain size

Age (years)	Brain Volume* (approx. cm^3)	Infusion volume (mL)	Total IT Dose (E14 vg)
4+	1312	10	5 to 10
3	1180	9	4.5 to 9
2	1080	8.2	4.1 to 8.2
1	955	7.3	3.6 to 7.3
0.5	525	4	2 to 4
Newborn	400	3	1.5 to 3

The infusion volume for children <4 years old will be calculated as follows according to normative values based on age according to the table above. The concentration of the injection solution will be kept constant at 1E14 vg/mL, so the total vg dose will be scaled according to the volume injected. *References: Dekaban and Sadowsky, 1978; Zacharia et al, 2006; Caviness et al, 1996.

- **Handling and preparation of Melpida for IT administration**

Melpida will be formulated as a concentrated stock in phosphate-buffered saline containing 5% D-sorbitol and stored at ≤ -60C until the day of the administration procedure(s). The solution will be thawed within 4 hours of administration and diluted to the appropriate final dosage concentration and volume using phosphate-buffered saline with 5% D-sorbitol. The concentration would be kept constant, but a lower dose would be administered intrathecally to younger subjects (according to brain volume) by reducing the injection volume (Table 6).

- **Dose staggering and stopping criteria**

There will be a 90 day wait between the first and second subject and a 60 day wait between subjects 2 and 3. This provides an adequate window in which to identify acute adverse events related to the dosing procedure itself and sub-acute adverse events related to transduction of cells and expression of AP4M1, based on the expectation that this self-complementary product will reach maximal expression by 14 to 28 days post injection (Chen et al, 2021).

18

Stopping criteria are based on development of unacceptable toxicity defined as the occurrence two or more Grade 3 or higher unanticipated treatment-related toxicities.

- **Study Risks**

Anticipated Adverse events

- Infusion reactions:

The Common Terminology Criteria for Adverse Events (CTCAE) Version 5.0 provides a grading system that is used to categorize the severity of adverse events, as follows:

(a) Grade 1:   Mild: transient, requires no special treatment or intervention, does not interfere with daily activities

(b) Grade 2:   Moderate: alleviated with simple treatments, may limit daily activities

(c) Grade 3:   Severe: requires therapeutic intervention and interrupts daily activities

(d) Grade 4:   Life-threatening or disabling

(e) Grade 5:   Death

Infusion will be terminated for evidence of an allergic reaction of Grade 2 or greater. Under CTCAE v.5 criteria, anaphylaxis is Grade 3 (symptomatic bronchospasm with or without urticaria; allergy-related edema/angioedema; hypotension), and would result in infusion termination and systemic treatment.

Participants will remain in a PICU bed following gene transfer and remain admitted to the hospital for at least 24 hours. Vital signs will be obtained every 15 minutes for the first two hours post-infusion, 30 minutes for the third and fourth hours post-infusion, then hourly for 4 hours following the injection, and finally every 4 hours until discharge. Transfer out of the PICU may be undertaken after the initial 24 hours of post-infusion monitoring if there are no medical safety concerns in the opinion of the PI.

- Immune response to the AAV9 capsid and transgene

In previous gene therapy studies, antigen specific T-cell responses to the AAV9 vector have been reported (Harrison et al, 1977). This is an expected response between 2 and 12 weeks following gene transfer, even when administered IT. One possible consequence to such antigen specific T- cell responses is clearance of the transduced cells and loss of transgene expression.

To reduce the risk of the host immune response to the AAV9-based Melpida, an initial proposal for an immunosuppression regimen has been designed based on advice from investigators in the ongoing trial of AAV9 gene transfer to CSF for giant axonal neuropathy (Clinicaltrials.gov # NCT02362438). This is summarized in Figure 1 and consists of:

1 Week Prior to Vector Administration (= day -7):

- Sirolimus (rapamycin) load: 1 mg/m2 every 4 hours x 3 doses; then begin 0.5 mg/m2/day divided in twice a day dosing (goal level: 4-8 ng/ml)

Day of Vector Administration (= day 1):
- Acetaminophen (15 mg/kg/dose; maximum 650 mg per dose)
- Diphenhydramine (0.5 mg/kg/dose; maximum 50 mg/dose)
- IV methylprednisolone (10 mg/kg to a maximum single dose of 500 milligrams, infused over 30 minutes)

Day after Vector Administration (= day 2):
- Begin daily prednisone 0.5 mg/kg/day x 4 weeks (4 months)
- Begin daily tacrolimus 1 mg twice daily (goal level 4-8 ng/ml)

Maintenance:
- Prednisone 0.5 mg/kg/day x 4 weeks, then taper (4 months, 4 week taper)
- Tacrolimus 1 mg twice daily dosing x 6 months, then taper
- Sirolimus 0.5 mg/m2/day divided in twice a day dosing x 12 months, then taper

Taper strategies
- Prednisone at 4 Months: Based on laboratory findings (White Blood Cell Count) from Lumber Puncture at 3m. If counts are acceptable (based on the pediatric neurologist's assessment), and in conjunction with opening pressure, eye exam and brain and spine MRI with contrast, no evidence of enhancement (i.e., if there is no evidence of ongoing active inflammation) then proceed with the taper at month 4.
  - 7 days of 0.3 mg/kg/day
  - 7 days of 0.2 mg/kg/day
  - 7 days of 0.1 mg/kg/day
  - 7 days of 0.1 mg/kg every other day, then off
- Tacrolimus at 6 Months: Taper is completed slowly over a 2-3 week period based on clinical exam and Prednisone taper experience.
- Sirolimus at 12 Months: Taper between 12-24 months following vector administration based on clinical judgement.

Figure 1   Immunosuppression protocol
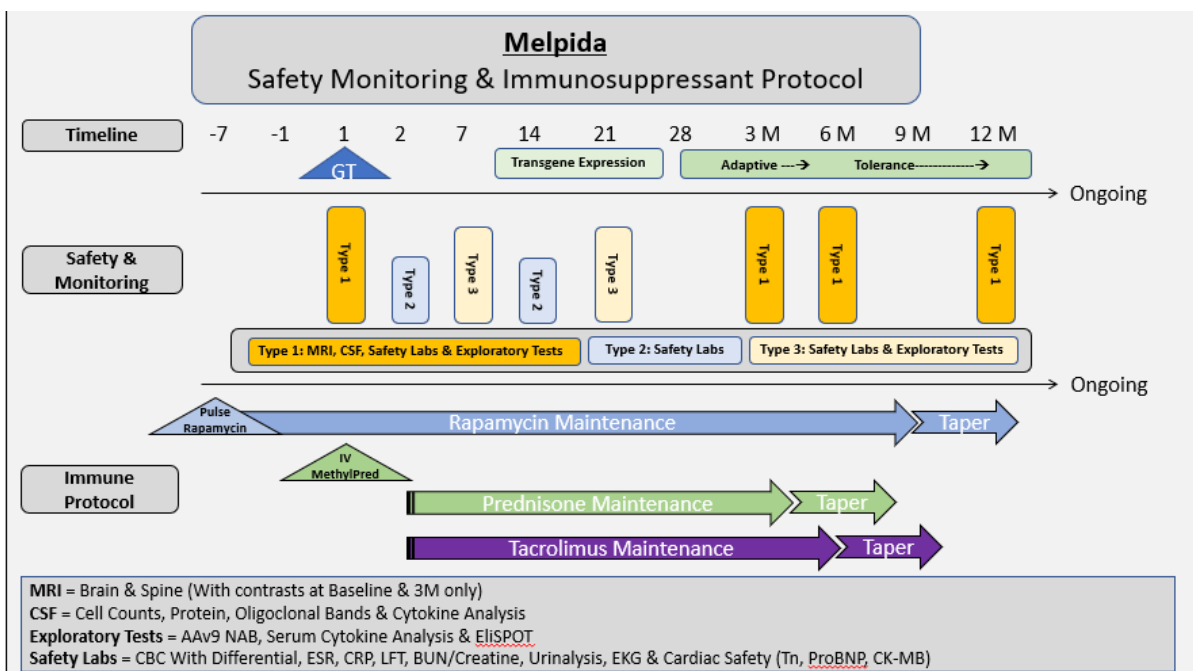
This regimen will be closely monitored as outlined in the concept protocol in Section 17.2. ELISPOT assays will be used to monitor anti-transgene and anti-AAV9 immune status.

- Risks associated with Immunosuppression

Methylprednisolone:

Possible side effects from a single dose as used in this protocol include changes in mood such as depression; agitation; excitement; sleeplessness; Increased blood sugar levels, especially if the patient also has diabetes; and fluid retention.

Prednisone:

Use of prednisone in this patient population has not been studied and specific effects of this drug in SPG50 are unknown. Similar patient populations with limited mobility who require prednisone treatment tolerate similar doses of prednisone relatively well (0.75 mg /kg /day in Duchenne muscular dystrophy).

In addition, based on experience with use of prednisone in children and adults for different indications, we suspect that therapy at the proposed doses for the indicated amount of time are less likely to lead to long-term sequelae associated with prolonged glucocorticoid use such as adrenal insufficiency, cataracts, cushingnoid changes, or osteoporosis to name a few.

However, several risks exist and will be discussed with the patients and reflected in the consent forms. The following are thought to be more likely to occur given the relatively short-term use of steroids proposed above.

21

Insomnia: this is a well-known effect of prednisone therapy in adults and children. We will try to minimize this by administering the medication in the morning.

Neuropsychiatric symptoms: Increased energy, mania, or suicidal ideation have been rarely reported. The patients will be monitored for such side effects and their caregivers will be specifically educated about this risk at the time of consent and/or at the time of hospital discharge after the first week of hospitalization.

Glucose intolerance: Elevated blood glucose levels will be monitored by serial blood testing.

Blood pressure: Elevated blood pressures will be monitored by vital signs measurements at each clinic visit.

Increased appetite and weight gain: This potential side effect will be monitored by vital sign and weight measurements though we anticipate this to be less of an issue given the relatively short period of prednisone therapy at the proposed doses.

Avascular necrosis of the bones: This is an idiosyncratic adverse event associated with steroid use in rare patients that may not be dose dependent. We will screen the patients at follow up visits for joint pain and have a low threshold for x ray evaluation should they develop persistent hip or knee pain.

Infections: Given the relative level of immunosuppression, the patients will be at higher risk of developing infections. SPG50 is not known to further reduce the patients' immunocompetency; however, we will monitor for any signs of infection especially during the period of steroid therapy and its taper both based on clinical symptoms and blood testing.

The patient will also be monitored for symptoms and signs of adrenal insufficiency during investigator follow up visits especially if any signs of superimposed infections are present. In the unlikely event that adrenal insufficiency develops, the patients will be treated with stress dose steroids per standards of care with consultation with endocrinology.

It may be difficult to conclusively ascertain whether a given side effects may be related to the prednisone therapy vs the vector administration in the first few weeks. However, prednisone has a known expected group of adverse events that can help in distinguishing between these to some extent.

Tacrolimus:

Tacrolimus is an immunosuppressive calcineurin inhibitor that interferes with several calcium-dependent processes in immune cells. The most common adverse reactions to tacrolimus include abnormal renal function, hypertension, diabetes mellitus, fever, tremor, paresthesias, hyperglycemia, cytopenia (leukopenia, anemia), abdominal complaints, electrolyte abnormalities (hyperkalemia, hypomagnesemia) and hyperlipemia. More severe neurotoxicity is described at higher whole blood trough concentrations and therapeutic drug monitoring is required during the trial. As with other immune suppressive agents, chronic use is associated with increased risk of

22

infection and malignancy, in particular, lymphoma and skin cancer. Tacrolimus should be used with supervision by a physician with experience in immunosuppressive therapy. Tacrolimus may induce changes in blood concentrations of concomitant medications and may also be affected by their use. Potential drug-drug interactions with tacrolimus must be considered during therapy (Manns et al, 2010).

Participants will be monitored closely and serum concentration of tacrolimus will be collected and dose adjusted if either greater than or below the target therapeutic range of 5-10 ng/mL.

Acute tacrolimus nephrotoxicity is usually manifested by a moderate decline in renal excretory function, which is readily reversible by a decrease in drug dosage. Although some degree of transient renal dysfunction may occur in patients with therapeutic levels of tacrolimus, significant renal toxicity is associated with elevated trough or steady state levels. In addition to an increase in BUN and creatinine, hyperkalemic hyperchloremic acidosis, low fractional excretion of sodium and the onset of hypertension with hypomagnesemia are seen with tacrolimus nephrotoxicity. Hypertension occurs in up to 60% of patients. Hypomagnesemia can be associated with neurologic symptoms, including seizures, cerebellar ataxia and depression. Dose-related hepatotoxicity, manifested by elevation of serum transaminases and bilirubin, has been reported.

Rapamycin:

Use of sirolimus is associated with a wide variety of well-described side effects (Wyeth Pharmaceuticals, Inc., 2010; Pfizer Europe MA EEIG, 2011). Warnings and precautions for sirolimus use include but are not limited to increased susceptibility to infection and the possible development of lymphoma, hypersensitivity reactions, angioedema, fluid accumulation and impairment of wound healing, hyperlipidemia, proteinuria, latent viral infections, and embryo-fetal toxicity. Exposure to sunlight and ultraviolet (UV) light should be limited by wearing protective clothing and using a sunscreen with a high protection factor. Most common adverse reactions (≥30% of participants) associated with sirolimus use for prophylaxis of organ rejection in clinical studies are peripheral edema, hypertriglyceridemia, hypertension, hypercholesterolemia, creatinine increased, constipation, abdominal pain, diarrhea, headache, fever, urinary tract infection, infection of the ear, nose, throat or sinus, anemia, nausea, arthralgia, pain and thrombocytopenia.

Participants will be monitored closely to minimize the risk of side effects related to use of sirolimus in the proposed study. Serum concentration of sirolimus will be collected and dose adjusted if either greater than or below the target therapeutic range of 4 to 8 ng/ml.

The anticipated toxicities of sirolimus in this trial are those related to its immune-suppressive properties, such as an increased likelihood of infection, and mucosal (including mouth, gastric, small bowel, or large bowel) ulcers, which may bleed. Other possible toxicities are listed here and include those reported with > 3% and <20% incidence in patients in any Sirolimus treatment group in the two controlled clinical trials for the prevention of acute organ graft rejection:

- Body as a Whole: abdomen enlarged, abscess, ascites, cellulitis, chills, face edema, flu syndrome, generalized edema, hernia, Herpes zoster infection, lymphocele, malaise, pelvic pain, peritonitis, sepsis;
- Cardiovascular System: atrial fibrillation, congestive heart failure, hemorrhage, hypervolemia, hypotension, palpitation, peripheral vascular disorder, postural hypotension, syncope, tachycardia, thrombophlebitis, thrombosis, vasodilatation;
- Digestive System: anorexia, dysphagia, eructation, esophagitis, flatulence, gastritis, gastroenteritis, gingivitis, gum hyperplasia, ileus, liver function tests abnormal, mouth ulceration, oral moniliasis, stomatitis;
- Endocrine System: Cushing's syndrome, diabetes mellitus, glycosuria, hypercholesterolemia, hyperlipidemia;
- Hematologic and Lymphatic System: ecchymosis, leukocytosis, lymphadenopathy, polycythemia, thrombotic thrombocytopenic purpura / hemolytic-uremic syndrome;
- Metabolic and Nutritional: acidosis, alkaline phosphatase increased, BUN increased, creatine phosphokinase increased, dehydration, healing abnormal, hypercalcemia, hyperglycemia, hyperphosphatemia, hypocalcemia, hypoglycemia, hypomagnesemia, hyponatremia, lactic dehydrogenase increased, SGOT increased, SGPT increased, weight loss;
- Musculoskeletal System: arthrosis, bone necrosis, leg cramps, myalgia, osteoporosis, tetany:
- Nervous System: anxiety, confusion, depression, dizziness, emotional lability, hypertonia, hypesthesia, hypotonia, insomnia, neuropathy, paresthesia, somnolence;
- Respiratory System: dyspnea, changes in PFTs, asthma, atelectasis, bronchitis, cough increased, epistaxis, hypoxia, lung edema, pleural effusion, pneumonia, rhinitis, sinusitis, diffuse alveolar hemorrhage;
- Skin and Appendages: fungal dermatitis, hirsutism, pruritus, skin hypertrophy, skin ulcer, sweating;
- Special Senses: abnormal vision, cataract, conjunctivitis, deafness, ear pain, otitis media, tinnitus;
- Urogenital System: albuminuria, bladder pain, dysuria, hematuria, hydronephrosis, impotence, kidney pain, kidney tubular necrosis, nocturia, oliguria, pyelonephritis, pyuria, scrotal edema, testis disorder, toxic nephropathy, urinary frequency, urinary incontinence, urinary retention.
- Less frequently occurring adverse events included: mycobacterial infections, Epstein-Barr virus infections, BK virus-associated nephropathy, skin cancer, lymphoma, pericardial effusion, posterior reversible encephalopathy syndrome (PRES), and pancreatitis.

- Risks related to other concurrent drug administration

Subjects may have concurrent medications that will require dose adjustment, or will necessitate adjustment of rapamycin and/or tacrolimus dosing. These may include anti-seizure medicine, and medicines for spasticity (such as baclofen). Consultation with a study site pharmacologist will occur prior to initiation of immunosuppression, in order to adjust medication dosing as necessary.

- Risks related to intrathecal administration of Meplida:

The most significant acute adverse effect of the experimental treatment that is reasonably anticipated would be a cytotoxic lymphocyte (CTL) response against the vector or against expressed wildtype AP4M1 protein. This could result in increased intracranial pressure, chemical meningitis, encephalitis, end organ damage, and death. Close serial examination and continuous monitoring in the PICU during the period of greatest threat of acute reaction to the investigational treatment, are expected to significantly reduce the risk of a poor outcome should this scenario present itself.

Patients who are presumed to have complete absence of the AP4M1 protein, CRIM-negative/'null' SPG50 patients, are at potentially higher risk of developing an immune response against the transgene. In order to minimize this risk to a foreign protein in the 'null' SPG50 patient, this proposed study will utilize the immune modulation regimen under use in predicted 'null' patients in the ongoing GAN IT gene transfer trial (NCT02362438) with demonstrated safety and tolerability to date.

- Risks related to lumbar puncture:

Lumbar puncture is a routine procedure performed in childhood that is safe and well tolerated. Local site discomfort (from needle insertion) may occur, and can be prevented with EMLA cream or equivalent prior to injection. The most common side effect from LP is post procedure headache (for reference, approximately 7% of patients with SMA administered SPINRAZA via LP experience headache). This is usually transient and responds well to NSAIDs/acetaminophen. There is an extremely small risk of infection with LP, and a small risk of spinal fluid leak. The primary symptoms of leak are headache and backpain. It may persist for 1 to 3 days. Persistent symptoms may require spinal patching accomplished with a brief interventional procedure. There is a very small risk of spinal cord injury due to the LP needle contacting the spinal cord or emerging nerve roots.

- Risks related to MRI and EEG assessments:

EEG is a well-tolerated procedure with minimal risk. There can be local irritation from the EEG leads, and the cleaning solution used to apply them.

MRI itself is a procedure with minimal risk. Gadolinium dye can be associated rarely with allergic reaction, requiring appropriate intervention (for example, anti-histamine therapy). If sedation is required for MRI, it can be associated with respiratory depression.

- **Rationale for Dose Selection**

The clinical dose will be scaled based on volume of CSF and age. The dose of 1E15 vg is anticipated to provide the maximum possible extent of gene replacement to target cells in the brain. Assuming that the AP4M1-KO mouse displays an adequate and quantifiable behavioral phenotype, the ongoing pharmacology study in this mouse model should confirm this anticipated benefit, and assumes no adverse findings in the ongoing toxicology study, CRL-5550008. Per FDA guidance, benefit is required in this instance as the subjects are pediatric and the risk is more than minimal, and redosing if efficacy is not achieved is not yet

a possibility. The clinical dose will be confirmed at the IND stage and will consider the expression of the AP4M1 subunit from the ongoing toxicology study.

- **Postponement of Dosing and Infusion Stopping Rules**

Delay of Melpida administration can occur if infection is found and should be fully resolved prior to dosing.

The infusion can be stopped at any time if there are any safety concerns or the following criteria are met:

- Pyrexia ≥ 38°C (the measurement should be repeated approximately 5 minutes after the first measurement to confirm the value).

- Heart rate >120 bpm and an increase from immediate pre-dose value of ≥ 30 bpm (both maintained for > 15 minutes); The infusion may be restarted if heart rate returns to pre-dose values and is evaluated as safe by the PI.

OR

- Any sign of anaphylaxis; infusion may not be restarted.

Adverse events will follow regulatory reporting rules per 21 CFR§312.32.

- **Controls and control of Bias**

This is an open-label safety study with no control. This design is appropriate based on the invasive nature of the administration and the lack of any treatment for SPG50. Descriptive statistics will be used to present the data.

- **Subject Characteristics and Stratification**

Subjects aged 1 to 10 years of age will be enrolled without stratification. This was chosen as symptoms present as early as 6 months of age, and because there is significant progression between the ages of 1 and 10 years (Section 15.1.2, Ebrahimi-Fakhari et al, 2020). Ten years was used as the upper bound as spasticity starts to appear in the upper extremities after that. As discussed by Gray et al, (2016), outcomes are often better in those subjects where treatment is administered earlier in the disease course.

- **Key Inclusion/Exclusion criteria**

Subjects must have a confirmed diagnosis of SPG50 disease by genomic DNA variant analysis demonstrating homozygous or compound heterozygous, definitively pathogenic and/or likely pathogenic variants in the AP4M1 gene, with a clinical history or examination features of neurologic or any other associated dysfunction.

Key exclusions are limited to concomitant medical conditions or other treatments that could confound the outcomes for Melpida, or increase the risk to benefit.

- **Schedule of Visits and Procedures and Duration of Follow-up**

See Table 17 for the schedule of visits and procedures. Subjects will be followed for a total of 5 years.

- **Data Safety Monitoring Board**

A Data and Safety Monitoring Board (DSMB) will be created consisting of at least 3 people who are expert in SPG50, gene therapy and safety/pharmacovigilance. The DSMB will review all safety data from all dosed subjects before dosing additional subjects.

- **Sample size and statistical analyses**

There are no sample size estimates for this safety and tolerability study.

- **Outcome measures**

Primary

Safety is a primary outcome for this clinical gene transfer trial. Safety will be assessed based on emerging adverse events, vital signs, clinical laboratory assessments, including hematology and clinical chemistry, 12-lead electrocardiograms (ECGs), and physical, neurological and ophthalmic exams. The sponsor proposes to define safety as failure to develop unacceptable toxicity, defined as the occurrence of two or more unanticipated Grade 3 or higher, possibly or probably treatment-related toxicities.

- Contrast-enhanced MRI of the brain and spinal cord.
- Sensory and motor nerve conduction studies.
- Video EEG.
- CSF cell count and protein.
- T-cell mediated immune responses to AAV9 and AP4M1 in blood.

Secondary Endpoints

Because of the lack of prior treatment trials and the rarity of the disease, to date, no specific outcome measure has been formally established as the optimal measure for therapeutic evaluation. Based on (1) the characteristic clinical presentation of AP4M1 patients, (2) pre-clinical data in AP4M1 mice and (3) published data, with limited cognitive and behavioral data measuring disease progression, the following secondary outcome measures out to 24 months are proposed:

- Modified Ashworth Scale (MAS)

The MAS instrument is provided in Section 17.3.

This instrument is primarily used to assess the effects of anti-spasticity drugs on spasticity in Multiple Sclerosis. It is suitable for ages 6 to 12y and 18 to 64y. It was chosen for this study to score changes in muscle tone. Scoring is performed as follows in a supine position:

0	No increase in muscle tone
1	Slight increase in muscle tone, manifested by a catch and release or by minimal resistance at the end of the range of motion when the affected part(s) is moved in flexion or extension
1+	Slight increase in muscle tone, manifested by a catch, followed by minimal resistance throughout the remainder (less than half) of the ROM
2	More marked increase in muscle tone through most of the ROM, but affected part(s) easily moved
3	Considerable increase in muscle tone, passive movement difficult
4	Affected part(s) rigid in flexion or extension

The final score is dependent on the number of muscles tested. Interrater reliability was performed on the elbow flexor muscle with a Kendall's tau correlation of 0.847 (p<0.001) (Bohannon and Smith, 1987).

Although identified for use in pediatrics aged 6 to 12y, it has been investigated for use in children ranging from 1.5 to 9 years with cerebral palsy (Mutlu et al, 2008). Each patient was assessed by 3 physiotherapists in 2 different sessions a week apart. Inter and intrarater reliability were evaluated by the intraclass correlation coefficient with scores between moderate to good; test-retest varied from poor to good (0.36 and 0.83).

- Tardieu Scale:

The Tardieu Scale instrument is provided in Section 17.4. This measures spasticity and takes into account resistance to passive movement at both slow and fast speed. Patients are in the sitting position to test. This has been used on stroke, brain injury, cerebral palsy with adequate to good interrater reliability. It is able to test the shoulder, elbow and wrist for the upper limbs and hip, knee and ankle for the lower limbs, with a total of 18 muscles. Scores are graded from 0 to 5 with 0 being no resistance to 5 being immobile joint. The range of possible scores is from 0 to 90. This also measures the velocity to stretch with V1 being as slow as possible, V2 being speed of limb segment falling and V3 being natural drop (as fast as possible). Only V2 and V3 are used to rate spasticity.

- Anti-AAV9 binding antibodies in serum and CSF.

Exploratory Endpoints
- Bayley 4 (Growth Scale Value) (Fine Motor & ADLS)
- Vineland (Inter-personal Domain, Fine Motor Domain, Personal Domain)
- Log Book Seizures
- Log Book # Of Falls

- **General Investigational Plan**

Future development plans are contingent on determining the safety of Melpida in subjects with the disease as proposed in this phase I/II trial. If the safety profile is satisfactory, it is

the sponsor's intent to continue development of the product to prolong survival and halt disease progression in patients with SPG50. If a suitable commercial partner is identified, this may include the submission of a Biologic License Application once appropriate data have been generated.

15   DATA TO SUPPORT DISCUSSION

15.1   Disease Background and Unmet Medical Need

15.1.1   Pathophysiology of SPG50

SPG50 is one of a group of adaptor protein complex 4 (AP-4) deficiencies (Figure 2). Homozygous (or compound heterozygous) loss-of-function variants in any of the four AP-4 subunits causes a neurological disorder characterized by spastic paraplegia, seizures, developmental delay and intellectual disability (Ebrahimi-Fakhari et al, 2020; Ebrahimi-Fakhari et al, 2018).

Figure 2   Schematic of Adaptor Protein complex 4
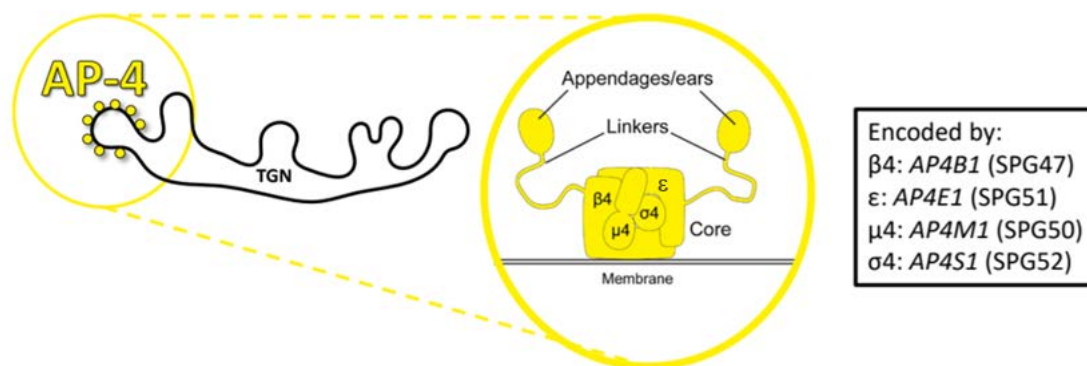
The four subtypes are SPG47, SPG50, SPG51 and SPG52 (Table 7).

Table 7   Subtypes of AP-4 deficiencies (Ebrahimi-Fakhari et al, 2018)

AP-4 subtype	OMIM	Mutation	Distribution	Male:Female
SPG47	#614066	AP4B1	34%	39% Female
SPG50	#612936	AP4M1	38%	43% Female
SPG51	#613744	AP4E1	13%	33% Female
SPG52	#614067	AP4S1	15%	52% Female

*From International Registry and Natural History Study (IRNHS) of Adaptor-Protein 4-Related Hereditary Spastic Paraplegia database (with 185 identified patients worldwide),

The AP-4 biology and molecular mechanisms of AP-4-hereditary spastic paraplegia (HSP) are not completely elucidated. Available data demonstrate that AP-4 complex consists of four subunits (β4, ε, μ4 and σ4) (Hirst et al, 2013) and has been implicated in trafficking of transmembrane proteins from the *trans*-Golgi network (TGN) to endosomes (Aguilar et al, 2001; Burgos et al, 2010; Toh et al, 2017). More recent cell culture studies have

30

demonstrated that ATG9A, an autophagy protein, is a cargo of AP-4 and loss of AP-4 leads to a mislocalization of ATG9A (Mattera et al, 2017; Davies et al 2018; De Pace et al, 2018; Ivankovic et al, 2020). Characterization of AP4B1- (Matsuda et al, 2008) and AP4E1-knockout mice has revealed widespread axonal pathology that includes reduced axonal development and prominent axonal swellings (De Pace et al, 2018; Ivankovic et al, 2020).

15.1.2   Natural history and seriousness of SPG50

Due to the rarity of the condition, limited data are available on the natural history of AP-4 deficiency. Ebrahimi-Fakhari et al, (2020) reports on 156 patients from 101 families from an AP-4 HSP registry. Subsets of patients have provided information on The Spastic Paraplegia Rating Scale (SPRS) (N=37), The Modified Ashworth Scale (MAS) (N=28), A SPATAX-EUROSPA Disability score (N=39) and a Four Stage Functional Mobility Score (N=85). This is the most extensive data available on these patients.

SPG50 is a serious and life-threatening disease with presentation and progression during childhood. Natural history data indicates age of symptom onset in infancy with diagnosis often delayed and occurring towards the end of the first decade (Ebrahimi-Fakhari et al, 2020) (Table 8). Of note, patients are often initially diagnosed with cerebral palsy (Jameel et al, 2014). Patients initially present with hypotonia, developmental delay, microcephaly and spasticity and paralysis in the lower limbs. As the disease progresses paralysis spreads to the hands and upper extremities and cognitive impairment worsens (Ebrahimi-Fakhari et al, 2018).

Table 8   Key demographic data for 156 AP-4 deficient patients from Ebrahimi-Fakhari et al, 2020

AP-4-HSP Subtype	Age at onset, years	Age at diagnosis, years	Age at last visit, years	Consanguinity	Familial case
AP4B1-HSP: n = 53	0.6 ± 0.4 (n = 34)	7.8 ± 6.9 (n = 31)	9.6 ± 6.1 (n = 48)	60% (n = 50)	55% (n = 53)
AP4M1-HSP: n = 59	0.9 ± 0.8 (n = 42)	11.7 ± 10.0 (n = 44)	13.7 ± 10.6 (n = 50)	77% (n = 52)	78% (n = 59)
AP4E1-HSP: n = 21	0.7 ± 0.3 (n = 6)	10.3 ± 6.7 (n = 14)	10.1 ± 6.6 (n = 15)	90% (n = 20)	86% (n = 21)
AP4S1-HSP: n = 23	0.8 ± 0.5 (n = 11)	10.4 ± 7.3 (n = 13)	10.6 ± 6.8 (n = 19)	47% (n = 19)	48% (n = 23)
Total: n = 156	0.8 ± 0.6 (n = 93)	10.2 ± 8.5 (n = 102)	11.4 ± 8.3 (n = 132)	69% (n = 141)	67% (n = 156)

There are relatively few adult patients for all phenotypes (Figure 3) (Ebrahimi-Fakhari et al, 2020). This is likely primarily due to the fact that the condition has only relatively recently been described, and that sequencing technologies such as whole exome sequencing are more frequently utilized in pediatric patients. It remains to be established whether the condition is life limiting.

Figure 3   **Age at last follow-up for 156 patients with AP-4 deficiency (from Ebrahimi-Fakhari et al, 2020)**
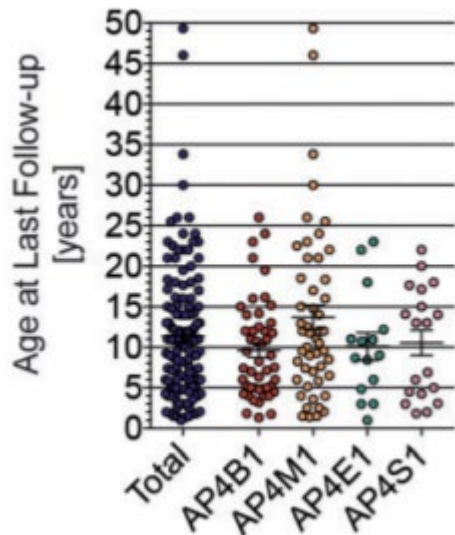
All phenotypes present with serious and quality of life limiting symptoms. From Ebrahimi-Fakhari, Behne et al (2018) GeneReview using data from the International Registry and Natural History Study of Adaptor-Protein 4-Related Hereditary Spastic Paraplegia database (updated 5-20-18 with 68 identified patients worldwide), characteristic clinical findings include:

- Progressive spastic paraplegia with progression to tetraplegia in the later stages (94%, 58/62)
- Early-onset developmental delay (100%, 68/68)
  - Delayed motor milestones (100%, 54/54)
  - Failure to achieve or loss of independent ambulation (93%, 41/44)
  - Impaired or absent speech development (98%, 51/52)
- Neonatal/infantile hypotonia (usually mild) (100%, 41/41)
- Postnatal microcephaly (77%, 47/61) (usually in -2SD to -3SD range)
- Early-onset seizures including frequent febrile seizures (42%, 25/59)
- Thinning of the corpus callosum (with prominent thinning of the posterior parts) (88%, 37/42)
- Delayed myelination and nonspecific loss of the periventricular white matter (69%, 29/42)
- Ex-vacuo ventriculomegaly, often with prominent enlargement of the posterior horns of the lateral ventricles (60%, 24/40)

When categorized by age, the following is a typical progression of motor function:

- 6 months: Microcephaly and low muscle tone become pronounced; MRI results show thinning of the corpus callosum.
- 1 year: Delays become evident, low muscle tone is more evident and microencephaly progresses such that head circumference becomes <2SD from age related mean.
- 2 years: Children are usually placed in multiple forms of therapy yet are unable to walk independently or speak. Spasticity begins to present in the ankles, calves and in some cases thighs.
- 3-5 years: Children exhibit greater spasticity, their ability to walk is severely impaired and a walker along with braces is used to keep children mobile. Botox injections have been used by many families as an intervention for spasticity. Some children develop a limited ability to speak a few words.
- 5-10 years: Children experience progressive spasticity and usually wheelchair-dependent. Typically, disease has not progressed to upper extremities yet. Some children are able to speak sentences, but others remain non-verbal.
- 10-15 years: Children are mostly wheelchair-dependent and many begin exhibiting spasticity in upper extremities.
- 15-20+ years: Children present with spasticity in all extremities and associated complications. Not much more is known beyond 15+ as there are very few patients in this category.

Published data from the 156 patients with AP-4 deficiency described by Ebrahimi-Fakhari et al, (2020) support earlier findings that symptoms are severely debilitating and manifest prior to adulthood (Table 9). Motor milestones were often missed or delayed and although some patients were able to sit and walk independently, these abilities were lost as the patients aged; the mean age of wheelchair dependency was 13.4 ± 9.8 years. Loss of previously acquired skills or development regression and cognitive decline was reported in 41% of patients.

Table 9   Clinical and Radiographic features of AP-4 deficiency (from Ebrahimi-Fakhari et al, (2020)

Principal clinical features of AP-4-HSP	
Developmental delay / intellectual disability	100%
Motor delay	100%
Speech delay	99%
Mild neonatal or infantile hypotonia	89%
Spasticity	97%
Spastic diplegia	54%
Spastic tetraplegia	43%
Hyperreflexia	92%
Babinski sign	88%
Contractures	50%
Drooling	70%
Postnatal microcephaly	83%
Dysmorphic facial features	78%
Foot deformities	69%
Febrile seizures	62%
Epilepsy	66%
Episodes of stereotypic laughter	56%
Principal radiographic features of AP-4-HSP	
Thin corpus callosum	90%
Ventriculomegaly	65%
White matter loss / changes	68%

15.1.3   The incidence and prevalence of SPG50

AP-4-HSP caused by mutations in AP-4 subunits is an ultra-rare autosomal recessive disease with ~156 patients identified worldwide and 59 identified with SPG50. There are ~9 patients with SPG50 in North America (AP4M1, OMIM #612936) (source: Ebrahimi-Fakhari et al, 2020).

The most robust data to support prevalence comes from the work by Ebrahimi-Fakhari et al, (2020) which describes 156 patients worldwide with AP-4 deficiency and 59 (38%) with SPG50 (Table 8). North America accounts for 15% of all known patients. Estimation for the number in North America is derived by:

$$59 * 0.15 = 8.85 \text{ persons}$$

Based on N=9 and a current US population size of 329,842,223 (source: U.S. Census Bureau and World Bank, June 25, 2020), prevalence for SPG50 is ([9/329,842,223]*100,000) 0.0027:100,000.

15.1.4   No Treatments are Available for Patients with SPG50

There are currently no commercial or investigational products available to treat SPG50.

15.2   Medical Plausibility of Melpida

Efficient transduction of the CNS is expected to positively impact the normal course of disease progression in SPG50 patients. The mode of action of Melpida is to target multiple types of cells including neurons and glia in the CNS after a single one-time intrathecal injection. Primary cellular targets proposed for the treatment of SPG50 are neurons and glia throughout the CNS. AP4M1 is a ubiquitous intracellular housekeeping gene, so the targeting of other cell types within the body is also desired.

The AAV9 vector utilized is expected to deliver the AP4M1 gene by the IT route to the brain, as the primary target (Bailey et al, 2018). Global transgene CNS delivery of AAV9 has been investigated in rodents, dogs, pigs and non-human primates (NHPs). Compared to other AAV vector serotypes and routes of administration, intrathecal (lumbar) administration of AAV9 vectors into the cerebrospinal fluid (CSF) achieves widespread distribution of the transgene to neurons and glia throughout the spinal cord and brain at a translationally-relevant dose (Snyder et al, 2011; Gray et al, 2011; Markakis et al, 2010; Masamizu et al, 2011). In pigs, a 50-100% transduction was achieved in spinal cord motor neurons along with transduction of neurons and glia in the brain at a dose of 1.7E11 vg/kg (Saraiva et al, 2016). In Cynomolgus monkeys, a dose of 2 to 3E12 vg per animal (~0.5E11 vg/kg) of AAV9/GFP vectors evenly distributed GFP-positive cells in a spatially homogenous manner throughout the entire brain (Choudhury et al, 2017). Similar results have been observed in cats, dogs, and non-human primates (Bradbury et al, 2020; Bucher et al, 2013; Haurigot et al, 2013; Samaranch et al, 2012; Samaranch et al, 2013).

Nonclinical proof-of-concept has been established with Melpida from various studies. These data are described in Section 15.3 of this document.

The introduced cDNA should exist primarily as an episome following transfer of Melpida, and express a normal version of functional human AP4M1 protein continuously, which is expected to prevent or slow the onset of SPG50 if treated pre-symptomatically, or slow/halt or reverse the progression of SPG50 if treated after symptom onset.

15.3   Preclinical Program Status

15.3.1   Brief Summary of Completed Studies and Conclusions

Several nonclinical studies have been conducted to date with Melpida or analogues of Melpida (Table 3).

The following nonclinical studies provide proof of concept that Melpida provides promise for the clinical treatment of SPG50:

- Fibroblasts from a patient with SPG50 (AP4M1(NM_004722.4):c.916C>T / (p.Arg306Ter) / c.694dupG (p.Glu232GlyfsTer21)) transduced with Melpida (***using an AAV2 capsid***) restored autophagy related 9A (ATG9A) trafficking and hence AP-4 function, at MOIs of 1E4 and 1E5 vg/cell with a suggestion of possible toxicity in the higher MOI group (Study #01) (Figure 4). Reducing the MOI to 1E2 and 1E3 vg/cell improved the phenotypes without noticeable toxicity in the same fibroblasts (Figure 5) as well as two other fibroblast cell lines (Figure 6 and Figure 7). Independent studies were duplicated in 2 additional patient lines at MOI 1E2, 1E3, 1E4 & 1E5 vg/cell and showed a dose-dependent reduction in ATG9A staining at the TGN, AP4E1 localization to the TGN and unchanged staining for TGN46 with phenotypic rescue in up to 77% of fibroblasts and no associated toxicity (Study #02) (Figure 8).
- In C57BL/6J mice, Melpida led to dose-dependent hAP4M1opt mRNA expression in all brain regions at 4 weeks post IT injection, with expression sustained up to at least 5 months post infusion. This confirmed that Melpida reached and achieved transgene expression at the targeted site of action (Study #05, Figure 9).
- No severe toxicity has been observed in the in-life portion of a 12 month non-GLP toxicology study of Melpida of either 1.25E11 or 5E11 vg in 5 µL in C57BL/6J mice (Study #05; Figure 10, Figure 11, Figure 12, Figure 13).


Ongoing studies include:
- **A 12-week GLP toxicology and biodistribution study in Sprague Dawley (SD) rats with the clinical product, Melpida, to support the safety of the proposed clinical dose (Study CRL-5550008). Dosing commenced on February 16th and will complete May 23rd. Intrathecal doses of 0 (vehicle), 0.36E12, 1.1E12, or 3.3E12 vg/mouse was administered in a volume of 20 or 60uL.**
- In vivo efficacy study in Ap4m1 knock out (KO) mice dosed at post-natal day (PND) 7 to 10 or PND 90, and assessed for potential phenotypic rescue (study 2020-06).

15.3.2   Study #01: Ex vivo efficacy study using patient-derived fibroblasts in Dr. Darius Ebrahimi-Fakhari Lab at Boston Children's Hospital (unpublished)

Dr. Ebrahimi-Fakhari's group at BCH found that transduction with Melpida vector in a fibroblast cell line from a SPG50 patient with the compound heterozygous variants of SPG50 (AP4M1(NM_004722.4):c.916C>T / (p.Arg306Ter) / c.694dupG (p.Glu232GlyfsTer21)) resulted in phenotype rescue including improved ATG9A trafficking (Figure 4A-B and Table 10) and restored AP4E1 levels (Figure 4), but with reduced cell number suggesting some toxicity in the 10^5 MOI group (Table 10). Their further experimentation demonstrated that treating the same cell line with Melpida at the MOI of 103 vg/cell resulted in similar benefits (Figure 5 and Table 11), without any obvious toxicity. Similar results were obtained in the fibroblast cell lines from two additional SPG50 patients with different mutations (Figure 6, Figure 7 and Table 12, Table 13). Taken together, these results confirmed the benefit of Melpida vector in SPG50 patient cells.

Figure 4 **Treatment with Melpida at the MOI of 10^4 and 10^5 vg/cell improved ATG9A trafficking and restored AP4E1 levels in fibroblasts from SPG50 patient with the mutation of p.R306X/p.E232GfsX21.**
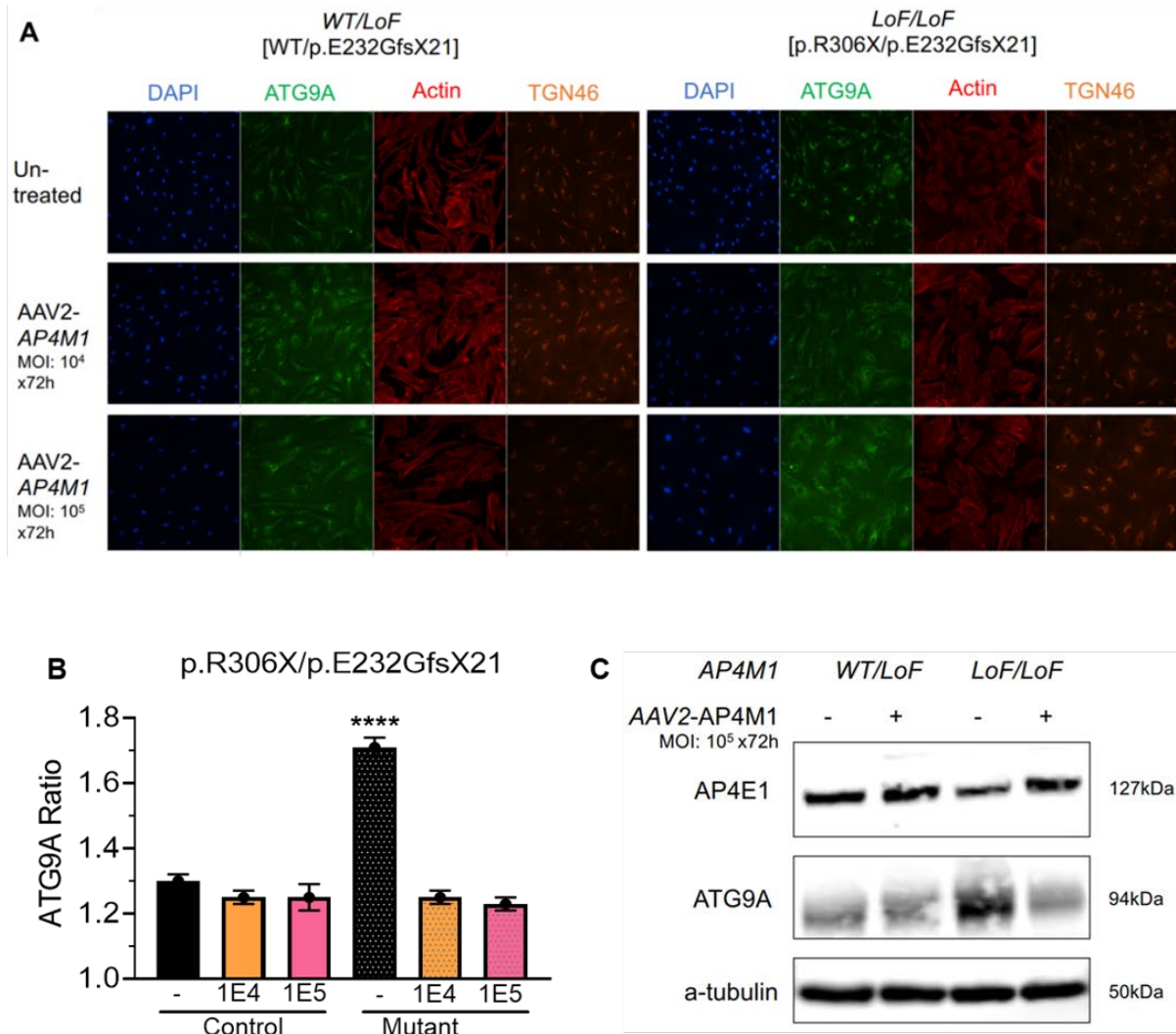
Footnote: A: Fibroblasts from a single SPG50 patient were treated with Melpida for 72 hours at the MOI of 10^4 and 10^5 vg/cell and then stained with DAPI and with antibodies against ATG9A, Actin, or TGN46. B: ATG9A ratio was calculated by dividing ATG9A inside TGN by ATG9A outside TGN. C: Cell lysate was used for Western blots to detect the protein levels of AP4E1, ATG9A, and α-tubulin. **** depicts $p<0.0001$ compared to the control fibroblasts without any treatment.

37

Table 10   **Treatment with Melpida at the MOI of 10^4 and 10^5 vg/cell improved ATG9A trafficking but decreased cell numbers with the 10^5 MOI in fibroblasts from SPG50 patient with compound heterozygous variants in AP4M1 of p.R306X/p.E232GfsX21.**

Mean	WT/LoF [WT/p.E232GfsX21]			LoF/LoF [p.R306X/p.E232GfsX21]		
	Untreated	+AAV2-AP4M1 (10^4)	+AAV2-AP4M1 (10^5)	Untreated	+AAV2-AP4M1 (10^4)	+AAV2-AP4M1 (10^5)
ATG9A Ratio (SD)	1.30 ± 0.02	1.25 ± 0.02	1.25 ± 0.04	1.71 ± 0.03	1.25 ± 0.02	1.23 ± 0.02
ATG9A inside TGN (A.U.) (SD)	1085.5 ± 45.8	1086.2 ± 26.2	1097.6 ± 97.9	1625.1 ± 41.7	1077.4 ± 22.4	1048.4 ± 55.1
ATG9A outside TGN (A.U.) (SD)	835.4 ± 33.3	868.7 ± 25.2	879.6 ± 110.7	953.2 ± 24.9	859.3 ± 16.8	851.7 ± 50.7
Cell count (per well) (SD)	482 ± 147	454 ± 80 (z=-0.3)	227 ± 34 (z= -7.5)	713 ± 193	415 ± 98 (z=-3.1)	131 ± 22 (z=-27.0)

Figure 5   **Treatment with Melpida at the MOI of 10^2 and 10^3 vg/cell improved ATG9A trafficking in fibroblasts from SPG50 patient with variants p.R306X/p.E232GfsX21.**
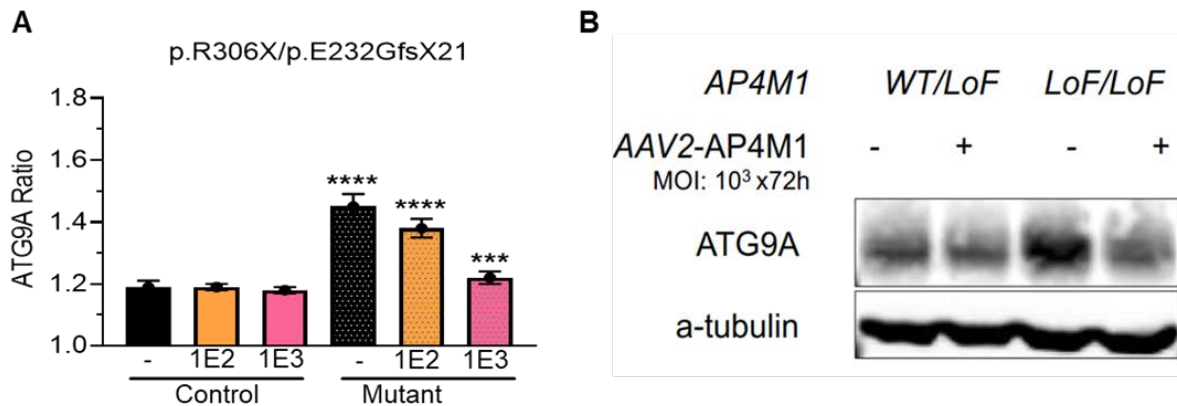

Footnote: A: Fibroblasts from a single SPG50 patient were treated with Melpida for 72 hours at the MOI of 10^2 and 10^3 vg/cell and then stained with DAPI and with antibodies against ATG9A, Actin, or TGN46. ATG9A ratio was calculated by dividing ATG9A inside TGN by ATG9A outside TGN. B: Cell lysate was used for Western blots to detect the protein levels of ATG9A and α-tubulin. **** depicts p<0.0001 and *** depicts compared to the control fibroblasts with the same treatment

Table 11   Treatment with Melpida at the MOI of 10^2 and 10^3 vg/cell improved ATG9A trafficking without significantly affecting cell numbers in fibroblasts from SPG50 patient with variants p.R306X/p.E232GfsX21.

Mean	WT/LoF [WT/p.E232GfsX21]			LoF/LoF [p.R306X/p.E232GfsX21]		
	Untreated	+AAV2-AP4M1 (10^2)	+AAV2-AP4M1 (10^3)	Untreated	+AAV2-AP4M1 (10^2)	+AAV2-AP4M1 (10^3)
ATG9A Ratio (SD)	1.19 ± 0.02	1.19 ± 0.01	1.18 ± 0.01	1.45 ± 0.04	1.38 ± 0.03	1.22 ± 0.02
ATG9A inside TGN (A.U.) (SD)	1534.3 ± 67.7	1495.2 ± 56.6	1482.9 ± 55.1	1982.1 ± 54.7	1829.7 ± 58.8	1521.1 ± 64.7
ATG9A outside TGN (A.U.) (SD)	1293.2 ± 62.2	1257.3 ± 40.9	1257.5 ± 37.6	1371.1 ± 70.8	1322.9 ± 53.9	1245.6 ± 46.2
Cell count (per well) (SD)	633 ± 57	594 ± 34 (z=-1.2)	529 ± 55 (z= -1.9)	650 ± 214	577 ± 216 (z=-0.3)	470 ± 158 (z=-1.1)

Figure 6   Treatment with Melpida at the MOI of 10^2 and 10^3 vg/cell improved ATG9A trafficking in fibroblasts from SPG50 patient with variants p.N73Kfs*43/p.Y284S
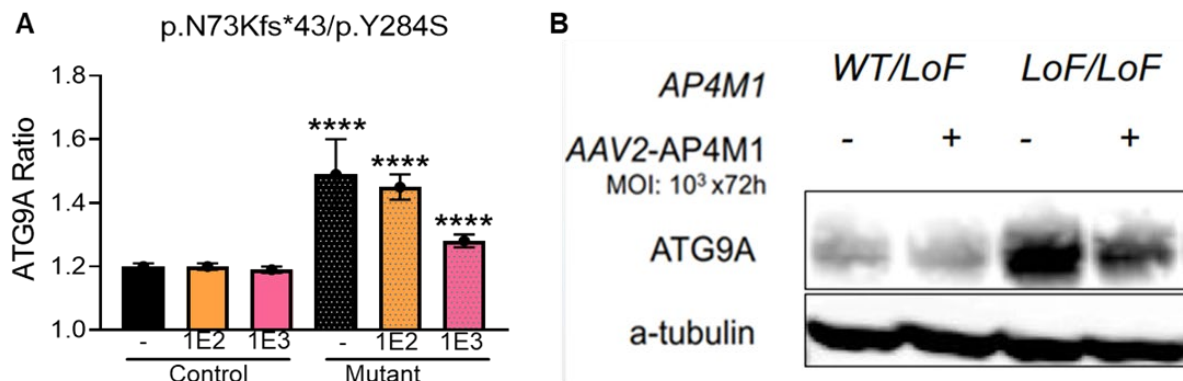

Footnote: A: Fibroblasts from a single SPG50 patient were treated with Melpida vector for 72 hours at the MOI of 10^2 and 10^3 vg/cell and then stained with DAPI and with antibodies against ATG9A, Actin, or TGN46. ATG9A ratio was calculated by dividing ATG9A inside TGN by ATG9A outside TGN. B: Cell lysate was used for Western blots to detect the protein levels of ATG9A and α-tubulin. **** depicts $p<0.0001$ compared to the control fibroblasts with the same treatment

Table 12   **Treatment with Melpida at the MOI of 10^2 and 10^3 vg/cell improved ATG9A trafficking without significantly affecting cell numbers in fibroblasts from SPG50 patient with variants p.N73Kfs*43/p.Y284S**

Mean	WT/LoF [WT/?]			LoF/LoF [p.N73Kfs*43/p.Y284S]		
	Untreated	+AAV2-AP4M1 (10^2)	+AAV2-AP4M1 (10^3)	Untreated	+AAV2-AP4M1 (10^2)	+AAV2-AP4M1 (10^3)
ATG9A Ratio (SD)	1.20 ± 0.01	1.20 ± 0.01	1.19 ± 0.01	1.49 ± 0.11	1.45 ± 0.04	1.28 ± 0.02
ATG9A inside TGN (A.U.) (SD)	1513.6 ± 59.1	1461.8 ± 33.9	1452.7 ± 44.2	2042.0 ± 254.5	1799.9 ± 56.6	1544.2 ± 39.9
ATG9A outside TGN (A.U.) (SD)	1257.2 ± 50.3	1215.3 ± 31.5	1217.7 ± 46.3	1388.0 ± 311.5	1242.9 ± 21.9	1203.6 ± 19.4
Cell count (per well) (SD)	877 ± 174	927 ± 132 (z=+0.4)	778 ± 122 (z= -0.8)	804 ± 226	755 ± 212 (z=-0.2)	528 ± 143 (z=-1.9)

Figure 7   **Treatment with Melpida at the MOI of 10^2 and 10^3 vg/cell improved ATG9A trafficking in fibroblasts from SPG50 patient with variants IVS13+2dupT/p.T69P**
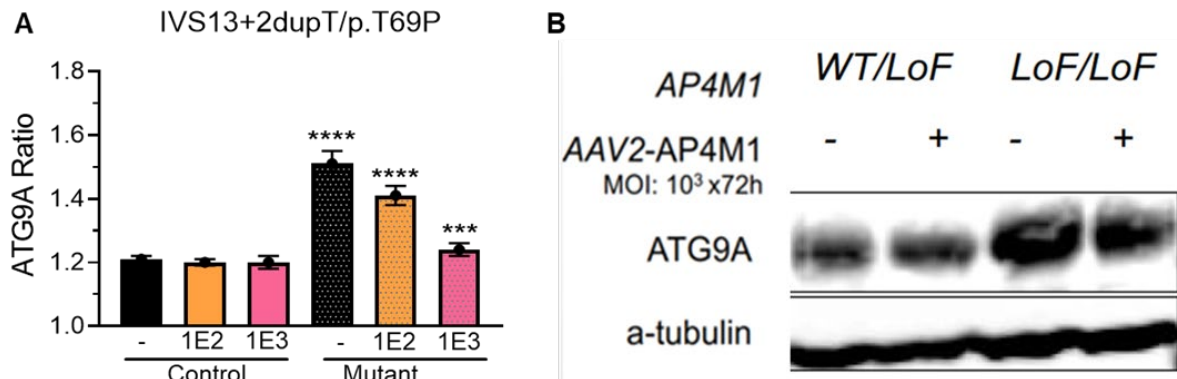

Footnote: A: Fibroblasts from a single SPG50 patient were treated with Melpida for 72 hours at the MOI of 10^2 and 10^3 vg/cell and then stained with DAPI and with antibodies against ATG9A, Actin, or TGN46. ATG9A ratio was calculated by dividing ATG9A inside TGN by ATG9A outside TGN. B: Cell lysate was used for Western blots to detect the protein levels of ATG9A and α-tubulin. **** depicts p<0.0001 and *** depicts p<0.001 compared to the control fibroblasts with the same treatment

40

Table 13 **Treatment with Melpida at the MOI of 10^2 and 10^3 vg/cell improved ATG9A trafficking without significantly affecting cell numbers in fibroblasts from SPG50 patient with variants IVS13+2dupT/p.T69P**

Mean	WT/LoF [WT/IVS13+2dupT]			LoF/LoF [IVS13+2dupT/p.T69P]		
	Untreated	+AAV2-AP4M1 (10^2)	+AAV2-AP4M1 (10^3)	Untreated	+AAV2-AP4M1 (10^2)	+AAV2-AP4M1 (10^3)
ATG9A Ratio (SD)	1.21 ± 0.01	1.20 ± 0.01	1.20 ± 0.02	1.51 ± 0.04	1.41 ± 0.03	1.24 ± 0.02
ATG9A inside TGN (A.U.) (SD)	1415.7 ± 43.2	1432.8 ± 54.0	1445.8 ± 79.6	1947.1 ± 108.5	1751.4 ± 73.5	1450.8 ± 63.9
ATG9A outside TGN (A.U.) (SD)	1171.1 ± 38.7	1194.1 ± 43.5	1206.2 ± 55.5	1293.4 ± 86.7	1240.5 ± 55.0	1168.9 ± 37.2
Cell count (per well) (SD)	820 ± 122	833 ± 128 (z=+0.1)	647 ± 90 (z= -1.9)	559 ± 170	549 ± 143 (z=-0.1)	375 ± 77 (z=-2.4)

15.3.3 Study #02: Ex vivo efficacy study using patient-derived fibroblasts in Dr. Juan Bonifacino's Laboratory at NIH (unpublished)

Dr. Bonifacino's group at NIH used two additional fibroblasts cell lines from two SPG50 sibling patients, with a homozygous donor splice site pathogenic variant in intron 14 of the AP4M1 gene. Cells were transduced with Melpida for 72 hours at 10^2, 10^3, 10^4 or 10^5 vg/cell MOI and then stained with DAPI for nuclear DNA and with antibodies to ATG9A, AP4E1 or TGN46. Untreated patient cells show concentration of ATG9A at the TGN, diffuse staining for AP4E1 and TGN staining for TGN46. AP4M1-transduced cells show reduced ATG9A staining at the TGN, AP4E1 localization to the TGN and unchanged staining for TGN46 demonstrating that transduction with Melpida resulted in phenotype rescue (Figure 8 and Table 14). At the highest virus dose of 10^5 vg/cell, the rescue is 49% and 77% of the cells for patient #1 and #2 respectively (Figure 8 and Table 14). Importantly, these cells did not show any sign of toxicity after infection, with nuclei, cell size, and shape looking normal after staining. Similar results were obtained from their second repeated experiment. Taken together, these results confirmed the benefit of Melpida in SPG50 patient cells.

Figure 8   Treatment with Melpida vector dose dependently rescued the phenotypes of fibroblasts from two sibling SPG50 patient with a donor splice site pathogenic mutation in intron 14 of the AP4M1 gene (c.1137+1G→T)
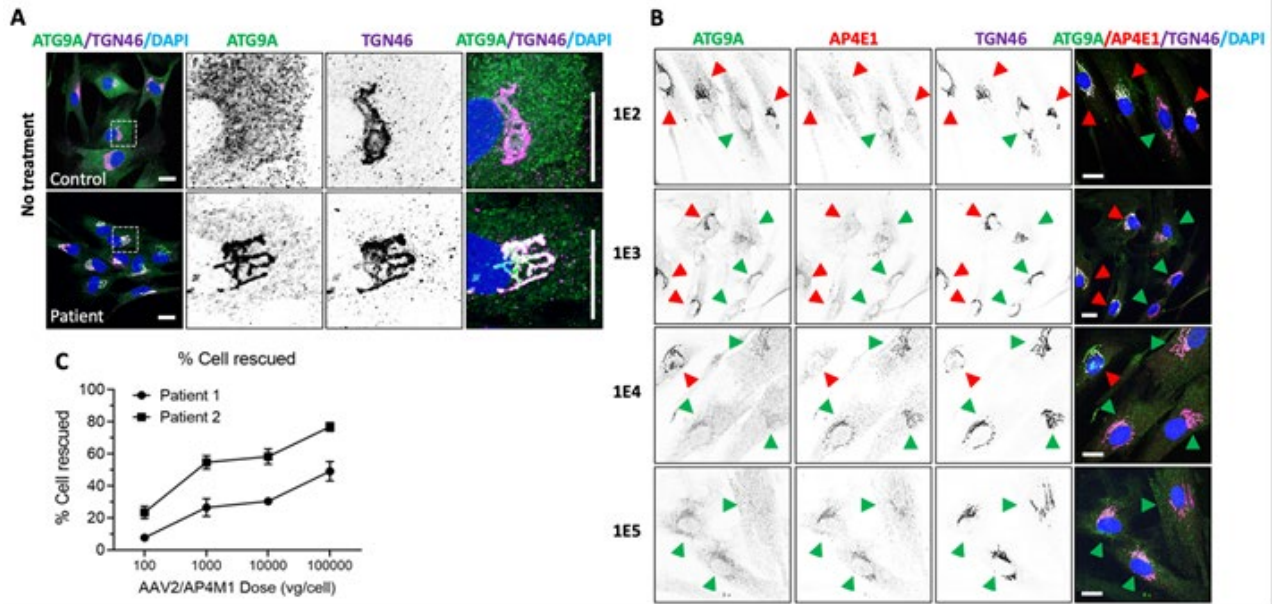
Footnote: A: AP4M1 mutation causes accumulation of ATG9A in the Golgi complex. Control and patient fibroblasts were immunostained for endogenous ATG9A and the Golgi marker TGN46. Magnified views of the boxed areas are shown at right. Notice the co-localization of ATG9A with TGN46 in the patient, but not control cells. B: Rescue of AP4M1 staining and ATG9A distribution with Melpida vector. Patient fibroblasts were infected with the indicated number of viral particles per cell. Cells were immunostained for endogenous ATG9A, AP-4 epsilon subunit (AP4E1) and TGN46. Green arrowheads indicate rescued cells. Red arrowheads indicate cells that were not rescued. Single-channel images are shown in inverted grayscale and merged images in color. Nuclei were stained with DAPI in blue. Scale bars: 20 micrometers. C: Total and rescued cells were counted and % rescue was calculated. Values are the means from 2 independent experiments

Table 14   **Treatment with Melpida at the MOI of 10^2, 10^3, 10^4, and 10^5 vg/cell dose dependently rescued the phenotypes of fibroblasts from two sibling SPG50 patients with a donor splice site pathogenic mutation in intron 14 of the AP4M1 gene (c.1137+1G→T).**

Patient	#1			#1			#1			#1		
# of viral particles	100			1000			10.000			100.000		
# of cells	imaged	rescued	% rescue	imaged	rescued	% rescue	imaged	rescued	% rescue	imaged	rescued	% rescue
Exp #1	91	8	8.8	95	21	22.1	125	36	28.8	128	55	43.0
Exp #2	106	7	6.6	111	32	28.8	181	58	32.0	116	64	55.2
Mean	98.5	7.5	**7.7**	103.0	26.5	**25.5**	153.0	47.0	**30.4**	122.0	59.5	**49.1**

Patient	#2			#2			#2			#2		
# of viral particles	100			1000			10.000			100.000		
# of cells	imaged	rescued	% rescue	imaged	rescued	% rescue	imaged	rescued	% rescue	imaged	rescued	% rescue
Exp #1	112	22	19.6	97	49	50.5	101	54	53.5	98	78	79.6
Exp #2	117	32	27.4	107	63	58.9	103	65	63.1	112	83	74.1
Mean	114.5	27.0	**23.5**	102.0	56.0	**54.7**	102.0	59.5	**58.3**	105.0	80.5	**76.8**

Footnote: Quantification of the rescue in fibroblasts derived from 2 different patients. Values are the means from 2 independent experiments

Conclusion based on Study #01 and Study #02:

It was found that pathologic variants in the AP4M1 gene caused ATG9A retention in TGN and reduced AP4E1 levels in multiple fibroblast cell lines from patients with different AP4M1 variants. Restoring the expression of WT AP4M1 in these patient fibroblast cell lines with AAV2 vectors can improve ATG9A trafficking and restore AP4E1 levels, indicating the improved function of AP-4 complex. Importantly, AP4M1-AAV2 was able to restore function in patient fibroblasts with diverse pathologic variants in AP4M1.

15.3.4   Study 2020-06: A 12-month (with 6 month interim) non-GLP study to determine the efficacy of AAV9/*AP4M1* (Melpida) in a mouse knock-out (KO) model of SPG50 when administered by the intrathecal route at 1.25 and 5E11 vg in 5uL.

The design of this study is provided in Table 15.

The in-life phase of this study was performed at University of Texas Southwestern (UTSW) Medical Center, Dallas, TX and assessments were as follows:

- Cage side observation to assess acute tolerability of Melpida following intrathecal administration

- Monitoring for body weight, clinical signs including behavioral changes and alterations in neurological status, adverse events and mortality.

43

- Three weeks post injection, 6 mice from each group were euthanized. Mouse brains were used for AP4M1 mRNA expression by RNAscope and mouse serum was used to check serum toxicity panel including Aspartate transaminase (AST), Total bilirubin (TBIL), Albumin (ALB), Creatine Kinase (CK), and Blood Urea Nitrogen (BUN). Splenocytes from mouse spleen and lymphocytes from lymph nodes were used in ELISpot assays to detect any immune responses to either AAV9 or transgene.

- Performance in a battery of behavioral tests is being assessed at 3, 5, 8 and 12 months of age compared to heterozygous (Het) control littermates.

- Blood and tissue samples will be collected from mice that were euthanized for humane reasons. Where possible, a detailed necropsy is also performed to investigate or identify the reason for the ailment by a trained technician or veterinary staff.

- Terminal serum and tissue samples at 12 months old will be collected for serum toxicity panel and histopathological assessment, respectively.

Table 15   12-month efficacy study in AP4M1 KO mouse (ongoing)

Ap4m1 Allele	AAV9/*AP4M1* Dose	Dose Group (Name)	Number of Animals (Male/Female)	Time of Dosing
Ap4m1 (+/-)	na	A (Het)	22 (11/11)	na
Ap4m1 (-/-)	Vehicle*	B	22 (11/11)	PND 7-10
Ap4m1 (-/-)	1.25E11 vg/animal*	C	22 (11/11)	PND 7-10
Ap4m1 (-/-)	5E11 vg/animal*	D	22 (11/11)	PND 7-10
Ap4m1 (-/-)	Vehicle*	E	22 (11/11)	PND 90
Ap4m1 (-/-)	1.25E11 vg/animal*	F	22 (11/11)	PND 90
Ap4m1 (-/-)	5E11 vg/animal*	G	22 (11/11)	PND 90
*Animals dosed via lumbar IT injection. Het, Heterozygous. KO, Knockout. PND, post-natal day.				

There will be 2 reports issued for this study, an interim from in-life for the initial 6 months, and a final report with in-life and histopathology assessments. Both will be provided in the IND submission assuming all treated mice are terminated prior to IND submission. The 6 month data were unavailable at the time of generating this PreIND briefing book.

15.3.1   Study #05: Confirmation that intrathecal administration with Melpida reaches the site of action and leads to expression in WT C57BL/6J mice in Dr. Steven Gray Lab at UTSW Medical Center

Mice were randomized into 3 treatment groups for vehicle, low (1.25E11 vg) and high (5E11 vg) dose of Melpida (n=10 per group; 5 male, 5 female per group). Melpida or vehicle was administered via intrathecal lumbar injection in a volume of 5 μL, and monitored for 16 weeks. Three (3) mice per gender per group were taken down 4 weeks post injection for AP4M1 mRNA expression by RNAscope. The following results were generated:

- Intrathecal administration of Melpida dose-dependently increased hAP4M1opt mRNA in all brain regions.

Animals receiving AAV9/AP4M1 had detectable levels of hAP4M1opt mRNA in all brain regions assessed (Figure 9, panel A). The high dose group had significantly higher mRNA levels than control animals. While the low dose animals did have detectable levels of mRNA, these levels were not significantly higher than the controls. Moreover, hAP4M1opt mRNA expression sustained up to 5-month post injection (panels B and C).

Figure 9 **Melpida dose-dependently increased hAP4M1opt mRNA in brain regions of WT mice.**
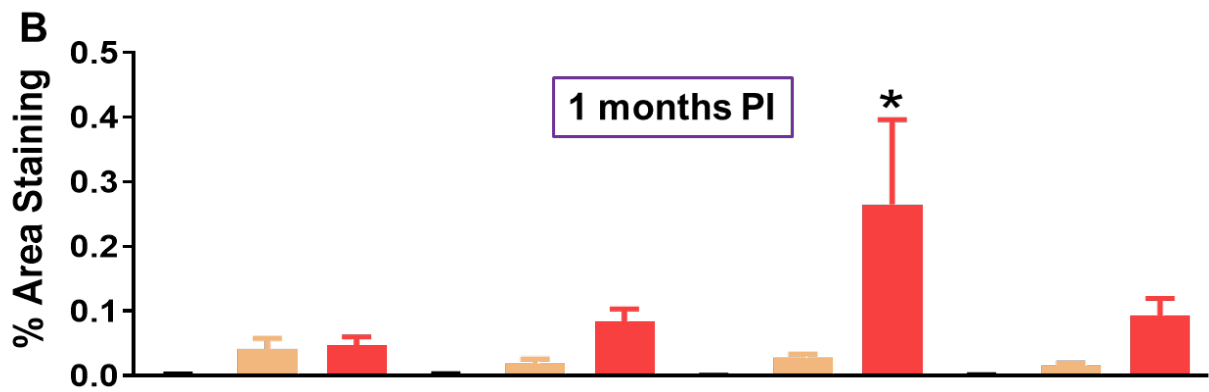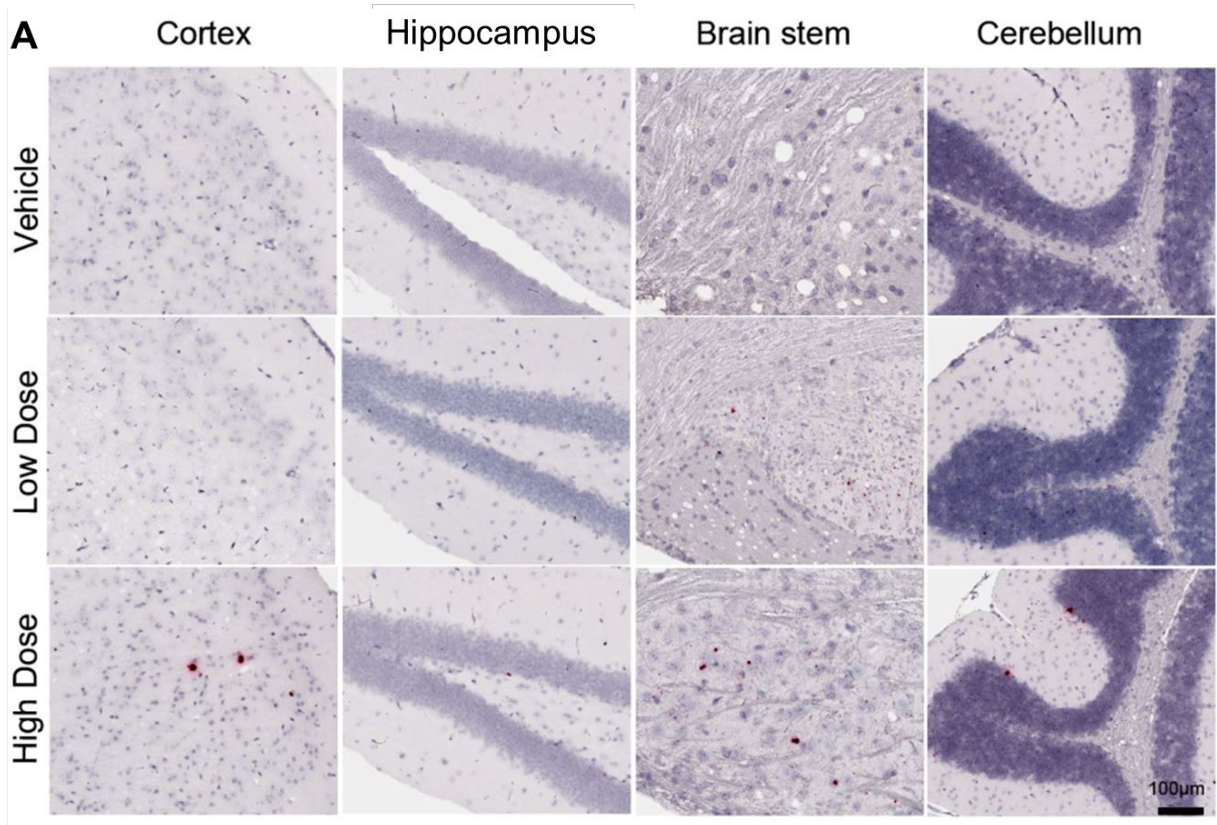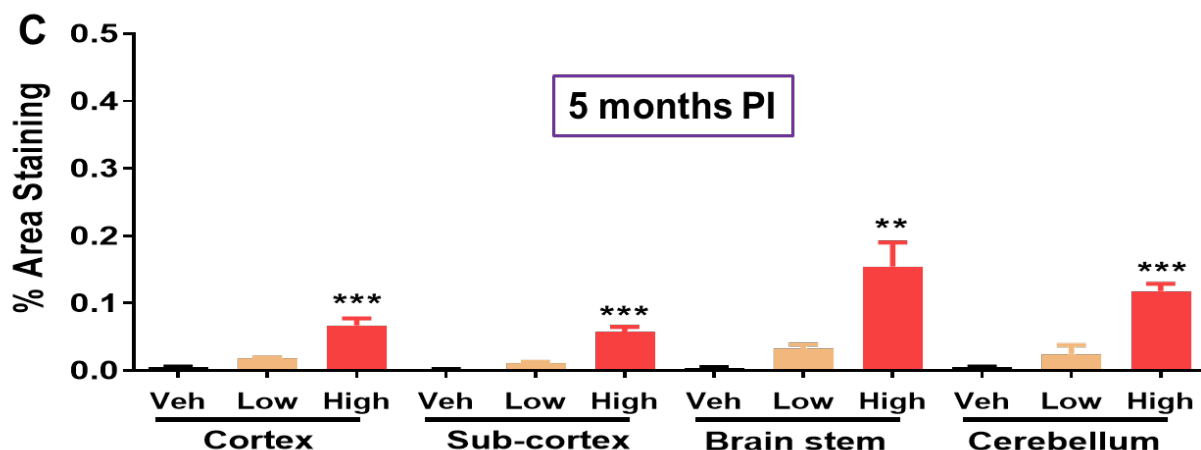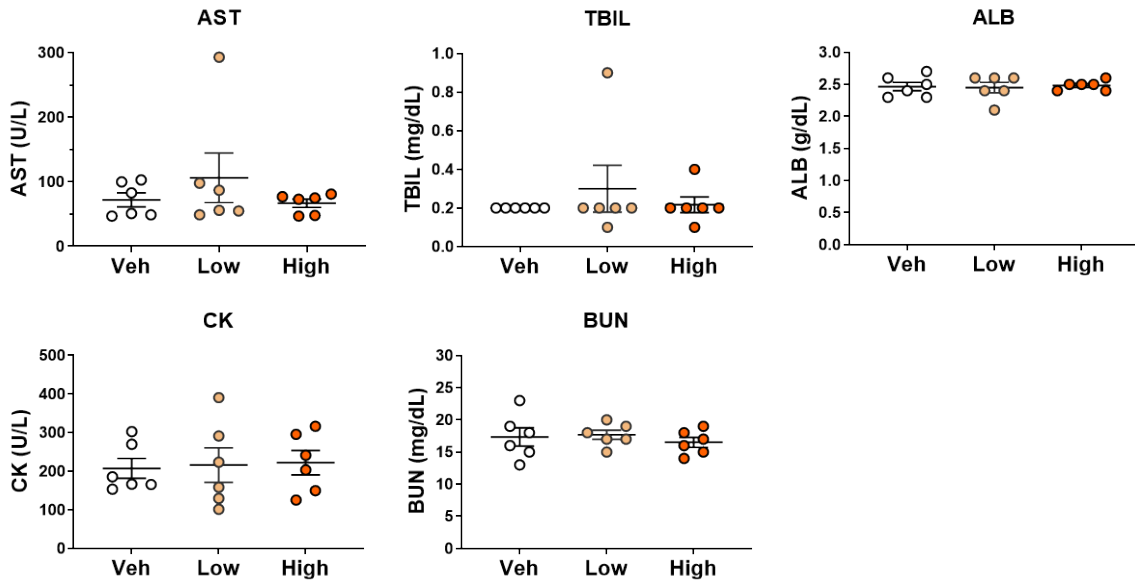
Either high (5E11 vg/mouse) or low (1.25E11 vg/mouse) dose of Melpida was administered IT to WT mice of 7 weeks old. At 1-month (A and B) and 5 months (C) post injection, mouse brain was harvested for RNAscope staining to detect hAP4M1opt mRNA. Histology images were digitized with a ScanScope slide scanner and analyzed using custom analysis settings in HALO™ Image Analysis Platform (A). Results are presented as % area staining positive for hAP4M1opt mRNA by tissue region (mean ± standard error, n=6/group in B and n=4/group C). ***P<0.001, **p<0.01, and *p<0.05 compared to mice treated with vehicle.

- IT Melpida caused no changes in a serum toxicity panel in most of the WT mice

Animals receiving AAV9/AP4M1 had normal levels of serum toxicity panel including AST, TBIL, ALB, CK, and BUN 1-month post injection in all except 1 male mouse (Figure 10). In this male mouse which received low dose 1.25E11 vg/mouse, AST and TBIL reached 293 U/L and 0.9 mg/dL, respectively. At 5-month post injection (Figure 11), serum toxicity panel were normal in all except 1 female mouse. In this female mouse which received vehicle, AST and TBIL reached 180 U/L and 0.76 mg/dL, respectively. At 12-month post injection (Figure 12), serum toxicity panel were also normal in all except 2 male mice which received high dose 5E11 vg/mouse. In one male mouse, AST, TBIL, and BUN reached 187 U/L, 0.72 mg/dL, and 124 mg/dL, respectively. In the other male mouse, AST reached 283 U/L. In conclusion, our results suggest that most of the WT mice tolerate AAV9/AP4M1 well, however there is the possibility that toxicity to the liver and kidney may occur sporadically in response to Melpida.

46

Figure 10.   Melpida caused no elevation of serum toxicity panel 1-month post injection in all mice except 1 male mouse which received low dose.

Either high (5E11 vg/mouse) or low (1.25E11 vg/mouse) dose of Melpida was administered IT to WT mice of 7 weeks old. At 1-month post injection, mouse serum was collected for serum chemistry. Results are presented as mean ± standard error, n=6/group. No significant difference was found between any groups.

Figure 11.   Melpida caused no elevation of serum toxicity panel 5-month post injection in all mice except 1 female mouse which received vehicle.
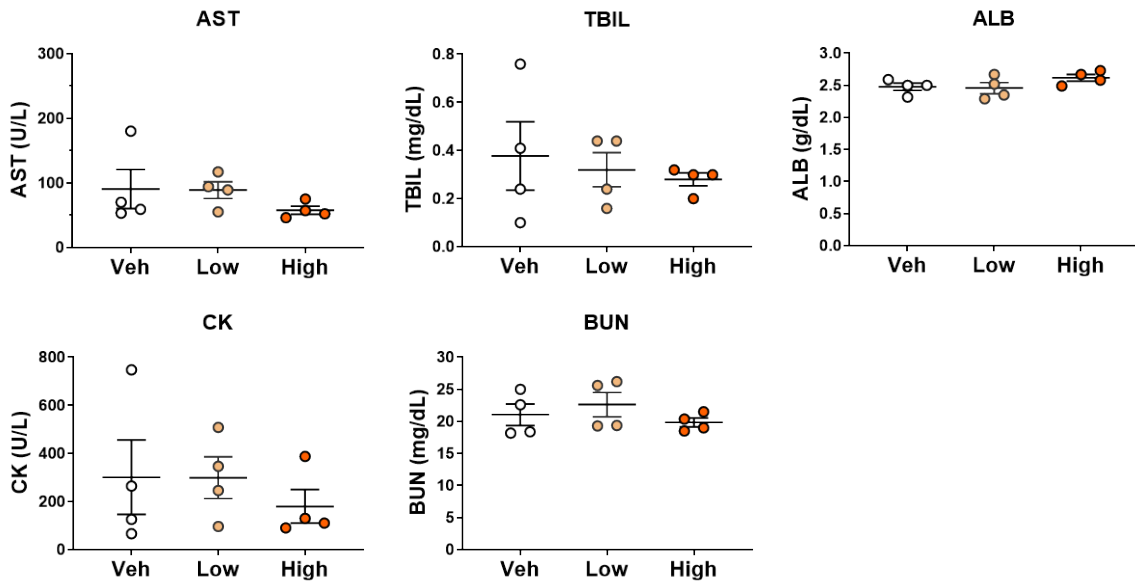
Either high (5E11 vg/mouse) or low (1.25E11 vg/mouse) dose of Melpida was administered IT to WT mice of 7 weeks old. At 5-month post injection, mouse serum was collected for serum chemistry. Results are presented as mean ± standard error, n=4/group. No significant difference was found between any groups.

Figure 12 **Melpida caused no elevation of serum toxicity panel 12-month post injection in all mice except 2 male mice which received high dose.**
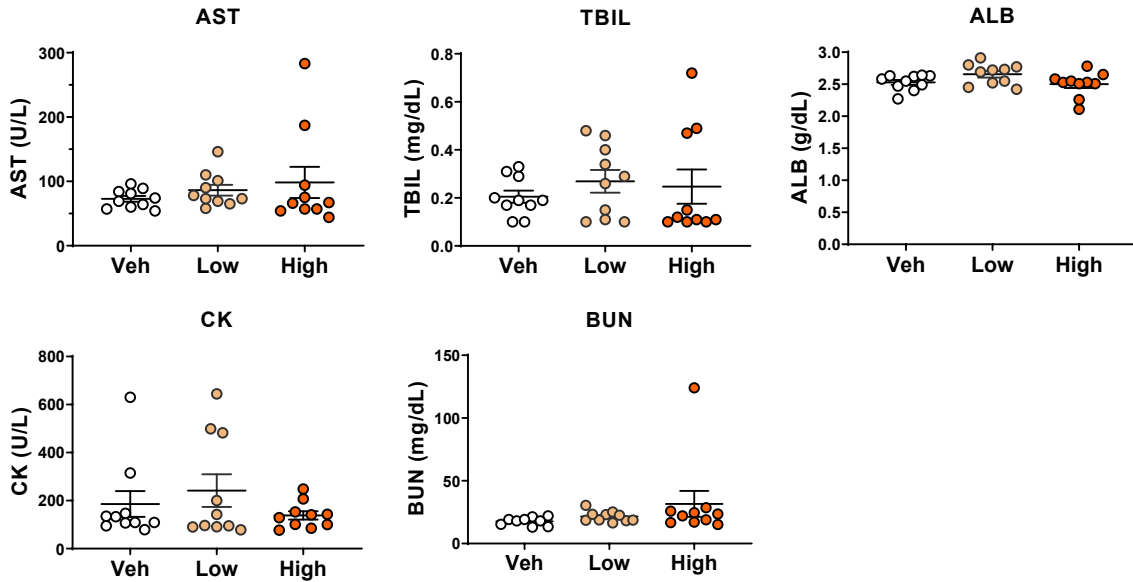

Either high (5E11 vg/mouse) or low (1.25E11 vg/mouse) dose of Melpida was administered IT to WT mice of 7 weeks old. At 12-month post injection, mouse serum was collected for serum chemistry. Results are presented as mean ± standard error, n=10/group. No significant difference was found between any groups.

- IT Melpida caused no effects on body weight in male or female mice

Body weight difference was monitored to assess the overall health of the animals. There was no significant difference in body weight between groups within male or female mice at any point of assessment (Figure 13), suggesting that doses up to 5E11 vg/mouse are well tolerated in the WT C57BL/6J mice up to 12 months following the treatment.

Figure 13   Melpida caused no effects on body weight in male or female mice.
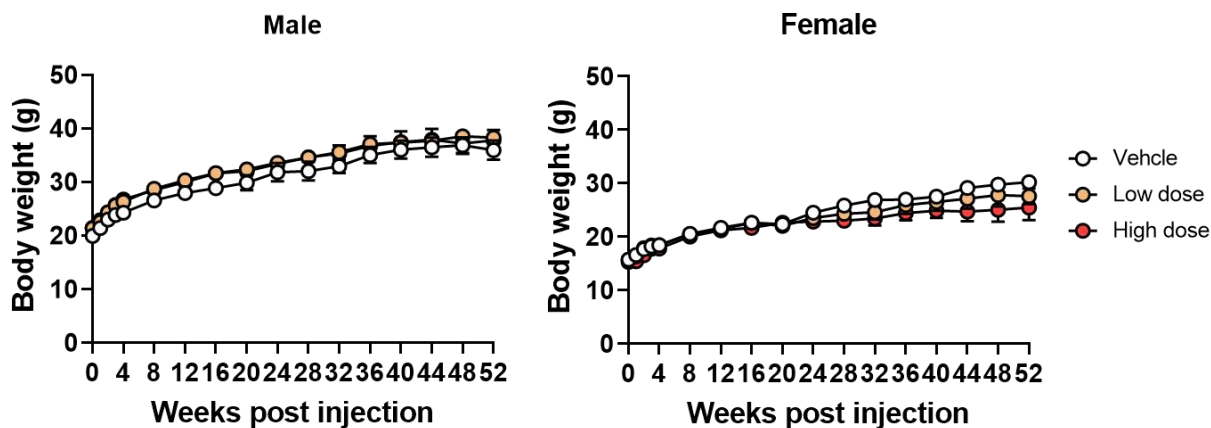

Either high (5E11 vg/mouse) or low (1.25E11 vg/mouse) dose of Melpida was administered IT to WT mice of 7 weeks old.
Mice were weighed weekly for the first month following the treatment and then monthly thereafter.

- IT Melpida has caused no deaths in WT mice

There were no obvious clinical signs of morbidity in the adult WT mice dosed with Melpida
at doses up to 5E11 vg/mouse. There were no unexpected deaths. All mice survived to their
respective sacrifice endpoints indicating that doses up to 5E11 vg/mouse are well tolerated in
WT C57BL/6J mice up to 12 months following the treatment.

- IT Melpida caused no clinical signs or adverse events in WT mice
No outward signs of toxicity were noted over the duration of the study.

- Histopathology
At 1, 5, and 12-month post injection, 6, 4, and 10 mice/group were anesthetized respectively
and perfused with phosphate-buffered saline containing 1 U/mL heparin and main
tissues/organs were harvested. No obvious abnormalities were noticed except for some
granular appearance in the liver of three mice (2 males and 1 female) which were treated with
high dose and evaluated at 12-months post injection. All tissues/organs collected were fixed
in 10% formalin for 24 hours and then transferred to 70% ethanol. The histopathological
evaluations on collected tissue samples were performed in a blinded fashion and reported by
Dr. Mary Wight-Carter, DVM, DACVP, Veterinary Pathologist. Dr. Wight-Carter concluded
that 1) all microscopic changes present in the mice harvested at 3 and 7 months old are
considered variations on normal microanatomy for mice this age, and 2) the tumors and
increased number of inflammatory cell infiltrates and degenerative lesions seen in the mice
harvested at 14 months old are expected in mice as they age.

In summary, Melpida administered IT at doses up to 5E11 vg/mouse appears to be safe and
well tolerated in WT mice in general. Nevertheless, we also saw some potential toxicity. For
example, 1 male mouse which received 1.25E11 vg/mouse dose had elevation of liver
enzymes at 1-month post injection. One female mouse which received vehicle had elevation
of liver enzyme at 5-months post injection. Two male mice which received 5E11 vg/mouse

had liver and/or kidney toxicity at 12-months post injection. The same 2 male mice plus 1 female mouse had granular appearance in the liver during necropsy, which was then diagnosed as hepatocellular adenomas by microscopic examination of major tissues/organs. The elevation in liver enzymes seen sporadically across the vehicle, low dose, and high dose groups, without a clear dose-response, suggests that these may not be directly related to Melpida. However, there remains the possibility that high doses of Melpida may be associated with sporadic liver toxicity.

15.3.2   Summary

The findings from these various nonclinical studies provide the proof of concept to support the potential of benefit of Melpida to patients with SGP50. The ongoing GLP toxicology study (CRL-5550008) will need to confirm the safety prior to future clinical dosing.

15.4   Clinical Development Program

15.4.1   Previous Human Experience with Melpida

There is no prior clinical experience with Melpida. There are limited analogous cases which have used AAV9 for the treatment of other diseases which are presented in Table 16. The CLN7 program proposed the same dose (1E15 vg) as proposed for Melpida.

Table 16   Other studies conducted with AAV9

Name	Description NCT#	Route of administration
CLN7	scAAV9 Gene therapy for CLN7 NCT04737460	Intrathecal (5E14 and 1E15 vg)
Zolgensma	scAAV9 gene therapy for Spinal Muscular Atrophy (SMA) NCT03381729	Intrathecal (6E13, 1.2E14 and 2.4E14 vg)
vLINCL6	scAAV9 gene therapy for variant late infantile neuronal ceroid lipofuscinosis NCT02725580	Intrathecal
GAN Gene Therapy	scAAV9 Gene Therapy for Giant Axonal Neuropathy NCT02362438	Intrathecal
CLN3 Gene Therapy	scAAV9 Gene Therapy for CLN3 Batten Disease NCT03770572	Intrathecal

15.4.2   General Investigational Plan for Melpida

Future development plans are contingent on determining the safety of Melpida in subjects with the disease as proposed in this phase I/II trial. If the safety profile is satisfactory, it is

the sponsor's intent to continue development of the product with the goal of prolonging survival and slowing/halting disease progression in patients with SPG50. If a suitable commercial partner is identified, this may include the submission of a Biologic License Application once appropriate data have been collected.

15.5   Regulatory

This PreIND application is the first regulatory interaction for Melpida. Rare Pediatric Disease designation was granted to Melpida September 2020 (#RPD-2020-441); although orphan designation was requested at the same time, there were no in vivo studies to support the application. An orphan designation will be resubmitted before the 1-year deadline requested in the ODD response (#DRU-2020-7740). The IND is proposed for submission 2H2021. Additional designations will be sought as and when the appropriate data are generated.

16 LIST OF REFERENCES

The following citations are ranked as most supportive for this briefing package and are provided with this submission; all remaining citations are available on request:

- Bradbury AM, Bagel JH, Nguyen D, et al. Krabbe disease successfully treated via monotherapy of intrathecal gene therapy. J Clin Invest. 2020;130(9):4906-4920. doi:10.1172/JCI133953

- Chen X, Snanoudj-Verber S, Pollard L, et al. Pre-clinical Gene Therapy with AAV9/AGA in Aspartylglucosaminuria Mice Provides Evidence for Clinical Translation. Mol Ther. 2021;29(3):989-1000. doi:10.1016/j.ymthe.2020.11.012

- Ebrahimi-Fakhari D, Teinert J, Behne R, et al. Defining the clinical, molecular and imaging spectrum of adaptor protein complex 4-associated hereditary spastic paraplegia. Brain. 2020;143(10):2929-2944. doi:10.1093/brain/awz307

- Ivankovic D, Drew J, Lesept F, et al. Axonal autophagosome maturation defect through failure of ATG9A sorting underpins pathology in AP-4 deficiency syndrome. Autophagy. 2020;16(3):391-407. doi:10.1080/15548627.2019.1615302

- Masamizu Y, Okada T, Kawasaki K, et al. Local and retrograde gene transfer into primate neuronal pathways via adeno-associated virus serotype 8 and 9. Neuroscience. 2011;193:249-258. doi:10.1016/j.neuroscience.2011.06.080.

All References Cited and available on request:

Aguilar RC, Boehm M, Gorshkova I, et al. Signal-binding specificity of the mu4 subunit of the adaptor protein complex AP-4. J Biol Chem. 2001;276(16):13145-13152. doi:10.1074/jbc.M010591200

Bailey RM, Armao D, Nagabhushan Kalburgi S, Gray SJ. Development of Intrathecal AAV9 Gene Therapy for Giant Axonal Neuropathy. Mol Ther Methods Clin Dev. 2018;9:160-171. Published 2018 Feb 15. doi:10.1016/j.omtm.2018.02.005

Behne R, Teinert J, Wimmer M, et al. Adaptor protein complex 4 deficiency: a paradigm of childhood-onset hereditary spastic paraplegia caused by defective protein trafficking. Hum Mol Genet. 2020;29(2):320-334. doi:10.1093/hmg/ddz310

Bohannon RW, Smith MB. Interrater reliability of a modified Ashworth scale of muscle spasticity. Phys Ther. 1987 Feb;67(2):206-7. doi: 10.1093/ptj/67.2.206. PMID: 3809245.

Bradbury AM, Bagel JH, Nguyen D, et al. Krabbe disease successfully treated via monotherapy of intrathecal gene therapy. J Clin Invest. 2020;130(9):4906-4920. doi:10.1172/JCI133953

Bucher T, Colle MA, Wakeling E, Dubreil L, Fyfe J, Briot-Nivard D, Maquigneau M, Raoul S, Cherel Y, Astord S, Duque S, Marais T, Voit T, Moullier P, Barkats M and Joussemet B (2013) scAAV9 Intracisternal Delivery Results in Efficient Gene Transfer to the Central Nervous System of a Feline Model of Motor Neuron Disease. Hum Gene Ther 24:670-82. doi: 10.1089/hum.2012.218

Burgos PV, Mardones GA, Rojas AL, et al. Sorting of the Alzheimer's disease amyloid precursor protein mediated by the AP-4 complex. Dev Cell. 2010;18(3):425-436. doi:10.1016/j.devcel.2010.01.015

Caviness VS, Kennedy DN, Richelme N, Rademacher J and Filipek PA (1996). The Human Brain Age 7–11 Years: A Volumetric Analysis Based on Magnetic Resonance Images. Cerebral Cortex 6:726-736.

Chen X, Snanoudj-Verber S, Pollard L, et al. Pre-clinical Gene Therapy with AAV9/AGA in Aspartylglucosaminuria Mice Provides Evidence for Clinical Translation. Mol Ther. 2021;29(3):989-1000. doi:10.1016/j.ymthe.2020.11.012

Choudhury SR, Hudry E, Maguire CA, Sena-Esteves M, Breakefield XO and Grandi P (2017). Viral vectors for therapy of neurologic diseases. Neuropharmacology120:63-80. doi: 10.1016/j.neuropharm.2016.02.013

Davies AK, Itzhak DN, Edgar JR, et al. AP-4 vesicles contribute to spatial control of autophagy via RUSC-dependent peripheral delivery of ATG9A. Nat Commun. 2018;9(1):3958. Published 2018 Sep 27. doi:10.1038/s41467-018-06172-7.

De Pace R, Skirzewski M, Damme M, et al. Altered distribution of ATG9A and accumulation of axonal aggregates in neurons from a mouse model of AP-4 deficiency syndrome. PLoS Genet. 2018;14(4):e1007363. Published 2018 Apr 26. doi:10.1371/journal.pgen.1007363.

Dekaban AS and Sadowsky D (1978). Changes in brain weights during the span of human life: relation of brain weights to body heights and body weights. Ann. Neurology, 4:345-356, 1978.

Ebrahimi-Fakhari D, Behne R, Davies AK, Hirst J. AP-4-Associated Hereditary Spastic Paraplegia. In: Adam MP, Ardinger HH, Pagon RA, et al., eds. GeneReviews®. Seattle (WA): University of Washington, Seattle; 1993, updated 2018.

Ebrahimi-Fakhari D, Teinert J, Behne R, et al. Defining the clinical, molecular and imaging spectrum of adaptor protein complex 4-associated hereditary spastic paraplegia. Brain. 2020;143(10):2929-2944. doi:10.1093/brain/awz307

Gray SJ, Matagne V, Bachaboina L, Yadav S, Ojeda SR and Samulski RJ (2011) Preclinical Differences of Intravascular AAV9 Delivery to Neurons and Glia: A Comparative Study of Adult Mice and Nonhuman Primates. Mol Ther. (6):1058-1069.

Gray SJ. Timing of Gene Therapy Interventions: The Earlier, the Better. Mol Ther. 2016;24(6):1017-1018. doi:10.1038/mt.2016.20

Harrison T, Graham F, Williams J (1977). Host-range mutants of adenovirus type 5 defective for growth in HeLa cells. Virology, 77:319-329.

Haurigot V, Marco S, Ribera A, Garcia M, Ruzo A, Villacampa P, Ayuso E, Anor S, Andaluz A, Pineda M, Garcia-Fructuoso G, Molas M, Maggioni L, Munoz S, Motas S, Ruberte J, Mingozzi F, Pumarola M and Bosch F (2013) Whole body correction of mucopolysaccharidosis IIIA by intracerebrospinal fluid gene therapy. J Clin Invest. doi: 10.1172/JCI66778

Hirst J, Irving C, Borner GH. Adaptor protein complexes AP-4 and AP-5: new players in endosomal trafficking and progressive spastic paraplegia. Traffic. 2013;14(2):153-164. doi:10.1111/tra.12028

Ivankovic D, Drew J, Lesept F, et al. Axonal autophagosome maturation defect through failure of ATG9A sorting underpins pathology in AP-4 deficiency syndrome. Autophagy. 2020;16(3):391-407. doi:10.1080/15548627.2019.1615302

Jameel M, Klar J, Tariq M, et al. A novel AP4M1 mutation in autosomal recessive cerebral palsy syndrome and clinical expansion of AP-4 deficiency. BMC Med Genet. 2014;15:133. Published 2014 Dec 14. doi:10.1186/s12881-014-0133-2

Manns MP, Czaja AJ, Gorham JD, et al. Diagnosis and management of autoimmune hepatitis. Hepatology. 2010;51(6):2193-2213. doi:10.1002/hep.23584

Markakis EA, Vives KP, Bober J, Leichtle S, Leranth C, Beecham J, Elsworth JD, Roth RH, Samulski RJ and Redmond DE, Jr. (2010) Comparative transduction efficiency of AAV vector serotypes 1-6 in the substantia nigra and striatum of the primate brain. Mol Ther 18:588-93.

Masamizu Y, Okada T, Kawasaki K, et al. Local and retrograde gene transfer into primate neuronal pathways via adeno-associated virus serotype 8 and 9. Neuroscience. 2011;193:249-258. doi:10.1016/j.neuroscience.2011.06.080.

Matsuda S, Miura E, Matsuda K, et al. Accumulation of AMPA receptors in autophagosomes in neuronal axons lacking adaptor protein AP-4. Neuron. 2008;57(5):730-745. doi:10.1016/j.neuron.2008.02.012

Mattera R, Park SY, De Pace R, Guardia CM, Bonifacino JS. AP-4 mediates export of ATG9A from the trans-Golgi network to promote autophagosome formation. Proc Natl Acad Sci U S A. 2017;114(50):E10697-E10706. doi:10.1073/pnas.1717327114

Morgan CJ, Pyne-Geithman GJ, Jauch EC, Shukla R, Wagner KR, Clark JF and Zuccarello M (2004). Bilirubin as a cerebrospinal fluid marker of sentinel subarachnoid hemorrhage: a preliminary report in pigs. J Neurosurg 101:1026-1029

Mutlu A, Livanelioglu A, Gunel MK. Reliability of Ashworth and Modified Ashworth scales in children with spastic cerebral palsy. BMC Musculoskelet Disord. 2008;9:44. Published 2008 Apr 10. doi:10.1186/1471-2474-9-44

Pardridge WM. 1991. Transnasal and intraventricular delivery of drugs. Raven Press, New York.

Pardridge WM. 2011. Drug transport in brain via the cerebrospinal fluid. Fluids Barriers CNS 8:7.

Samaranch L, Salegio EA, San Sebastian W, Kells AP, Bringas JR, Forsayeth J and Bankiewicz KS (2013) Strong cortical and spinal cord transduction after AAV7 and AAV9 delivery into the cerebrospinal fluid of nonhuman primates. Hum Gene Ther 24:526-32. doi: 10.1089/hum.2013.005

Samaranch L, Salegio EA, San Sebastian W, Kells AP, Foust KD, Bringas JR, Lamarre C, Forsayeth J, Kaspar BK and Bankiewicz KS (2012) Adeno-associated virus serotype 9 transduction in the central nervous system of nonhuman primates. Hum Gene Ther 23:382-9. doi: 10.1089/hum.2011.200

Saraiva J, Nobre RJ and Pereira de Almeida L (2016). Gene therapy for the CNS using AAVs: The impact of systemic delivery by AAV9. J Control Release 241:94-109. doi: 10.1016/j.jconrel.2016.09.011.

Snyder BR, Gray SJ, Quach ET, Huang JW, Leung CH, Samulski RJ, Boulis NM and erici T (2011) Comparison of Adeno-Associated Viral Vector Serotypes for Spinal Cord and Motor Neuron Gene Delivery. Hum Gene Ther. 22(9):1129-1135

Sullivan HG, Miller DJ, Griffith RL, Carter W and Rucker S (1979). Bolus versus steady-state infusion for determination of CSF outflow resistance. Ann. Neurology. 5:228-238

Toh WH, Tan JZ, Zulkefli KL, Houghton FJ, Gleeson PA. Amyloid precursor protein traffics from the Golgi directly to early endosomes in an Arl5b- and AP4-dependent pathway. Traffic. 2017;18(3):159-175. doi:10.1111/tra.12465

Zacharia A, Zimine S, Lovblad KO, Warfield S, Thoeny H, Ozdoba C, Bossi E, Kreis R, Boesch C, Schroth Gand Hüppi PS (2006). Early Assessment of Brain Maturation by MR Imaging Segmentation in Neonates and Premature Infants. American Journal of Neuroradiology. 27:972-977

17 APPENDICES

17.1   Abbreviations

AAV	adeno-associated virus
AP-4	Adaptor Protein complex
ATG9A	Autophagy Related 9A
BCH	Boston Children's Hospital
BGH	Bovine growth hormone
CDMO	Contract development and manufacturing organization
CMC	Chemistry, manufacturing and controls
CNS	Central nervous system
CSF	Cerebrospinal fluid
DAPI	4′,6-diamidino-2-phenylindole
DNA	Deoxyribonucleic acid
FDA	Food and Drug Administration
GFP	Green fluorescent protein
GLP	Good laboratory practice
h	Human
hAP4M1opt	Human optimized AP4M1
HSP	Hereditary spastic paraplegia
IND	Investigational New Drug
iPSCs	Induced pluripotent stem cells
IRNHS	International registry Natural History Study
IT	Intrathecal
ITR	Inverted terminal repeat(s)
kg	Kilogram
MOI	Multiplicity of Infection
NIH	National Institutes of Health
opt	Optimized
OOPD	Office of Orphan Products Development
sc	Self-complimentary
SPG50	Spastic Paraplegia 50
RNA	Ribonucleic acid
TGN	Trans-Golgi network
US	Unites States of America
UTSW	University of Texas Southwestern Medical Center
VCC	Viralgen Vector Core, Spain
vg	Vector genome(s)
WT	Wild type

17.2 Concept Protocol for Melpida

Title	Phase I/II gene transfer clinical trial of Melpida for treatment of subjects with SPG50 disease.
Number of Subjects	N = 3
Clinical Study Phase	Phase I/II trial
Number of Centers	To be confirmed
Study Objectives	Primary outcome is safety Secondary outcomes explore efficacy
Study Design	Open-label, single dose, clinical trial of Melpida injected intrathecally.
Study Dose	Subjects will receive an intrathecal (IT) infusion of 10 mL at 1E14 vg/mL for a total dose of 1E15 vg

Inclusion Criteria	• Age 1 to 10 years old
	• Confirmed diagnosis of SPG50 disease by:
	   • Genomic DNA mutation analysis demonstrating homozygous or compound heterozygous, pathogenic and/or potentially pathogenic variants in the *AP4M1* gene
	   • Clinical history or examination features consistent with SPG50 and that include neurologic dysfunction
	• Parent/legal guardian willing to accompany the participant to all study visits and who will provide permission for their child's participation.

Exclusion Criteria	• Inability to participate in the clinical evaluation • Presence of a concomitant medical condition that precludes lumbar puncture or use of anesthetics • Bleeding disorder or any other medical condition or circumstance in which a lumbar puncture is contraindicated according to local institutional policy • Inability to be safely sedated in the opinion of the clinical anesthesiologist • Active infection based on clinical observations • Concomitant illness or requirement for chronic drug treatment that in the opinion of the PI creates unnecessary risks for gene transfer • Any item which would exclude the patient from being able to undergo MRI according to local institutional policy • Any other situation that would exclude the patient from undergoing any other procedure required in this study • The presence of significant non-SPG50 related CNS impairment or behavioral disturbances that would confound the scientific rigor or interpretation of results of the study • Have received an investigational drug within 30 days prior to screening or plan to receive an investigational drug (other than gene therapy) during the study.
Study Procedures	**Administration**: AP4M1 subjects will have a spinal needle inserted percutaneously at the lumbar level into the intrathecal space of the spinal column. A volume of CSF approximately equal to the infusion volume is withdrawn from lumbar thecal sac. The vector solution is then infused at a rate of 1 mL per minute. Subject will remain in a 15-degree Trendelenburg (head down) position for 1 hour following vector administration. **Dosing volume**: Will be calculated per Table 6, depending on final vector product concentration. A tapering course of prophylactic enteral prednisolone will be administered.

57

	Location: The procedure will be performed in the Radiology Fluoroscopy suite with an anesthesiologist or qualified physician present to administer sedation as needed. Subjects will stay in Pediatric ICU overnight. **Subject monitoring**: Physiologic monitoring in accord with the standards set by the American Society of Anesthesiologists will be utilized for all subjects while they are receiving analgesia/anesthesia and until they have fully recovered from its effects. Vital signs (BP, HR, RR, T, O2 saturation, EKG) will be checked hourly while hospitalized after anesthesia. The full schedule of assessments is provided in Table 17.
Primary Outcome	Determination of safety based on the development of unacceptable toxicity. Unacceptable toxicity will be defined as the occurrence of one or more unanticipated Grade 3 or higher treatment-related toxicities.
Secondary Outcomes	Stability or improvement in spasticity based on the Modified Ashworth scale (MAS) & Tardieu.
Exploratory Outcomes	• Bayley 4 (Growth Scale Value) (Fine Motor & ADLS) • Vineland (Inter-personal Domain, Fine Motor Domain, Personal Domain) • Log Book Seizures • Log Book # Of Falls
Study Duration	Initial screening and evaluation will be performed up to 4 weeks before the administration of Melpida. Subjects will be evaluated for safety over a 5-year period. Patients will be tested at baseline (-28 to -1 days) and return for follow up visits on days 7, 14, 28, Month 3, 6 and 12, then every 6 months thereafter out to 24 months. After the 24-month visit, they will be followed according to an annual monitoring plan out to 5 years post dose; both safety and efficacy will be assessed at these annual visits.
Sample Size	This is a single dose study in 3 subjects
Statistical Analysis	This is a Phase I/II trial, with safety as the primary measure. Secondary outcomes include potential efficacy measures. Data will be presented as summary tables and graphs.
Long-term follow-up	Safety follow-up will continue over a two-year period that incorporates the active phase of the protocol. Patients will then transfer to an annual monitoring program where data will be collected from annual standard care visits for up to 5 years.

Table 17   Schedule of Events

Visit/ Screen¥§	1	2	3	4	5	6	7	8	9	10	11	12	13
Day	-28 to -7	-1	1	2	7	14	21	28	3M	6M	9M	12M	24M
Informed Consent	X												
Informed Consent Review			X	X	X		X		X	X	X	X	X
Genetic confirmation	X												
Vitals	X	X	X	X	X		X	X	X	X	X	X	X
Medical History	X		X	X					X	X	X	X	X
Physical Exam	X	X	X	X	X		X	X	X	X	X	X	X
Outcome Evaluations	X								X	X	X	X	X
Con Meds	X	X	X	X				X	X	X	X	X	X
AE Review	X	X	X	X	X	X	X	X	X	X	X	X	X
Screen Labs*	X												
Exploratory Labs****			X		X		X		X	X		X	X
Safety Labs**	X		X	X	X	X	X		X	X		X	X
AAV Dosing			X										
EKG	X		X						X	X	X	X	X
Neurologic Exam	X		X	X	X	X	X		X	X	X	X	X
Lumbar Puncture			X				-		X	X		X	X
CSF Analysis***			X				-		X	X		X	X
Neuropsych	X								X	X		X	X
MRI			X+				-		X+	X		X	X
EEG	X		X		X		X		X	X		X	X
AAV NAb Titers	X		X	X	X	X	X		X	X		X	X
Clinical Assess	X		X		X		X		X	X	X	X	X

¥Some visits are in-patient admissions and may last for more than the day of admittance.

§Between study visits there will be biweekly phone calls to assess con meds and AEs.

*Screening labs include HIV Ab, Hepatitis A Ab, Hepatitis B Surface Ab, Hepatitis Surface Ag, Hepatitis C Core Ab, PPD, HTLV1

**Safety labs include CBC With Differential, ESR, CRP, LFT, HCT, MCV, Na, K, Cl, CO2, BUN, Cr, glucose, ALT, AST, T. bili, D. bili, Alk phos, GGT, Calcium, PT, PTT, Urinalysis, EKG, Cardiac Safety (Tn, ProBNP, CK-MB), Sirolimus Levels, Tacrolimus levels & Lipid Profile.

***CSF Analysis includes cell count, differential, protein, glucose, gram stain, culture, oligoclonal bands, cytokine analysis.

****Exploratory Tests = AAv9 NAB, Serum Cytokine Analysis & EliSPOT

X+ = MRI Brain & Spine (With contrasts at Baseline & 3M only)

17.3   Modified Ashworth Scale (MAS) instrument

Modified Ashworth Scale Instructions

<u>General Information (derived Bohannon and Smith, 1987):</u>

- Place the patient in a supine position
- If testing a muscle that primarily flexes a joint, place the joint in a maximally flexed position and move to a position of maximal extension over one second (count "one thousand one")
- If testing a muscle that primarily extends a joint, place the joint in a maximally extended position and move to a position of maximal flexion over one second (count "one thousand one")
- Score based on the classification below

<u>Scoring (taken from Bohannon and Smith, 1987):</u>

0   No increase in muscle tone

1   Slight increase in muscle tone, manifested by a catch and release or by minimal resistance at the end of the range of motion when the affected part(s) is moved in flexion or extension

1+   Slight increase in muscle tone, manifested by a catch, followed by minimal resistance throughout the remainder (less than half) of the ROM

2   More marked increase in muscle tone through most of the ROM, but affected part(s) easily moved

3   Considerable increase in muscle tone, passive movement difficult

4   Affected part(s) rigid in flexion or extension

<u>Patient Instructions:</u>
The patient should be instructed to relax.

Modified Ashworth Scale Testing Form

Name:_____ Date:_____

Muscle Tested   **Score**

_____   _____

_____   _____

_____   _____

_____   _____

_____   _____

_____   _____

_____   _____

_____   _____

_____   _____

Reference for test instructions:

Bohannon, R. and Smith, M. (1987). "Interrater reliability of a modified Ashworth scale of muscle spasticity." Physical Therapy 67(2): 206.

17.4   Tardieu Scale instrument

TARDIEU SCALE

This scale quantifies muscle spasticity by assessing the response of the muscle to stretch applied at specified velocities.

Grading is always performed at the same time of day, in a constant position of the body for a given limb. For each muscle group, reaction to stretch is rated at a specified stretch velocity with 2 parameters x and y.

Velocity to stretch (V)

V1	As slow as possible
V2	Speed of the limb segment falling
V3	As fast as possible (> natural drop)

V1 is used to measure the passive range of Motion. (PROM). Only V2 and V3 are used to rate spasticity

Quality of muscle reaction (X)

0	No resistance throughout passive movement
1	Slight resistance throughout, with no clear catch at a precise angle
2	Clear catch at a precise angle, followed by release
3	Fatigable clonus (<10secs) occurring at a precise angle
4	Unfatigable clonus (>10secs) occurring at a precise angle
5.	Joint Immobile

Angle of muscle reaction (Y)

Measure relative to the position of minimal stretch of the muscle (corresponding at angle)

Spasticity Angle

R1	Angle of catch seen at Velocity V2 or V3	R2	Full range of motion achieved when muscle is at rest and tested at V1 velocity

Boyd, Graham 1999
- A large difference between R1 & R2 values in the outer to middle range of normal m. length indicates a large dynamic component
- A small difference in the R1 & R2 measurement in the middle to inner range indicates predominantly fixed contracture

Date	Joint/ Muscle	L/R	V	X	R1	R2	Active ROM	Power MRC	Ashworth Rating	°

Krabbe disease successfully treated via monotherapy of intrathecal gene therapy

Allison M. Bradbury,[1] Jessica H. Bagel,[1] Duc Nguyen,[2] Erik A. Lykken,[3] Jill Pesayco Salvador,[4] Xuntian Jiang,[5] Gary P. Swain,[1] Charles A. Assenmacher,[6] Ian J. Hendricks,[1] Keiko Miyadera,[1] Rebecka S. Hess,[1] Arielle Ostrager,[1] Patricia ODonnell,[1] Mark S. Sands,[5] Daniel S. Ory,[5] G. Diane Shelton,[4] Ernesto R. Bongarzone,[2] Steven J. Gray,[3] and Charles H. Vite[1]

[1]Department of Clinical Sciences and Advanced Medicine, School of Veterinary Medicine, University of Pennsylvania, Philadelphia, Pennsylvania, USA. [2]Department of Anatomy and Cell Biology, College of Medicine, University of Illinois at Chicago, Chicago, Illinois, USA. [3]Department of Pediatrics, University of Texas Southwestern Medical Center, Dallas, Texas, USA. [4]Department of Pathology, School of Medicine, University of California San Diego, La Jolla, California, USA. [5]Department of Medicine, Washington University School of Medicine, St. Louis, Missouri, USA. [6]Department of Pathobiology, School of Veterinary Medicine, University of Pennsylvania, Philadelphia, Pennsylvania, USA.

Globoid cell leukodystrophy (GLD; Krabbe disease) is a progressive, incurable neurodegenerative disease caused by deficient activity of the hydrolytic enzyme galactosylceramidase (GALC). The ensuing cytotoxic accumulation of psychosine results in diffuse central and peripheral nervous system (CNS, PNS) demyelination. Presymptomatic hematopoietic stem cell transplantation (HSCT) is the only treatment for infantile-onset GLD; however, clinical outcomes of HSCT recipients often remain poor, and procedure-related morbidity is high. There are no effective therapies for symptomatic patients. Herein, we demonstrate in the naturally occurring canine model of GLD that presymptomatic monotherapy with intrathecal AAV9 encoding canine GALC administered into the cisterna magna increased GALC enzyme activity, normalized psychosine concentration, improved myelination, and attenuated inflammation in both the CNS and PNS. Moreover, AAV-mediated therapy successfully prevented clinical neurological dysfunction, allowing treated dogs to live beyond 2.5 years of age, more than 7 times longer than untreated dogs. Furthermore, we found that a 5-fold lower dose resulted in an attenuated form of disease, indicating that sufficient dosing is critical. Finally, postsymptomatic therapy with high-dose AAV9 also significantly extended lifespan, signifying a treatment option for patients for whom HSCT is not applicable. If translatable to patients, these findings would improve the outcomes of patients treated either pre- or postsymptomatically.

Introduction

Globoid cell leukodystrophy (GLD; Krabbe disease, OMIM 245200), a hereditary disorder due to mutations in the *GALC* gene, is characterized by deficiency of the hydrolytic lysosomal enzyme galactosylceramidase (GALC), which catabolizes the major myelin lipid galactosylceramide during normal myelin turnover (1). In the infantile form of GLD, undigested galactosylceramide accumulation in macrophages results in globoid cell formation in the central nervous system (CNS), and galactolipid inclusions are accumulated in histiocytes in the peripheral nervous system (PNS). GALC is also responsible for the degradation of galactosylsphingosine (psychosine), an intermediate in the biosynthesis of cerebrosides.

Cytotoxic accumulation of psychosine in oligodendrocytes in GLD causes cell death. The abnormal turnover of myelin and the death of oligodendrocytes compromise normal myelination in the developing infant, leading to irritability, paresis/paralysis, hearing loss, blindness, decerebration, and death by 2 years of age (2–5). Presymptomatic hematopoietic stem cell transplantation (HSCT) is the only treatment for infantile GLD; however, long-term outcomes of transplanted patients remain poor, and morbidity associated with the procedure is high (5–9). Moreover, HSCT does not treat the PNS disease associated with GLD (5–9). HSCT is no longer indicated for postsymptomatic patients.

Naturally occurring canine GLD is due to a spontaneous missense mutation in the *GALC* gene, c.473A>C (10), and disease progression in GLD dogs closely recapitulates human disease (10–14). The predictable disease progression (onset of neurological dysfunction at 6 weeks of age) and lifespan (15.7 ± 4.8 weeks of age) (12) allow for timely identification of pathological changes and evaluation of therapeutic interventions. Intrathecal delivery of adeno-associated virus serotype 9 (AAV9) encoding murine GALC to postsymptomatic twitcher mice, a naturally occurring murine model of Krabbe disease, modestly extended lifespan from 40 to 50.5 days, improved pathology, and partially reduced psychosine levels (15). We undertook a similar strategy in both presymptomatic and postsymptomatic GLD dogs, an animal model with a gyrencephalic brain more similar in size to an infant's brain. Herein we demonstrate that a
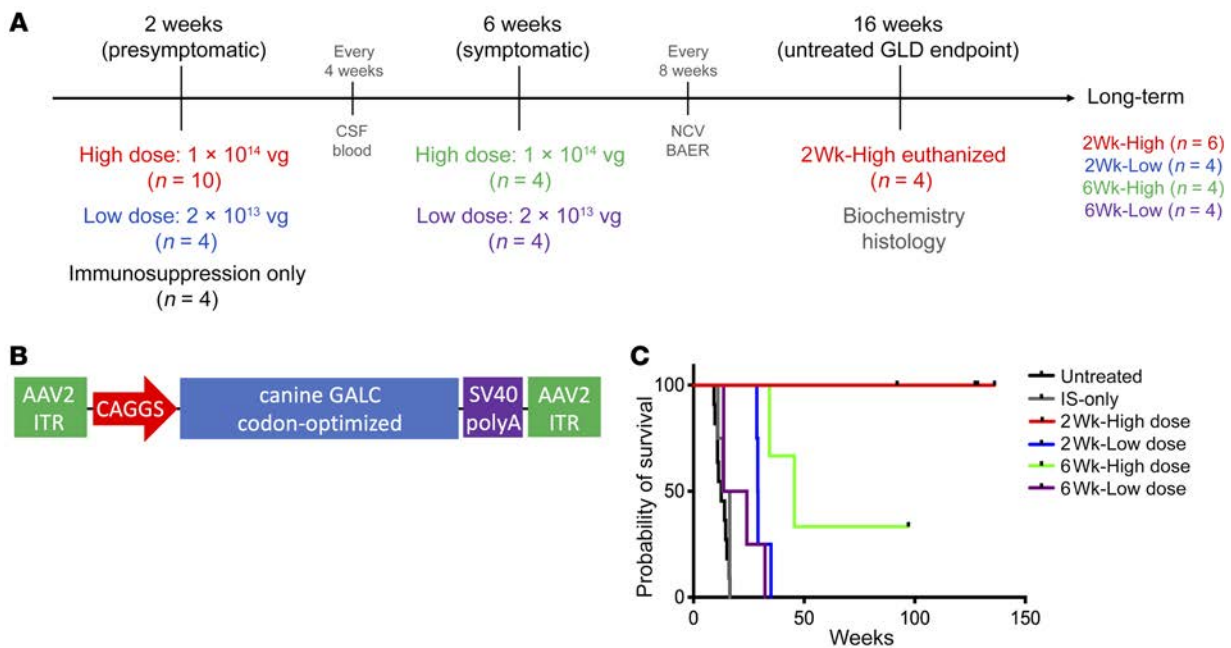
Figure 1. Experimental design, vector construct, and survival. (**A**) GLD dogs were treated with AAV9 delivered to the cisterna magna in a 1-mL volume. Ten GLD dogs were treated at 2 weeks of age with 1×10^{14} vg (2Wk-High); 4 GLD dogs were treated at 2 weeks of age with 2×10^{13} vg (2Wk-Low); 4 GLD dogs were treated at 6 weeks of age with 1×10^{14} vg (6Wk-High); 4 GLD dogs were treated at 6 weeks of age with 2×10^{13} vg (6Wk-Low). All dogs received an immunosuppression protocol consisting of 20 mg/kg intravenous methylprednisolone 1 hour before AAV infusion followed by 4 months of daily oral prednisone (0.5 mg/kg) with a 2-week taper. Four GLD dogs received immunosuppression protocol alone (IS-only). Four 2Wk-High dogs were euthanized at a predetermined endpoint of 16 weeks, while the remaining 22 dogs were followed long-term. (**B**) The AAV9 construct consisted of inverted terminal repeats (ITR), a CAGGS promoter, a codon-optimized canine *GALC* transgene, and a polyadenylation signal. (**C**) Percentage survival of untreated GLD (black), IS-only (gray), 2Wk-High (red), 2Wk-Low (blue), 6Wk-High (green), and 6Wk-Low (purple). A drop in the line indicates a death due to disease progression, and a black tick mark indicates dogs still alive ($n = 1$ in the 6Wk-High cohort, $n = 6$ in the 2Wk-High cohort). NCV, nerve conduction velocity testing; BAER, brainstem auditory evoked response testing.

single intrathecal injection at the cisterna magna (intracisternal) of AAV9 encoding canine GALC (AAV9-cGALC) was capable of clinically, biochemically, and histologically amending both CNS and PNS disease, delaying the onset of neurological dysfunction and prolonging survival. In fact, presymptomatic delivery of high-dose AAV increased lifespan to more than 7 times that of untreated GLD dogs, with all treated dogs remaining neurologically normal beyond 1.5 years of age. Moreover, in this robust evaluation of 26 GLD dogs, we demonstrate that this intracisternal protocol is sufficient to globally deliver therapeutic GALC enzyme, reduce cytotoxic psychosine concentrations, and correct the myelination abnormalities present in both the CNS and PNS. Importantly, this therapy obviates the need for HSCT. Furthermore, our data in the canine GLD model confirm a positive effect in dogs treated postsymptomatically, an improvement that has not been described in pediatric patients with HSCT. Last, the minimal effective dose determined in the canine model should inform translation of intrathecal AAV9 gene therapy into the clinic for the treatment of Krabbe disease.

Results

Pre- or postsymptomatic intracisternal administration of 1×10^{14} vector genomes of AAV9-cGALC to GLD dogs mitigates neurological dysfunction. Four cohorts of GLD dogs were injected intrathecally at the cisterna magna with AAV9 encoding canine GALC driven by a CAGGS promoter, which combines the cytomegalovirus (CMV) early enhancer element with the chicken β-actin promoter (AAV9-

cGALC; Figure 1, A and B). All AAV9-treated dogs received prednisone at an immunosuppressive dose immediately before and for 4 months after injection. Two cohorts of GLD dogs were treated presymptomatically at 2 weeks of age with either a high dose of vector (2Wk-High, receiving 1×10^{14} vector genomes [vg], $n = 10$) or a lower dose (2Wk-Low, receiving 2×10^{13} vg, $n = 4$). All 2-week-old GLD dogs were neurologically normal at the time of injection. The remaining 2 cohorts were treated postsymptomatically at 6 weeks of age, again with either a high dose (6Wk-High, receiving 1×10^{14} vg, $n = 4$) or a low dose of vector (6Wk-Low, receiving 2×10^{13}, $n = 4$). All 6-week-old GLD dogs exhibited tremors and pelvic limb weakness at the time of injection. Dogs either were euthanized at 16 weeks of age, the mean age of death of untreated GLD dogs, or were followed long-term. A control cohort of GLD dogs that received immunosuppression regimen alone (IS-only) was also evaluated (Figure 1A).

Untreated GLD dogs developed tremors and pelvic limb weakness at 6 weeks of age and progressed to pelvic limb ataxia, thoracic limb dysmetria, and urinary incontinence. Endpoint disease, defined as pelvic limb paralysis, occurred at 15.7 ± 4.8 weeks of age (12). GLD dogs in the IS-only cohort showed a disease progression indistinguishable from that of untreated GLD dogs with endpoint disease occurring between 11.0 and 16.4 weeks of age (14.29 ± 2.29 weeks; $P = 0.2954$) (Supplemental Video 1, IS-only dog at 10 weeks of age; supplemental material available online with this article; https://doi.org/10.1172/JCI133953DS1). There was no evidence that GLD dogs showed any benefit from IS alone.
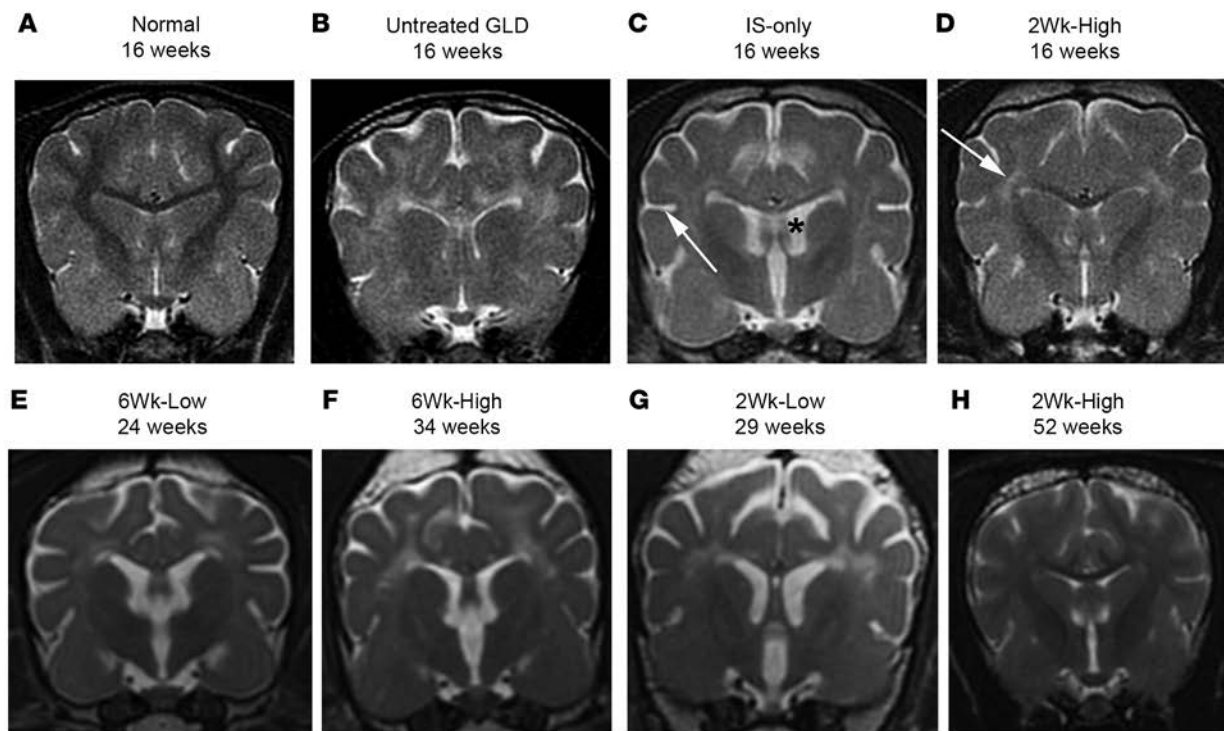
Figure 2. MRI of the brain at 1.5T. T2-weighted images at the level of the caudate nucleus in a normal dog at 16 weeks of age (**A**), an untreated GLD dog at endpoint (16 weeks of age) (**B**), IS-only at endpoint (16 weeks of age) (**C**), 2Wk-High at 16 weeks of age (**D**), 6Wk-Low at endpoint (24 weeks of age) (**E**), 6Wk-High at endpoint (34 weeks of age) (**F**), 2Wk-Low at endpoint (29 weeks of age) (**G**), and 2Wk-High at 52 weeks of age (**H**). White arrow in **C** indicates widened sulcus; black asterisk in **C** indicates enlarged ventricle. White arrow in **D** indicates hyperintensity of the centrum semiovale relative to gray matter.

Remarkably, all 10 GLD dogs in the 2Wk-High cohort were clinically normal at 16 weeks of age. Four dogs in this cohort were euthanized for biochemical and histological evaluation of tissues at 16 weeks of age, with results presented below. Six of these dogs, which are being evaluated long-term, remain neurologically normal and are currently all over 1.5 years of age (136.0, 128.4, 127.3, 127.3, 92.0, and 92.0 weeks of age) (Supplemental Video 2, GLD 2Wk-High at 116 weeks of age; and Figure 1C).

In contrast to the 2Wk-High cohort, each of the 4 dogs in the 2Wk-Low cohort developed pelvic limb ataxia by 16 weeks of age but remained able to walk. In order to evaluate disease progression in this cohort, no dogs were euthanized at 16 weeks of age and all were followed long-term. Three of 4 dogs developed behavioral abnormalities (disorientation and anxiety) and postretinal (central) blindness by 25 weeks of age. On ophthalmic examination, the fundus, retina, and optic disc appeared structurally normal (Supplemental Figure 1, C and F). Intriguingly, behavioral changes and blindness were not identified in any dogs in the untreated GLD or IS-only cohorts. Endpoint disease, defined as (a) severe disorientation with blindness ($n = 3$) and/or (b) pelvic limb paralysis ($n = 2$), occurred at 28.6–35.0 weeks of age ($P = 0.0002$ vs. IS only; 30.43 ± 2.65 weeks, $n = 4$) (Supplemental Video 3, GLD 2Wk-Low at 27 weeks of age; and Figure 1C).

Assessment of the effect of administration of AAV9-cGALC to 6-week-old GLD dogs with signs of neurological dysfunction revealed that postsymptomatic therapy was less effective than presymptomatic therapy at the respective doses evaluated. Of the 4 dogs in the 6Wk-High cohort, 2 developed pelvic limb paralysis

at 34.4 and 45.6 weeks of age. One dog in this cohort is currently 97.1 weeks of age and shows mild pelvic limb ataxia. The remaining dog in this cohort was euthanized at 17 weeks of age owing to severe bilateral patellar luxations that limited its ability to walk. This confounding orthopedic abnormality is not associated with GLD. GLD dogs in the 6Wk-Low cohort fared worse than the 6Wk-High cohort. All 4 dogs were euthanized between 13.6 and 32.3 weeks of age (20.89 ± 7.66 weeks, $n = 4$) owing to pelvic limb paralysis; survival time was not significantly different ($P = 0.2425$) from that of GLD dogs that received IS only.

MRI of the brain shows global amelioration of myelination abnormalities and atrophy in GLD dogs treated presymptomatically with 1×10^{14} vg AAV9-cGALC. On T2-weighted images, all 16-week-old untreated GLD dogs showed bilaterally symmetrical hyperintensities, relative to gray matter, of the corona radiata, corpus callosum, centrum semiovale, internal capsule (Figure 2B), and cerebellar white matter (not shown) when compared with normal, age-matched control dogs (Figure 2A). These changes are consistent with loss of myelin. Furthermore, brain atrophy, characterized by cerebral ventricular dilation and widened sulci, was also seen in untreated GLD dogs (Figure 2B). Imaging results of IS-only dogs at endpoint were indistinguishable from those of untreated GLD dogs showing diffuse white matter hyperintensity (Supplemental Table 1, MRI) as well as widened sulci (Figure 2C, arrow) and enlarged ventricles (Figure 2C, asterisk).

Dogs in the 2Wk-High cohort (Figure 2D) showed white matter signal intensities more similar to those of normal dogs (Figure 2A). The following white matter structures were normal (hypointense
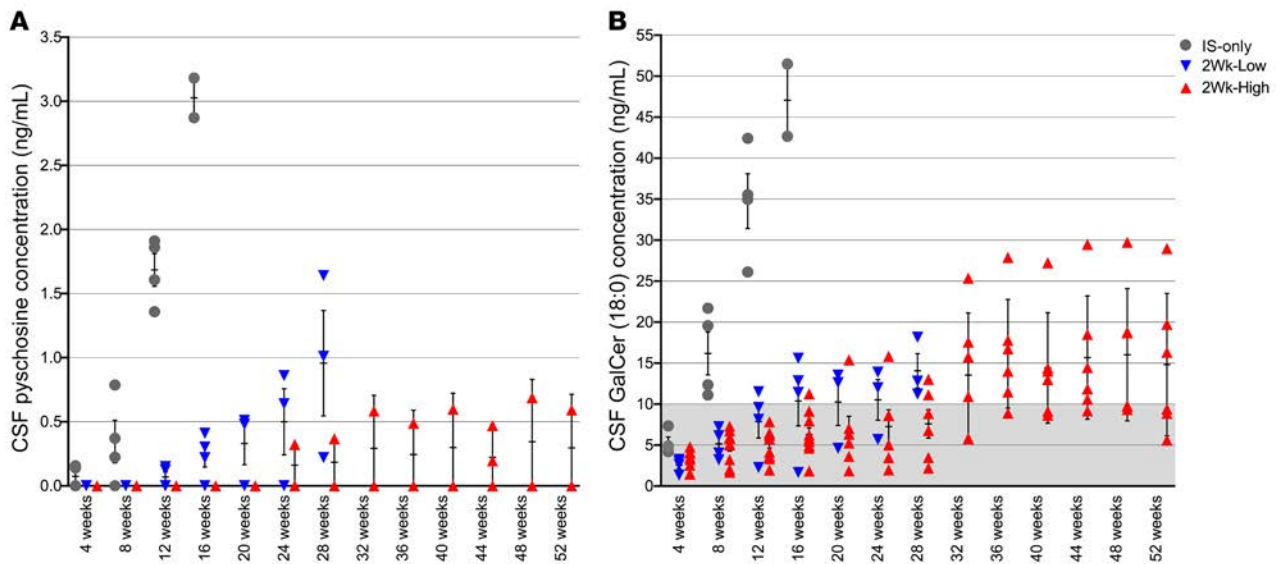
Figure 3. CSF concentrations of psychosine and galactosylceramide. Psychosine (**A**) and galactosylceramide (GalCer) (**B**) were measured by mass spectrometry every 4 weeks up to 52 weeks of age. Psychosine and GalCer are reported in ng/mL. Psychosine was below the level of detection in normal dogs. Gray shading indicates normal range for canine samples collected at the cisterna magna (<10 ng/mL) for GalCer. IS-only (*n* = 4, gray circles), 2Wk-High (*n* = 10, ≤16 weeks of age; *n* = 6, >16 weeks of age; red triangles), 2Wk-Low (*n* = 4, ≤16 weeks of age; *n* = 3, >16 weeks of age; blue triangles). Lines represent mean with SEM. Nonparametric Kruskal-Wallis test and Mann-Whitney test were performed. A *P* value of less than 0.05 was considered significant.

relative to gray matter) at 16 weeks of age: corona radiata in 2/4 dogs; corpus callosum in 4/4 dogs; centrum semiovale in 1/4 dogs; internal capsule in 3/4 dogs; and cerebellar white matter in 4/4 dogs (Supplemental Table 1, MRI). At 52 weeks of age, white matter signal intensities were normal in the corona radiata (4/6 dogs), corpus callosum (5/6 dogs), centrum semiovale (1/6 dogs), internal capsule (4/6 dogs), and cerebellar white matter (6/6 dogs) (Figure 2H). In the 2Wk-Low cohort at endpoint (Figure 2G), signal intensity was normal in the cerebellum, the brain region nearest the injection site, in 3/4 dogs; normalization of white matter signal intensity did not occur in the corona radiata, centrum semiovale, or internal capsule in any dog. The dog in this cohort that did not develop behavioral abnormalities or blindness was the dog with the least white matter signal abnormalities, including normal signal intensity in the corpus callosum and the occipital radiations. In contrast to the other cohorts, all dogs (4/4) in the 2Wk-Low cohort at endpoint showed gadolinium enhancement diffusely throughout the cerebral white matter including the optic radiations, suggesting an inflammatory phase of disease progression (Supplemental Figure 1, A and D, and Supplemental Table 1, MRI).

In the postsymptomatic cohorts (Figure 2, E and F), white matter signal intensity was similar to that in untreated dogs. Normalization of the white matter signal intensity was observed in the corpus callosum of 2/7 dogs and in the cerebellar white matter of 2/7 dogs but was not seen in any other brain region analyzed (Supplemental Table 1).

For all cohorts, the white matter that showed the most signal abnormalities was the centrum semiovale. As this is an initiating point for pathology in Krabbe disease, it is plausible that lesions were present in the centrum semiovale at the time of treatment. It is interesting to note that in the 2Wk-High cohort signal abnormalities in the centrum semiovale remained stable from 16 to 52 weeks.

In order to quantify brain atrophy, the areas of the mass intermedia and of the cerebellum were determined on mid-sagittal images. The mass intermedia area of the 2Wk-High cohort was not different from normal (*P* = 0.624) and was significantly larger than those of the untreated GLD (*P* = 0.012), 2Wk-Low (*P* = 0.005), and 6Wk-High (*P* = 0.011) cohorts. The 2Wk-Low (*P* = 0.011), 6Wk-High (*P* = 0.020), and 6Wk-Low (*P* = 0.011) cohorts all had mass intermedia areas significantly smaller than that of normal dogs. The cerebellar areas of both the 2Wk-High and 2Wk-Low cohorts were not different from normal (*P* = 0.741, *P* = 0.321) and were significantly larger than that of untreated GLD dogs (*P* = 0.010, *P* = 0.046). Both postsymptomatic cohorts were not significantly different from normal or untreated GLD dogs (*P* > 0.05), suggesting an intermediate level of correction. These findings demonstrate substantial attenuation of brain atrophy with presymptomatic high-dose treatment, but not with low-dose or delayed treatment.

Cerebrospinal fluid psychosine, galactosylceramide, and total protein concentrations are normalized in GLD dogs treated presymptomatically with 1 × 10^14 vg AAV9-cGALC. Similar to recent findings in untreated GLD dogs (16), cerebrospinal fluid (CSF) psychosine concentrations were elevated in IS-only dogs at 4 weeks of age and increased with disease progression (Figure 3A). Psychosine was not detectable in the CSF of normal dogs at any time point. In the 2Wk-High cohort, psychosine was not detectable in any treated animal up to 20 weeks of age; at 24 weeks of age, psychosine was detectable in 1 of 6 dogs, and it remained relatively stable beyond 32 weeks of age. Psychosine was also detectable at a single time point, 44 weeks of age, in a second dog of this cohort (Figure 3A). Psychosine concentrations were significantly reduced as compared with IS-only at 4 (*P* = 0.020), 8 (*P* = 0.003), and 12 (*P* = 0.0004) weeks and were not significantly different (*P* > 0.05) from those in
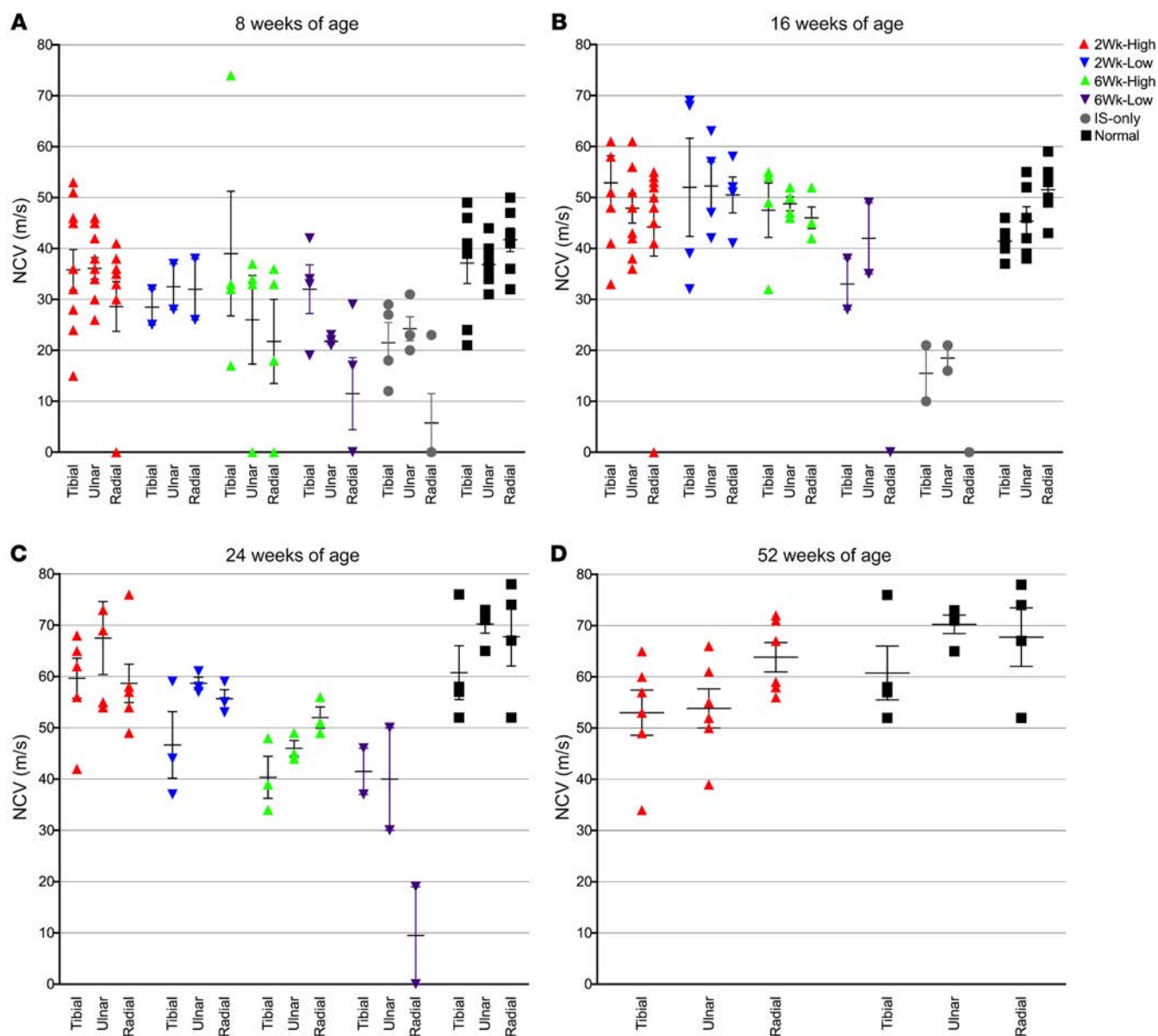
Figure 4. Motor and sensory nerve conduction velocities at 8, 16, 24, and 52 weeks of age. The motor nerve conduction velocities (NCVs) of the tibial and ulnar nerves and the sensory NCVs of the radial nerves were analyzed at 8 weeks of age for normal ($n = 7$, black squares), 2Wk-High ($n = 10$, red triangles), 2Wk-Low ($n = 2$, blue triangles), 6Wk-High ($n = 4$, green triangles), 6Wk-Low ($n = 4$, purple triangles), and IS-only ($n = 4$, gray circles) (**A**); 16 weeks of age for normal ($n = 6$), 2Wk-High ($n = 9$), 2Wk-Low ($n = 4$), 6Wk-High ($n = 4$), and 6Wk-Low ($n = 2$) (**B**); 24 weeks of age for normal ($n = 6$), 2Wk-High ($n = 6$), 2Wk-Low ($n = 3$), 6Wk-High ($n = 3$), and 6Wk-Low ($n = 2$) (**C**); and 52 weeks of age for normal ($n = 4$) and 2Wk-High ($n = 6$) (**D**). Lines represent mean with SEM. Nonparametric Kruskal-Wallis test and Mann-Whitney test were performed. A P value of less than 0.05 was considered significant.

normal age-matched controls at any time point (Supplemental Table 1). In the 2Wk-Low cohort, the accumulation of psychosine was delayed until 12 weeks of age and increased steadily in all dogs until endpoint (Figure 3A). The levels remained significantly lower than in IS-only dogs at 8 ($P = 0.0472$) and 12 ($P = 0.0202$) weeks of age. The 2Wk-High cohort was significantly lower than the 2Wk-Low cohort from 12 weeks ($P = 0.0203$) to 28 weeks of age ($P = 0.0237$). These data identify CSF psychosine as a robust, disease-specific biomarker of disease severity and therapeutic efficacy.

The natural substrate of GALC, galactosylceramide (GalCer), was also significantly elevated in CSF of untreated GLD dogs, and 18:0 was determined to be the most abundant species (16). Sim-

ilarly, the IS-only cohort showed an early and rapid rise in CSF GalCer 18:0 (Figure 3B). Normal values are represented by gray shading (<10 ng/mL). As seen with psychosine concentration, in the 2Wk-High and 2Wk-Low cohorts CSF GalCer 18:0 was significantly reduced in comparison with IS-only dogs at 8 ($P = 0.0047$, $P = 0.0209$) and 12 ($P = 0.0047$, $P = 0.0209$) weeks of age, respectively. CSF GalCer in the 2Wk-High cohort was significantly different from normal from 36 to 48 weeks of age ($P = 0.0201$); however, it was not significantly different before 36 weeks or at 1 year of age ($P = 0.1213$) (Supplemental Table 1).

Similarly to CSF psychosine and GalCer, CSF total protein increased with disease progression in untreated GLD dogs (Sup-
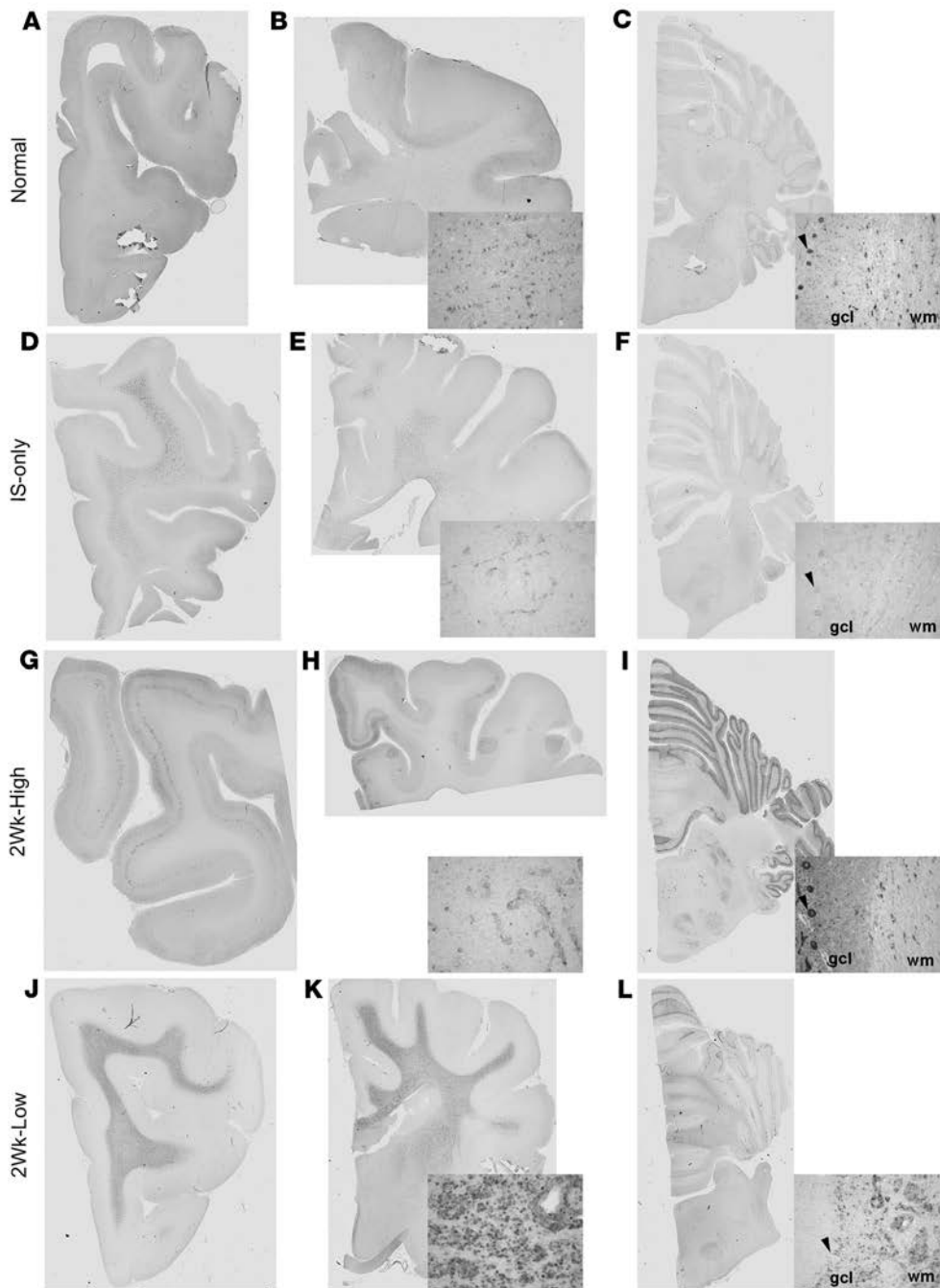
Figure 5. GALC immunohistochemical staining of the brain. IHC staining with GALC antibody of the frontal lobe, corona radiata/internal capsule, and cerebellum in normal dog (**A**–**C**), IS-only dog (**D**–**F**), 2Wk-High dog (**G**–**I**), and 2Wk-Low dog (**J**–**L**). Insets show higher-magnification images of whole-slide scans. Black arrowheads indicate Purkinje cells. gcl, granule cell layer; wm, white matter.

untreated GLD dogs as compared with normal age-matched control dogs, with the degree of velocity reduction consistent with demyelination (12, 17). IS-only GLD dogs were not significantly different from untreated GLD dogs in the 3 nerves analyzed at 8 weeks of age (Figure 4A). At 16 weeks of age, the 2Wk-High, 2Wk-Low, and 6Wk-High cohorts had nerve conduction velocities not significantly different from normal for each of the 3 nerves analyzed ($P >$ 0.05) (Figure 4B). At 24 weeks of age, the 2Wk-High and 2Wk-Low cohorts remained not significantly different from normal, while the 6Wk-High cohort showed significantly reduced velocities for the tibial ($P = 0.0201$), ulnar ($P = 0.0201$), and radial ($P = 0.0389$) nerves (Figure 4C). At 52 weeks of age, the 2Wk-High cohort remained not significantly different from normal for the tibial and radial nerves ($P > 0.05$), but showed reduced velocities in the ulnar nerve ($P = 0.019$) (Figure 4D). The 6Wk-Low cohort had significantly slower nerve conduction velocity in ulnar ($P =$

plemental Figure 2). In contrast, the 2Wk-High cohort showed normal CSF protein (≤30 mg/dL) throughout the entire period of observation. The 2Wk-Low and 6Wk-High cohorts showed CSF protein concentrations that increased with age and exceeded normal concentrations by 28 weeks of age, and the 6Wk-Low cohort exhibited a more rapid increase in CSF protein that exceeded normal levels by 16 weeks of age (Supplemental Figure 2). Thus, like CSF psychosine and GalCer, total CSF protein is associated with disease severity and therapeutic efficacy.

Peripheral nerve conduction velocities and auditory central conduction times are improved in GLD dogs treated presymptomatically with 1×10^{14} vg AAV9-cGALC. Motor (tibial, ulnar) and sensory (radial) nerve conduction velocities are significantly reduced in

0.008) and radial ($P = 0.0079$) nerves at 8 weeks of age. As only 2 dogs in this cohort lived to 16 weeks of age, statistics could not be done. Together, these results reveal that intracisternal delivery of AAV9-cGALC was capable of correcting nerve conduction velocity associated with demyelination when performed presymptomatically, while the postsymptomatic effect was transient.

Brainstem auditory evoked response testing showed that wave forms were degraded and central conduction times (I-V peak latency of waves) were significantly increased in untreated GLD dogs at 16 weeks of age as compared with normal age-matched controls (left ear, $P = 0.0105$; right ear, $P = 0.0196$) (Supplemental Figure 3 and Supplemental Table 1). At 16 weeks of age, the 2Wk-High cohort exhibited normalized central conduction times (left ear,
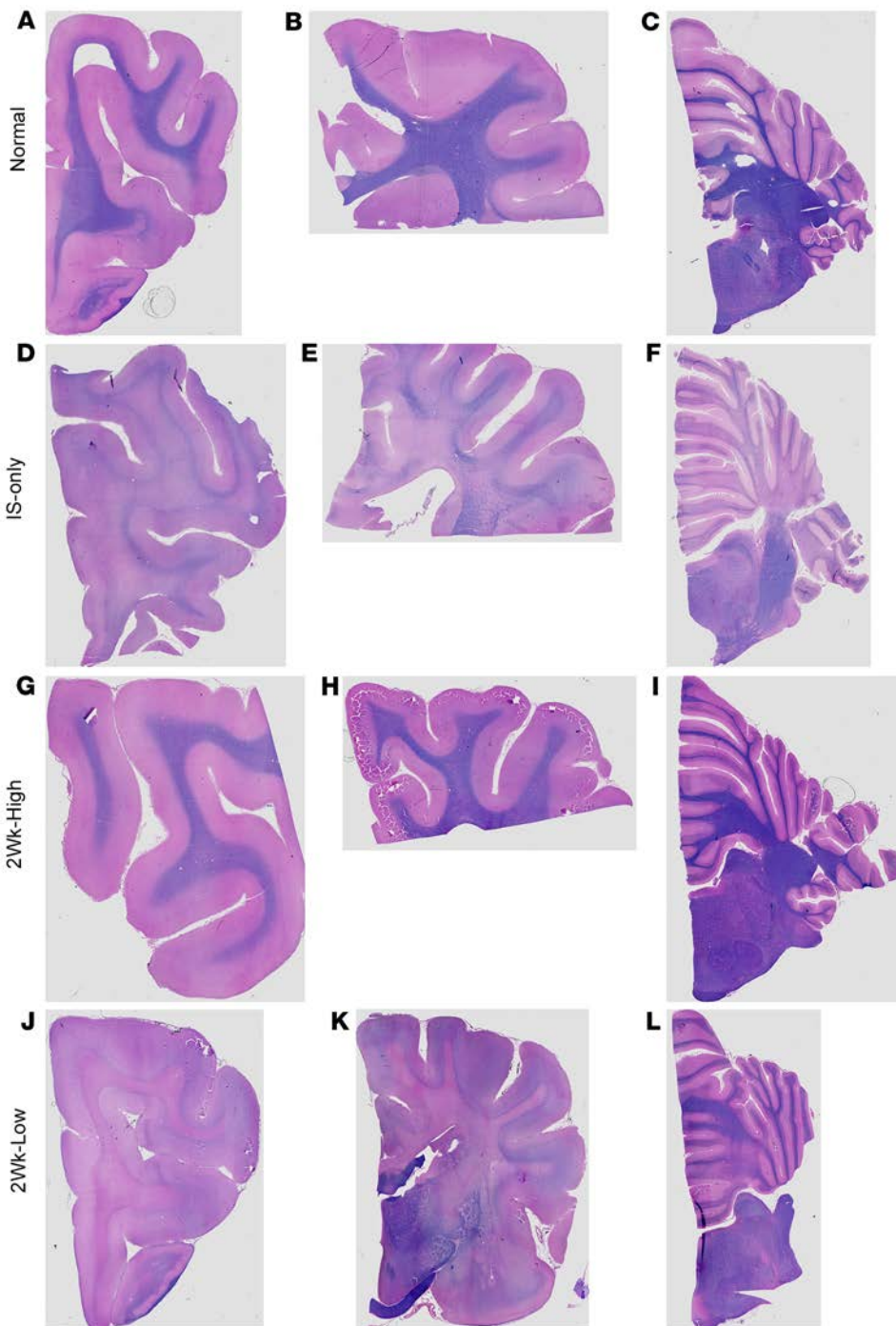
Figure 6. Iron eriochrome staining of the brain. Iron eriochrome staining of myelin in normal dog (**A–C**), IS-only dog (**D–F**), 2Wk-High dog (**G–I**), and 2Wk-Low dog (**J–L**).

increased (Supplemental Figure 3). At 52 weeks of age the 2Wk-High cohort remained not significantly different from normal (left ear, $P = 0.4472$; right ear, $P = 0.8057$). Together, these results reveal that intracisternal delivery of AAV9-cGALC was capable of normalizing central conduction time when performed presymptomatically.

Global expression of GALC and attenuation of both CNS and PNS pathology in dogs treated presymptomatically with 1×10^{14} vg AAV9-cGALC. Immunohistochemical (IHC) staining with an antibody specific to GALC revealed GALC expression at low levels in glial cells of the white matter throughout the brain of normal dogs (Figure 5, A–C). GALC expression was not detectable in cortical neurons (Figure 5A) but was present in Purkinje cells (Figure 5C, inset, arrowhead). In untreated and IS-only dogs (Figure 5, D–F), GALC was present throughout the white matter in dense regions of globoid cell accumulation. GALC expression was not seen in cortical neurons (Figure 5D) and was just at the level of detection in Purkinje cells (Figure 5F, inset, arrowhead). In contrast to all other cohorts, in 16-week-old dogs in the 2Wk-High cohort, strong GALC expression in the majority of neurons of cortical layer V was detected (Figure 5G). GALC expression was present in both glia throughout the white matter and

$P = 0.4762$; right ear, $P = 0.3275$) that were significantly improved in comparison with untreated GLD dogs (left ear, $P = 0.0066$; right ear, $P = 0.0132$). Similarly, the 2Wk-Low cohort had conduction times that were not significantly different from normal (left ear, $P = 0.5169$; right ear, $P = 0.169$) and were significantly reduced in comparison with untreated GLD (left ear, $P = 0.0339$; right ear, $P = 0.0253$). The 6Wk-High cohort had central conduction times not significantly different from those in normal or untreated GLD ($P > 0.05$), suggesting an intermediate correction. The 6Wk-Low and IS-only cohorts had 2 dogs alive at 16 weeks of age, so statistics could not be done; however, conduction times remained

limited globoid cells isolated to the centrum semiovale (Figure 5H and Supplemental Table 1, Globoid Cells). In the cerebellum there was robust expression of GALC in nearly every Purkinje cell to a greater degree than in normal dogs and strong positive expression in glial cells in cerebellar white matter (Figure 5I, and inset). Cells in the white matter are presumed to be oligodendrocytes based on morphology (Figure 5I, inset, wm); however, colabeling with GALC and oligodendrocytes was not feasible because of antibody incompatibility in canine tissues. In the 2Wk-Low cohort at endpoint, GALC expression was seen throughout the white matter in dense regions of globoid cell accumulation (Figure 5, J–L). GALC
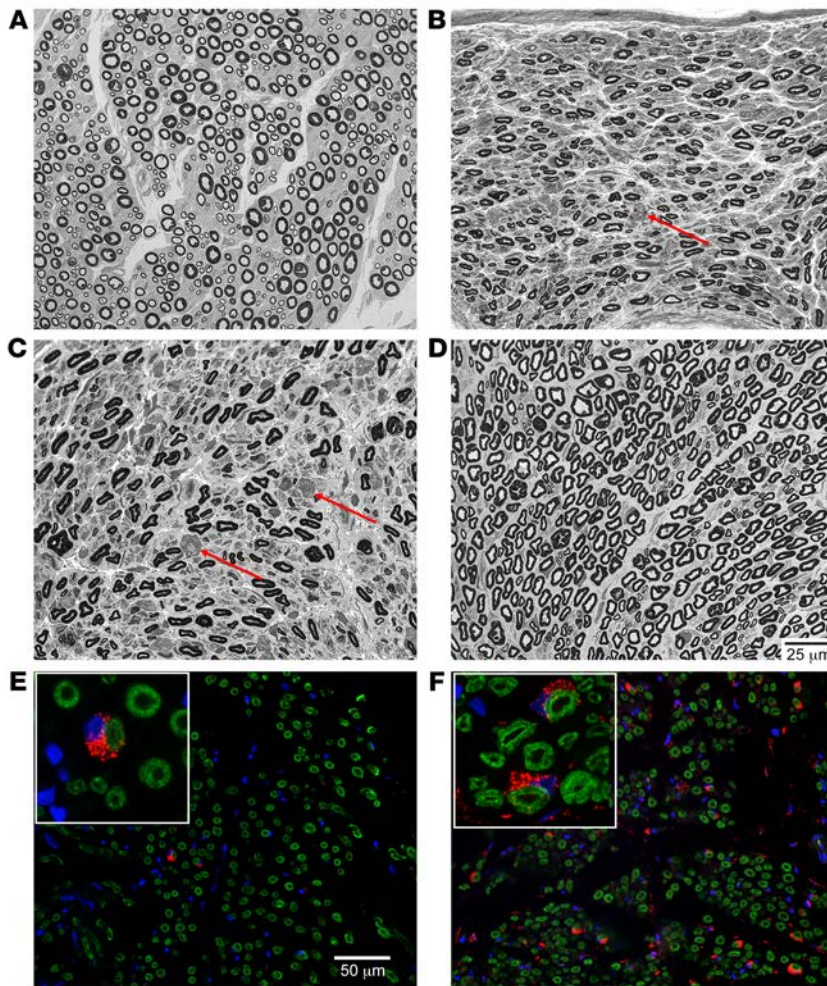
Figure 7. Light-level 1-μm resin sections and GALC immunofluorescence of tibial nerve. Resin-embedded samples from the tibial nerve were stained with paraphenylenediamine, then evaluated in 1-μm sections. (**A**) Normal dog 16 weeks of age. (**B**) IS-only 13 weeks of age. (**C**) 2Wk-Low 29 weeks of age. (**D**) 2Wk-High 16 weeks of age. (**E** and **F**) Immunofluorescent staining for GALC in red and myelin basic protein in green at ×40 original magnification in 2Wk-Low (**E**) and 2Wk-High (**F**) cohorts. Arrows in **B** and **C** point to myelin ovoids. Insets show Schwann cells at high magnification (×100). Scale bars: 25 μm, **A**–**D**; 50 μm, **E** and **F**.

more severe than in the IS-only cohort, likely owing to the advanced age of the dogs. Generally, there was a lessening of globoid cell infiltration in the cerebellum, nearest the injection site, and spinal cord in the 2Wk-Low cohort (Supplemental Table 1).

Both untreated and IS-only–treated GLD dogs had marked loss of myelin throughout the brain as visualized and semiquantified by iron eriochrome stain (Figure 6 and Supplemental Table 1, Demyelination). In the 2Wk-High cohort, as with globoid cell accumulation, demyelination was isolated to the centrum semiovale and corona radiata, which corroborates MRI signal intensity findings. In the 2Wk-Low cohort at humane endpoint, myelination was nearly absent in the most rostral brain as well as the centrum semiovale, corpus callosum, and internal capsule, exceeding severity of the IS-only cohort, likely owing to the advanced age (Figure 6K and Supplemental Table 1). Myelin was more preserved in the cerebellar folia but was diminished in the deep cerebellar white matter. These findings corroborate MRI findings in which the 2Wk-Low cohort had preservation in the cerebellum but not more rostral brain regions.

We next evaluated regions where gadolinium enhancement and presumed blood-brain barrier disruption were detected on MRI. Histology showed perivascular cuffing and infiltration of lymphocytes (Supplemental Figure 1G) in these regions, in addition to both severe demyelination (Supplemental Figure 1H) and infiltration of periodic acid–Schiff–positive storage granules (Supplemental Figure 1I).

In the PNS, GALC enzyme expression was present in numerous Schwann cells (>12 in a ×40 field; Figure 7F) of the tibial nerves of dogs in the 2Wk-High cohort. In the 2Wk-Low cohort, substantially fewer GALC-expressing Schwann cells were seen (2 in a ×40 field; Figure 7E). There also appears to be a subjective increase in the expression of myelin basic protein staining in the 2Wk-High cohort as compared with the 2Wk-Low cohort (Figure 7, E and F). Representative paraphenylenediamine-stained resin sections (1 μm) are shown of the tibial nerve. Compared with IS only, there was a subjective increase in the population of small- and large-caliber nerve fibers in both AAV-treated cohorts. Active axonal degeneration (swollen axons, accumulation of degenerating organelles)

was absent in the cerebral cortex and present in superficial Purkinje cells, but absent in deeper regions of the folia.

The 2Wk-High cohort dog with the lowest level of GALC enzyme activity in the internal capsule and cerebellum by enzyme assay is represented in Figure 5 to ensure no overrepresentation. GALC IHC in additional normal, IS-only, 2Wk-High, and 2Wk-Low dogs can be seen in Supplemental Figure 4. A similar pattern of expression was present in all dogs. Supplemental Figure 4 represents the 2Wk-High dog with the highest level of GALC enzyme activity in the cerebellum by enzyme assay so that the spectrum of expression can be appreciated. GALC expression from a third dog from the 2Wk-High cohort can be seen in the graphical abstract.

Globoid cell accumulation is the hallmark pathology in GLD and was evaluated in all cohorts by semiquantitation of H&E stain (Supplemental Table 1, Globoid Cell Accumulation). The IS-only cohort was indistinguishable from untreated GLD dogs, with marked, widespread globoid cell accumulation in the white matter. In contrast, in the 2Wk-High cohort, throughout the entire brain the only presence of globoid cells was in the centrum semiovale, the origin of pathology in Krabbe disease, and the corona radiata in 1 of 4 dogs (Supplemental Table 1). The globoid cell presence was less severe than in the IS-only and 2Wk-Low cohorts. In the 2Wk-Low cohort, globoid cell accumulation was
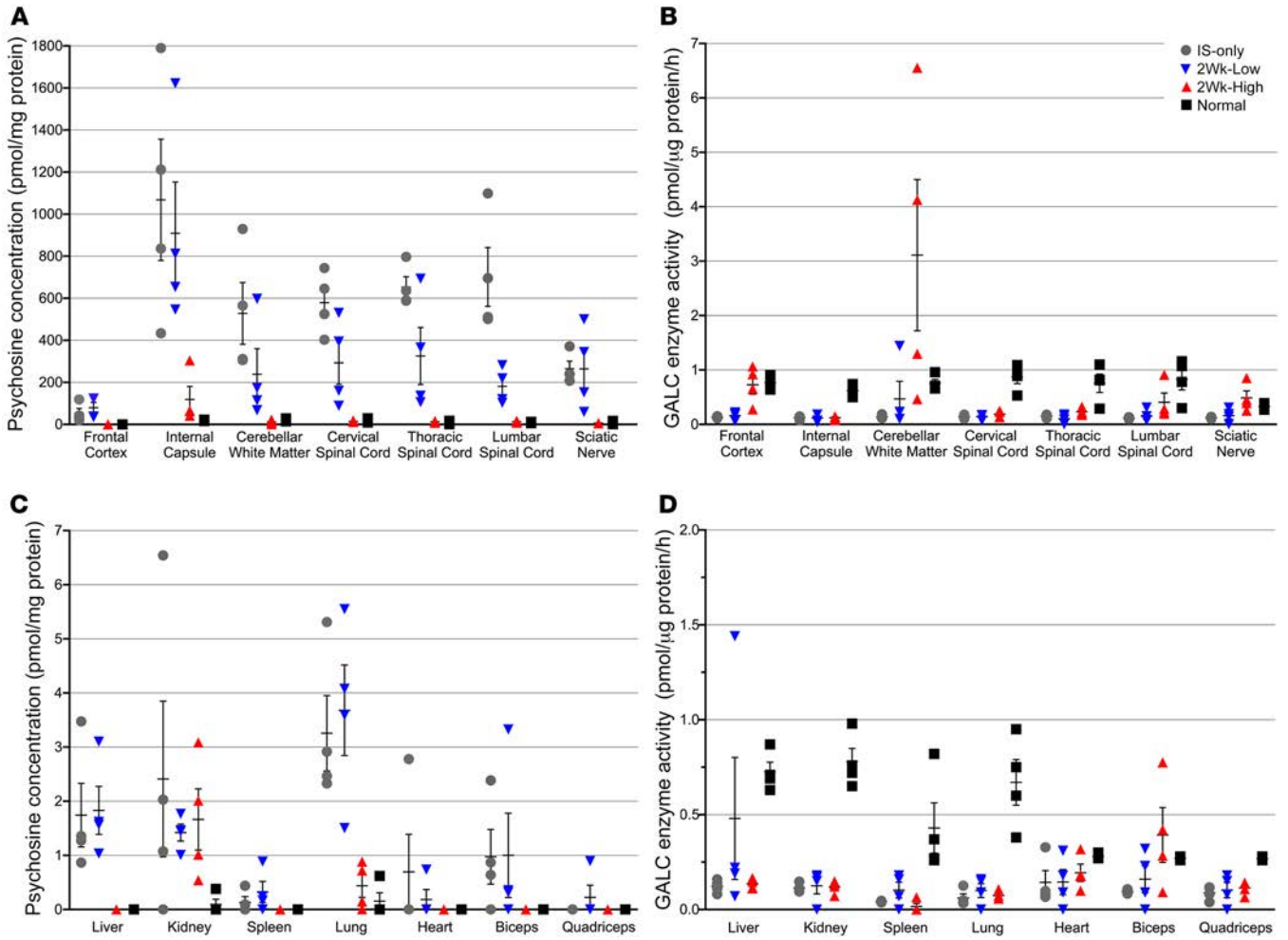
Figure 8. Psychosine concentration and GALC enzyme activity. Psychosine concentration was determined by mass spectrometry and GALC enzyme activity was measured using a synthetic 4MU substrate in punch biopsies taken from flash-frozen tissue samples of the frontal cortex, internal capsule, cerebellar white matter, cervical spinal cord, thoracic spinal cord, lumbar spinal cord, sciatic nerve, liver, kidney, spleen, lung, heart, biceps, and quadriceps. Psychosine (**A** and **C**) is reported in pmol/mg protein and GALC enzyme activity (**B** and **D**) in pmol/μg protein per hour. IS-only cohort at endpoint ($n = 4$, gray circles), 2Wk-High cohort at 16 weeks of age ($n = 4$, red triangles), 2Wk-Low cohort at endpoint ($n = 4$, blue triangles), normal at 16 weeks of age ($n = 4$, black squares). Lines represent mean with SEM. Nonparametric Kruskal-Wallis test and Mann-Whitney test were performed. A P value of less than 0.05 was considered significant.

was not observed in any cohort; however, rare myelin ovoids consistent with end-stage axonal degeneration were found in the IS-only (Figure 7B, arrow) and 2WK-Low GLD (Figure 7C, arrows) cohorts. Myelin ovoids were not found in the 2WK-High GLD (Figure 7D) cohort. Myelinated fiber density (MFD; myelinated fibers/mm²) of the tibial nerve of normal 16-week-old dogs was determined to be 9891.5 ± 1704.7 and the percentage of thinly myelinated fibers (<5 μm) 23.8% ± 3.1% ($n = 4$) (Figure 7A). Untreated GLD dogs had a reduction in MFD to 7764 ± 1734 and an increase in the percentage of thinly myelinated fibers to 31.4% ± 7.1% ($n = 4$). In the 2Wk-Low dose cohort, data were available from 2 dogs with MFD of 9940 and 5544 and percentage of thinly myelinated fibers 23.7% and 15.2%, respectively (Figure 7C). The 2Wk-High dose cohort showed improvement over untreated GLD dogs with MFD in 2 dogs with data available at 7632 and 11,025 and percentage of thinly myelinated fibers 27.1% and 26.1%, respectively (Figure 7D). Together, our results indicate that after a single intra-

cisternal injection of high-dose AAV9-cGALC, GALC expression is evident in Schwann cells and myelination is clearly improved.

Finally, given recent concern regarding toxicity to the dorsal root ganglia associated with AAV administration, we examined dorsal root ganglia as well as spinal cord gray matter. Within these regions we identified neuronal cytoplasmic swelling and Nissl substance loss (Supplemental Figure 5, red arrow) and, less frequently, cytoplasmic vacuolation (Supplemental Figure 5B, black arrow) with occasional accumulation of brightly eosinophilic granules (Supplemental Figure 5, blue arrows) and adjacent axonal swelling. These changes are unusual and may represent a secondary lesion due to chronic neuronal degeneration or axonal damage. This change is seen in most animals and is therefore likely unrelated to the treatment. A few animals also had minimal multifocal increased cellularity in the dorsal root ganglia, which may represent inflammatory cell infiltrates (Supplemental Figure 5C, green arrow); however, this was present across cohorts and thus is likely unrelated to treatment.

Psychosine, GALC enzyme activity, and vector copy quantification in AAV9-GALC–treated dogs. Remarkably, in the 2Wk-High cohort at 16 weeks of age, psychosine concentration was significantly reduced in comparison with IS-only dogs in all CNS tissues analyzed (frontal cortex, $P = 0.02$; internal capsule, $P = 0.02$; cerebellar white matter, $P = 0.02$; cervical spinal cord, $P = 0.02$; thoracic spinal cord, $P = 0.02$; lumbar spinal cord, $P = 0.02$) as well as in the sciatic nerve ($P = 0.02$) (Figure 8A). The internal capsule remained significantly higher than normal ($P = 0.02$); however, no other CNS or PNS tissues had psychosine values significantly different from those in normal age-matched control dogs ($P > 0.05$). Interestingly, in the cerebellar white matter and sciatic nerve, where GALC enzyme activity exceeded normal (Figure 8B), psychosine levels were 1.9- and 1.3-fold lower than normal, respectively. In the 2Wk-Low cohort, significant reduction of psychosine was seen only in the lumbar spinal cord ($P = 0.02$) (Figure 8A). Further, all nervous system tissue had psychosine values that remained significantly higher than in normal age-matched control dogs and the 2Wk-High cohort ($P < 0.05$).

In somatic tissues, the 2Wk-High cohort's lung psychosine levels were significantly reduced as compared with those of IS-only dogs ($P = 0.02$) and not significantly different from those of normal age-matched control dogs ($P > 0.05$) (Figure 8C). In the kidney, the psychosine concentration was not significantly different from that in the IS-only or the normal cohort. Numerous tissues from the 2Wk-High cohort had psychosine concentrations below the level of detection (liver, spleen, heart, biceps, and quadriceps). In contrast, the 2Wk-Low cohort had detectable levels of psychosine that were not significantly reduced as compared with IS-only–treated dogs in every somatic tissue sampled (Figure 8C). Additionally, liver, lung, and biceps psychosine levels remained significantly higher than in normal age-matched control and 2Wk-High cohorts ($P < 0.05$).

In the 2Wk-High cohort, GALC enzyme activity was significantly increased in comparison with the IS-only–treated cohort in all CNS (frontal cortex, $P = 0.02$; cerebellar white matter, $P = 0.02$; thoracic spinal cord, $P = 0.04$; lumbar spinal cord, $P = 0.02$) and PNS (sciatic nerve, $P = 0.02$) tissues analyzed except the internal capsule and cervical spinal cord ($P > 0.05$) (Figure 8B). Most notably, GALC enzyme activity was 4-fold higher than normal in the cerebellum, the area closest to the injection site, and 1.5-fold higher than normal in the sciatic nerve (Figure 8B). This corroborates our findings of GALC enzyme expression by IHC and immunofluorescence (Figures 5 and 7). In the 2Wk-Low cohort at endpoint, GALC was not significantly increased in comparison with the IS-only cohort in any CNS or PNS tissue ($P < 0.05$). GALC levels were not significantly different from normal ($P > 0.05$) in the cerebellar white matter or sciatic nerve, suggesting an intermediate level of restoration in those 2 tissues. There was no significant difference between the 2Wk-High and 2Wk-Low cohorts in somatic tissues ($P > 0.05$) (Figure 8D). A single intrathecal injection of high-dose, but not low-dose, AAV9-cGALC was able to significantly increase GALC enzyme activity and reduce psychosine concentration in CNS, PNS, and somatic tissues.

To evaluate AAV9 biodistribution after intracisternal delivery, we quantified vector genome (vg) copies per diploid genome in untreated, 2Wk-High, and 2Wk-Low GLD dogs. In alignment with the psychosine and GALC data, vg copies were significantly increased in the 2Wk-High cohort as compared with untreated dogs in all CNS tissues (frontal cortex, $P = 0.02$; cerebellar white matter, $P = 0.02$; cervical spinal cord, $P = 0.02$; thoracic spinal cord, $P = 0.02$; and lumbar spinal cord, $P = 0.02$) except the internal capsule. The 2Wk-Low cohort had significantly increased vg copies as compared with untreated animals in the frontal cortex ($P = 0.03$) and thoracic ($P = 0.03$) and lumbar ($P = 0.03$) spinal cord. However, all CNS tissues had significantly fewer vg copies than the 2Wk-High cohort ($P < 0.05$) except the internal capsule (Supplemental Table 1, Vector Genome Copies). The sciatic nerve was not analyzed for vg copies because of the limited amount of tissue for biochemistry (GALC and psychosine) and histology. In somatic tissues, the 2Wk-High cohort had a significant increase in vg copies as compared with untreated animals in all tissues except the quadriceps. The 2Wk-Low cohort had significantly more vg copies than untreated animals only in the liver ($P = 0.03$) and kidney ($P = 0.03$), and had significantly fewer vgs than the 2Wk-High cohort in all tissues except the quadriceps (Supplemental Table 1, Vector Genome Copies). Our results indicate that an intracisternal injection of AAV9 is capable of disseminating therapeutic transgenes throughout the CNS and somatic tissues, with the greatest number of vg copies in the spinal cord and liver, and with copies persisting for at least 16 weeks. These studies in a large-animal model provide strong evidence that a single injection of AAV9 into the CSF is capable of distributing functional therapeutic enzyme to the CNS, PNS, and somatic tissues where long-term expression prevents substrate accumulation, preserves myelin integrity, and prevents disease progression in a clearly dose-dependent manner.

Discussion

In GLD, both CNS and PNS myelination abnormalities occur, resulting in cognitive decline and motor deterioration that ultimately results in early death. Newborn screening for Krabbe disease is currently performed in many states, allowing for treatment of presymptomatic babies with HSCT. The exact therapeutic mechanism of HSCT is unknown; however, it is believed to involve transit of GALC-positive donor-derived monocytes into the CNS, which allows secretion of GALC to be endocytosed by neurons and glia via the mannose-6-phosphate receptor to cross-correct the enzyme deficiency (18). There are also data showing that HSCT has a significant immunomodulatory effect (19). Although HSCT is the standard of care for presymptomatic Krabbe infants, the majority of treated patients show limited improvements in motor ability and PNS myelination (5–9). Treated children are frequently wheelchair bound, unable to communicate effectively, and respirator dependent for an extended time. As HSCT in postsymptomatic children provides no increase in survival (6), it is no longer indicated for babies diagnosed beyond a couple of months of age. Clearly, there is a need for more effective therapies that treat both CNS and PNS aspects of disease at both presymptomatic and postsymptomatic stages.

Intrathecal administration of AAV9 permits dissemination of transgenes throughout the nervous system and is currently in clinical trials for the treatment of neuronal ceroid lipofuscinosis 3 (CLN3; ClinicalTrials.gov NCT03770572), CLN6 (NCT02725580), spinal muscular atrophy (NCT03381729), and

giant axonal neuropathy (NCT02362438). Because of its ability to cross the blood-brain barrier, AAV9 can be delivered intravenously to treat the CNS. However, intrathecal administration has many advantages, including higher transduction efficiency of the CNS (20); sustained expression with the absence of toxicity (21) seen with systemic delivery (22); evasion of anti-AAV neutralizing antibodies (23), which have been shown to be detrimental to systemic delivery (24); and requirement of substantially less vector product, increasing the feasibility of translation to human patients. Intrathecal AAV9-mediated gene therapy for Krabbe disease was first evaluated in the twitcher mouse (25, 26). When postnatal day 10–11 twitcher mice received a single lumbar intrathecal injection at a dose of 2×10^{11} vg, survival was modestly extended by about 10.5 days. This treatment improved the pathology and reduced psychosine levels but did not restore them to baseline levels (15). Notably, at postnatal day 10–11, twitcher mice are postsymptomatic, with reduced body weight and disease pathology present. Presymptomatic intrathecal injections were not performed, presumably because of the small size of the newborn mouse and the compressed timeline of disease progression.

In the GLD dog, we evaluated the efficacy of intrathecal administration of AAV9-cGALC in both presymptomatic and symptomatic dogs. Vector was administered at the cisterna magna, since we and others have shown that intracisternal AAV9 administration is safe in cats, dogs, and nonhuman primates and results in up to 100-fold more efficient gene transfer to the brain than does administration via lumbar puncture (27) or intravenously (20). Intracisternal AAV9 is currently being administered to patients with mucopolysaccharidosis I (NCT02362438) and GM1 gangliosidosis (NCT04273269) in clinical trials, making this a clinically relevant route of administration. Herein we have established that presymptomatic administration of high-dose (1×10^{14} vg) AAV9-cGALC into the CSF of GLD dogs ameliorates disease beyond 2.5 years of age, with all dogs in the 2Wk-High cohort currently alive and neurologically normal between 92 and 136 weeks of age (117.2 ± 18.0, $n = 6$), more than 7 times longer than untreated GLD dogs. These dogs continue to be monitored by neurological examination, MRI, nerve conduction velocity testing, and brainstem auditory evoked response. Serum and CSF samples are routinely collected for additional long-term analyses.

The results in the dog far exceed expectations based on the findings in the twitcher mouse. The intrathecal dose of 2×10^{11} vg in the twitcher mouse is roughly equivalent to the low dose administered to GLD dogs if scaled by brain weight or CSF volume. Indeed, we saw a clear dose response to AAV9-cGALC in the GLD dogs. Reduction of the dose to 2×10^{13} vg resulted in doubling of lifespan in the GLD dog (untreated GLD dogs, 15.7 ± 4.8 weeks of age [ref. 12]; 2Wk-Low, 30.43 ± 2.65 weeks of age). Postsymptomatic administration of 2×10^{13} vg to dogs (6Wk-Low), the experimental protocol most similar to the twitcher mice, did not significantly increase survival time in comparison with untreated GLD dogs. Additionally, the twitcher mouse results from a nonsense mutation (c.339G>A) and makes no functional GALC protein (26). Twitcher mice dosed intrathecally with AAV9-mGALC did not receive immunosuppression (15) and thus may have developed an immune response that diminished transgenic protein expression. In fact, CNS-directed AAV-mediated gene therapy has previously

been shown to elicit an immune reaction even in newborn twitcher mice (19). In contrast, GLD in the dog results from a missense mutation (c.473A>C; p.158Y>S) (10) with low levels of GALC enzyme detectable in the CNS, PNS, and somatic tissues (ref. 17 and Figure 7). In addition to this immunological advantage, GLD dogs received high-dose immunosuppression before gene transfer and maintenance immunosuppression for 4 months, preventing immune-driven decreases in transgenic protein expression. Thus, the canine model will likely express greater levels of both endogenous and transgenic GALC following AAV9-GALC therapy than will twitcher mice.

Importantly, presymptomatic dogs that received 2×10^{13} vg exhibited incomplete disease correction and the emergence of clinical signs not typically seen in untreated GLD dogs, which reach humane endpoint (pelvic limb paralysis) at a significantly younger age (12). The delayed progression of motor deficits seen in these dogs correlates with normalization of cerebellar white matter signal intensity and cerebellar area on MRI. While cerebellar disease was ameliorated, pathological signs emerging in 2Wk-Low–treated dogs included behavioral abnormalities and visual deficits. Blindness is likely central in origin as no retinal abnormalities were observed and demyelination and perivascular cuffing were observed in the occipital lobes. Fascinatingly, these clinical findings are similar to those in late-infantile-onset and juvenile-onset patients, who all fall below the 5th percentile in cognitive development by 40 months of age, with vision deterioration observed in the majority (3). These data suggest that treatment with an inadequate dose of AAV9-cGALC provides insufficient GALC enzyme resulting in an attenuated form of the disease with substantial impairments.

Additionally, the canine model of GLD allowed for comparison of pre- and postsymptomatic gene delivery. Our studies found that postsymptomatic therapy was less effective than presymptomatic therapy at the respective doses evaluated. Remarkably, however, dogs treated with 1×10^{14} vg postsymptomatically showed slowing of clinical disease progression, significantly prolonged survival, and reduced CSF protein levels. This outcome stands in stark contrast to HSCT, which is only effective presymptomatically (6). We speculate that postsymptomatically treated dogs did not fare as well as those treated presymptomatically because of reduced vg dose relative to their larger brain and body size at the time of treatment. Two-week-old normal dogs from this specific breeding line have an average brain weight of 26.06 ± 2.23 g ($n = 10$), while analogous 6-week-old dogs have an average brain weight of 52.91 ± 5.56 g ($n = 10$). Based on this, the dogs in the 2Wk-High cohort received an estimated 3.84×10^{12} vg/g of brain weight while dogs in the 6Wk-High cohort received an estimated 1.89×10^{12} vg/g of brain weight, essentially reducing the normalized dose by half. Notably, the single remaining dog in the 6Wk-High cohort, currently 97.1 weeks of age, was the smallest dog within that cohort at the time of treatment, effectively giving the dog a larger dose per gram of body weight and brain weight. While systemic delivery of AAV is conventionally normalized to body weight, our data suggest that intrathecal delivery of AAV would also benefit from normalization to body weight, estimated brain weight, or CSF volume. As such, we predict that normalization of dosing is likely to further improve prognosis for dogs treated postsymptomatically.

Krabbe disease in patients results from more than 200 pathogenic variants. In patients of northern European decent, a 30-kb deletion and 2 missense mutations, c.1586C>T; p.T529M and c.1700A>C; p.Y567S, are expected to account for 50% to 60% of pathogenic alleles in the infantile onset (28, 29). While the naturally occurring canine model has genetic limitations, the missense mutation may be representative of a large population of Krabbe disease patients and how they would respond to gene therapy. Since we were able to establish a robust, clinically relevant biomarker in the canine model, this could potentially be useful to normalize therapeutic responses among different mutations. In Krabbe disease patients, psychosine is a diagnostic marker of phenotype severity and treatment effect (30, 31). Similarly, we have shown that CSF psychosine increased early and steadily in untreated GLD and strongly correlated with disease progression (16). In the 2Wk-Low cohort, detection of psychosine in the CSF was delayed until 12 weeks of age. In the 2Wk-High cohort, CSF psychosine remained undetectable up to 24 weeks, and from 24 to 52 weeks psychosine was detected in the CSF of only 1 dog, which currently remains asymptomatic. If psychosine is indeed a robust biomarker of therapeutic outcome, we predict that this one dog will eventually fare less well than other dogs in the cohort.

CSF protein concentration has recently been shown to predict age of disease onset and survival in a study of 248 Krabbe disease patients (4). Comparably, we show that CSF protein increases early and steadily, with levels rising above normal in untreated GLD dogs by 8 weeks of age. Notably, CSF protein concentration in the 2Wk-High cohort remains within normal levels beyond 52 weeks of age, consistent with their increased longevity and reduced pathology. In contrast, the 2Wk-Low and 6Wk-High cohorts reached above normal CSF protein levels, and the 6Wk-Low cohort emulated untreated GLD dogs with an early, rapid increase in CSF protein. The single 2Wk-High cohort dog with elevated psychosine also has the highest CSF protein, 21 mg/dL at 1 year of age, although still within normal limits.

Postmortem evaluation of the 2Wk-High cohort at 16 weeks of age demonstrated global transduction of the CNS with a significant increase in GALC enzyme activity and significant reduction in psychosine concentration in the most rostral brain region sampled, the frontal cortex. GALC enzyme activity levels approximately 4 times normal were seen in the cerebellar white matter, the tissue sampled closest to the injection site. Interestingly, psychosine concentration was below normal levels in this brain region. Despite attainment of supraphysiological levels of a normally low-expressing enzyme, no evidence of toxicity was noted in any dog, and no lesions were noted on MRI or on histological evaluation near the injection site. MRI lesions have previously been demonstrated in nonhuman primates, in which toxicity due to overexpression of a different secreted hydrolytic lysosomal enzyme occurred (32).

Variability in tissue psychosine concentrations and GALC activity was minimal within the 2Wk-High cohort, all sacrificed at 16 weeks of age, signifying reproducibility of this treatment approach. In contrast, variability was seen within the IS-only and 2Wk-Low cohorts, which were followed until humane endpoint. We recently reported that CSF psychosine concentrations vary and closely correlate with disease progression in GLD dogs (16), and this is likely true for tissues. Interestingly, the youngest dog to develop pelvic

limb paralysis in the IS-only cohort had the highest psychosine levels in the sciatic nerve (Dog 1, Supplemental Table 1). Similarly, in the 2Wk-Low cohort, the single dog that reached humane endpoint solely due to pelvic limb paralysis and not combinatorial factors of blindness and behavior concerns had the highest psychosine concentration in the sciatic nerve (Dog 16, Supplemental Table 1). It is hypothesized that assessment of psychosine concentrations following biopsy of peripheral nerves in patients may yield important information regarding clinical outcome.

Psychosine concentrations were highest in all cohorts in the internal capsule. The internal capsule was the single nervous system tissue in which presymptomatic high-dose AAV did not normalize psychosine and GALC and did not achieve a significant increase in vg copies. It is probable that psychosine had already accumulated to irreversible levels by the time of treatment at 2 weeks of age or, alternatively, cell death and globoid cell formation in this area did not allow for sufficient transduction of therapeutic GALC. Ongoing studies using MALDI mass spectrometry will help elucidate the temporospatial accumulation of psychosine in canine GLD. It has recently been shown in the twitcher mouse that inhibitory effects of psychosine are visible as early as embryonic day 12 (33). Taken together, these findings reiterate the importance of early intervention.

Biochemical findings were corroborated by MRI and histology. In the 2Wk-High cohort, T2-weighted hyperintensity was most apparent on MRI at the centrum semiovale, a region for pathology initiation in Krabbe disease (34, 35). Notably, the lesion was stable from 16 to 52 weeks, suggesting that pathology was likely present at the time of treatment and did not progress thereafter. Histology confirmed this to be a region of demyelination, necrosis, and globoid cell accumulation.

Histological evaluation of GALC by IHC revealed that in untreated and IS-only GLD dogs GALC was detectable in globoid cells densely accumulated in the white matter. The same distribution was seen in the 2Wk-Low cohort, but in greater intensity likely due to the prolonged age. The 2Wk-High cohort demonstrated cortical neurons and Purkinje cells strongly expressing GALC to a greater degree than normal age-matched controls, suggesting either the transduction of these cells or the accumulation of GALC due to mannose-6-phosphate receptor–mediated endocytosis. Quantification of IHC-positive GALC cells was not informative or reliable. The ability of the enzyme to actively cleave a substrate as measured by enzyme assay is more revealing as to the effect of AAV-delivered GALC.

Despite being delivered into the CSF, AAV vector copies were detectable in all somatic tissues analyzed. Intrathecally delivered AAV vectors are redistributed from the subarachnoid space to systemic circulation likely via the arachnoid villi (20). However, recent identification of the glymphatic, or glia-associated lymphatic, system has provided more insight into additional mechanisms that may control AAV clearance. Dysregulation of membrane channels in aged and diseased mouse brains correlated with significantly increased retention of AAV vectors in the brain and reduced systemic leakage (36). This has yet to be investigated in Krabbe disease.

Although effective therapies for CNS disease are being developed, the current inability to treat peripheral neuropathies

continues to impact the prognosis for patients with many lysosomal storage diseases. While cognitive function is improved in infants with Krabbe disease who receive HSCT, motor deficits and peripheral nerve dysfunction often persist (6, 37, 38). Here, in the canine GLD model, early delivery of high-dose, but not low-dose, AAV9-cGALC resulted in a significant increase in GALC enzyme activity and significant reduction of psychosine to below normal levels in the sciatic nerve after intracisternal delivery. Levels of GALC in the 2Wk-High cohort are 3.5 times higher in the sciatic nerve than in the liver, suggesting that the correction to the PNS is not due to leakage of vector or GALC into the periphery. The increase in sciatic nerve GALC activity could be due either to transduction of the lower motor neuron or dorsal root ganglia, resulting in increased axonal GALC, or to transduction of Schwann cells. The delivery of lysosomal enzymes to Schwann cells and axons of peripheral nerves has been previously described in dogs with mucopolysaccharidosis VII that received canine GUSB via intracisternally delivered AAV (39) and likely results from AAV passage down the nerves through endoneurial fluid (40–42) or axonal transport (43, 44). Importantly, in this study, nerve conduction velocity testing and PNS ultrastructure analysis show improved PNS myelination in treated dogs and corroborate the biochemical findings. Together, these findings provide what is to our knowledge the first demonstration of clinical, biochemical, and histological correction of PNS abnormalities in a large-animal model following intracisternal delivery of AAV9. This finding holds implications for treatment of other peripheral nerve disorders using this safe, effective, and proven route of administration.

We previously evaluated combination intravenous and intracerebroventricular administration of AAVrh10 in canine GLD (17). The studies cannot be directly compared because of different AAV serotypes, routes of administration, doses, and immunosuppression protocols. Nonetheless, intracisternal AAV9 evaluated herein resulted in what we believe to be the first extension of lifespan beyond 1 year of age in the GLD dog and more global correction of nervous system disease. Additionally, intracisternal delivery allowed for earlier intervention and required significantly less vector, permitting higher dosing and a more robust study design. Intracisternal AAV9 has shown unprecedented results in this large-animal model and is the most translatable approach evaluated to date. Long-term evaluation of the immune response to AAV9-cGALC, and its relation to circulating GALC enzyme activity, is ongoing and will be reported at the 2-year time point. Additionally, assessment of lumbar intrathecal delivery of AAV9-cGALC is under way and will help guide translation to the clinic.

Conclusions. In this robust study of 26 GLD dogs, we demonstrated that intracisternal delivery of 1×10^{14} vg AAV9-GALC into presymptomatic GLD dogs ameliorated neurological signs of disease beyond 2.5 years of age. Reducing the dose 5-fold resulted in significant extension of lifespan; however, an attenuated form of Krabbe disease developed, including behavioral abnormalities and blindness. Administration of 1×10^{14} vg at a symptomatic age, when HSCT no longer has clinical benefit, significantly extended lifespan and delayed disease progression, with 1 dog still alive beyond 1.5 years of age. Finally, in contrast to HSCT, which only

treats CNS disease, intracisternal administration of AAV-GALC improved both CNS and PNS myelination. These results reiterate findings from other AAV9 clinical trials that high-dose and early intervention are necessary for AAV9 to provide the greatest benefit. In light of safety data of intrathecal delivery of AAV9 emerging from clinical trials for other diseases, we believe that this positive finding in a large-animal model of Krabbe disease warrants timely translation to the clinic.

Methods

Animals, immunosuppression, and AAV vector injections. Dogs were raised in the National Referral Center for Animal Models of Human Genetic Disease of the University of Pennsylvania School of Veterinary Medicine (NIH P40-OD-010939). GLD in dogs is due to a missense mutation in the *GALC* gene, c.473A>C; p.158Y>S. Whole blood from dogs was tested for the *GALC* mutation as previously described (12, 17).

One hour before intracisternal injection, methylprednisolone was delivered intravenously at a dose of 20 mg/kg. Immediately before intracisternal injection, the skin was clipped and scrubbed with 4% chlorhexidine followed by 70% isopropyl alcohol, and approximately 0.5 mL of CSF was collected from the cerebellomedullary cistern. Then 1.0 mL of AAV9-cGALC was delivered as a bolus over less than 1 minute. Dogs received oral prednisone at a dose of 0.5 mg/kg daily for 4 months followed by a 2-week taper. GLD dogs were euthanized using an overdose of intravenous barbiturate at a predetermined or standard humane endpoint. After sacrifice, animals were perfused through the left ventricle with 0.9% cold saline and tissues collected.

Vector production. AAV9-cGALC vector was produced with single-stranded AAV genome comprising an AAV2 inverted terminal repeat (ITR), the CAGGS version of the CBA promoter (1.6 kb total CMV enhancer, chicken β-actin promoter, and partial 5′-untranslated region), codon-optimized canine *GALC* DNA coding sequence (2055 bp), SV-40 polyadenylation signal (143 bp), and an AAV2 ITR. AAV vectors were produced at the University of North Carolina Vector Core as previously described (45). Purified AAV was dialyzed in PBS supplemented with 5% D-sorbitol and an additional 212 mM NaCl (350 mM NaCl total). Vector was titered by quantitative PCR (46), and confirmed by PAGE and silver stain.

Nerve conduction velocity, brainstem auditory evoked response, and MRI. Dogs were anesthetized with propofol, endotracheally intubated, and maintained on isoflurane anesthesia. Nerve conduction velocity was tested using an electrodiagnostics machine (Nicolet Viking Quest). Brainstem auditory evoked response data were recorded using a Nicolet Viking Quest machine (Nicolet Biomedical). Imaging was performed on anesthetized dogs on a 1.5-tesla MRI scanner (Signa, GE Corp.). Nerve conduction velocity testing, brainstem auditory evoked response recording, and MRI were performed as previously described (12, 13, 17).

Histology. Perfused brains were fixed in 4% paraformaldehyde and paraffin-embedded. Myelin staining and periodic acid–Schiff staining were performed as previously described (12, 17). For immunofluorescence, deparaffinized and rehydrated slides were heated to a boil followed by a 30-minute incubation in antigen retrieval solution (HK086, Biogenex). Primary rabbit polyclonal anti-GALC (AB137750, Abcam; 1:200) and rat monoclonal anti–myelin basic protein (NB600-717, Novus Biologics; 1:500) antibodies were diluted in antibody dilu-

ent solution (003118, Life Technologies) and incubated at 37°C for 1 hour. Following three 5-minute washes with PBS, donkey anti–rabbit IgG conjugated to Alexa Fluor 568 (A10042, Thermo Fisher Scientific) and donkey anti–rat IgG conjugated to Alexa Fluor 488 (A21208, Thermo Fisher Scientific) secondary antibodies were diluted 1:500 in antibody diluent solution and incubated at 37°C for 30 minutes. Following three 5-minute washes with PBS, slides were stained with DAPI for 1 minute and mounted. For IHC, following rehydration and antigen retrieval, slides were incubated in 3% hydrogen peroxide for 15 minutes to quench endogenous peroxidases and then rinsed. Sections were blocked for endogenous biotin with an avidin/biotin blocking kit (SP-2001, Vector Laboratories). GALC antibody was diluted and incubated as described for immunofluorescence, washed 3 times for 5 minutes in PBS, and incubated with a 1:500 dilution of biotinylated goat anti–rabbit IgG secondary antibody (BA-1000, Vector Laboratories) at 37°C for 30 minutes. Following three 5-minute PBS washes, sections were incubated with avidin–biotin–horseradish peroxidase complex (PK-6100, Vector Laboratories) at 37°C for 30 minutes. Following three 5-minute PBS washes, colorimetric signal was developed using a DAB kit (SK-4100, Vector Laboratories). Sections were dehydrated through ethanols, cleared in xylene, and mounted with Cytoseal XYL (8312-4, Thermo Fisher Scientific).

Detailed histological evaluation was performed in a blind fashion without knowledge of the experimental groups by a board-certified pathologist. Semiquantitative analysis of globoid cell accumulation, gliosis, and inflammation was performed on H&E sections, while the evaluation of demyelination was performed on adjacent sections stained with iron eriochrome stain.

Peripheral nerve analysis: light microscopy and morphometry. Peripheral nerve specimens were collected from the tibial nerves and prepared as previously described (12, 17). Qualitative morphometry was performed on nerve fibers adequately fixed and free of artifacts. Determinations included myelinated fiber density, split myelinated fiber density, thin myelinated fiber density, and cluster density.

Quantification of tissue GALC enzyme activity. Tissue homogenates (20 μg) in pure H_2O were incubated with fluorescent GALC substrate (6HMU-β-D-galactoside, Moscerdam Substrates) for 17 hours at 37°C. Enzymatic activity was assessed via fluorescence measured with a Beckmann Coulter DTX 880 multimode detector using excitation/emission wavelengths of 385 nm/450 nm.

Quantification of tissue psychosine. Psychosine from tissue homogenates (200 μg) was extracted via a methanol–acetic acid solution and analyzed as previously described (47). Analysis was then performed on a Shimadzu Nexera ultra-high-performance liquid chromatography system equipped with a Waters Acquity UPLC BEH amide column and coupled to a Shimadzu LCMS-8050 triple quadrupole mass spectrometer equipped with positive ion electrospray. D-Lactosyl-β1-1′-D-*erythro*-sphingosine (Avanti Polar Lipids) was used as an internal standard.

Quantification of CSF psychosine. CSF psychosine was determined as previously described (48). Protein precipitation was performed to extract psychosine from 50 μL of dog CSF. Deuterated galactosyl-sphingosine (psychosine-d_5; 1 ng/mL) was used as an internal standard. Sample analysis was performed with a Shimadzu 20AD HPLC system, coupled to a triple quadrupole mass spectrometer (API 4000 QTrap) operated in MRM mode. The positive ion ESI mode was used for detection of psychosine and psychosine-d_5. Data processing was conducted with Analyst 1.5.1 (Applied Biosystems).

Vector quantification. Vector biodistribution was done by quantitative PCR. Tissue DNA was purified and quantified as previously described (24) except that a QIACube HT system was used for genomic DNA purification. Quantification was directed to the codon-optimized canine *GALC* transgene, using primers that would not recognize the endogenous *GALC* gene. The primer sequences were as follows: cGALC-F-5′-GGCGTCCATGCTGCTTGATAG-3′; cGALC-R-5′-ACATCGCTGTTCAGGGTGGAG-3′; cSDHA-F-5′-GC-GTTCCACTTGTCCCTGTA-3′; cSDHA-R-5-TCATCACTTCCCAA-CCTGGC-3′. Data are reported as the number of double-stranded *GALC* molecules per 2 double-stranded copies of the canine SDHA locus (the number of vector DNA copies per diploid canine genome).

Statistics. Data were evaluated for normal distribution by the skewness and kurtosis tests for normality, and the nonparametric Kruskal-Wallis test was used for the initial comparison of each variable between the different treatment groups. The Mann-Whitney test was performed for follow-up pairwise comparisons if the *P* value of the Kruskal-Wallis test was less than 0.05. A *P* value of less than 0.05 on the Mann-Whitney test, which does not assume that the variable is normally distributed, was considered significant. All statistical evaluations were performed using a statistical software package (Stata 14.0 for Macintosh, Stata Corp.).

Study approval. Dogs were raised in the National Referral Center for Animal Models of Human Genetic Disease of the University of Pennsylvania School of Veterinary Medicine (NIH P40-OD-010939) under NIH and US Department of Agriculture guidelines for the care and use of animals in research. The experimental protocol was approved by the University's Institutional Animal Care and Use Committee.

Author contributions

Acknowledgments

Address correspondence to: Allison M. Bradbury, Abigail Wexner Research Institute, Center for Gene Therapy, Nationwide Children's Hospital, 700 N. Children's Drive, WA3016, Columbus, Ohio USA 43205. Phone: 614.355.2694; Email: Allison.Bradbury @nationwidechildrens.org.

AMB's present address is: Nationwide Children's Hospital, Abigail Wexner Research Institute, Center for Gene Therapy, Columbus, Ohio, USA.

1. Wenger DA, Escolar ML, Luzi P, Rafi MA. *Krabbe Disease (Globoid Cell Leukodystrophy)*. Columbus, Ohio, USA: McGraw-Hill; 2014.

2. Beltran-Quintero ML, et al. Early progression of Krabbe disease in patients with symptom onset between 0 and 5 months. *Orphanet J Rare Dis*. 2019;14(1):46.

3. Bascou N, DeRenzo A, Poe MD, Escolar ML. A prospective natural history study of Krabbe disease in a patient cohort with onset between 6 months and 3 years of life. *Orphanet J Rare Dis*. 2018;13(1):126.

4. Komatsuzaki S, et al. Clinical characteristics of 248 patients with Krabbe disease: quantitative natural history modeling based on published cases. *Genet Med*. 2019;21(10):2208–2215.

5. Wasserstein MP, et al. Clinical outcomes of children with abnormal newborn screening results for Krabbe disease in New York State. *Genet Med*. 2016;18(12):1235–1243.

6. Escolar ML, et al. Transplantation of umbilical-cord blood in babies with infantile Krabbe's disease. *N Engl J Med*. 2005;352(20):2069–2081.

7. Aldenhoven M, Kurtzberg J. Cord blood is the optimal graft source for the treatment of pediatric patients with lysosomal storage diseases: clinical outcomes and future directions. *Cytotherapy*. 2015;17(6):765–774.

8. Wright MD, Poe MD, DeRenzo A, Haldal S, Escolar ML. Developmental outcomes of cord blood transplantation for Krabbe disease: a 15-year study. *Neurology*. 2017;89(13):1365–1372.

9. Orsini JJ, et al. Newborn screening for Krabbe disease in New York State: the first eight years' experience. *Genet Med*. 2016;18(3):239–248.

10. Victoria T, Rafi MA, Wenger DA. Cloning of the canine GALC cDNA and identification of the mutation causing globoid cell leukodystrophy in West Highland White and Cairn terriers. *Genomics*. 1996;33(3):457–462.

11. Bradbury A, Peterson D, Vite C, Chen S, Ellinwood NM, Provenzale J. Diffusion tensor imaging analysis of the brain in the canine model of Krabbe disease. *Neuroradiol J*. 2016;29(6):417–424.

12. Bradbury AM, et al. Clinical, electrophysiological, and biochemical markers of peripheral and central nervous system disease in canine globoid cell leukodystrophy (Krabbe's disease). *J Neurosci Res*. 2016;94(11):1007–1017.

13. Cozzi F, Vite CH, Wenger DA, Victoria T, Haskins ME. MRI and electrophysiological abnormalities in a case of canine globoid cell leucodystrophy. *J Small Anim Pract*. 1998;39(8):401–405.

14. Wenger DA, et al. Globoid cell leukodystrophy in cairn and West Highland white terriers. *J Hered*. 1999;90(1):138–142.

15. Karumuthil-Melethil S, Marshall MS, Heindel C, Jakubauskas B, Bongarzone ER, Gray SJ. Intrathecal administration of AAV/GALC vectors in 10-11-day-old twitcher mice improves survival and is enhanced by bone marrow transplant. *J Neurosci Res*. 2016;94(11):1138–1151.

16. Corado CR, et al. Cerebrospinal fluid and serum glycosphingolipid biomarkers in canine globoid cell leukodystrophy (Krabbe Disease). *Mol Cell Neurosci*. 2020;102:103451.

17. Bradbury AM, et al. AAVrh10 gene therapy ameliorates central and peripheral nervous system disease in canine globoid cell leukodystrophy (Krabbe disease). *Hum Gene Ther*. 2018;29(7):785–801.

18. Wu YP, McMahon EJ, Matsuda J, Suzuki K, Matsushima GK, Suzuki K. Expression of immune-related molecules is downregulated in twitcher mice following bone marrow transplantation. *J Neuropathol Exp Neurol*. 2001;60(11):1062–1074.

19. Reddy AS, et al. Bone marrow transplantation augments the effect of brain- and spinal cord-directed adeno-associated virus 2/5 gene therapy by altering inflammation in the murine model of globoid-cell leukodystrophy. *J Neurosci*. 2011;31(27):9945–9957.

20. Schuster DJ, et al. Biodistribution of adeno-associated virus serotype 9 (AAV9) vector after intrathecal and intravenous delivery in mouse. *Front Neuroanat*. 2014;8:42.

21. Hordeaux J, et al. Safe and sustained expression of human iduronidase after intrathecal administration of adeno-associated virus serotype 9 in infant rhesus monkeys. *Hum Gene Ther*. 2019;30(8):957–966.

22. Hinderer C, et al. Severe toxicity in nonhuman primates and piglets following high-dose intravenous administration of an adeno-associated virus vector expressing human SMN. *Hum Gene Ther*. 2018;29(3):285–298.

23. Gray SJ, Nagabhushan Kalburgi S, McCown TJ, Jude Samulski R. Global CNS gene delivery and evasion of anti-AAV-neutralizing antibodies by intrathecal AAV administration in non-human primates. *Gene Ther*. 2013;20(4):450–459.

24. Gray SJ, Matagne V, Bachaboina L, Yadav S, Ojeda SR, Samulski RJ. Preclinical differences of intravascular AAV9 delivery to neurons and glia: a comparative study of adult mice and nonhuman primates. *Mol Ther*. 2011;19(6):1058–1069.

25. Suzuki K, Suzuki K. The twitcher mouse: a model for Krabbe disease and for experimental therapies. *Brain Pathol*. 1995;5(3):249–258.

26. Sakai N, et al. Molecular cloning and expression of cDNA for murine galactocerebrosidase and mutation analysis of the twitcher mouse, a model of Krabbe's disease. *J Neurochem*. 1996;66(3):1118–1124.

27. Ohno K, et al. Kinetics and MR-based monitoring of AAV9 vector delivery into cerebrospinal fluid of nonhuman primates. *Mol Ther Methods Clin Dev*. 2019;13:47–54.

28. Madsen AMH, Wibrand F, Lund AM, Ek J, Dunø M, Østergaard E. Genotype and phenotype classification of 29 patients affected by Krabbe disease. *JIMD Rep*. 2019;46(1):35–45.

29. Tappino B, et al. Identification and characterization of 15 novel GALC gene mutations causing Krabbe disease. *Hum Mutat*. 2010;31(12):E1894–E1914.

30. Escolar ML, et al. Psychosine, a marker of Krabbe phenotype and treatment effect. *Mol Genet Metab*. 2017;121(3):271–278.

31. Langan TJ, et al. Development of a newborn screening tool based on bivariate normal limits: using psychosine and galactocerebrosidase determination on dried blood spots to predict Krabbe Disease. *Genet Med*. 2019;21(7):1644–1651.

32. Golebiowski D, et al. Direct intracranial injection of AAVrh8 encoding monkey β-N-acetyl-hexosaminidase causes neurotoxicity in the primate brain. *Hum Gene Ther*. 2017;28(6):510–522.

33. Sural-Fehr T, et al. Inhibition of the IGF-1-PI3K-Akt-mTORC2 pathway in lipid rafts increases neuronal vulnerability in a genetic lysosomal glycosphingolipidosis. *Dis Model Mech*. 2019;12(5):dmm036590.

34. Poretti A, et al. Novel diffusion tensor imaging findings in Krabbe disease. *Eur J Paediatr Neurol*. 2014;18(2):150–156.

35. Sasaki M, Sakuragawa N, Takashima S, Hanaoka S, Arima M. MRI and CT findings in Krabbe disease. *Pediatr Neurol*. 1991;7(4):283–288.

36. Murlidharan G, Crowther A, Reardon RA, Song J, Asokan A. Glymphatic fluid transport controls paravascular clearance of AAV vectors from the brain. *JCI Insight*. 2016;1(14):e88034.

37. Duffner PK, et al. The long-term outcomes of presymptomatic infants transplanted for Krabbe disease: report of the workshop held on July 11 and 12, 2008, Holiday Valley, New York. *Genet Med*. 2009;11(6):450–454.

38. Siddiqi ZA, Sanders DB, Massey JM. Peripheral neuropathy in Krabbe disease: effect of hematopoietic stem cell transplantation. *Neurology*. 2006;67(2):268–272.

39. Gurda BL, et al. Evaluation of AAV-mediated gene therapy for central nervous system disease in canine Mucopolysaccharidosis VII. *Mol Ther*. 2016;24(2):206–216.

40. McCabe JS, Low FN. The subarachnoid angle: an area of transition in peripheral nerve. *Anat Rec*. 1969;164(1):15–33.

41. Kagiava A, Kleopa KA. Intrathecal delivery of viral vectors for gene therapy. *Methods Mol Biol*. 2018;1791:277–285.

42. Kagiava A, et al. Intrathecal gene therapy rescues a model of demyelinating peripheral neuropathy. *Proc Natl Acad Sci U S A*. 2016;113(17):E2421–E2429.

43. Hennig AK, et al. Intravitreal gene therapy reduces lysosomal storage in specific areas of the CNS in mucopolysaccharidosis VII mice. *J Neurosci*. 2003;23(8):3302–3307.

44. Griffey M, Macauley SL, Ogilvie JM, Sands MS. AAV2-mediated ocular gene therapy for infantile neuronal ceroid lipofuscinosis. *Mol Ther*. 2005;12(3):413–421.

45. Clément N, Grieger JC. Manufacturing of recombinant adeno-associated viral vectors for clinical trials. *Mol Ther Methods Clin Dev*. 2016;3:16002.

46. Gray SJ, Choi VW, Asokan A, Haberman RA, McCown TJ, Samulski RJ. Production of recombinant adeno-associated viral vectors and use in in vitro and in vivo administration. *Curr Protoc Neurosci*. 2011;57(1):4.17.1–4.17.30.

47. Marshall MS, et al. Long-term improvement of neurological signs and metabolic dysfunction in a mouse model of Krabbe's disease after global gene therapy. *Mol Ther*. 2018;26(3):874–889.

48. Sidhu R, et al. A HILIC-MS/MS method for simultaneous quantification of the lysosomal disease markers galactosylsphingosine and glucosylsphingosine in mouse serum. *Biomed Chromatogr*. 2018;32(7):e4235.

Pre-clinical Gene Therapy with AAV9/AGA in Aspartylglucosaminuria Mice Provides Evidence for Clinical Translation

Xin Chen,[1] Sarah Snanoudj-Verber,[2] Laura Pollard,[3] Yuhui Hu,[1] Sara S. Cathey,[3] Ritva Tikkanen,[4] and Steven J. Gray[1]

[1]Department of Pediatrics, UTSW Medical Center, Dallas, TX 75390, USA; [2]Metabolic Biochemistry, University Hospital of Rouen, Rouen, France; [3]Greenwood Genetics Center, Greenwood, SC 29646, USA; [4]Institute of Biochemistry, Medical Faculty, University of Giessen, Giessen, Germany

Aspartylglucosaminuria (AGU) is an autosomal recessive lysosomal storage disease caused by loss of the enzyme aspartylglucosaminidase (AGA), resulting in AGA substrate accumulation. AGU patients have a slow but progressive neurodegenerative disease course, for which there is no approved disease-modifying treatment. In this study, AAV9/AGA was administered to $Aga^{-/-}$ mice intravenously (i.v.) or intrathecally (i.t.), at a range of doses, either before or after disease pathology begins. At either treatment age, AAV9/AGA administration led to (1) dose dependently increased and sustained AGA activity in body fluids and tissues; (2) rapid, sustained, and dose-dependent elimination of AGA substrate in body fluids; (3) significantly rescued locomotor activity; (4) dose-dependent preservation of Purkinje neurons in the cerebellum; and (5) significantly reduced gliosis in the brain. Treated mice had no abnormal neurological phenotype and maintained body weight throughout the whole experiment to 18 months old. In summary, these results demonstrate that treatment of $Aga^{-/-}$ mice with AAV9/AGA is effective and safe, providing strong evidence that AAV9/AGA gene therapy should be considered for human translation. Further, we provide a direct comparison of the efficacy of an i.v. versus i.t. approach using AAV9, which should greatly inform the development of similar treatments for other related lysosomal storage diseases.

INTRODUCTION

Aspartylglucosaminuria (AGU) is an autosomal recessive inherited lysosomal storage disease caused by the loss of functional aspartylglucosaminidase (AGA) enzyme.[1] The AGA enzyme is required for the breakdown of glycoproteins within cellular lysosomes. Most individuals with a mutated *AGA* gene produce either small quantities of defective protein or an inactive precursor polypeptide, which results in the accumulation of the AGA substrate (aspartylglucosamine, GlcNAc-Asn) in the lysosomes of all tissues and body fluids. The accumulated substrate GlcNAc-Asn is excreted in urine of patients in large quantities.

AGU is a slow but progressive and severe neurodegenerative disease characterized by intellectual disability, skeletal and motor abnormalities, and early mortality.[1,2] The median lifespan of AGU patients is approximately 30 to 40 years. The major consequence of substrate accumulation is lysosomal hypertrophy that manifests as intellectual disability as well as additional symptoms including skeletal and joint abnormalities. AGU patients have developmental delays including delayed speech and impaired learning caused by progressive brain atrophy. By the third decade of life, patients have severe intellectual and physical disabilities and are highly dependent on supportive care.

There is no approved therapy for AGU patients that targets the root cause of the disease. A few approaches have been tested to treat AGU. Limited attempts at bone marrow transplantation (BMT) have not shown any benefit.[3] Enzyme replacement therapy (ERT) has the potential to be an effective treatment, but peripheral administration does not adequately treat the central nervous system (CNS). In addition, manufacture of functional AGA with correct post-translational modifications is technically challenging, leading to significant challenges to implement ERT as a viable clinical treatment.[4,5] Moreover, long-term ERT in a mouse model has been shown to induce immune responses, which abolish its therapeutic effects.[4] More recently, treatment of patient fibroblasts in cell culture with small molecule compounds suggested that these substances may be suitable for AGU as a pharmacological chaperone (PC) mediated therapy,[6,7] and its *in vivo* performance is being tested.

Over the last two decades, there have been numerous viral vector-based gene-therapy (GT) approaches tested for other rare inherited disorders and proved to be clinically therapeutic and safe, in some cases resolving the majority of patients' symptoms.[8] Recombinant adeno-associated viral vector type 9 (AAV9) has particularly been shown to be a safe and efficacious neurotropic vector to deliver transgenes to the CNS.[9] These vectors are non-pathogenic, non-replicating, and transduce both dividing and non-dividing cells. Importantly, they are incapable of coding viral proteins and are primarily non-integrating, making them an ideal vector for gene delivery to the CNS.[10] AAV9 mediates broad gene transfer across the entire

A

B

imals were reported to display severe ataxia, and terminally ill animals show extensive gliosis in the brain along with pathological changes in the liver and kidney.

Here, we present preclinical data to support the use of either i.v.- or i.t.-administered AAV9/*AGA* to rescue disease AGU phenotypes in a dose-dependent fashion, either before or after the onset of disease pathology in the $Aga^{-/-}$ mouse model. This AAV9-based GT strategy has the potential to be broadly applied to correct other loss-of-function mutations that lead to CNS disorders.

RESULTS
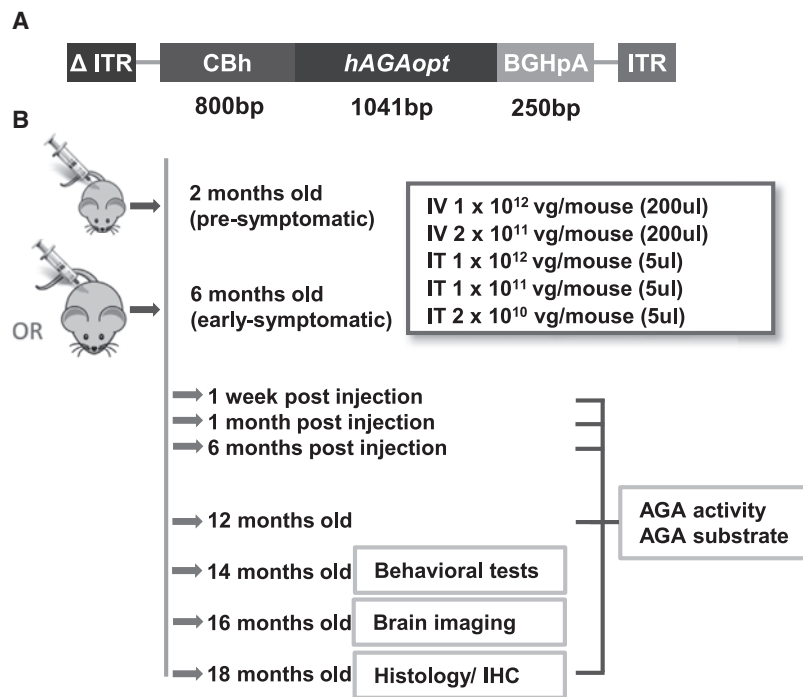
To test whether we could use AAV9/*AGA* vector construct to rescue the phenotypes in the $Aga^{-/-}$ mice, we created a recombinant AAV9 vector encoding a codon-optimized human *AGA* transgene (h*AGA*opt). The AAV9/*AGA* vector consists of AAV9 capsids that are packaged with the self-complementary (sc) AAV genome comprising a mutant AAV2 inverted terminal repeat (ITR) with the D element deleted (Δ ITR), the CBh promoter (cytomegalovirus [CMV] enhancer, chicken beta actin promoter, and synthetic intron),[31] h*AGA*opt DNA coding sequence, the bovine growth hormone polyadenylation (BGHpA) signal, and wild-type (WT) AAV2 ITR (Figure 1A). The AGA enzyme is highly conserved between human and rodents. The human protein has an 82.37% sequence identity with the mouse protein, with the largest variations found within the signal peptide and the C-terminal propeptide of the α-subunit. These peptides are removed during protein maturation and the sequence of the active enzyme is extremely conserved among species, as is the three-dimensional structure of the AGA enzyme.[32]

To test the safety and efficacy of AAV9/*AGA* vector, we used $Aga^{-/-}$ mice generated and described in 1996 by Kaartinen et al.[26] The mice have a targeted neomycin cassette insertion in exon 3, which leads to premature termination of the polypeptide at amino acid residue 103 and no mRNA transcript. The study plan was as follows, which is outlined in Figure 1B: AAV9/*AGA* was administered to the $Aga^{-/-}$ mice either i.v. with 200 μL of 1×10^{12} or 2×10^{11} vector genome (vg)/

CNS in a way that translates from mice to larger animal models.[9–19] Furthermore, AAV9 can be purified in large quantities at high concentrations for potential use in delivering a functional copy of a gene directly to the CNS using either an intravenous (i.v.)[20–22] or intrathecal (i.t.)[9–19] route of administration. The AAV9 vector is being utilized via i.v. administration in the Food and Drug Administration (FDA)-approved GT Zolgensma, for infants with spinal muscular atrophy (SMA). It is also being used in multiple GT clinical trials delivered by an i.t. route, including for giant axonal neuropathy (GAN), SMA, CLN6 Batten disease, and CLN3 Batten disease (ClinicalTrials.gov: NCT02362438, NCT03381729, NCT04273243, and NCT03770572, respectively).

For AGU patients, GT represents a reasonable and promising approach to provide a meaningful and long-term therapeutic benefit for this patient population. AGU is an attractive candidate for GT, as a portion of the expressed enzyme is secreted, and i.v. delivered AGA can be taken up by other cells via the mannose-6-phosphate pathway, potentially treating the condition in non-transduced diseased cell populations.[23] There is also data on restoration of AGA expression in cell lines and animal models supporting an *AGA* GT approach.[24,25]

The $Aga^{-/-}$ mouse model is an accurate genetic model that mirrors the human AGU phenotype for efficacy testing. $Aga^{-/-}$ mice do not have detectable AGA activity, have substrate GlcNAc-Asn accumulation in tissues and body fluids, and exhibit lysosomal hypertrophy in visceral organs, recapitulating the salient features of the human disease.[26–28] By 5 months old, $Aga^{-/-}$ mice have extensive morpho-
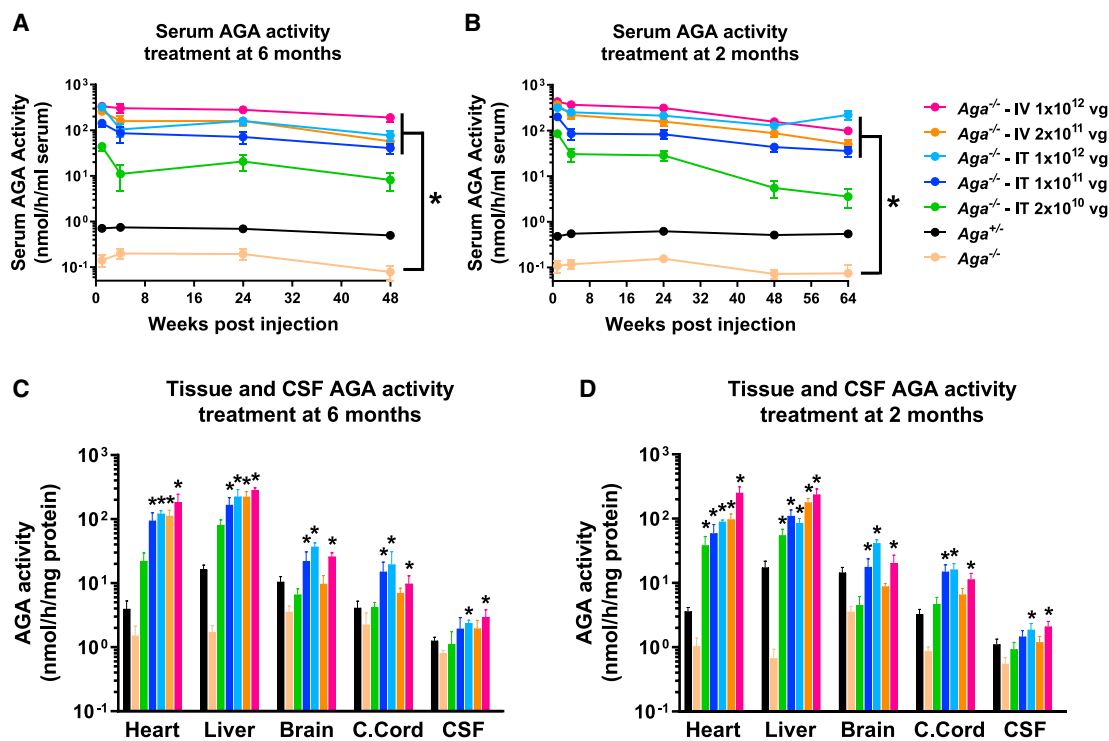
Figure 2. AAV9/*AGA* Gene Therapy (GT) Dose Dependently Increases AGA Activity in Serum, Tissues, and Cerebrospinal Fluid (CSF) to a Supraphysiological Level

(A–D) Various doses of AAV9/*AGA* vector were administered either i.t. or i.v. to *Aga*$^{-/-}$ mice at 6 months old (A and C) or 2 months old (B and D). AGA activity was assayed in serum sampled at 1, 4, 24, 48 (A and B), and 64 (B) weeks following AAV9/*AGA* administration. AGA activity was assayed in tissue lysates from heart, liver, brain, and cervical spinal cord (c. cord) and in CSF collected at necropsy (C and D) when the mice reached 18 months old. All data are presented as mean ± SEM. * depicts significant difference ($p < 0.05$) by ordinary one-way ANOVA followed by Dunnett's multiple-comparisons test compared to the untreated *Aga*$^{-/-}$ control. n = 12~39 in (A), n = 15~66 in (B), n = 3–6 in (C), and n = 4–8 in (D).

mouse or i.t. with 5 μL of 1×10^{12}, 1×10^{11}, or 2×10^{10} vg/mouse. Cohorts of mice were injected when they were still pre-symptomatic at 2 months old or at 6 months old when they were at early stages of showing AGU-related pathology. AGA activity and AGA substrate GlcNAc-Asn levels were measured in both 2-month and 6-month cohorts at 1 week, 1 month, and 6 months post-injection, and at 12 and 18 months old. Behavioral tests were conducted in all treated animals at 14 months old, and brain imaging was conducted at 16 months old. All remaining mice were sacrificed at 18 months old for histology and immunohistochemistry (IHC) tests.

AAV9/*AGA* GT Increases AGA Activity in *Aga*$^{-/-}$ Mice

To examine the effects of AAV9/*AGA* vector delivery on levels of AGA protein in mice, serum AGA activity was measured longitudinally following a single dose of AAV9/*AGA* in mice treated at 6 or 2 months old. AGA activity in heterozygous *Aga*$^{+/-}$ mice is about 40% to 50% that of AGA activity in WT mice, which is sufficient enzyme activity to prevent disease. In the GT-treated *Aga*$^{-/-}$ mice, AGA activity was increased to supraphysiological levels in a dose-dependent manner in the serum compared to heterozygous carriers (Figures 2A and 2B). At each dose, sustained AGA activity was

achieved in the serum over the course of 48 and 64 weeks following the one-dose treatment in 6- or 2-month-old mice (Figures 2A and 2B). AGA activity was also measured in tissue lysates from the heart, liver, brain, and cervical spinal cord, and in cerebral spinal fluid (CSF) collected at necropsy when the mice treated at 6 or 2 months old reached 18 months old. We found a significant dose-dependent increase of AGA activity in different tissues and in CSF to a supraphysiological level (Figures 2C and 2D). We conclude that a one-time delivery of AAV9/*AGA* to *Aga*$^{-/-}$ mice results in the expression of *AGA* transgene and high levels of AGA enzyme that result in sustained supraphysiological levels of AGA activity.

AAV9/*AGA* GT Reduces AGA Substrate GlcNAc-Asn Accumulation in *Aga*$^{-/-}$ Mice

Absence of AGA enzymatic activity results in the accumulation of AGA substrate GlcNAc-Asn in the lysosomes of various tissues and body fluids.[33] Large amounts of GlcNAc-Asn substrate can be readily detected in urine of AGU patients and is thereby used as a diagnostic biomarker. GlcNAc-Asn levels were measured longitudinally in the serum and urine at 1, 4, 24, 48, and 64 weeks and in CSF at 18 months old in both mouse cohorts treated with AAV9/*AGA* vector at either 6
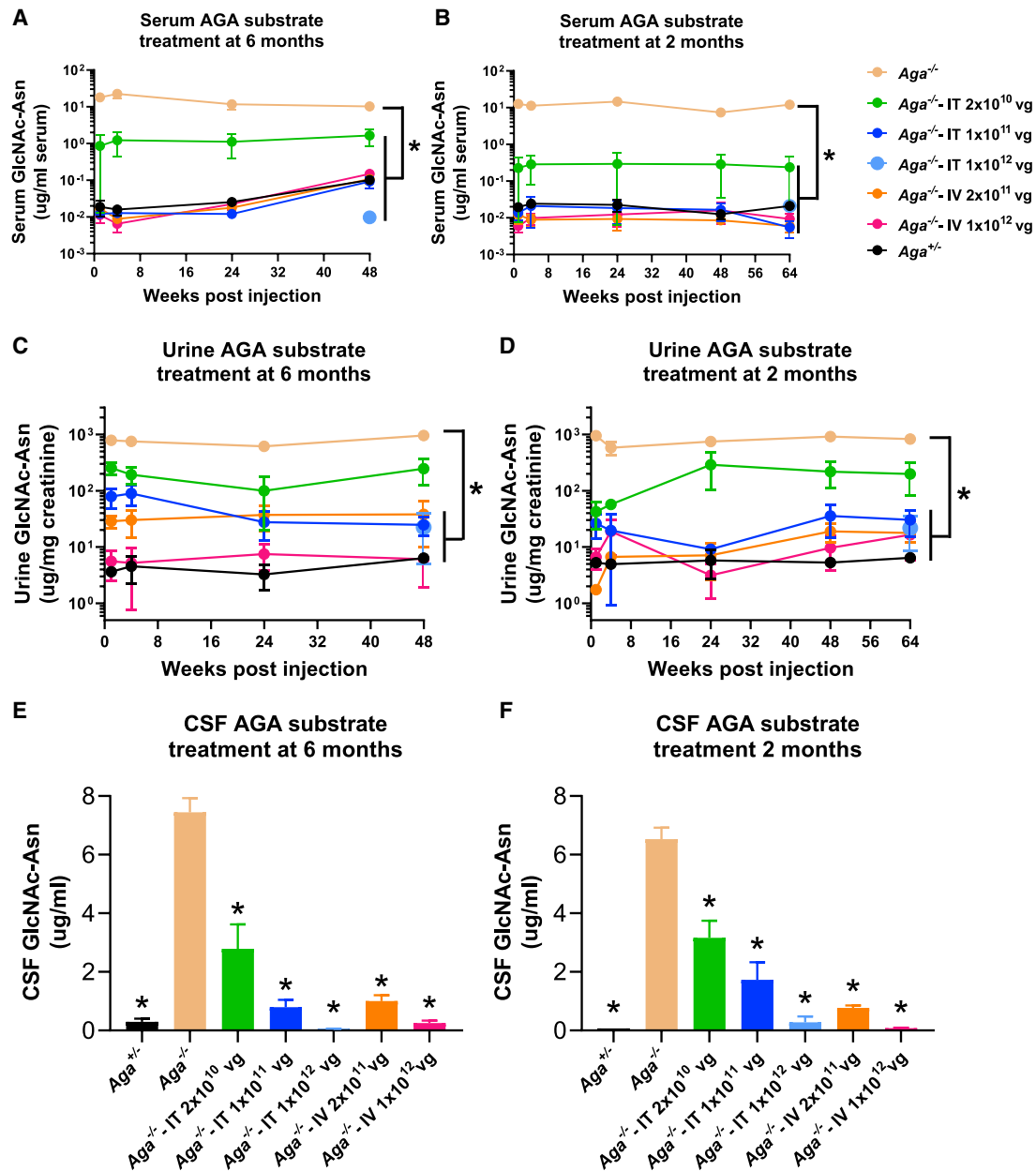
Figure 3. AAV9/*AGA* GT Rapidly and Sustainedly Reduces AGA Substrate Accumulation in Serum, Urine, and CSF

(A–F) Various doses of AAV9/*AGA* vector were administered either i.t. or i.v. to *Aga*$^{-/-}$ mice at 6 months old (A, C, and E) or 2 months old (B, D, and F). AGA substrate was assayed in serum (A and B) and urine (C and D) sampled at 1, 4, 24, 48 (A–D), and 64 (B and D) weeks following AAV9/*AGA* GT. AGA substrate was assayed in CSF (E and F) collected at necropsy when the mice reached 18 months old. All data are presented as mean ± SEM. * depicts significant difference (p < 0.05) by ordinary one-way ANOVA followed by Dunnett's multiple-comparisons test compared to the untreated *Aga*$^{-/-}$ control. n = 4–12 in (A), n = 4–10 in (B), n = 4–16 in (C), n = 3–10 in (D), n = 2–14 in (E), and n = 4–14 in (F).

or 2 months old (Figure 3). In the *Aga*$^{-/-}$ mice treated either with an i.v. or i.t. AAV9/*AGA* delivery, serum levels of GlcNAc-Asn were rapidly reduced close to undetectable levels by week 4 post-therapy and maintained at these low levels through week 64 in all treated cohorts except the i.t. low-dose cohort (Figures 3A and B). A similar

trend was observed with the urinary excretion of GlcNAc-Asn (Figures 3C and 3D). We also found significant and dose-dependent decreases in the accumulation of GlcNAc-Asn in CSF collected at 18 months old (Figures 3E and 3F). Collectively, compared to control untreated *Aga*$^{-/-}$ mice, mice treated at 6 months or 2 months old i.v.
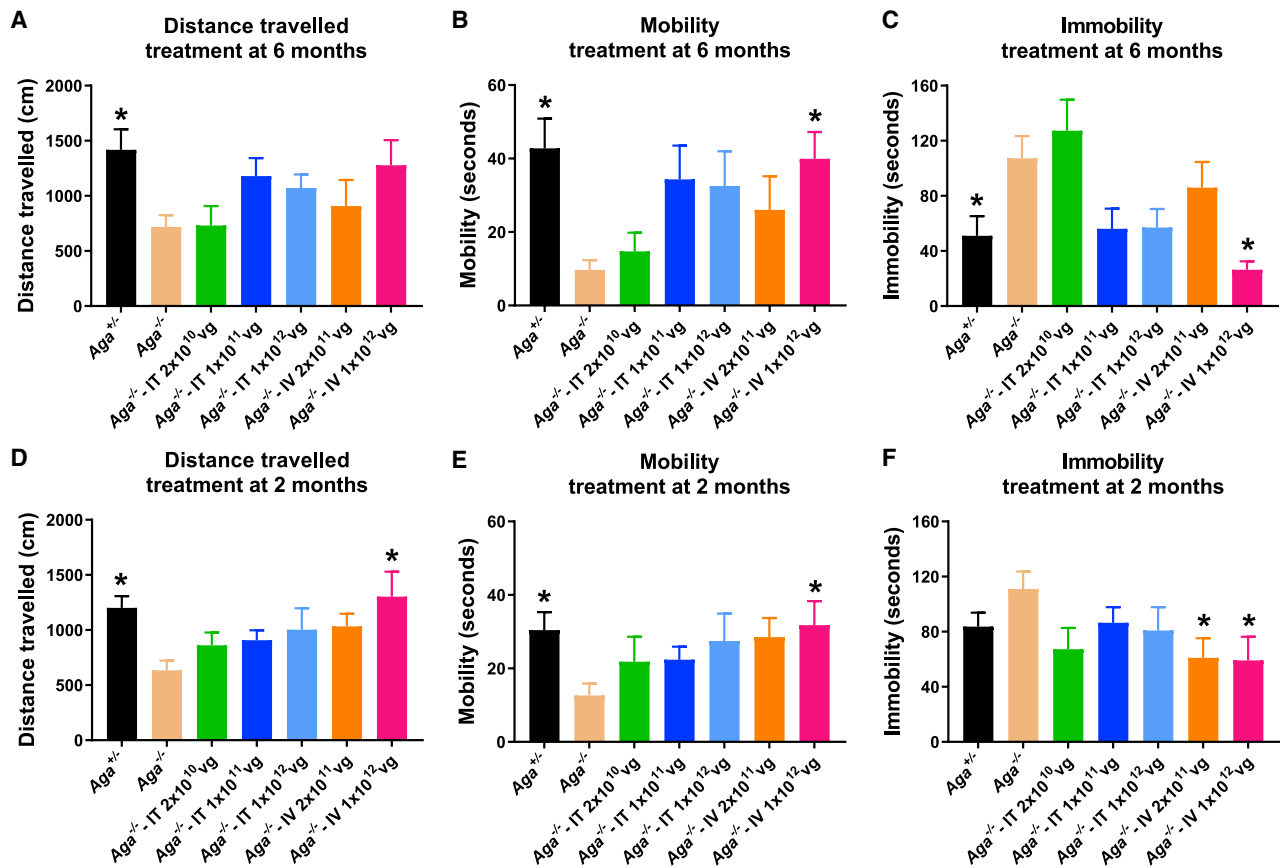
Figure 4. AAV9/*AGA* GT Rescues Abnormal Behavior of *Aga*^{−/−} Mice during the First 5 Min of Open-Field Tests

(A–F) Various doses of AAV9/*AGA* vector were administered either i.t. or i.v. to *Aga*^{−/−} mice at 6 months old (A–C) or 2 months old (D–F). At 14 months old, the mice were allowed to survey an open-field apparatus. The distance traveled in the first 5 min (distance traveled, A and D), time spent highly moving around (mobility, B and E), and time spent still (immobility, C and F) were recorded and quantified by an automated Noldus video tracking system. All data are presented as mean ± SEM. * depicts significant difference ($p < 0.05$) by ordinary one-way ANOVA followed by Dunnett's multiple-comparisons test compared to the untreated *Aga*^{−/−} control. n = 7–21 in (A)–(C), and n = 11–37 in (D)–(F).

or i.t. with high doses of AAV9/*AGA* vector had rapid, sustained, and dose-dependent reductions of the AGA substrate GlcNAc-Asn in the serum, urine, and CSF, to levels similar to those found in the control *Aga*^{+/−} mice.

AAV9/*AGA* GT Rescues Abnormal Behavior of *Aga*^{−/−} Mice during the First 5 Minutes of Open-Field Tests

Based on the progressive nature of AGU, correction of GlcNAc-Asn substrate accumulation is expected to slow or even halt the neurodegeneration, resulting in an amelioration of the phenotypes seen in patients. To test this directly, mice treated at either 6 or 2 months old with AAV9/*AGA* were evaluated at 14 months old, when untreated *Aga*^{−/−} mice show reduced activity in an open-field test. Contrary to previous publication,[26] our colony of AGU mice displayed mild phenotypes overall, with limited tests showing statistically significant differences between *Aga*^{+/−} and *Aga*^{−/−} mice. The open-field test is a tool to assess novel environment exploration, anxiety-related behavior, and general locomotor activity.[34] The mice were allowed

to survey an open field, and we measured their distance traveled in the first 5 min as well as time spent with high movement versus time spent still. The first 5 min of the test session was chosen because it sufficiently captures the significant difference of locomotor activity between *Aga*^{−/−} mice and their *Aga*^{+/−} littermates (Figure S1). At 14 months old, *Aga*^{+/−} mice were highly mobile, inspecting the new and unfamiliar surroundings, and spent less time immobile or stationary. In contrast, the untreated *Aga*^{−/−} mice displayed lower exploratory behavior and traveled significantly shorter distances relative to their *Aga*^{+/−} littermates (Figure 4).

Aga^{−/−} mice that received an i.v.- or i.t.-delivered high dose of AAV9/*AGA* had improved activity in open-field tests when compared to the untreated *Aga*^{−/−} mice, irrespective of whether the mice were treated at 6 months (Figures 4A–4C) or at 2 months old (Figures 4D–4F). Both cohorts of mice that had i.v. or i.t. delivery of high-dose AAV9/*AGA* showed a decrease in the time spent still (Figures 4C and 4F), increase in the time spent highly moving around (mobility)
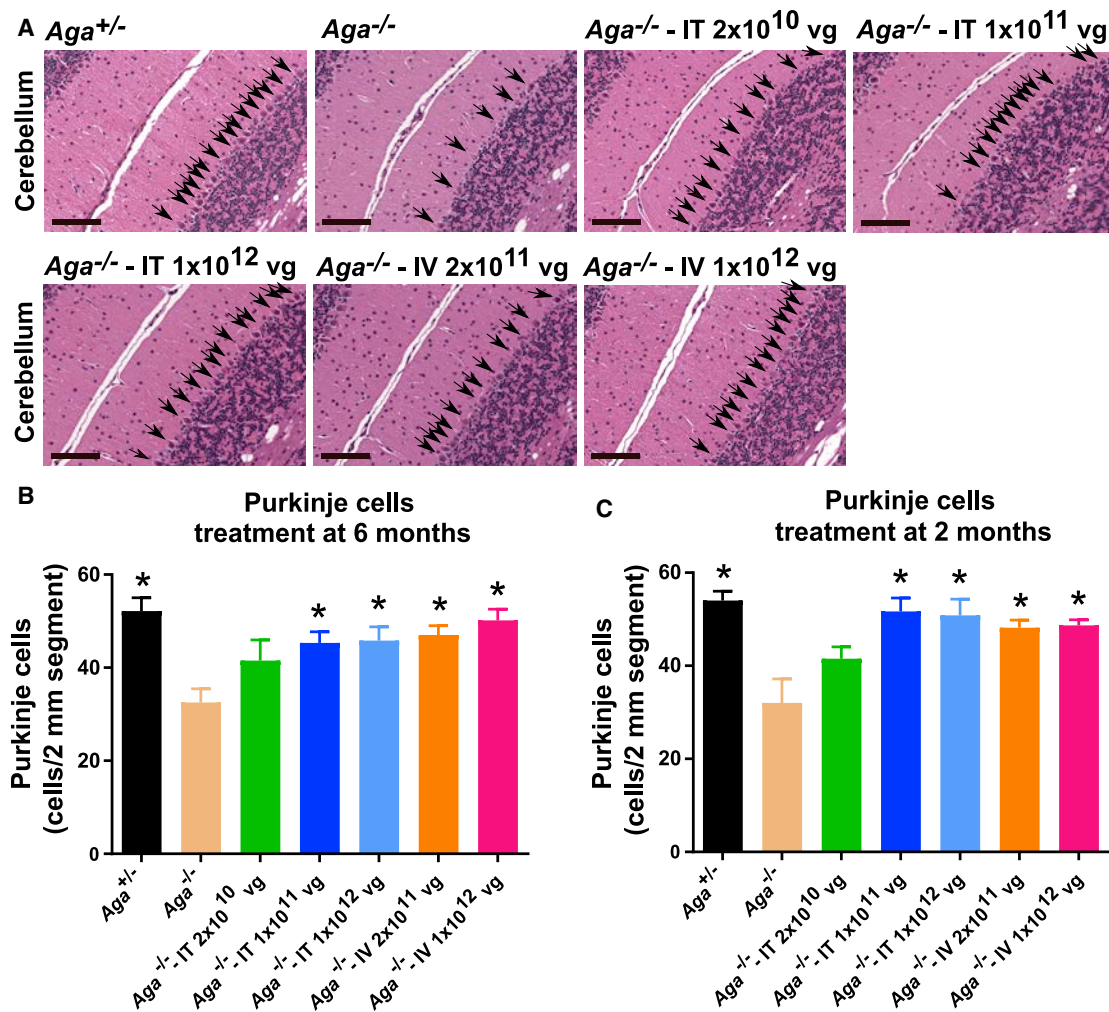
Figure 5. AAV9/*AGA* GT Significantly Preserves Purkinje Cells in the Cerebellum in *Aga*^{−/−} Mice

(A–C) Various doses of AAV9/*AGA* vector were administered either i.t. or i.v. to *Aga*^{−/−} mice treated at 6 months old (A and B) or 2 months old (C). At 18 months old, mouse brain was harvested for hematoxylin and eosin (H&E) staining. Arrows in (A) indicate Purkinje cells, and scale bars in (A) represent 200 μm. All data in (B) and (C) are presented as mean ± SEM. * depicts significant difference ($p < 0.05$) by ordinary one-way ANOVA followed by Dunnett's multiple-comparisons test compared to the untreated *Aga*^{−/−} control. n = 6 in (B), and n = 3–6 in (C).

(Figures 4B and 4E), and increase in distance traveled (Figures 4A and 4D). The i.v. application had a trend toward the strongest corrective effect on these behavioral measures.

AAV9/*AGA* GT Preserves Purkinje Cells in the Cerebellum in *Aga*^{−/−} Mice

Lysosomal hypertrophy as exhibited by cellular vacuolation in visceral organs of the *Aga*^{−/−} mice resembles human AGU histopathology.[28,29] Neuronal, glial, and endothelial cells of the frontal cortex, cerebellum, brain stem, and spinal cord of the AGU mice become vacuolated around 6 months old and progressively worsen. By ten months, *Aga*^{−/−} mice have extensive loss of cerebellar Purkinje neurons, and by > 18 months old ∼70%–80% of the Purkinje neurons in the cerebellar cortex are reportedly lost compared to

their age-matched *Aga*^{+/−} littermates. We examined the cerebellar histopathology of GT-treated mice compared to their untreated *Aga*^{−/−} controls of the same age (Figure 5A). At 18 months old, hematoxylin and eosin (H&E) staining of cerebellum sections exhibited significant preservation of Purkinje neurons in both cohorts of mice, treated at 6 months or at 2 months old, compared to untreated *Aga*^{−/−} control mice, which exhibited loss of Purkinje neurons in the cerebellum (Figures 5A–5C). These results were further confirmed with IHC staining of Purkinje cells in the cerebellum with an antibody against calbindin (Figure S2). Although we saw a less severe (∼40%) loss of Purkinje neurons than what was previously reported (∼70%–80% loss) for this *Aga*^{−/−} model, there was significant preservation of these neurons in mice that were treated at 6 months or 2 months old with the two
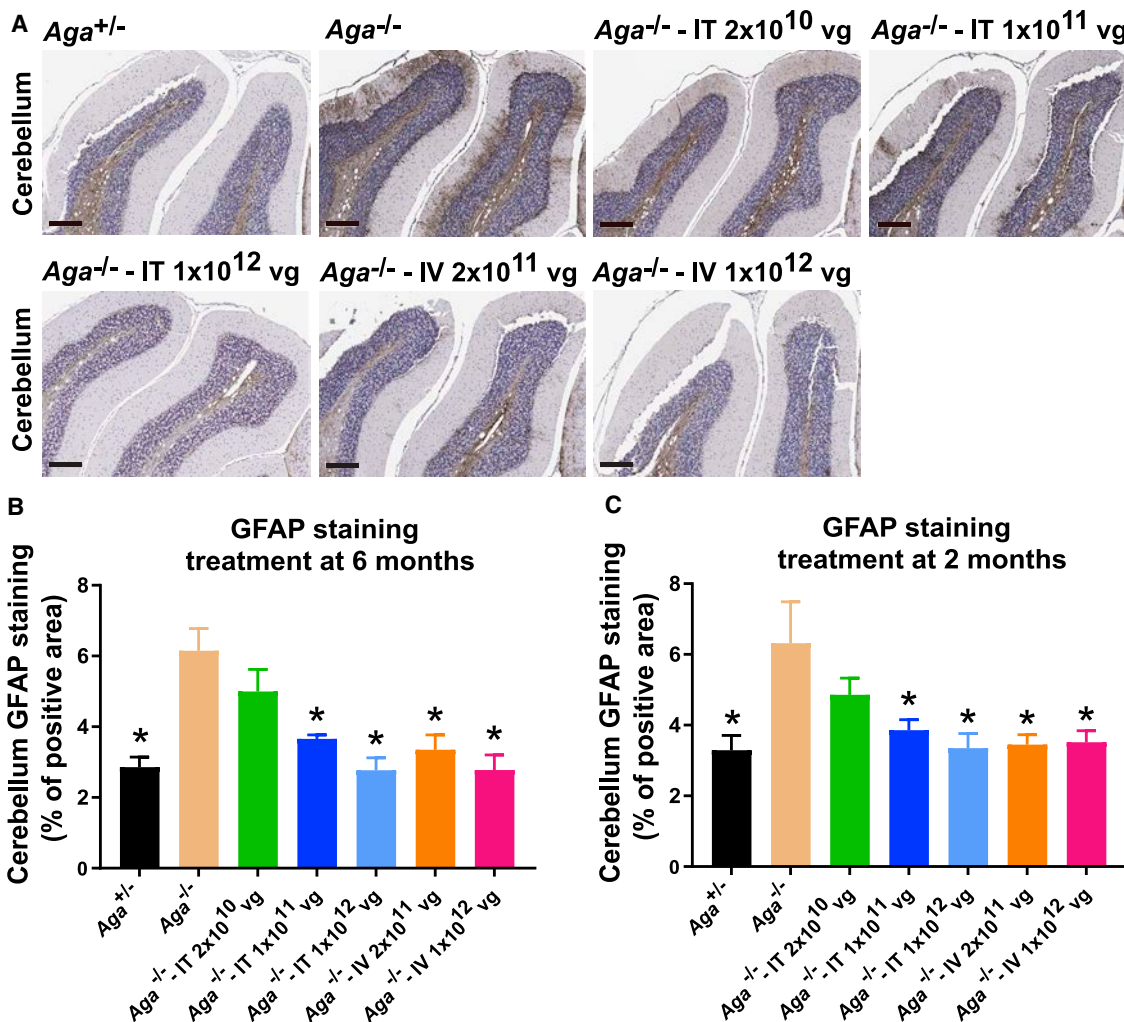
Figure 6. AAV9/AGA GT Significantly Reduces Gliosis in Aga−/− Mice

(A–C) Various doses of AAV9/AGA vector were administered either i.t. or i.v. to Aga−/− mice at 6 months old (A and B) or 2 months old (C). At 18 months old, mouse brain was harvested for glial fibrillary acidic protein (GFAP) staining. Scale bars in (A) represent 500 μm. All data in (B) and (C) are presented as mean ± SEM. Asterisk (*) depicts significant difference (p < 0.05) by ordinary one-way ANOVA followed by Dunnett's multiple-comparisons test compared to the untreated Aga−/− control. n = 6–7 in (B), and n = 7 in (C).

highest i.t. doses and with the low and high i.v. doses (Figures 5B and 5C).

AAV9/AGA GT Reduces Gliosis in the CNS in Aga−/− Mice

Terminally ill Aga−/− mice reportedly show extensive gliosis in the brain.[29] To establish when the onset of gliosis occurs and to what degree in the brains of our Aga−/− mice, we initially tested for gliosis at 2 and 6 months old in untreated mice to establish a baseline. Using glial fibrillary acidic protein (GFAP) staining, the 2-month-old Aga−/− mice did not have more gliosis in the cerebellum and midbrain compared to their Aga+/− littermates (Figures S3B, S3D, and S3E). By 6 months old, the Aga−/− mice displayed moderate but not significantly more gliosis in these brain regions compared to their Aga+/− littermates (Figures S3A, S3C, and S3E).

We then stained mouse brain for GFAP to evaluate for gliosis[35] after necropsy of the AAV9/AGA-treated animals at 18 months old (Figure 6A). Compared to untreated Aga−/− control mice, the mice treated at both i.v. doses and the mice treated with the two highest i.t. doses at 6 months or at 2 months old had significantly reduced gliosis, comparable to that seen in the Aga+/− control animals (Figures 6B and 6C).

We also assessed GFAP staining within the isocortex, subcortex (hippocampus, thalamus, and hypothalamus), the MPM (midbrain, pons, and medulla), cervical spinal cord, and the lumbar spinal cord to assess for gliosis in these brain regions (Figure S4). Among those animals that received i.v. AAV9/AGA at 6 months old, there was a significant decrease in gliosis in the MPM (Figure S4C). Among those

animals that received i.v. AAV9/*AGA* at 2 months old, there was a significant decrease in gliosis in the subcortex and MPM (Figures S4G and S4H). Among the animals that were treated at 2 months old with the highest i.t. dose, there was a significant decrease in gliosis in the subcortex, MPM, and cervical spinal cord (Figures S4G–S4I).

AAV9/*AGA* GT Is Safe and Well-Tolerated in the *Aga*$^{-/-}$ Mice

To assess the safety of the AAV9/*AGA* vector and to ensure there are no non-specific adverse effects on the animal model, brain size and brain weight were assessed in the control *Aga*$^{+/-}$ and *Aga*$^{-/-}$ mice injected with various doses of the AAV9/*AGA* vector, either i.v. or i.t. Sizes of the cerebellum, isocortex, striatum, and ventricle were measured at 16 months old in the animals using magnetic resonance imaging (MRI) (Figures S5A–S5D). There were no significant differences in the sizes of the brain regions between the untreated *Aga*$^{-/-}$, treated *Aga*$^{-/-}$, and *Aga*$^{+/-}$ littermates. Following necropsy at 18 months old, there were also no differences in whole-brain weight (Figure S5E). Additionally, it is worth noting that we were not able to reproduce previously published findings[27,28] of MRI abnormalities in the *Aga*$^{-/-}$ mice.

Injection of AAV9/*AGA* vector with any dose, by either i.v. or i.t. route of delivery, did not reduce survival rate in either the pre-symptomatic or early-symptomatic mice, suggesting the AAV9/*AGA* GT is overall safe and well tolerated (Figure S6). This conclusion is further supported by the histopathological safety report (Supplemental Report) summarized by a blinded licensed veterinary pathologist who concluded that none of the microscopic findings are suggestive of adverse effects related to AAV9/*AGA* vector administration in *Aga*$^{-/-}$ mice.

DISCUSSION

Recombinant AAV9-mediated GT has been extensively used in preclinical and clinical studies for the treatment of CNS disorders. Efficacy with AAV9 has been demonstrated in numerous pre-clinical models of CNS disorders and in some clinical studies, using either an i.v. or i.t. route of administration. Here, we tested the feasibility and efficacy of an AAV9-based strategy to deliver the human *AGA* gene to the *Aga*$^{-/-}$ mouse, a model of AGU, an autosomal recessive inherited lysosomal storage disease. Of note, the study was designed as a comprehensive comparison of i.v. and i.t. routes of administration to treat AGU, which could serve as a model for the treatment of other lysosomal storage disorders with similar characteristics as AGU (i.e., CNS pathology and soluble lysosomal enzyme capable of cross-correction).

Apart from the main purpose of the study to evaluate the potential efficacy of AAV9/*AGA*, we also report additional characterization of the mouse model. In general, the phenotype in our colony of *Aga*$^{-/-}$ mice was notably less severe than was previously described.[26,29] Survival was not significantly impacted up to 18 months old, weight was unaffected up to 18 months old, pathology was milder than reported at 6 months and 18 months old, and we did not note the severe morbidity of mice as they approached

18 months old, as originally reported for the model. The caveat to this is that the *Aga*$^{-/-}$ mouse model was on a mixed background (the product of four distinct mouse strain backgrounds), which generated a mouse colony with four different fur colors (silver gray, light brown, dark brown, and black). Although a larger battery of behavioral tests were explored at different ages (rotarod, activity chamber, social novelty, and the Morris water-maze tests, data not shown), the mice generally showed a high degree of variability, and only the open-field test in aged mice was identified as a suitable behavioral outcome. The greatest phenotype affecting morbidity was extreme urinary retention as mice approached 20–21 months of age, which was the primary reason for our predetermined endpoint of 18 months old in our study design. The relatively mild phenotype in mice may be reflective of the protracted disease course in humans. Nevertheless, the mice display key features of the disease and our opinion is that they represent an adequate model to assess treatment efficacy and predict a translational benefit of AAV9/*AGA*.

The *Aga*$^{-/-}$ mice received a single injection of the AAV9/*AGA* before the emergence of disease pathology at 2 months old or at the early stage of disease pathology at 6 months old, in order to test whether the GT could restore AGA function and ameliorate the symptoms associated with AGU. Compared to their *Aga*$^{+/-}$ littermates, AAV9/*AGA* GT increased AGA activity to supraphysiological levels in the *Aga*$^{-/-}$ mice in a dose-dependent manner in serum with pre- and early-symptomatic intervention irrespective of the route of treatment. The activity levels were sustained in the GT-treated *Aga*$^{-/-}$ mice at the last instance of testing, up to 16 months after dosing, confirming stable expression of the human *AGA* transgene and enduring enzyme functionality. High levels of AGA activity detected in the brain tissue indicated efficient AGA enzyme biodistribution to the CNS following GT in the *Aga*$^{-/-}$ mice. The presence of AGA activity in the blood and peripheral tissues of the i.v.- and i.t.-dosed mice indicated that either i.v. or i.t. delivery of AAV9/*AGA* provides functional enzyme throughout the body. Of significance is the high levels of AGA activity in the blood and peripheral tissues following i.t. administration, which is consistent with prior observations that AAV9 distributes to peripheral organs following this route of administration.[11,14,36]

In the treated *Aga*$^{-/-}$ mice, we saw supraphysiological AGA enzyme activity within the CNS and throughout the entire body following GT, either from local expression or cross-correction by circulating enzyme. AGA enzyme activity is a key and relevant biochemical biomarker that is translatable to humans. These increased AGA enzyme levels correlated, in a dose-responsive fashion, with correction of another key translatable biochemical biomarker (AGA substrate GlcNAc-Asn), improved behavioral outcomes (movement in open field), and histopathological improvement (preservation of Purkinje neurons and reduced gliosis). Importantly, the totality of this data converges to an overall conclusion of a comprehensive rescue of the disease at the high dose, achievable via either an i.v. or i.t. route of administration of AAV9/*AGA*.

Although injection of AAV9/*AGA* by either route induces sustained circulating AGA levels that are over 100 times normal, this overabundance of AGA did not create any adverse consequences that we could discern. Compared to their WT littermates, $Aga^{-/-}$ mice are reported to have poor survival, with only 40% surviving past the 20-month mark.[30] In our hands, $Aga^{-/-}$ mice have a median survival rate of over 18 months. There were no signs of morbidity seen in the treatment groups compared to normal $Aga^{+/-}$ mice and untreated $Aga^{-/-}$ mice. There were no differences in weight in treated versus untreated cohorts and no significant differences in survival. Further, treated mice displayed normalized movement patterns rather than any adverse signs. While observations of subtle toxic effects from AAV9/*AGA* are not completely ruled out, our data suggest a favorable long-term safety profile of AAV9/*AGA* at up to one year post-injection.

Both the i.t. and i.v. approaches provided a strong benefit to the $Aga^{-/-}$ mice, and both approaches can translate to humans. A single 1×10^{11} vg i.t. dose provided clear biochemical, histological, and behavioral benefit to $Aga^{-/-}$ mice, as did the higher 1×10^{12} vg i.t. or i.v. dose. A 5-fold lower i.t. dose (2×10^{10} vg) or a 5-fold lower i.v. dose (2×10^{11} vg) resulted in only a partial rescue. The highest 1×10^{12} vg i.t. dose did not provide any further benefit above the 1×10^{11} vg i.t. dose. Thus, our studies set a therapeutic target dose of either 1×10^{11} vg administered i.t. or 1×10^{12} vg (approximately 4×10^{13} vg/kg) administered i.v. Considering that a 10-fold lower dose can be administered i.t. versus i.v. with similar therapeutic effect, our conclusion would be to favor the i.t. route for human translation. Further, the apparent safety of a 10-fold higher (1×10^{12} vg) i.t. dose provides a favorable safety margin.

When considering human translation of the approach, a number of useful points can be derived from this study. First is a target dose, which in mice was 1×10^{11} vg administered i.t. If the dose is scaled by CSF volume, then this would equate to a dose of 4×10^{14} vg total in a human (assuming 0.035 mL of CSF in mice and 140 mL CSF in a human). The CSF volume of humans is relatively static after 3 years old,[37] so this strategy would suggest a target dose of 4×10^{14} vg total in AGU patients > 3 years old, regardless of age. Beyond setting a target dose, our studies characterized two relevant biomarkers that can be measured longitudinally and correlate to a therapeutic response to AAV9/*AGA*: AGA enzyme activity and the AGA enzyme substrate GlcNAc-Asn. AGA enzyme activity can be assessed longitudinally in blood and CSF. AGA enzyme substrate GlcNAc-Asn can be assayed longitudinally in blood, CSF, and urine. Our pre-clinical results predict that both of these biomarkers should respond within weeks of treatment, with AGA enzyme levels elevating to at or above normal levels and AGA enzyme substrate GlcNAc-Asn levels reducing to normal in all 3 body fluids. These $Aga^{-/-}$ studies further predict a behavioral benefit to AGU patients, but extrapolation of the activity in mice (open-field test) to clinical outcomes in humans is clearly less straightforward.

In conclusion, the results achieved in these preclinical studies demonstrate the efficacy and safety of AAV9/*AGA* and strongly support the clinical evaluation in AGU patients, pending the outcomes for further (and more rigorous) pre-clinical safety studies. While either an i.v. or i.t. approach would be predicted to work, we conclude that an i.t. approach should be favored. The conclusions from this study may translate to other AAV9-based gene replacement strategies for related neurological disorders.

MATERIALS AND METHODS

Plasmid Design and Development

We designed and developed the CBh-*hAGAopt*-BGHpA plasmid (Figure 1A) containing the transgene of a human *AGA* codon-optimized construct (*hAGAopt*). The DNA sequence was modified such that the final amino acid sequence is unchanged but there is a significant increase in expression levels of the heterologous gene.[38] The transgene consists of a human *AGA* DNA coding sequence of 1,041 bp between an 800-bp CBh promoter and a 250-bp BGHpA signal. The gene regulatory elements (CBh promoter, BGHpA) are identical to the construct utilized and characterized in these publications, in mice, rats, pigs, and non-human primates.[13,14,20,31] The CBh promoter and BGHpA are utilized for their small size and ability to drive strong expression, allowing for packaging into an scAAV vector.[31]

scAAV9/*AGA* Vector Preparation

Research-grade AAV9/*AGA* vector for pre-clinical testing was manufactured at University of North Carolina Vector Core (UNC-VC). The established plasmid was packaged into sc AAV9 vector,[31] which is 10–100 times more efficient at transduction compared to traditional single-stranded (ss) AAV vectors.[39,40] The final purified product was dialyzed in phosphate-buffered saline (PBS) with an additional 212 mM NaCl and 5% D-sorbitol. Viral titer was determined by qPCR and confirmed by silver stain.[41] The quality control summary of the AAV9/*AGA* vector is included in the Supplemental Information.

$Aga^{-/-}$ Mice

All researches working with mice were approved by the Institutional Animal Care and Use Committee of the University of North Carolina at Chapel Hill (UNC-CH) or the University of Texas Southwestern (UTSW) Medical Center. An $Aga^{-/-}$ mouse was generated and described in 1996 by Kaartinen et al.[26] The mice have a targeted neomycin cassette insertion in exon 3, which leads to premature termination of the polypeptide at amino acid residue 103. The $Aga^{-/-}$ mice do not have a detectable AGA activity and recapitulate the salient features of the human disease.[26,29]

$Aga^{+/-}$ breeders were obtained from Jackson Laboratories. A colony of these mice was established by breeding heterozygous female with homozygous male, and the natural course of the disease was monitored. In general, the disease progression of the colony was slower than was reported by Kaartinen et al.[26] and Gonzalez-Gomez et al.,[29] but the disease was still apparent and consistent with the human phenotype. Mice were identified by toe clipping at post-natal 7 to 10 days and then randomized into treatment groups based on the ID

numbers assigned to them at genotyping. Genotyping was performed using genomic DNA extracted from clipped toe and three primers, AGA-10144 (5′-AGCGTGTGTGTGGTATGCTC-3′), AGA-10145 (5′-TCTGCAAATGCTGTGGTCTC-3′), AGA-Oimr7415 (5′-GCCA GAGGCCACTTGTGTAG-3′). A touchdown protocol with annealing temperature initially from 68°C to 64°C for 7 cycles and then 64°C for 27 cycles more was used for genotyping, which generated a WT band of 361 bp and mutant band of 240 bp.

Mouse Study Plan

The mouse study plan is summarized in Figure 1B. In brief, both male and female $Aga^{-/-}$ mice were injected either i.v. or i.t. at 2 months old (pre-symptomatic cohorts) or 6 months old (early-symptomatic cohorts). For i.v. administration, 200 μL of either a high (1×10^{12} vg/mouse) or low (2×10^{11} vg/mouse) dose of scAAV9/AGA vector was administrated via tail vein. For i.t., 5 μL of either a very high (1×10^{12} vg/mouse), high (1×10^{11} vg/mouse), or low (2×10^{10} vg/mouse) dose of scAAV9/AGA vector was administrated via lumber puncture. Injection volumes and vehicle composition was held constant across all dose levels. Serum and urine were collected for the measurement of AGA activity and AGA substrate at different time points post-injection. Behavioral tests and brain imaging were performed at 14 or 16 months old, respectively. Necropsy, histopathology, and toxicity evaluation were performed at the end of the experiment when mice reached 18 months old. $Aga^{+/-}$ mice were phenotypically normal, and age/sex-matched littermates were used as normal controls.

AGA Activity Assay

AGA activity assay was conducted using the method described previously[33] with some modification. To measure serum AGA activity, 5 μL of each mouse serum was mixed with 20 μL of substrate buffer (pH 6.5) containing 1 mM of L-aspartic acid-β-7-amido-4-methyl-coumarin (A1057-50 mg, Sigma-Aldrich) and 5 μL of reaction buffer containing 1× Hank's balanced salt solution (HBSS) and 10 mM HEPES. This reaction was incubated at 37°C and 200 rpm for 1 h for samples from treated mice or 24 h for samples from untreated mice. The serum AGA activity was calculated against a standard curve and expressed as nmol/h/mL serum. To measure tissue AGA activity, approximately 25 mg of heart, liver, brain, or cervical spinal cord were mixed with 400 μL of deionized water and a 4.5-mm steel bead and physically lysed for 5 min at a speed of 25/s with a Tissuelyzer. After a freeze at −80°C overnight and thaw at room temperature, the samples were lysed again the same way and then centrifuged 3,000 × g at 4°C for 10 min. Tissue AGA activity was measured using 5 μL of supernatant of each sample. CSF AGA activity was measured using 2.5 μL of CSF. The AGA activity from both tissue and CSF was normalized against their respective protein concentration and expressed as nmol/h/mg protein.

AGA Substrate Assay

Analysis of the AGA substrate was conducted at Greenwood Genetics Center in a blinded fashion using coded samples. 15 μL of each sample, 3 μL of AGU internal standard (50 μg/mL), and 132 μL of 90%

acetonitrile were added into one 1.5-mL centrifuge tube and vortexed immediately. Following the centrifugation at 13,000 rpm for 5 min, all supernatant was transferred into a 0.22-μm filter spin tube and centrifuged at 13,000 rpm for 1 min. The filtrate was then transferred from the filter tube to the polyspring insert in a wide-mouth screw cap vial and capped with a split liner.

Ultraperformance liquid chromatography (UPLC) separation utilized an Acquity I-class system equipped with a UPLC glycan BEH amide column (1.7 μm, 2.1 mm × 50 mm) with a VanGuard glycan BEH amide 1.7 μm guard column (5 × 2.1 mm, 1.7 μm), all from Waters. Analytes were separated utilizing an elution gradient with water with 50 mM ammonium formate at pH 4.5 (mobile phase A) and acetonitrile (mobile phase B), a column temperature of 60°C, and a flow rate of 0.5 mL/min. A triple-quadrupole tandem mass spectrometer (Xevo TQ-S; Waters) was used in positive-ion detection mode. The tandem mass spectrometry (MS/MS) transition for the analytes was 336.14 > 204.05 and for the internal standard was 339.14 > 207.05. The capillary voltage was 2 kV, the cone voltage was 40 V, and the collision energy was 10 eV. The source temperature was 120°C, and the desolvation temperature was 60°C.

Open-Field Test

The open-field test consisted of an arena that was a 40 cm × 40 cm × 30 cm (L × W × H) plastic apparatus. The central square 20-cm × 20-cm region was designated as the central area, and the rest of the open field was considered as peripheral area.[42] Mice were habituated to the experimental room for more than ten minutes prior to testing and then placed in the center of the arena at the beginning of the test period. As soon as the experimenter is out of view of the camera the testing period begins and last for 5 min. The apparatus was sprayed with 70% ethanol between each mouse, dried with paper towels, and left to air dry for 5 min. The video-tracking software Ethovision 12 (Noldus Information Technologies; Wageningen, the Netherlands) was used to measure the following parameters: total distance traveled, duration of mobility, and duration of immobility.

H&E and IHC Staining

Mouse tissues were drop fixed for 3 days in 10% phosphate-buffered formalin following perfusion of the mouse with PBS containing 1 U/mL heparin and transferred into 70% ethanol. Mouse brain, cervical spinal cord, and lumber spinal cord were paraffin processed, embedded, and cut into 5-μm sections either for H&E or IHC staining. For IHC, the sections were treated with antigen retrieval solution (H3300, Vector Laboratories) and then with 3% hydrogen peroxide (H_2O_2) to remove endogenous peroxidase activity. After incubation for 1 h at room temperature in blocking buffer containing 5% goat serum and avidin solution (SP2001, Vector Laboratories) in 1× PBS, the sections were incubated overnight at 4°C in primary antibody solution containing 5% goat serum and 1:4,000 rabbit anti-GFAP antibody (Z0334, Dako) or 1:200 rabbit anti-calbindin antibody (2173S, Cell Signaling) in 1× PBS and then incubated for 1 h at room temperature in second antibody solution containing 5% goat serum and 1:200 biotinylated anti-rabbit immunoglobulin

G (IgG) (BA-1000, Vector Laboratories) in 1× PBS. Color development was performed with a Vectstain ABC kit (PK-6100, Vector Laboratories) with 3,3'-diaminobenzidine tetrachloride (DAB) (TA-125-QHDX, Thermo Scientific) substrate and counterstaining with modified Mayer's hemotoxylin (72804, Richard-Allan Scientific). All stained slides were digitized with a ScanScope slide scanner (Aperio Technologies), and scanned slides were viewed with ImageScope software package (version 10.0; Aperio Technologies). GFAP staining intensity was quantified with Halo software package (Halo2.2; Indica Labs).

MRI
T2 weighted images were acquired with a 3D RARE sequence on a Bruker 9.4 T animal MRI scanner. The sequence parameters are as follows: TR = 3000 ms, TE = 56 ms, RARE factor = 8, matrix size 133 × 96 × 96, voxel size = 0.15 × 0.15 × 0.15 mm^3, and total duration = 39.06 min. During the scan, the animals were anesthetized by inhaling ∼2% isoflurane and oxygen mixture through a nose cone. They were placed on a custom-made cradle in a prone position, and their heads were fixed using tooth and ear bars. Body temperature and respiratory rate were continuously monitored and maintained within normal ranges over the duration of the scan (37 ± 0.5 °C, 80 ± 20 bpm, respectively). The T2 weighted images were segmented using a fully automated rodent brain MR image processing pipeline.[43] Based on the segmentation masks, the volumes of the cerebellum, isocortex, striatum, and ventricle were calculated and compared between the six groups. Operators and image analyzers were blind to genotype and treatment, which was conducted by the Animal MRI (CAMRI) and Biomedical Research Imaging Center (BRIC) at UNC.

Statistical Analysis
All data in this paper were presented as mean ± SEM, analyzed, and graphed using GraphPad Prism software (version 7.04, GraphPad Software). Student's unpaired t test was used for two-group comparison and one-way ANOVA followed by Dunnett's multiple comparisons test compared to the untreated $AGA^{-/-}$ control was used for equal or more-than-three-group comparison. Statistical significance was set as p <0.05.

SUPPLEMENTAL INFORMATION
Supplemental Information can be found online at https://doi.org/10.1016/j.ymthe.2020.11.012.

AUTHOR CONTRIBUTIONS
X.C. and S.J.G. designed the experiments, coordinated studies with collaborators and core facilities, and wrote the manuscript. X.C., S.S.-V., L.P., and Y.H. performed the experiments. S.S.C. served as a consultant on this project. X.C. analyzed all data and prepared all figures for the manuscript. L.P. and Y.H. helped writing the Materials and Methods section. R.T. advised the project, shared protocols, and reviewed the manuscript. S.J.G. oversaw all activities related to the project and acquired all funding for the work.

DECLARATION OF INTERESTS
S.J.G. has received patent royalties for intellectual property (IP) licensed to Asklepios Biophama, but this IP was not used in this study. S.J.G. is an inventor of the AGA vector design and has received patent royalties on this technology from Neurogene.

REFERENCES

1. Arvio, M., and Mononen, I. (2016). Aspartylglycosaminuria: a review. Orphanet J. Rare Dis. 11, 162.

2. Arvio, P., and Arvio, M. (2002). Progressive nature of aspartylglucosaminuria. Acta Paediatr. 91, 255–257.

3. Arvio, M., Sauna-Aho, O., and Peippo, M. (2001). Bone marrow transplantation for aspartylglucosaminuria: follow-up study of transplanted and non-transplanted patients. J. Pediatr. 138, 288–290.

4. Dunder, U., Kaartinen, V., Valtonen, P., Väänänen, E., Kosma, V.M., Heisterkamp, N., Groffen, J., and Mononen, I. (2000). Enzyme replacement therapy in a mouse model of aspartylglycosaminuria. FASEB J. 14, 361–367.

5. Dunder, U., Valtonen, P., Kelo, E., and Mononen, I. (2010). Early initiation of enzyme replacement therapy improves metabolic correction in the brain tissue of aspartylglycosaminuria mice. J. Inherit. Metab. Dis. 33, 611–617.

6. Banning, A., Gülec, C., Rouvinen, J., Gray, S.J., and Tikkanen, R. (2016). Identification of small molecule compounds for pharmacological chaperone therapy of aspartylglucosaminuria. Sci. Rep. 6, 37583.

7. Banning, A., Schiff, M., and Tikkanen, R. (2018). Amlexanox provides a potential therapy for nonsense mutations in the lysosomal storage disorder Aspartylglucosaminuria. Biochim. Biophys. Acta Mol. Basis Dis. 1864, 668–675.

8. Naldini, L. (2015). Gene therapy returns to centre stage. Nature 526, 351–360.

9. Saraiva, J., Nobre, R.J., and Pereira de Almeida, L. (2016). Gene therapy for the CNS using AAVs: The impact of systemic delivery by AAV9. J. Control. Release 241, 94–109.

10. Choudhury, S.R., Hudry, E., Maguire, C.A., Sena-Esteves, M., Breakefield, X.O., and Grandi, P. (2017). Viral vectors for therapy of neurologic diseases. Neuropharmacology 120, 63–80.

11. Bailey, R.M., Armao, D., Nagabhushan Kalburgi, S., and Gray, S.J. (2018). Development of intrathecal AAV9 gene therapy for giant axonal neuropathy. Mol. Ther. Methods Clin. Dev. 9, 160–171.

12. Karumuthil-Melethil, S., Marshall, M.S., Heindel, C., Jakubauskas, B., Bongarzone, E.R., and Gray, S.J. (2016). Intrathecal administration of AAV/GALC vectors in 10-11-day-old twitcher mice improves survival and is enhanced by bone marrow transplant. J. Neurosci. Res. 94, 1138–1151.

13. Federici, T., Taub, J.S., Baum, G.R., Gray, S.J., Grieger, J.C., Matthews, K.A., Handy, C.R., Passini, M.A., Samulski, R.J., and Boulis, N.M. (2012). Robust spinal motor neuron transduction following intrathecal delivery of AAV9 in pigs. Gene Ther. *19*, 852–859.

14. Gray, S.J., Nagabhushan Kalburgi, S., McCown, T.J., and Jude Samulski, R. (2013). Global CNS gene delivery and evasion of anti-AAV-neutralizing antibodies by intra-thecal AAV administration in non-human primates. Gene Ther. *20*, 450–459.

15. Snyder, B.R., Gray, S.J., Quach, E.T., Huang, J.W., Leung, C.H., Samulski, R.J., Boulis, N.M., and Federici, T. (2011). Comparison of adeno-associated viral vector serotypes for spinal cord and motor neuron gene delivery. Hum. Gene Ther. *22*, 1129–1135.

16. Masamizu, Y., Okada, T., Kawasaki, K., Ishibashi, H., Yuasa, S., Takeda, S., Hasegawa, I., and Nakahara, K. (2011). Local and retrograde gene transfer into primate neuronal pathways via adeno-associated virus serotype 8 and 9. Neuroscience *193*, 249–258.

17. Bucher, T., Colle, M.A., Wakeling, E., Dubreil, L., Fyfe, J., Briot-Nivard, D., Maquigneau, M., Raoul, S., Cherel, Y., Astord, S., et al. (2013). scAAV9 intracisternal delivery results in efficient gene transfer to the central nervous system of a feline model of motor neuron disease. Hum. Gene Ther. *24*, 670–682.

18. Haurigot, V., Marcó, S., Ribera, A., Garcia, M., Ruzo, A., Villacampa, P., Ayuso, E., Añor, S., Andaluz, A., Pineda, M., et al. (2013). Whole body correction of mucopo-lysaccharidosis IIIA by intracerebrospinal fluid gene therapy. J. Clin. Invest. *123*, 3254–3271.

19. Samaranch, L., Salegio, E.A., San Sebastian, W., Kells, A.P., Bringas, J.R., Forsayeth, J., and Bankiewicz, K.S. (2013). Strong cortical and spinal cord transduction after AAV7 and AAV9 delivery into the cerebrospinal fluid of nonhuman primates. Hum. Gene Ther. *24*, 526–532.

20. Gray, S.J., Matagne, V., Bachaboina, L., Yadav, S., Ojeda, S.R., and Samulski, R.J. (2011). Preclinical differences of intravascular AAV9 delivery to neurons and glia: a comparative study of adult mice and nonhuman primates. Mol. Ther. *19*, 1058–1069.

21. Duque, S., Joussemet, B., Riviere, C., Marais, T., Dubreil, L., Douar, A.M., Fyfe, J., Moullier, P., Colle, M.A., and Barkats, M. (2009). Intravenous administration of self-complementary AAV9 enables transgene delivery to adult motor neurons. Mol. Ther. *17*, 1187–1196.

22. Foust, K.D., Nurre, E., Montgomery, C.L., Hernandez, A., Chan, C.M., and Kaspar, B.K. (2009). Intravascular AAV9 preferentially targets neonatal neurons and adult as-trocytes. Nat. Biotechnol. *27*, 59–65.

23. Sands, M.S., and Davidson, B.L. (2006). Gene therapy for lysosomal storage diseases. Mol. Ther. *13*, 839–849.

24. Peltola, M., Kyttälä, A., Heinonen, O., Rapola, J., Paunio, T., Revah, F., Peltonen, L., and Jalanko, A. (1998). Adenovirus-mediated gene transfer results in decreased lyso-somal storage in brain and total correction in liver of aspartylglucosaminuria (AGU) mouse. Gene Ther. *5*, 1314–1321.

25. Harkke, S., Laine, M., and Jalanko, A. (2003). Aspartylglucosaminidase (AGA) is effi-ciently produced and endocytosed by glial cells: implication for the therapy of a lyso-somal storage disorder. J. Gene Med. *5*, 472–482.

26. Kaartinen, V., Mononen, I., Voncken, J.W., Noronkoski, T., Gonzalez-Gomez, I., Heisterkamp, N., and Groffen, J. (1996). A mouse model for the human lysosomal disease aspartylglycosaminuria. Nat. Med. *2*, 1375–1378.

27. Jalanko, A., Tenhunen, K., McKinney, C.E., LaMarca, M.E., Rapola, J., Autti, T., Joensuu, R., Manninen, T., Sipilä, I., Ikonen, S., et al. (1998). Mice with an aspartyl-glucosaminuria mutation similar to humans replicate the pathophysiology in pa-tients. Hum. Mol. Genet. *7*, 265–272.

28. Tenhunen, K., Uusitalo, A., Autti, T., Joensuu, R., Kettunen, M., Kauppinen, R.A., Ikonen, S., LaMarca, M.E., Haltia, M., Ginns, E.I., et al. (1998). Monitoring the CNS pathology in aspartylglucosaminuria mice. J. Neuropathol. Exp. Neurol. *57*, 1154–1163.

29. Gonzalez-Gomez, I., Mononen, I., Heisterkamp, N., Groffen, J., and Kaartinen, V. (1998). Progressive neurodegeneration in aspartylglycosaminuria mice. Am. J. Pathol. *153*, 1293–1300.

30. Kaartinen, V., Mononen, I., Gonzalez-Gomez, I., Noronkoski, T., Heisterkamp, N., and Groffen, J. (1998). Phenotypic characterization of mice with targeted disruption of glycosylasparaginase gene: a mouse model for aspartylglycosaminuria. J. Inherit. Metab. Dis. *21*, 207–209.

31. Gray, S.J., Foti, S.B., Schwartz, J.W., Bachaboina, L., Taylor-Blake, B., Coleman, J., Ehlers, M.D., Zylka, M.J., McCown, T.J., and Samulski, R.J. (2011). Optimizing pro-moters for recombinant adeno-associated virus-mediated gene expression in the pe-ripheral and central nervous system using self-complementary vectors. Hum. Gene Ther. *22*, 1143–1153.

32. Tikkanen, R., Peltola, M., Oinonen, C., Rouvinen, J., and Peltonen, L. (1997). Several cooperating binding sites mediate the interaction of a lysosomal enzyme with phos-photransferase. EMBO J. *16*, 6684–6693.

33. Mononen, I.T., Kaartinen, V.M., and Williams, J.C. (1993). A fluorometric assay for glycosylasparaginase activity and detection of aspartylglucosaminuria. Anal. Biochem. *208*, 372–374.

34. Prut, L., and Belzung, C. (2003). The open field as a paradigm to measure the effects of drugs on anxiety-like behaviors: a review. Eur. J. Pharmacol. *463*, 3–33.

35. Yang, Z., and Wang, K.K. (2015). Glial fibrillary acidic protein: from intermediate filament assembly and gliosis to neurobiomarker. Trends Neurosci. *38*, 364–374.

36. Sinnett, S.E., Hector, R.D., Gadalla, K.K.E., Heindel, C., Chen, D., Zaric, V., Bailey, M.E.S., Cobb, S.R., and Gray, S.J. (2017). Improved MECP2 gene therapy extends the survival of MeCP2-null mice without apparent toxicity after intracisternal deliv-ery. Mol. Ther. Methods Clin. Dev. *5*, 106–115.

37. Bleyer, W.A., and Dedrick, R.L. (1977). Clinical pharmacology of intrathecal metho-trexate. I. Pharmacokinetics in nontoxic patients after lumbar injection. Cancer Treat. Rep. *61*, 703–708.

38. Banning, A., König, J.F., Gray, S.J., and Tikkanen, R. (2017). Functional analysis of the Ser149/Thr149 variants of human aspartylglucosaminidase and optimization of the coding sequence for protein production. Int. J. Mol. Sci. *18*, 706–718.

39. McCarty, D.M., Fu, H., Monahan, P.E., Toulson, C.E., Naik, P., and Samulski, R.J. (2003). Adeno-associated virus terminal repeat (TR) mutant generates self-comple-mentary vectors to overcome the rate-limiting step to transduction in vivo. Gene Ther. *10*, 2112–2118.

40. McCarty, D.M., Monahan, P.E., and Samulski, R.J. (2001). Self-complementary re-combinant adeno-associated virus (scAAV) vectors promote efficient transduction independently of DNA synthesis. Gene Ther. *8*, 1248–1254.

41. Gray, S.J., Choi, V.W., Asokan, A., Haberman, R.A., McCown, T.J., and Samulski, R.J. (2011). Production of recombinant adeno-associated viral vectors and use in in vitro and in vivo administration. Curr. Protoc. Neurosci. *57*, 4.17.1–4.17.30.

42. Christakis, D.A., Ramirez, J.S., and Ramirez, J.M. (2012). Overstimulation of newborn mice leads to behavioral differences and deficits in cognitive performance. Sci. Rep. *2*, 546.

43. Budin, F., Hoogstoel, M., Reynolds, P., Grauer, M., O'Leary-Moore, S.K., and Oguz, I. (2013). Fully automated rodent brain MR image processing pipeline on a Midas server: from acquired images to region-based statistics. Front. Neuroinform. *7*, 15.

BRAIN
A JOURNAL OF NEUROLOGY

Defining the clinical, molecular and imaging spectrum of adaptor protein complex 4-associated hereditary spastic paraplegia

Darius Ebrahimi-Fakhari,[1] Julian Teinert,[1,2] Robert Behne,[1,3] Miriam Wimmer,[1] Angelica D'Amore,[1,4] Kathrin Eberhardt,[1] Barbara Brechmann,[1] Marvin Ziegler,[1] Dana M. Jensen,[5] Premsai Nagabhyrava,[1,6] Gregory Geisel,[1,6] Erin Carmody,[1,6] Uzma Shamshad,[1,6] Kira A. Dies,[1,6] Christopher J. Yuskaitis,[1] Catherine L. Salussolia,[1] Daniel Ebrahimi-Fakhari,[7,8] Toni S. Pearson,[9] Afshin Saffari,[2] Andreas Ziegler,[2] Stefan Kölker,[2] Jens Volkmann,[3] Antje Wiesener,[10] David R. Bearden,[11] Shenela Lakhani,[12] Devorah Segal,[12,13] Anaita Udwadia-Hegde,[14] Andrea Martinuzzi,[15] Jennifer Hirst,[16] Seth Perlman,[17] Yoshihisa Takiyama,[18] Georgia Xiromerisiou,[19] Katharina Vill,[20] William O. Walker,[21] Anju Shukla,[22] Rachana Dubey Gupta,[23] Niklas Dahl,[24] Ayse Aksoy,[25] Helene Verhelst,[26] Mauricio R. Delgado,[27] Radka Kremlikova Pourova,[28] Abdelrahim A. Sadek,[29] Nour M. Elkhateeb,[30] Lubov Blumkin,[31] Alejandro J. Brea-Fernández,[32] David Dacruz-Álvarez,[33] Thomas Smol,[34] Jamal Ghoumid,[34] Diego Miguel,[35] Constanze Heine,[36] Jan-Ulrich Schlump,[37] Hendrik Langen,[38] Jonathan Baets,[39] Saskia Bulk,[40] Hossein Darvish,[41] Somayeh Bakhtiari,[42] Michael C. Kruer,[42] Elizabeth Lim-Melia,[43] Nur Aydinli,[44] Yasemin Alanay,[45] Omnia El-Rashidy,[46] Sheela Nampoothiri,[47] Chirag Patel,[48] Christian Beetz,[49] Peter Bauer,[49] Grace Yoon,[50] Mireille Guillot,[51] Steven P. Miller,[51] Thomas Bourinaris,[52] Henry Houlden,[52] Laura Robelin,[53] Mathieu Anheim,[53] Abdullah S. Alamri,[54] Adel A. H. Mahmoud,[55] Soroor Inaloo,[56] Parham Habibzadeh,[57] Mohammad Ali Faghihi,[57,58] Anna C. Jansen,[59] Stefanie Brock,[59] Agathe Roubertie,[60] Basil T. Darras,[1] Pankaj B. Agrawal,[61] Filippo M. Santorelli,[4] Joseph Gleeson,[62] Maha S. Zaki,[63] Sarah I. Sheikh,[64] James T. Bennett[5] and Mustafa Sahin[1,6]

Bi-allelic loss-of-function variants in genes that encode subunits of the adaptor protein complex 4 (AP-4) lead to prototypical yet poorly understood forms of childhood-onset and complex hereditary spastic paraplegia: SPG47 (*AP4B1*), SPG50 (*AP4M1*), SPG51 (*AP4E1*) and SPG52 (*AP4S1*). Here, we report a detailed cross-sectional analysis of clinical, imaging and molecular data of 156 patients from 101 families. Enrolled patients were of diverse ethnic backgrounds and covered a wide age range (1.0–49.3 years). While the mean age at symptom onset was 0.8 ± 0.6 years [standard deviation (SD), range 0.2–5.0], the mean age at diagnosis was 10.2 ± 8.5 years (SD, range 0.1–46.3). We define a set of core features: early-onset developmental delay with delayed motor milestones and significant speech delay (50% non-verbal); intellectual disability in the moderate to severe range; mild hypotonia in infancy followed by spastic diplegia (mean age: 8.4 ± 5.1 years, SD) and later tetraplegia (mean age: 16.1 ± 9.8 years, SD); postnatal microcephaly (83%); foot deformities (69%); and epilepsy (66%) that is intractable in a subset. At last follow-up, 36% ambulated with assistance (mean age:

8.9 ± 6.4 years, SD) and 54% were wheelchair-dependent (mean age: 13.4 ± 9.8 years, SD). Episodes of stereotypic laughing, possibly consistent with a pseudobulbar affect, were found in 56% of patients. Key features on neuroimaging include a thin corpus callosum (90%), ventriculomegaly (65%) often with colpocephaly, and periventricular white-matter signal abnormalities (68%). Iron deposition and polymicrogyria were found in a subset of patients. *AP4B1*-associated SPG47 and *AP4M1*-associated SPG50 accounted for the majority of cases. About two-thirds of patients were born to consanguineous parents, and 82% carried homozygous variants. Over 70 unique variants were present, the majority of which are frameshift or nonsense mutations. To track disease progression across the age spectrum, we defined the relationship between disease severity as measured by several rating scales and disease duration. We found that the presence of epilepsy, which manifested before the age of 3 years in the majority of patients, was associated with worse motor outcomes. Exploring genotype-phenotype correlations, we found that disease severity and major phenotypes were equally distributed among the four subtypes, establishing that SPG47, SPG50, SPG51 and SPG52 share a common phenotype, an 'AP-4 deficiency syndrome'. By delineating the core clinical, imaging, and molecular features of AP-4-associated hereditary spastic paraplegia across the age spectrum our results will facilitate early diagnosis, enable counselling and anticipatory guidance of affected families and help define endpoints for future interventional trials.

1 Department of Neurology, Boston Children's Hospital, Harvard Medical School, Boston, MA, USA
2 Division of Child Neurology and Metabolic Medicine, Centre for Paediatric and Adolescent Medicine, University Hospital Heidelberg, Heidelberg, Germany
3 Department of Neurology, University Hospital Würzburg, Würzburg, Germany
4 Molecular Medicine, IRCCS Fondazione Stella Maris, Pisa, Italy
5 Division of Genetic Medicine, Department of Pediatrics, University of Washington, Seattle, WA, USA
6 Translational Neuroscience Center, Boston Children's Hospital, Harvard Medical School, Boston, MA, USA
7 Pediatric Neurology, Saarland University Medical Center, Homburg/Saar, Germany
8 Department of General Pediatrics, University Children's Hospital Muenster, Muenster, Germany
9 Department of Neurology, Washington University School of Medicine, St. Louis, MO, USA
10 Institute of Human Genetics, Friedrich-Alexander Universität Erlangen-Nürnberg, Erlangen, Germany
11 Child Neurology, University of Rochester School of Medicine, Rochester, NY, USA
12 Center for Neurogenetics, Weill Cornell Medical College, New York, NY, USA
13 Division of Child Neurology, Weill Cornell Medicine, New York City, NY, USA
14 Department of Pediatric Neurology, Jaslok Hospital and Research Centre, Mumbai, India
15 Scientific Institute, IRCCS E. Medea, Unità Operativa Conegliano, Treviso, Italy
16 Cambridge Institute for Medical Research, University of Cambridge, Cambridge, UK
17 Division of Neurology, Department of Pediatrics, University of Iowa Carver College of Medicine, Iowa City, IA, USA
18 Department of Neurology, University of Yamanashi, Yamanashi, Japan
19 Department of Neurology, Papageorgiou Hospital, Thessaloniki, Greece
20 Pediatric Neurology and Developmental Medicine, Dr. v. Hauner Children's Hospital, Ludwig-Maximilians-University, Munich, Germany
21 Department of Pediatrics, Seattle Children's Hospital, University of Washington School of Medicine, Seattle, WA, USA
22 Department of Medical Genetics, Kasturba Medical College, Manipal Academy of Higher Education, Manipal, India
23 Pediatric Neurology, Medanta Hospital, Indore, India
24 Department of Immunology, Genetics and Pathology, Science for Life Laboratory, Uppsala University, Uppsala, Sweden
25 Pediatric Neurology, Dr. Sami Ulus Hospital, Ankara, Turkey
26 Pediatric Neurology, Ghent University Hospital, Ghent, Belgium
27 Department of Neurology, University of Texas Southwestern Medical Center, Dallas, TX, USA
28 Department of Biology and Medical Genetics, Second Medical Faculty, Charles University and UH Motol, Prague, Czech Republic
29 Pediatric Neurology, Faculty of Medicine, Sohag University, Sohag, Egypt
30 Pediatric Neurology, Cairo University, Cairo, Egypt
31 Movement Disorders Clinic, Pediatric Neurology Unit, Wolfson Medical Center, Holon, Sackler School of Medicine, Tel-Aviv University, Israel
32 Grupo de Medicina Xenómica, CIBERER, Santiago de Compostela, Spain
33 Neurología Pediátrica, Complexo Hospitalario Universitario, Santiago de Compostela, Spain
34 CHU Lille, Institut de Génétique Médicale, RADEME, Lille, France
35 Serviço de Genética Médica, Universidade Federal da Bahia, Salvador, Brazil
36 Institute of Human Genetics, University Hospital Leipzig, Leipzig, Germany
37 Pediatrics, Evangelisches Krankenhaus Oberhausen, Oberhausen, Germany
38 Sozialpädiatrisches Zentrum Hannover, Hannover, Germany
39 Neurogenetics Group and Neuromuscular Reference Center, University of Antwerp and Antwerp University Hospital, Antwerp, Belgium
40 Medical Genetics, Centre Hospitalier Universitaire de Liège, Liège, Belgium
41 Cancer Research Center and Department of Medical Genetics, Semnan University of Medical Sciences, Semnan, Iran
42 Barrow Neurological Institute, Phoenix Children's Hospital, Phoenix, AZ, USA

43 Pediatric Medical Genetics, Maria Fareri Children's Hospital, Valhalla, NY, USA
44 Pediatric Genetics, Department of Pediatrics, Acibadem Mehmet Ali Aydinlar University, Istanbul, Turkey
45 Pediatric Neurology, Istanbul Medical Faculty, Istanbul, Turkey
46 Pediatrics, Ain Shams University, Cairo, Egypt
47 Amrita Institute of Medical Sciences and Research Centre, Cochin, India
48 Genetic Health Queensland, Royal Brisbane and Women's Hospital, Brisbane, Australia
49 Centogene AG, Rostock, Germany
50 Division of Clinical and Metabolic Genetics, Department of Paediatrics, The Hospital for Sick Children, University of Toronto, Toronto, Canada
51 Department of Paediatrics, The Hospital for Sick Children and The University of Toronto, Toronto, Canada
52 Department of Molecular Neuroscience, UCL Institute of Neurology, London, UK
53 Service de Neurologie, Hôpitaux Universitaires de Strasbourg, Strasbourg, France
54 Pediatric Neurology, National Neuroscience Institute, King Fahad Medical City, Riyadh, Saudi Arabia
55 Pediatrics, Imam Abdulrahman Bin Faisal University, Dammam, Saudi Arabia
56 Neonatal Research Center, Shiraz University of Medical Sciences, Shiraz, Iran
57 Persian BayanGene Research and Training Center, Shiraz University of Medical Sciences, Shiraz, Iran
58 Center for Therapeutic Innovation and Department of Psychiatry and Behavioral Sciences, University of Miami, Miami, FL, USA
59 Pediatric Neurology Unit, Department of Pediatrics, UZ Brussel, Brussels, Belgium
60 Pediatric Neurology, CHU Montpellier, Montpellier, France
61 Divisions of Newborn Medicine and Genetics and Genomics, The Manton Center for Orphan Disease Research, Boston Children's Hospital, Harvard Medical School, Boston, MA, USA
62 Rady Children's Institute for Genomic Medicine, Rady Children's Hospital, San Diego, CA, USA
63 Clinical Genetics, Human Genetics and Genome Research Division, National Research Centre, Cairo, Egypt
64 Translational Neuroscience, Celgene, Cambridge, MA, USA

Correspondence to: Dr Darius Ebrahimi-Fakhari
Department of Neurology, The F.M. Kirby Neurobiology Center
Boston Children's Hospital, Harvard Medical School
3 Blackfan Circle, CLSB 14060, MA 02115, USA
E-mail: darius.ebrahimi-fakhari@childrens.harvard.edu

Introduction

The hereditary spastic paraplegias (HSP) are a group of more than 80 neurodegenerative diseases that lead to progressive neurological decline (Blackstone, 2018). Collectively the HSPs present the most common cause of inherited spasticity and associated disability. Bi-allelic loss-of-function variants in genes that encode subunits of the adaptor protein complex 4 (AP-4) lead to prototypical yet poorly understood forms of complex HSP in children, called AP-4-associated HSP (AP-4-HSP) (Verkerk et al., 2009; Abou Jamra et al., 2011; Moreno-De-Luca et al., 2011; Ebrahimi-Fakhari et al., 2018a). This includes four different conditions: SPG47 (AP4B1, OMIM #614066), SPG50 (AP4M1, OMIM #612936), SPG51 (AP4E1, OMIM #613744), and SPG52 (AP4S1, OMIM #614067). The molecular mechanism in all four diseases is a loss-of-function of the AP-4; hence they are thought to share a similar clinical phenotype.

AP-4 belongs to a family of adaptor proteins (AP-1–AP-5) that are evolutionarily conserved heterotetrameric protein complexes. The adaptor protein complexes facilitate the selective incorporation of transmembrane cargo proteins into vesicles and mediate their intracellular trafficking. AP-4 is composed of four subunits (β4, ϵ, μ4 and σ4) that form an obligate complex (Hirst et al., 1999). AP-4 is known to mediate protein trafficking from the trans-Golgi network to early (Burgos et al., 2010; Toh et al., 2017) and late endosomes (Aguilar et al., 2001). The autophagy protein ATG9 has emerged as an important cargo of AP-4 and mislocalization of ATG9A is a robust indicator of AP-4 deficiency including in patient-derived fibroblasts and induced pluripotent stem cell-derived neurons (Behne et al., 2020). While the molecular pathology of AP-4 deficiency remains largely unknown, AP-4-HSP is becoming an increasingly recognized form of complex HSP with a thin corpus callosum (da Graca et al., 2018). Published reports, however, consist of single case reports or small case series only, and no studies have systematically delineated the spectrum of the disease or its progression.

Here, we report a detailed cross-sectional analysis of clinical, radiographic, and molecular features of 156 patients from 101 families with AP-4-associated HSP. We define a core set of clinical and imaging features, delineate disease manifestations and progression in a standardized manner, and describe the molecular spectrum.

Materials and methods

Patients with AP-4-HSP

To systematically document the clinical presentation and natural history of AP-4-related HSP we developed an international cohort (www.CureAP4.org). Inclusion criteria include a clinical diagnosis of AP-4-HSP and the presence of bi-allelic variants in *AP4B1*, *AP4M1*, *AP4E1* or *AP4S1*. By 15 July 2019, 156 patients from 101 families were enrolled. A few patients were identified through the DECIPHER (Firth *et al.*, 2009) and CentoMD (Trujillano *et al.*, 2017) databases and subsequently referred by the treating clinician. Written informed consent for participation was obtained. For patients who were lost to follow-up, a waiver of consent was used. This study was approved by the Institutional Review Board at Boston Children's Hospital (#10-02-0053 and #A00033016-1).

Clinical data

A cross-sectional analysis of patients enrolled in the AP-4-HSP Registry was undertaken using the AP-4-HSP Natural History Study Questionnaire (Supplementary material). For 46 previously reported patients from 23 families (Verkerk *et al.*, 2009; Moreno-De-Luca *et al.*, 2011; Najmabadi *et al.*, 2011; Kong *et al.*, 2013; Lamichhane, 2013; Tuysuz *et al.*, 2014; Hardies *et al.*, 2015; Karaca *et al.*, 2015; Langouet *et al.*, 2015; Tan *et al.*, 2016; Tessa *et al.*, 2016; Accogli *et al.*, 2018; Ebrahimi-Fakhari *et al.*, 2018b), no follow-up data were available, and here a detailed review of published information was conducted. The Spastic Paraplegia Rating Scale (SPRS) (Schule *et al.*, 2006) was used to assess 37 patients, and total and spasticity subscores (Karle *et al.*, 2013) were calculated. The Modified Ashworth Scale (MAS) was used in 28 patients. A SPATAX-EUROSPA Disability Score (Chrestian *et al.*, 2017), ranging from 0 (no disability) to 7 (severe disability/confined to bed), and a Four Stage Functional Mobility Score (1 = mild symptoms walking without an aid; 2 = walking without aid but unable to run; 3 = walking with aid; and 4 = wheelchair-dependent) (Erichsen *et al.*, 2009) were assigned for 39 and 85 patients, respectively. Brain imaging was performed on 104 patients.

Genetic testing

In the majority of cases, clinical exome sequencing was employed to detect variants in *AP4B1*, *AP4M1*, *AP4E1* and *AP4S1* (75%). A multi-gene panel (9%) or Sanger sequencing (14%) was performed in a subset of patients. A chromosomal microarray detected microdeletions covering *AP4E1* in four patients. Variants were annotated using the gnomAD database (http://gnomad.broadinstitute.org) and interrogated *in silico* to predict damaging effects by calculating Combined Annotation Dependent Depletion (CADD) scores (Kircher *et al.*, 2014).

Statistical analysis

Statistical analysis was performed with GraphPad Prism version 6.0 (GraphPad Software, Inc.) and IBM SPSS Statistics Version 25. Descriptive statistics are provided for demographic and clinical variables. Frequency count and percentages are provided for categorical variables. Mean, standard deviation (SD), and ranges were calculated for continuous variables. For data shown in Fig. 5F and G, a linear (red line) and non-linear (blue line) regression analysis were performed, and a Pearson correlation coefficient was calculated for linear regression. One-way ANOVA with Tukey correction (data shown in Fig. 5I and J) or an unpaired *t*-test (data shown in Fig. 5K) were used to determine the significance of differences between conditions. $P < 0.05$ was considered significant, denoted with an asterisk.

Data availability

The data that support the findings of this study are available from the corresponding author, upon reasonable request.

Results

Detailed clinical characterization of AP-4-HSP defines a set of core clinical features

Demographic and anthropometric features

This study includes 156 patients from 101 families with AP-4-HSP; 83 patients are reported here for the first time, and new or follow-up data are reported on 27 previously published patients (Fig. 1A and Supplementary Fig. 1). All patients had a genetically confirmed diagnosis of AP-4-HSP. Demographic data are summarized in Fig. 1, and clinical data are presented on a cohort level in Table 1 and on an individual level in Supplementary Fig. 1. Patients were recruited from over 50 medical centres with the majority of families based in Europe (32%), the Middle East (25%), North America (15%) and North Africa (15%) (Supplementary Table 1 for details). In our cohort, *AP4M1*-associated SPG50 was the most common subtype, accounting for about 38% of patients, closely followed by *AP4B1*-associated SPG47 in 34% of patients (Fig. 1A). *AP4S1*-associated SPG51 and *AP4E1*-associated SPG52 were less common (15% and 13%, respectively, Fig. 1A). The mean age at last follow-up was 11.4 ± 8.3 years (SD) while the mean age at diagnosis was 10.2 ± 8.5 years (SD) (Fig. 1B and Table 2). The latter varied considerably, ranging from 1 month to 46 years, and in general patients diagnosed since 2015 were diagnosed at a younger age due to the increased availability of multi-gene panels and exome sequencing. When compared to the age at onset of symptoms, a significant delay in diagnosis was found, averaging around 10 years (Table 2). Consanguinity was reported in two-thirds of patients although this varied between subtypes. More than one family member was affected in 67% of patients (Table 2). No aggregation or association with other neurological disease was found upon assessment of a three-generation family history. Patients originated from 30 countries and were of different ethnic backgrounds (Fig. 1C, D and Supplementary
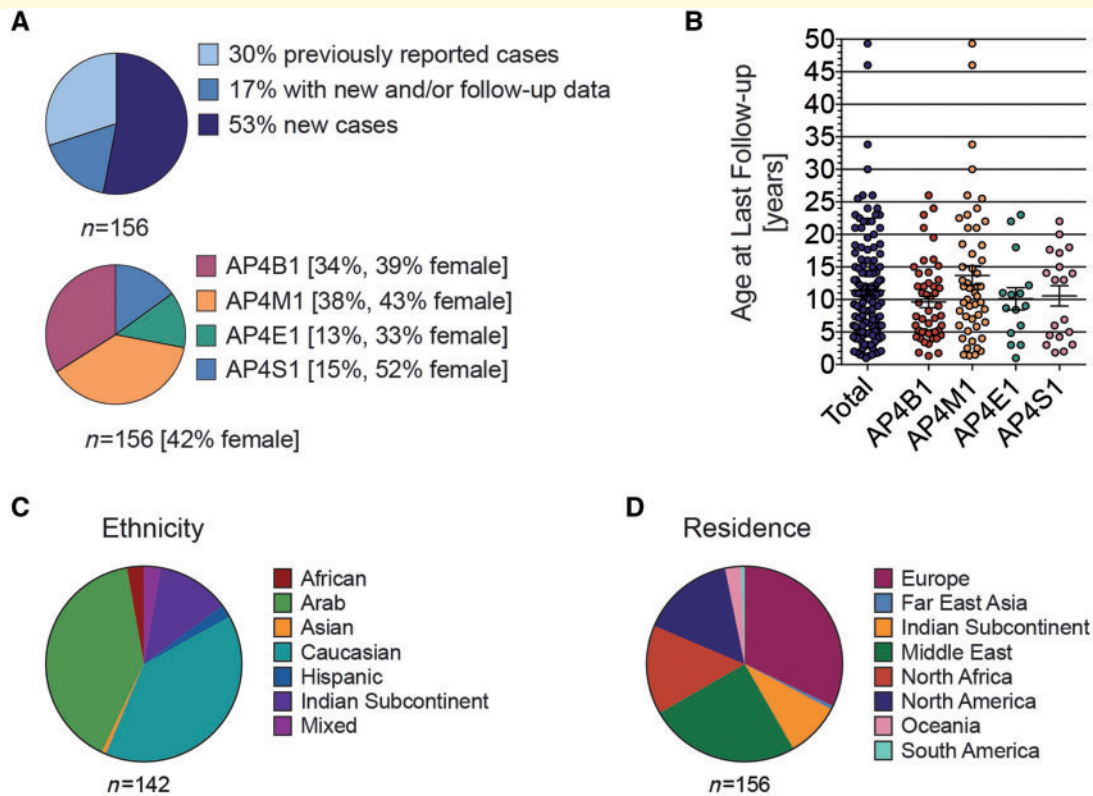
Figure 1 Demographic data of the study cohort. (**A**) A total of 156 patients were enrolled in the study, the majority carrying bi-allelic variants in *AP4B1* and *AP4M1*. (**B**) Most patients were under the age of 18 years at the last follow-up with only a few adult patients reported. (**C** and **D**) Enrolled patients cover all major ethnicities with the majority being Caucasian or of Arab descent. Most families are located in Europe, the Middle East, North America and North Africa.

Table 1). This includes, although is not limited to, regions with high rates of consanguinity.

Clinical features were assessed using a standardized questionnaire (Supplementary material) developed for the purpose of this study. A set of core clinical and imaging features is defined based on their presence in more than 50% of individuals with AP-4-HSP (Box 1). Most patients were born at term (92%). There was no aggregation of any specific prenatal or neonatal complications although ventriculomegaly was detected prenatally in eight patients, and hypotonia and poor feeding in the neonatal period were noted in 16% of patients. Fifteen per cent of patients required admission to a neonatal intensive care unit. Average birth weight across all patients was 3.10 ± 0.46 kg (SD). Review of anthropometric data at the last follow-up showed an average height at −1.69 SD (range −5.76 to +2.45 SD) and weight at −0.53 SD (range −4.8 to +5.0), respectively, according to sex- and age-appropriate CDC growth charts (Table 1 and Fig. 2A). A subset of patients showed significant growth failure with a height (35%) and/or weight (22%) below the −2 SD mark. Postnatal microcephaly has been described in AP-4-HSP (Verkerk *et al.*, 2009; Abou Jamra *et al.*, 2011; Hardies *et al.*, 2015; Ebrahimi-Fakhari *et al.*, 2018*b*), and we found postnatal

Box 1 Principal clinical and radiographic features of AP-4-HSP

Principal clinical features of AP-4-HSP	
Developmental delay / intellectual disability	100%
Motor delay	100%
Speech delay	99%
Mild neonatal or infantile hypotonia	89%
Spasticity	97%
Spastic diplegia	54%
Spastic tetraplegia	43%
Hyperreflexia	92%
Babinski sign	88%
Contractures	50%
Drooling	70%
Postnatal microcephaly	83%
Dysmorphic facial features	78%
Foot deformities	69%
Febrile seizures	62%
Epilepsy	66%
Episodes of stereotypic laughter	56%
Principal radiographic features of AP-4-HSP	
Thin corpus callosum	90%
Ventriculomegaly	65%
White matter loss/changes	68%

Table I Summary of clinical features of AP-4-HSP

Anthropometric data			
Height	−1.69 ± 1.63 (mean, SD) [range −5.76 to +2.45, n = 79]		
Weight	−0.53 ± 1.77 (mean, SD) [range −4.8 to +5.0, n = 78]		
Head circumference	−2.80 ± 1.36 (mean, SD) [range −7.2 to +0.25, n = 114]		
Dysmorphology			
Microcephaly (n = 101/122): 83%	AP4B1: 84%, n = 36/43 AP4E1: 85%, n = 11/13	AP4M1: 85%, n = 41/48 AP4S1: 72%, n = 13/18	
Dysmorphic facial features (n = 78/100): 78%	AP4B1: 84%, n = 31/37 AP4E1: 82%, n = 9/11	AP4M1: 66%, n = 23/35 AP4S1: 88%, n = 15/17	
Development			
Developmental delay / intellectual disability (n = 135/135): 100%	AP4B1: 100%, n = 50/50 AP4E1: 100%, n = 15/15	AP4M1: 100%, n = 51/51 AP4S1: 100%, n = 19/19	Severe: 58% Moderate: 33% Mild: 9%
Developmental regression or progressive cognitive deficits (n = 39/95): 41%	AP4B1: 26%, n = 9/35 AP4E1: 50%, n = 4/8	AP4M1: 51%, n = 20/39 AP4S1: 46%, n = 6/13	
Age at onset of developmental delay (n = 93, months): 9.2 ± 7.5 (SD)	AP4B1: 6.9 ± 4.6 (SD), range: 2–24, n = 34 AP4E1: 8.2 ± 3.1 (SD), range 3–12, n = 6	AP4M1: 11.3 ± 9.5 (SD), range 3–60, n = 42 AP4S1: 9.2 ± 6.1 (SD), range 3–24, n = 11	
Delayed motor development (n = 132/132): 100%	AP4B1: 100%, n = 46/46 AP4E1: 100%, n = 18/18	AP4M1: 100%, n = 49/49 AP4S1: 100%, n = 19/19	
Delayed speech development (n = 124/125): 99% Non-verbal: 50%, (n = 54/109)	AP4B1: 98%, n = 42/43 AP4E1: 100%, n = 15/15	AP4M1: 100%, n = 49/49 AP4S1: 100%, n = 18/18	
Shy character (n = 31/96): 32%	AP4B1: 35%, n = 12/34 AP4E1: 25%, n = 3/12	AP4M1: 32%, n = 12/38 AP4S1: 33%, n = 4/12	
Stereotypic laughter (56/100): 56%	AP4B1: 53%, n = 19/36 AP4E1: 82%, n = 9/11	AP4M1: 50%, n = 20/40 AP4S1: 62%, n = 8/13	
Motor symptoms			
Neonatal hypotonia (n = 97/109): 89%	AP4B1: 87%, n = 39/45 AP4E1: 100%, n = 10/10	AP4M1: 90%, n = 35/39 AP4S1: 87%, n = 13/15	
Neonatal hypotonia progressing to spasticity (n = 104/116): 90%	AP4B1: 88%, n = 38/43 AP4E1: 100%, n = 10/10	AP4M1: 92%, n = 43/47 AP4S1: 81%, n = 13/16	
Spasticity (n = 130/134): 97%	AP4B1: 96%, n = 46/48 Spastic diplegia: 61% Spastic tetraplegia: 35% AP4E1: 100%, n = 16/16 Spastic diplegia: 50% Spastic tetraplegia: 50%	AP4M1: 98%, n = 50/51 Spastic diplegia: 47% Spastic tetraplegia: 51% AP4S1: 95%, n = 18/19 Spastic diplegia: 63% Spastic tetraplegia: 31%	
Hyperreflexia (n = 97/106)	92%		
Babinski sign (n = 80/91)	88%		
Drooling (n = 64/91)	70%		
Contractures (n = 49/98)	50%		
Foot deformity (n = 68/99)	69%		
Extrapyramidal movement disorders (n = 33/79)	42%		
Cerebellar signs (n = 26/76)	34%		
Swallowing dysfunction / aspiration (n = 18/63)	29%		
Seizures			
Seizures (n = 84/126): 67%	AP4B1: 65%, n = 32/49 AP4E1: 67%, n = 8/12	AP4M1: 70%, n = 33/47 AP4S1: 61%, n = 11/18	Focal: 29% Generalized: 63% Focal + generalized: 8%
Febrile seizures (n = 74/120): 62%	AP4B1: 69%, n = 31/45 AP4E1: 36%, n = 4/11	AP4M1: 60%, n = 27/45 AP4S1: 63%, n = 12/19	
Epilepsy (n = 69/105): 66%	AP4B1: 76%, n = 28/37 AP4E1: 67%, n = 8/12	AP4M1: 62%, n = 24/39 AP4S1: 53%, n = 9/17	
Status epilepticus (n = 24/65): 37%	AP4B1: 48%, n = 14/29 AP4E1: 40%, n = 2/5	AP4M1: 24%, n = 6/25 AP4S1: 33%, n = 2/6	
Response to AEDs (n = 64)	Complete 69% Incomplete 31%		
Therapy with multiple AED or medically-refractory epilepsy (n = 67)	27%		

Table 2 AP-4-HSP: summary of key demographic features and stratification based on genotype

AP-4-HSP Subtype	Age at onset, years	Age at diagnosis, years	Age at last visit, years	Consanguinity	Familial case
AP4B1-HSP: n = 53	0.6 ± 0.4 (n = 34)	7.8 ± 6.9 (n = 31)	9.6 ± 6.1 (n = 48)	60% (n = 50)	55% (n = 53)
AP4M1-HSP: n = 59	0.9 ± 0.8 (n = 42)	11.7 ± 10.0 (n = 44)	13.7 ± 10.6 (n = 50)	77% (n = 52)	78% (n = 59)
AP4E1-HSP: n = 21	0.7 ± 0.3 (n = 6)	10.3 ± 6.7 (n = 14)	10.1 ± 6.6 (n = 15)	90% (n = 20)	86% (n = 21)
AP4S1-HSP: n = 23	0.8 ± 0.5 (n = 11)	10.4 ± 7.3 (n = 13)	10.6 ± 6.8 (n = 19)	47% (n = 19)	48% (n = 23)
Total: n = 156	0.8 ± 0.6 (n = 93)	10.2 ± 8.5 (n = 102)	11.4 ± 8.3 (n = 132)	69% (n = 141)	67% (n = 156)

microcephaly in 83% of patients, while only a small subset was born microcephalic (8%). Microcephaly was mostly in a moderate range, in 50% patients between −2 SD and −4 SD, yielding an overall average of −2.80 SD (range −7.2 to +0.25, Fig. 2A). Dysmorphic facial features were described by clinicians in 78% of patients and included a broad range of features including a wide nasal bridge, bulbous nose, short philtrum and epicanthal folds in some. No uniform *gestalt* was discernible, however. Of note, a significant subset of patients (69%) were found to have foot deformities, most commonly pes equinovarus (54%), pes planus (22%) or deformities such as syndactyly (4%) or macrodactyly (4%) (Fig. 2B).

Developmental history and cognitive function
Most patients presented to medical attention because of early-onset global developmental delay. Delayed developmental milestones were noticed at an average age of 9.2 ± 7.5 months (SD) months (range: 2–60 months) (Table 1). Motor milestones were delayed with unsupported sitting (mean age: 17 ± 11 months, SD), crawling (mean age: 23 ± 11 months, SD), and standing (mean age: 34 ± 19 months, SD) achieved late (Table 1 and Fig. 2C). Eighty-five per cent of patients achieved walking with assistance at an average age of 37 ± 21 months (SD). Unsupported walking was achieved in a subset of patients (43%), a skill that was lost over time in most with only 11% ambulating independently at last follow-up. Thirty-six per cent of patients were able to walk with assistance at last follow-up, and 54% of patients required a wheelchair for any substantial distance. The latter occurred at an average age of 9.0 ± 5.3 years (SD) with the mean age of wheelchair-dependent patients being 13.4 ± 9.8 years (SD) at last follow-up. Fine motor skills were also universally delayed although not systematically assessed in this study. Speech development was prominently delayed in nearly all patients, and 50% remained non-verbal (Table 1). Behavioural problems including inattention and hyperactivity were frequently reported. Common character traits or behaviours reported previously in AP-4-HSP include a shy character (Abou Jamra *et al.*, 2011) and stereotypic episodes of laughter (Ebrahimi-Fakhari *et al.*, 2018*b*). We failed to identify a high rate of shyness in our cohort (32%), and many patients were reported to be quite social. Episodes of stereotypic laughter were found in a subset of patients although they did not seem to be a universal

feature (56%). In older patients, intellectual disability was usually in the moderate to severe range. Loss of previously acquired skills or developmental regression and cognitive decline was reported in 41% of patients (Table 1).

Motor symptoms and movement disorders
Progressive spasticity is a key clinical feature of AP-4-HSP (Fig. 2D). The first motor symptom, however, was usually truncal and appendicular hypotonia, which was noted in the neonatal period or infancy in 89% of patients and was usually mild. Over time, muscle tone increased in the distal lower extremities leading to spastic diplegia (54% of patients, mean age: 8.4 ± 5.1 years, SD) with progression to spastic tetraplegia (43% of patients) in late childhood/adolescence (mean age: 16.1 ± 9.8 years, SD) (Fig. 2D). Along with spasticity, other pyramidal signs in a similar distribution were noted and included hyperreflexia and a Babinski sign (Fig. 2D and Table 1). Contractures developed over time and mainly involved the ankles and knees. Extrapyramidal movement disorders were less common although ataxia, dystonia and others were found in a subset of patients (Fig. 2E). Besides cerebellar ataxia, other cerebellar signs included dysarthria, nystagmus and dysdiadochokinesia in a small group of patients (Fig. 2F). Progressive motor symptoms were associated with swallowing dysfunction and sialorrhea. Aspiration with associated respiratory complications occurred in patients with advanced disease.

Seizures and epilepsy
Seizures (67%) including unprovoked seizures and seizures in the setting of fever were common in AP-4-HSP patients and 66% of patients qualified for a diagnosis of epilepsy based on the occurrence of two unprovoked seizures or seizures that required treatment with antiepileptic drugs (AEDs) (Fig. 2G–I and Table 1). Seizure onset occurred in the first 3 years of life, including in infancy, though usually not in the neonatal period. Of note, a significant number of patients presented with status epilepticus (37%), often with their first febrile or unprovoked seizure (Fig. 2I). Severe or medically refractory epilepsy, defined as persistence of seizures despite therapy with two AEDs, was only seen in 27% (Table 1). The majority of patients experienced a significant reduction of seizures or complete cessation of seizures with standard AEDs (Table 1). Levetiracetam and valproate were the AED most commonly
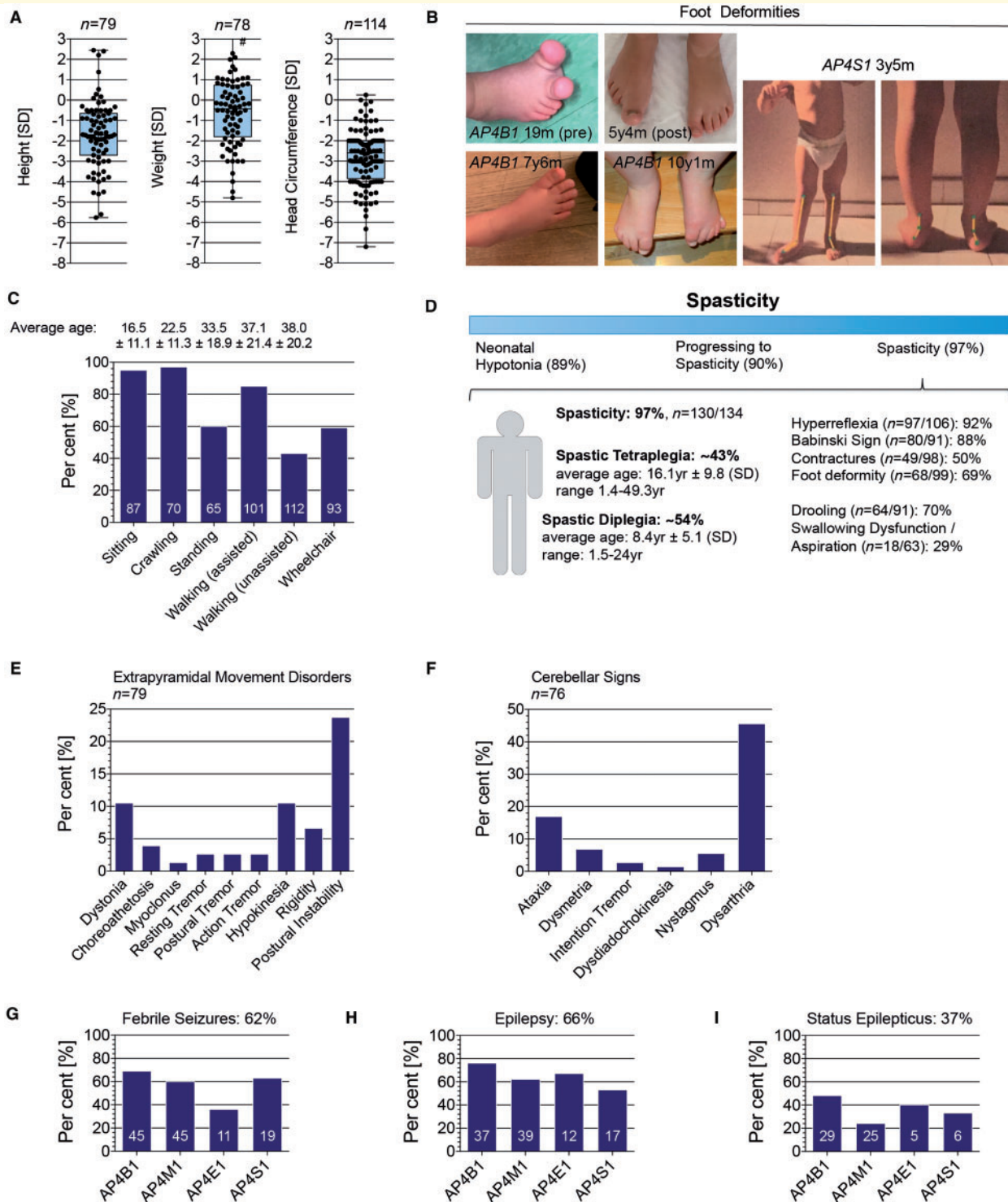
Figure 2 Key clinical features in AP-4-HSP. (**A**) Distribution of height, weight and head circumference according to sex- and age-appropriate CDC growth charts. A subset of patients shows significant growth failure with a height and/or weight under the −2 SD mark (hash symbol indicates two patients with a weight above +3 SD). Postnatal microcephaly is found in the majority of patients, most commonly in a moderate range between −2 SD and −4 SD. (**B**) Foot deformities may include macrodactyly (*top*, macrodactyly of the right foot shown before and after surgical debulking), and pes equinovarus as well as pes planus. (**C**) Developmental delay is a universal feature and motor milestones are often prominently delayed. The bar graph shows the percentage of patients who achieved a given motor milestone. The average age at which each milestone was achieved is shown above the graph. White numbers on bars indicate the number of individuals for whom information was available. (**D**) Motor symptoms evolve from mild hypotonia in infancy to spastic diplegia and later tetraplegia. Progressive spasticity is a hallmark feature of AP-4-HSP and accounts for a large part of the morbidity. (**E** and **F**) Extrapyramidal movement disorders and cerebellar signs are found in a subset of patients, often with advanced disease. (**G** and **H**) Seizures in AP-4-HSP include frequent seizures in the setting of fever as well unprovoked seizures leading to a diagnosis of epilepsy in about two-thirds of patients. (**I**) About 40% of all patients present with at least one episode of status epilepticus, often with their first seizure. White numbers on bars indicate the number of individuals for whom information was available.

For Information Purposes Only. Permissions granted to reproduce by partners and collaborators.

used although others were used as well and no single AED seemed specifically effective. Both focal and primary generalized seizures were common (Table 1). Seizure semiology was variable, and generalized seizures were tonic-clonic (51%), tonic (13%) or myoclonic (16%) in the majority of patients. Structure-related epilepsy occurred in patients with focal brain malformations (see below). Except in these patients and patients with refractory epilepsy during early childhood, seizures became less frequent over time and many patients were able to ultimately stop treatment with AEDs.

Other symptoms

Urinary and stool incontinence were commonly reported, including in older children. A short attention span and decreased perception of hazardous or noxious stimuli were anecdotally reported by several parents.

Treatment and developmental support

Most patients received physical therapy, occupational therapy and speech and language therapy. Depending on the available resources, the majority of children received an individualized education plan. In addition to AEDs, many patients were treated with anti-spasticity agents including oral baclofen or botulinum toxin injections.

Imaging features of AP-4-HSP

MRI characteristics of AP-4-HSP patients are summarized in Fig. 3. Thinning of the corpus callosum was found in the vast majority of patients with AP-4-HSP (90%). Thinning predominantly affected the posterior aspects of the corpus callosum, the splenium (Fig. 3). A complete agenesis of the corpus callosum was not found. Non-specific T_2 signal changes in the supratentorial white matter were common and were mainly present in the periventricular region. Ventriculomegaly was common (65%) and often presented as asymmetric colpocephaly, likely secondary to a loss of periventricular white matter volume. Global cerebral atrophy was seen in some patients (37%), including in toddlers and young children but seemed more common in older patients with significant disease progression (Fig. 3). Cerebellar atrophy was overall uncommon but evident in a subset of patients mainly with advanced disease. Less common imaging findings included symmetric iron deposition in the globus pallidus, found in a single family with *AP4M1*-related SPG50 (Fig. 3 and Roubertie *et al.*, 2018), and one individual with *AP4S1*-related SPG52 (Vill *et al.*, 2017). Three newly diagnosed patients who presented with early-onset seizures had bilateral symmetric polymicrogyria (Fig. 3).
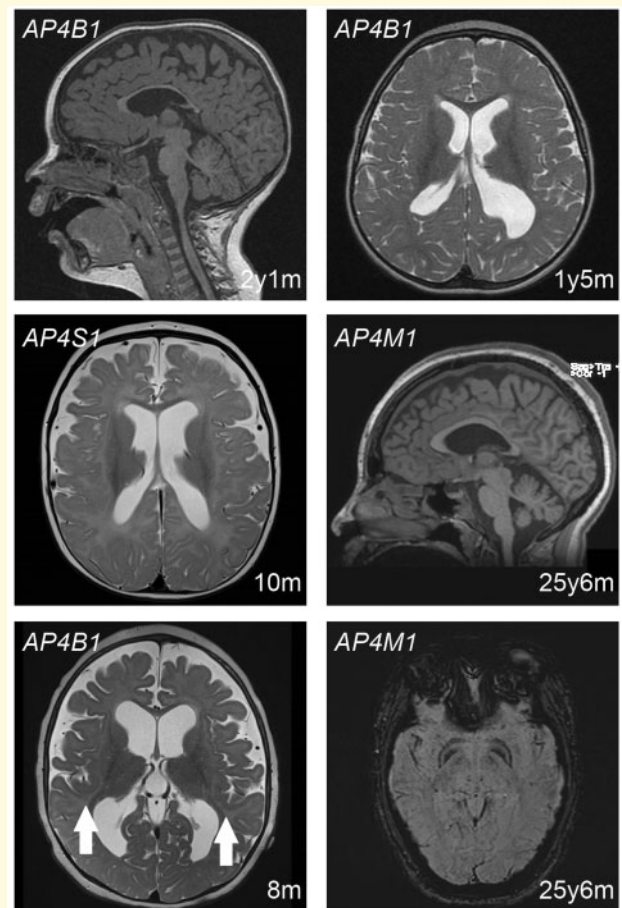
Figure 3 Key imaging features in AP-4-HSP. Brain MR images of AP-4-HSP patients [mean age: 7.4 ± 7.3 years (SD)]. Representative images of key imaging features are shown. *Top left*: Thinning of the corpus callosum, shown here on a sagittal T_1-weighted image, is found in 90% (94/104) of patients and is prominent in the posterior parts. Non-specific white matter abnormalities are noted in 68% (69/102). *Top right*: Ventriculomegaly, shown here on an axial T_2-weighted image, is common (65%, 67/103) and often presents as asymmetric colpocephaly. *Middle left*: Cortical atrophy, shown here on an axial T_2-weighted image, is more commonly found in patients with advanced disease but can be present in young patients as well. Cerebral atrophy is overall found in 37% of cases (38/102). *Middle right*: Cerebellar atrophy, shown here on a sagittal T_1-weighted image, is found in a subset of patients (23%, 20/89). *Bottom left*: Bilateral perisylvian polymicrogyria (arrows), shown on an axial T_2-weighted image. *Bottom right*: Bilateral symmetric hypointensity of the globus pallidus on axial susceptibility-weighted imaging is suggestive of iron accumulation in this previously reported patient with *AP4M1*-associated HSP (Roubertie *et al.*, 2018).

The molecular spectrum of AP-4-HSP

Most patients were identified through exome sequencing and variants in *AP4M1* and *AP4B1* were detected in the majority of families. A total of 75 unique variants were
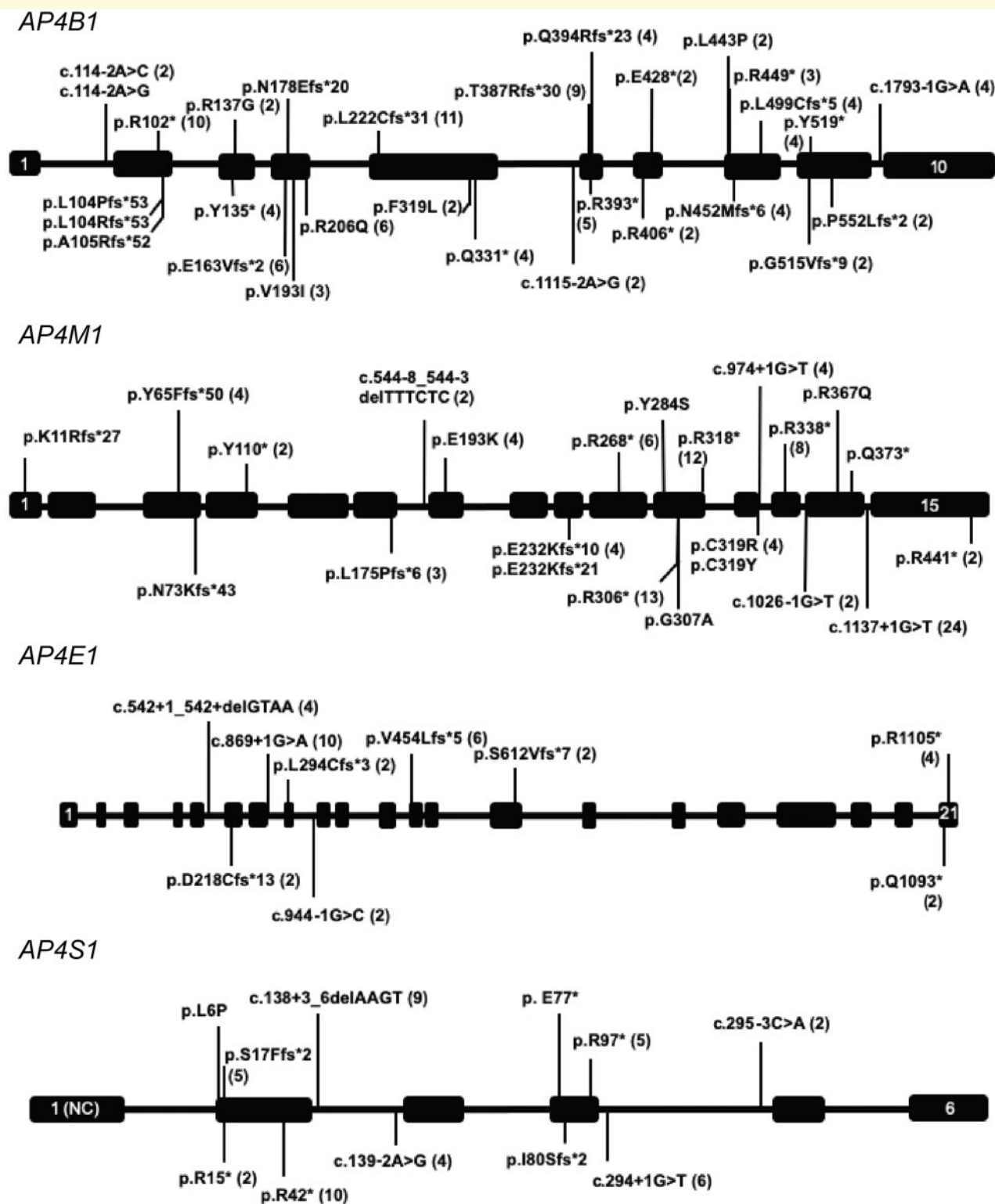
Figure 4 The molecular spectrum of AP-4-HSP. Schematic representation showing the four genes encoding subunits of the AP-4 (*AP4B1*, *AP4M1*, *AP4E1*, *AP4S1*) and the distribution of the reported variants. Parentheses indicate the number of alleles with that variant. Reference sequences: *AP4B1*: NM_001253852.1; *AP4M1*: NM_004722.3; *AP4E1*: NM_007347.4; *AP4S1*: NM_007077.4. NC = non-coding.

identified (Supplementary Table 2 and Fig. 4). All patients carried bi-allelic variants: 82% had homozygous variants, and 18% had compound heterozygous variants. Four

patients showed bi-allelic microdeletions. The vast majority of variants were nonsense or frameshifting predicted to result in a truncated protein, and only a small number of
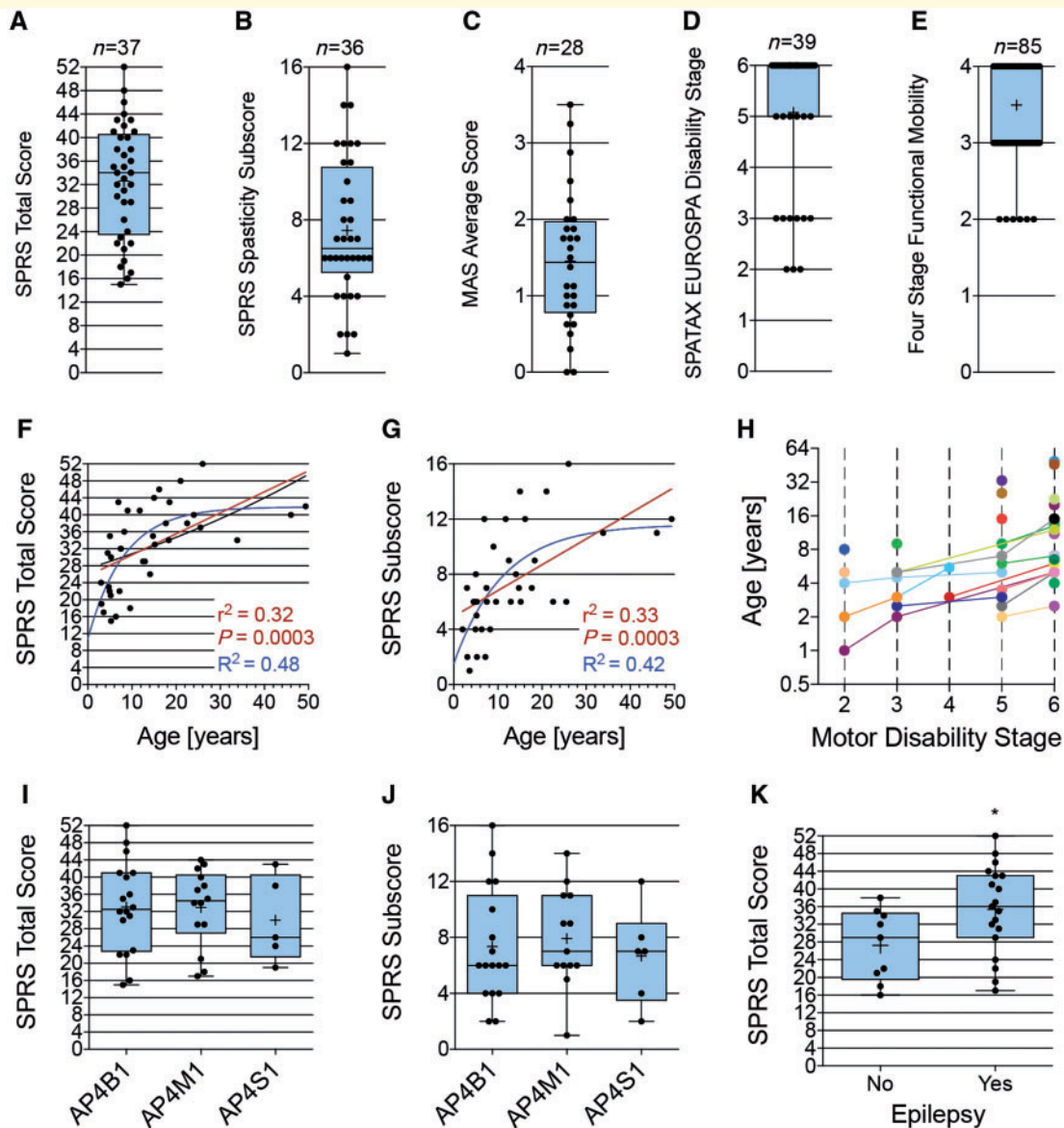
Figure 5 Clinical rating scales and disease progression in AP-4-HSP. Standardized assessment of disease severity using the (**A**) SPRS, (**B**) SPRS spasticity subscore (items 7–10 of the SPRS), (**C**) Modified Ashworth Scale (MAS), (**D**) SPATAX EUROSPA disability score (0 = no functional handicap, 1 = no functional handicap but signs at examination, 2 = mild, able to run, walking unlimited, 3 = moderate, unable to run, limited walking without aid, 4 = severe, walking with one stick, 5 = walking with two sticks or four-wheel walker, 6 = unable to walk, requiring wheelchair, 7 = confined to bed), (**E**) Four Stage Functional Mobility score (1 = mild symptoms walking without an aid; 2 = walking without aid but unable to run; 3 = walking with aid; and 4 = wheelchair dependent). The number of individuals with data available is indicated above each graph. Assessing disease severity across the age spectrum, we found a moderate but significant linear correlation between the (**F**) SPRS total score (n = 37) and (**G**) SPRS spasticity subscore (n = 36) with age as determined by Pearson correlation index for linear regression. The red line indicates a linear regression curve while the blue line indicated a non-linear (exponential) curve. (**H**) Longitudinal assessment of SPATAX-EUROPA disability stages in patients who achieved ambulation (n = 39). Each patient is shown in a different colour with lines between different time points. A general trend towards higher scores, indicating greater motor disability, with increasing age becomes apparent. (**I** and **J**) A subanalysis by genotype showed no significant difference in disease severity by (**I**) SPRS total score and (**J**) SPRS spasticity subscore. (**K**) Significantly higher SPRS scores are present in individuals with epilepsy (unpaired t-test, P = 0.04).

missense variants or splice-site variants were identified. Recurrent variants in *AP4B1* included the two truncating variants p.Arg102* in exon 2 and p.Leu222Cysfs*31 in exon 5 found on 10 and 11 alleles, respectively. Similarly, for *AP4M1* two truncating variants in exon 11

were common as was the c.1137+1G>T variant in a canonical splice site which was found on 24 alleles. Variants in *AP4B1* and *AP4M1* covered most exons while variants in *AP4E1* and *AP4S1* showed a predilection for early truncating variants. *In silico* prediction of pathogenicity using

CADD scores (Supplementary Table 2) showed high scores for the majority of variants.

Clinical rating scales and disease progression

Standardized assessment of disease severity using rating scales showed a mean SPRS score of 32.6 ± 9.7 (SD, range 15–52) and the majority of patients (62%) had SPATAX disability scores of 6 (range 2–6) (Fig. 5A and D). The spasticity subscale of the SPRS, which is independent of ambulation, showed an average score of 7.4 ± 3.7 (SD, range 1-16) (Fig. 5B). The MAS showed an average score of 1.5 ± 0.9 (SD) (Fig. 5C). The Four Stage Functional Mobility confirmed that the vast majority of patients required assistance with ambulation (=level 3, 36%) or depended on a wheelchair for any significant distance (=level 4, 56%) (Fig. 5E). Assessing disease severity across the age spectrum, we found a moderate but significant correlation between the SPRS total score and SPRS spasticity subscore with age (Fig. 5F and G). This was also reflected in the longitudinal assessment of SPATAX-EUROPA disability stages in patients who achieved ambulation (Fig. 5H). A subanalysis of the four genes involved in AP-4-HSP showed no significant difference in disease severity, exemplified by SPRS total and spasticity subscores (Fig. 5I and J) or major clinical features (Table 1). Of note, we detected significantly higher SPRS scores in individuals with epilepsy (Fig. 5K), a finding that could not be accounted for by a difference in age since the age spectrum of patients with and without epilepsy was greatly overlapping [patients with epilepsy: 9.9 ± 6.3 years (SD) versus patients without epilepsy: 11.1 ± 6.9 years (SD)]. This indicates that the presence or absence of epilepsy, which manifested in the first 3 years of life in the vast majority of patients, is a prognostic indicator of later motor complications.

Discussion

In this study we detail the clinical and molecular signature of AP-4-HSP, establishing this condition as a paradigm of childhood-onset complex HSP associated with defective protein trafficking. Most of the enrolled patients were only diagnosed in the last 3 years, indicating that AP-4-HSP is likely under-recognized. From our data, we conclude that all four subtypes of AP-4-HSP share a common clinical phenotype, an 'AP-4 deficiency syndrome'. The core clinical features that should lead clinicians to suspect AP-4-HSP are summarized in Box 1. The combination of global developmental delay, progressive spasticity, seizures and a thin corpus callosum should raise the suspicion for AP-4-HSP although these features are also common to other forms of HSP (Stevanin *et al.*, 2008; Pensato *et al.*, 2014; Ebrahimi-Fakhari *et al.*, 2016, 2018*a, b*; Kara *et al.*, 2016). Episodes of stereotypic laughter, perhaps indicating a pseudobulbar affect (Wild *et al.*, 2003), are a peculiar and specific finding in a subset of patients and thus may

help in establishing a differential diagnosis. Microcephaly, short statue in some and the high prevalence of foot deformities are also features that help distinguish AP-4-HSP from other conditions with developmental delay and spasticity. Prior to the availability of clinical exome sequencing and multi-gene panels that cover the AP-4 subunit genes, some of our patients had received a diagnosis of cerebral palsy. The slowly progressive nature of AP-4-HSP may be mistaken for a static disease course, at least initially, and AP-4-HSP should be added to the list of 'cerebral palsy mimics' (Leach *et al.*, 2014; Appleton and Gupta, 2019; Pearson *et al.*, 2019). The absence of prenatal or neonatal risk factors (i.e. prematurity, infections, birth complications), a history of consanguinity, and the progression of symptoms in mid to late childhood may help to distinguish AP-4-HSP from cerebral palsy clinically. The high prevalence of characteristic imaging findings (a posterior-dominant thinning of the corpus callosum and colpocephaly) may also be important distinguishing features although these have been reported in series of patients with a clinical diagnosis of cerebral palsy in the absence of comprehensive genetic testing (Kwong *et al.*, 2004; Bax *et al.*, 2006; Rana *et al.*, 2016).

In AP-4-HSP, the first reported manifestation is early developmental delay with prominent motor and speech delay. Motor milestones are usually delayed by several months and only a subset of patients ever achieved independent walking. Speech development is delayed, and 50% of patients remain non-verbal. Intellectual disability in older children is typically moderate to severe. Importantly, regression and loss of skills were reported in about half the patients. Anecdotally, loss of skills occurred transiently in young children in the setting of an intercurrent illness or with onset of seizures. However, true regression seems to occur later in patients with more advanced disease.

Delayed development and later regression are paralleled by progressive motor symptoms. Mild truncal hypotonia in infancy is retrospectively reported in the vast majority of patients and often coincides with delayed early motor milestones. Spasticity begins with an often largely symmetric diplegia in late infancy or toddler years. Over time, spasticity progresses and other pyramidal signs become apparent including hyperreflexia and a Babinski sign. Spasticity progresses to cause contractures, mainly of the ankles and knees, and by adolescence often involves the arms, leading to spastic tetraplegia. The average age for patients with spastic tetraplegia was 16.1 ± 9.8 years (SD) and although the youngest reported patient was 1.4 years old, the majority of patients were older than 10 years. This leads us to conclude that significant disease progression occurs between the age of 5 and 16 years. At last follow-up, most patients were able to ambulate with assistance, i.e. with a posterior walker, but about 60% used a wheelchair for significant distances. Of note, in addition to pyramidal symptoms, extrapyramidal movement disorders and cerebellar signs were reported in a subset of patients. Taken together with the finding of cognitive decline, this points to a neurodegenerative process that involves widespread brain

areas, including the cerebral and cerebellar cortices, basal ganglia and corticospinal tracts. This is supported by the findings of cerebral and cerebellar atrophy on brain imaging in a subset of patients, mainly with advanced disease.

A standardized assessment using the SPRS (Schule *et al.*, 2006) revealed an average score of 33, which is in the moderate range. The SPRS is an established tool to track disease severity in HSP though it is only validated for individuals older than 9 years (Schule *et al.*, 2006). This poses a challenge for our patient population and may limit its interpretation. Nevertheless, a longitudinal assessment using the SPRS may reveal trends of progression and hence the reported values here serve as important baseline values. The SPRS spasticity subscore does not depend on ambulation and hence was included in a subanalysis. This subscore mirrored the total score, and both scores showed a moderate correlation with age, which may reflect disease progression. A stratification based on longitudinal data in future studies will help to define the SPRS as an indicator of disease progression in AP-4-HSP.

Standardized assessment of spasticity using the MAS (Bohannon and Smith, 1987) was available for a subset of patients not allowing us to draw any conclusions for the broader AP-4-HSP population at this point but establishing a starting point for longitudinal studies. The SPATAX-EUROSPA disability score was 6 in the majority of cases reflecting high rates of wheelchair-dependence. The Four Stage Functional Mobility Score confirmed the latter finding. Given the early age of wheelchair-dependence and the a priori lack of independent walking in most patients, both scores do not seem sensitive enough to track disease progress but help establish a level of functionality.

Complications related to progressive spasticity such as contractures, drooling and swallowing dysfunction were reported in patients with advanced disease. The latter, just like the pseudobulbar affect with unprovoked and stereotyped episodes of laughter, might point to involvement of corticobulbar tracts. We failed to detect high rates of sensory deficits (pain sensation, temperature sensation, proprioception, vibration sense) in our cohort but acknowledge that this is often difficult to assess particularly in children with developmental delay or intellectual disability.

Seizures and/or epilepsy are found in the majority of patients with seizure-onset commonly in the first three years of life. Importantly, many patients presented with status epilepticus with their first seizure. Seizures in the setting of fever were frequent in AP-4-HSP patients who both do and do not go on to develop epilepsy. Both focal and generalized seizures were common, and no clear dominant seizure semiology or EEG signature was found. In the majority of patients, seizures responded to standard AEDs and two or more agents were only needed in about a quarter of patients. Anecdotally it appears that seizures become less frequent with age, and in some patients AEDs were discontinued without seizure recurrence. Although polymicrogyria was rarely reported in our cohort (only in three patients), developmental brain malformations should be evaluated for, particularly in AP-4-HSP

patients with seizures given the strong association with epilepsy (Leventer *et al.*, 2010; Shain *et al.*, 2013). Of note, the presence of epilepsy was correlated with higher SPRS scores at last follow-up and thus might be predictive of greater disease severity in the long-term.

On brain imaging, thinning of the corpus callosum was almost universal, making AP-4-HSP part of the spectrum of autosomal-recessive and complex HSPs that present with a thin corpus callosum (Kara *et al.*, 2016). The thinning prominently affects the posterior parts of the corpus callosum, the splenium. Ventriculomegaly, seen in the majority of patients, mostly involves the lateral ventricles and often presents as asymmetric colpocephaly. This points to a loss of periventricular white matter, i.e. loss of axons of the posterior corona radiata. Together with the finding of a thin corpus callosum, loss of periventricular volume points to a degeneration of the long projecting neurons, including the interhemispheric, corticobulbar and corticospinal tracts. Bilateral symmetric perisylvian polymicrogyria was found in three families with compound heterozygous variants in *AP4S1* (Patient 98) and *AP4B1* (Patient 86) or homozygous splice-site variants in *AP4S1* (Patient 64), respectively. It is interesting to speculate that AP-4 deficiency could possibly cause abnormalities during late neuronal migration or early cortical organization. The true prevalence of malformations of cortical development remains to be evaluated in larger series and AP-4 variants should be assessed in patients with polymicrogyria of unclear aetiology (Stutterd and Leventer, 2014). Interestingly, symmetric hypointense SWI signal in the globus pallidus, suggestive of iron deposition, was found in a previously reported family with *AP4M1*-related SPG50 and one individual with *AP4S1*-related SPG52 (Vill *et al.*, 2017; Roubertie *et al.*, 2018). Findings suggestive of iron deposition were not discovered in any other patients in our cohort although dedicated MRI sequences were not available in all scans examined. Interestingly, the three members of the family with *AP4M1*-related SPG50 and brain iron accumulation were among the oldest in our cohort. Thus, it remains to be seen if iron deposition in the basal ganglia is an age-dependent phenotype. Arguing against this is the young age of the male patient with *AP4S1* splice site mutations and brain iron deposition reported by Vill *et al.* (2017) and the absence of AP-4 variants in a cohort of patients with brain iron accumulation of unclear aetiology (S. Hayflick, personal communication). Cerebral atrophy, mainly in a fronto-temporal pattern, and cerebellar atrophy were described in patients with an average age of 11.3 ± 8.5 and 19.5 ± 13.5 years (SD), respectively. This argues that there might be some dependency of atrophic changes on age and disease progression although prominent cerebral atrophy was also seen in some of the youngest patients in our cohort (Fig. 3). Cerebellar atrophy, however, was rare in young patients. Genotype to imaging correlations and indicators of disease progression remain to be established through standardized and longitudinal imaging studies in AP-4-HSP patients of different age groups.

Variants in the AP-4 subunit genes in our cohort were found in a wide range of different ethnicities. Consanguinity was reported in ~70% of patients but interestingly rates were lower for patients with *AP4B1*- and *AP4S1*-associated HSP while over two-thirds of patients with *AP4M1*- and *AP4E1*-associated HSP were of consanguineous parents, often of North African or Middle Eastern descent. *AP4M1* and *AP4B1* were most commonly mutated, together accounting for over 70% of patients. This is a larger percentage than expected simply based the relative size of the four different genes. At 1137 amino acids, AP4E1 is the largest of the four subunits so would be expected to have the most mutations under a simple loss of function model. Interestingly, variants were not homogenously distributed throughout the *AP4E1* gene, being absent from exons 15 through 20. The reason for this skewing of the variant distribution in *AP4E1* is unknown, but may reflect a distinct function of this region of the protein.

While the majority of AP-4 variants were private, we identified a number of seemingly recurrent variants. As an example, a homozygous c.617G>A [p.R206Q] variant in *AP4B1* was found in three families originating from the Jain community and the same discrete geographic within the state of Rajasthan, India, suggesting a possible founder effect. Most AP-4 variants identified were single nucleotide substitutions with a predicted truncating effect on the respective subunit protein (nonsense or frameshift). Canonical splice site variants were the third most common group. About 80% of patients had homozygous variants while compound heterozygous variants occurred in about 20%. The latter naturally occurred in many patients with no reported consanguinity. Microdeletions were found in a few patients and although rare, genetic investigations for AP-4-HSP should include techniques capable of detecting deletions.

Despite some variability, there was homogeneity concerning the core clinical features (Box 1), probably reflecting that most variants are predicted to cause at least partial loss of the AP-4 subunit protein rather than more subtle alterations of functionally critical domains. Stratification of disease severity by affected subunit did not reveal any clear correlation. This finding of a shared phenotype is supported by the presence of similar cellular phenotypes with loss of any of the AP-4 subunits, as recently demonstrated in patient-derived neurons (Behne *et al.*, 2020).

In summary, we here describe for the first time a detailed cross-sectional assessment of the clinical, imaging and molecular spectrum of AP-4-HSP. We define a core set of clinical features, delineate manifestations across the age spectrum, and explore genotype-phenotype correlations. Our results suggest that children with developmental delay, microcephaly, spasticity and a thin corpus callosum on imaging should undergo evaluation for AP-4-HSP to reduce the delay between presentation and diagnosis. Our findings also, for the first time, allow counselling of affected families. The development of this international cohort (www.CureAP4.org) and natural history study will enable us to understand disease progression more precisely and will define endpoints for future interventional trials.

Acknowledgements

Funding

Competing interests

D.E.F. and M.S. report support through a joint research agreement with Astellas Pharma Inc. M.S. reports grant support from Novartis, Roche, Pfizer, Ipsen, LAM Therapeutics and Quadrant Biosciences and served on Scientific Advisory Boards for Sage, Roche, Celgene and Takeda. A.S. received grants from Biogen and Sarepta Therapeutics. S.S. is an employee of Celgene Corporation. C.B. and P.B. are employees of CENTOGENE AG. All other authors report no conflict of interest.

Supplementary material

Supplementary material is available at *Brain* online.

References

Abou Jamra R, Philippe O, Raas-Rothschild A, Eck SH, Graf E, Buchert R, et al. Adaptor protein complex 4 deficiency causes severe autosomal-recessive intellectual disability, progressive spastic paraplegia, shy character, and short stature. Am J Hum Genet 2011; 88: 788–95.

Accogli A, Hamdan FF, Poulin C, Nassif C, Rouleau GA, Michaud JL, et al. A novel homozygous AP4B1 mutation in two brothers with AP-4 deficiency syndrome and ocular anomalies. Am J Med Genet A 2018; 176: 985–91.

Aguilar RC, Boehm M, Gorshkova I, Crouch RJ, Tomita K, Saito T, et al. Signal-binding specificity of the mu4 subunit of the adaptor protein complex AP-4. J Biol Chem 2001; 276: 13145–52.

Appleton RE, Gupta R. Cerebral palsy: not always what it seems. Arch Dis Child 2019; 104: 809–14.

Bax M, Tydeman C, Flodmark O. Clinical and MRI correlates of cerebral palsy: the European Cerebral Palsy Study. JAMA 2006; 296: 1602–8.

Behne R, Teinert J, Wimmer M, D'Amore A, Davies AK, Scarrott JM, et al. Adaptor protein complex 4 deficiency: a paradigm of childhood-onset hereditary spastic paraplegia caused by defective protein trafficking. Hum Mol Genet 2020; 29: 320–34.

Blackstone C. Hereditary spastic paraplegia. Handb Clin Neurol. 2018; 148: 633–52.

Bohannon RW, Smith MB. Interrater reliability of a modified Ashworth scale of muscle spasticity. Phys Ther 1987; 67: 206–7.

Burgos PV, Mardones GA, Rojas AL, daSilva LL, Prabhu Y, Hurley JH, et al. Sorting of the Alzheimer's disease amyloid precursor protein mediated by the AP-4 complex. Dev Cell 2010; 18: 425–36.

Chrestian N, Dupre N, Gan-Or Z, Szuto A, Chen S, Venkitachalam A, et al. Clinical and genetic study of hereditary spastic paraplegia in Canada. Neurol Genet 2017; 3: e122.

da Graca FF, de Rezende TJR, Vasconcellos LFR, Pedroso JL, Barsottini OGP, Franca MC, Jr. Neuroimaging in hereditary spastic paraplegias: current use and future perspectives. Front Neurol 2018; 9: 1117.

Ebrahimi-Fakhari D. Congenital disorders of autophagy: what a pediatric neurologist should know. Neuropediatrics 2018; 49: 18–25.

Ebrahimi-Fakhari D, Behne R, Davies AK, Hirst J. AP-4-associated hereditary spastic paraplegia. In: Adam MP, Ardinger HH, Pagon RA, Wallace SE, Bean LJH, Stephens K, et al., editors. GeneReviews((R)). Seattle (WA); 2018a.

Ebrahimi-Fakhari D, Cheng C, Dies K, Diplock A, Pier DB, Ryan CS, et al. Clinical and genetic characterization of AP4B1-associated SPG47. Am J Med Genet A 2018b; 176: 311–8.

Ebrahimi-Fakhari D, Saffari A, Wahlster L, Lu J, Byrne S, Hoffmann GF, et al. Congenital disorders of autophagy: an emerging novel class of inborn errors of neuro-metabolism. Brain 2016; 139: 317–37.

Erichsen AK, Koht J, Stray-Pedersen A, Abdelnoor M, Tallaksen CM. Prevalence of hereditary ataxia and spastic paraplegia in southeast Norway: a population-based study. Brain 2009; 132: 1577–88.

Firth HV, Richards SM, Bevan AP, Clayton S, Corpas M, Rajan D, et al. DECIPHER: database of chromosomal imbalance and phenotype in humans using ensembl resources. Am J Hum Genet 2009; 84: 524–33.

Hardies K, May P, Djemie T, Tarta-Arsene O, Deconinck T, Craiu D, et al. Recessive loss-of-function mutations in AP4S1 cause mild fever-sensitive seizures, developmental delay and spastic paraplegia through loss of AP-4 complex assembly. Hum Mol Genet 2015; 24: 2218–27.

Hirst J, Bright NA, Rous B, Robinson MS. Characterization of a fourth adaptor-related protein complex. Mol Biol Cell 1999; 10: 2787–802.

Kara E, Tucci A, Manzoni C, Lynch DS, Elpidorou M, Bettencourt C, et al. Genetic and phenotypic characterization of complex hereditary spastic paraplegia. Brain 2016; 139: 1904–18.

Karaca E, Harel T, Pehlivan D, Jhangiani SN, Gambin T, Coban Akdemir Z, et al. Genes that affect brain structure and function identified by rare variant analyses of mendelian neurologic disease. Neuron 2015; 88: 499–513.

Karle KN, Schule R, Klebe S, Otto S, Frischholz C, Liepelt-Scarfone I, et al. Electrophysiological characterisation of motor and sensory tracts in patients with hereditary spastic paraplegia (HSP). Orphanet J Rare Dis 2013; 8: 158.

Kircher M, Witten DM, Jain P, O'Roak BJ, Cooper GM, Shendure J. A general framework for estimating the relative pathogenicity of human genetic variants. Nat Genet 2014; 46: 310–5.

Kong XF, Bousfiha A, Rouissi A, Itan Y, Abhyankar A, Bryant V, et al. A novel homozygous p.R1105X mutation of the AP4E1 gene in twins with hereditary spastic paraplegia and mycobacterial disease. PLoS One 2013; 8: e58286.

Kwong KL, Wong YC, Fong CM, Wong SN, So KT. Magnetic resonance imaging in 122 children with spastic cerebral palsy. Pediatr Neurol 2004; 31: 172–6.

Lamichhane DM. New AP4B1 mutation in an African-American child associated with intellectual disability. J Pediatr Genet 2013; 2: 191–5.

Langouet M, Siquier-Pernet K, Sanquer S, Bole-Feysot C, Nitschke P, Boddaert N, et al. Contiguous mutation syndrome in the era of high-throughput sequencing. Mol Genet Genomic Med 2015; 3: 215–20.

Leach EL, Shevell M, Bowden K, Stockler-Ipsiroglu S, van Karnebeek CD. Treatable inborn errors of metabolism presenting as cerebral palsy mimics: systematic literature review. Orphanet J Rare Dis 2014; 9: 197.

Leventer RJ, Jansen A, Pilz DT, Stoodley N, Marini C, Dubeau F, et al. Clinical and imaging heterogeneity of polymicrogyria: a study of 328 patients. Brain 2010; 133: 1415–27.

Moreno-De-Luca A, Helmers SL, Mao H, Burns TG, Melton AM, Schmidt KR, et al. Adaptor protein complex-4 (AP-4) deficiency causes a novel autosomal recessive cerebral palsy syndrome with microcephaly and intellectual disability. J Med Genet 2011; 48: 141–4.

Najmabadi H, Hu H, Garshasbi M, Zemojtel T, Abedini SS, Chen W, et al. Deep sequencing reveals 50 novel genes for recessive cognitive disorders. Nature 2011; 478: 57–63.

Pearson TS, Pons R, Ghaoui R, Sue CM. Genetic mimics of cerebral palsy. Mov Disord 2019; 34: 625–36.

Pensato V, Castellotti B, Gellera C, Pareyson D, Ciano C, Nanetti L, et al. Overlapping phenotypes in complex spastic paraplegias SPG11, SPG15, SPG35 and SPG48. Brain 2014; 137: 1907–20.

Rana KS, Narwal V, Chauhan L, Singh G, Sharma M, Chauhan S. Structural and perfusion abnormalities of brain on MRI and technetium-99m-ECD SPECT in children with cerebral palsy: a comparative study. J Child Neurol 2016; 31: 589–92.

Roubertie A, Hieu N, Roux CJ, Leboucq N, Manes G, Charif M, et al. AP4 deficiency: a novel form of neurodegeneration with brain iron accumulation? Neurol Genet 2018; 4: e217.

Schule R, Holland-Letz T, Klimpe S, Kassubek J, Klopstock T, Mall V, et al. The spastic paraplegia rating scale (SPRS): a reliable and valid measure of disease severity. Neurology 2006; 67: 430–4.

Shain C, Ramgopal S, Fallil Z, Parulkar I, Alongi R, Knowlton R, et al. Polymicrogyria-associated epilepsy: a multicenter phenotypic study from the epilepsy phenome/genome project. Epilepsia 2013; 54: 1368–75.

Stevanin G, Azzedine H, Denora P, Boukhris A, Tazir M, Lossos A, et al. Mutations in SPG11 are frequent in autosomal recessive spastic paraplegia with thin corpus callosum, cognitive decline and lower motor neuron degeneration. Brain 2008; 131: 772–84.

Stutterd CA, Leventer RJ. Polymicrogyria: a common and heterogeneous malformation of cortical development. Am J Med Genet C Semin Med Genet 2014; 166C: 227–39.

Tan CA, Topper S, Del Gaudio D, Nelakuditi V, Shchelochkov O, Nowaczyk MJM, et al. Characterization of patients referred for non-specific intellectual disability testing: the importance of autosomal genes for diagnosis. Clin Genet 2016; 89: 478–83.

Tessa A, Battini R, Rubegni A, Storti E, Marini C, Galatolo D, et al. Identification of mutations in AP4S1/SPG52 through next generation sequencing in three families. Eur J Neurol 2016; 23: 1580–7.

Toh WH, Tan JZ, Zulkefli KL, Houghton FJ, Gleeson PA. Amyloid precursor protein traffics from the Golgi directly to early endosomes in an Arl5b- and AP4-dependent pathway. Traffic 2017; 18: 159–75.

Trujillano D, Oprea GE, Schmitz Y, Bertoli-Avella AM, Abou Jamra R, Rolfs A. A comprehensive global genotype-phenotype database for rare diseases. Mol Genet Genomic Med 2017; 5: 66–75.

Tuysuz B, Bilguvar K, Kocer N, Yalcinkaya C, Caglayan O, Gul E, et al. Autosomal recessive spastic tetraplegia caused by AP4M1 and AP4B1 gene mutation: expansion of the facial and neuroimaging features. Am J Med Genet A 2014; 164A: 1677–85.

Verkerk AJ, Schot R, Dumee B, Schellekens K, Swagemakers S, Bertoli-Avella AM, et al. Mutation in the AP4M1 gene provides a model for neuroaxonal injury in cerebral palsy. Am J Hum Genet 2009; 85: 40–52.

Vill K, Muller-Felber W, Alhaddad B, Strom TM, Teusch V, Weigand H, et al. A homozygous splice variant in AP4S1 mimicking neurodegeneration with brain iron accumulation. Mov Disord 2017; 32: 797–9.

Wild B, Rodden FA, Grodd W, Ruch W. Neural correlates of laughter and humour. Brain 2003; 126: 2121–38.
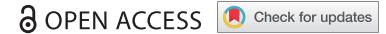
Taylor & Francis
Taylor & Francis Group

Axonal autophagosome maturation defect through failure of ATG9A sorting underpins pathology in AP-4 deficiency syndrome

Davor Ivankovic [a], James Drew [a], Flavie Lesept [a], Ian J. White[b], Guillermo López Doménech [a], Sharon A. Tooze [c], and Josef T. Kittler [a]

aNeuroscience, Physiology and Pharmacology, UCL, London, UK; bMRC Laboratory for Molecular Cell Biology, UCL, London, UK; cMolecular Cell Biology of Autophagy, The Francis Crick Institute, London, UK

ABSTRACT
Adaptor protein (AP) complexes mediate key sorting decisions in the cell through selective incorporation of transmembrane proteins into vesicles. Little is known of the roles of AP-4, despite its loss of function leading to a severe early onset neurological disorder, AP-4 deficiency syndrome. Here we demonstrate an AP-4 epsilon subunit knockout mouse model that recapitulates characteristic neuroanatomical phenotypes of AP-4 deficiency patients. We show that ATG9A, critical for autophagosome biogenesis, is an AP-4 cargo, which is retained within the *trans*-Golgi network (TGN) *in vivo* and in culture when AP-4 function is lost. TGN retention results in depletion of axonal ATG9A, leading to defective autophagosome generation and aberrant expansions of the distal axon. The reduction in the capacity to generate axonal autophagosomes leads to defective axonal extension and *de novo* generation of distal axonal swellings containing accumulated ER, underlying the impaired axonal integrity in AP-4 deficiency syndrome.

Abbreviations: AP: adaptor protein; AP4B1: adaptor-related protein complex AP-4, beta 1; AP4E1: adaptor-related protein complex AP-4, epsilon 1; ATG: autophagy-related; EBSS: Earle's balanced salt solution; ER: endoplasmic reticulum; GFAP: glial fibrillary acidic protein; GOLGA1/Golgin-97/GOLG97: golgi autoantigen, golgin subfamily a, 1; GOLGA2/GM130: golgi autoantigen, golgin subfamily a, 2; HSP: hereditary spastic paraplegia; LC3/MAP1LC3B: microtubule-associated protein 1 light chain 3 beta; MAP2: microtubule-associated protein 2; MAPK8IP1/JIP1: mitogen-acitvated protein kinase 8 interacting protein 1; NEFH/NF200: neurofilament, heavy polypeptide; RBFOX3/NeuN (RNA binding protein, fox-1 homolog [C. elegans] 3); SQSTM1/p62: sequestosome 1; TGN: trans-Golgi network; WIPI2: WD repeat domain, phosphoinositide interacting protein 2

Introduction

Adaptor protein (AP) complexes have roles in the selection of transmembrane proteins (cargo) for inclusion into vesicles. AP complexes interact with sorting motifs within the cytoplasmic facing tails of cargoes, leading to their specific enrichment at sites on donor membranes. Upon motif recognition and binding to cargoes, AP complexes recruit coat proteins which assemble to generate free vesicles [1]. Of the 5 members of the AP complex family, AP-1 and AP-2 are the best understood thus far, functioning in clathrin-dependent sorting from the *trans*-Golgi network (TGN) and endocytosis from the plasma membrane, respectively. Assembling as hetero-tetramers, AP complexes require the presence of all subunits to maintain functionality [2–4]. Indeed, mutations in genes encoding all subunits of AP-4 (ε1; *AP4E1*, β1; *AP4B1*, μ1; *AP4M1* and σ1; *AP4S1*) have been identified as leading to a complex form of hereditary spastic paraplegia (HSP) termed AP-4 deficiency syndrome (henceforth AP-4 deficiency) [5,6]. AP-4 deficiency patients present with early-onset severe intellectual disability, absence of speech and progressive spasticity leading to para- or tetraplegia [7]. Thinning of the corpus callosum axonal tracts and ventriculomegaly are characteristic neuroanatomical

features arising from white matter loss in AP-4 deficiency patients [5,7–10]. Despite this severe pathology little is known of AP-4 other than its localization to the TGN in cell lines [11,12], and mislocalization of AMPA receptors to autophagosomes in the axons of a mouse model lacking *ap4b1* [13]. The entire repertoire of cargoes sorted by AP-4 in neurons and the functional consequence of their altered handling and subsequent trafficking as a result of disruption of the AP-4 complex remain poorly understood.

Macroautophagy (henceforth autophagy) is the process by which organelles and macromolecules are recycled for the maintenance of cellular homeostasis. Autophagy can be simplified into 3 fundamental steps; induction, autophagosome biogenesis and lysosomal degradation. Progression through the pathway is in part mediated by the concerted recruitment of autophagy-related (ATG) proteins [14], the sequence and necessity of which are understood to be conserved in the neuron [15]. After the induction of autophagy, membrane elongation from sites on the endoplasmic reticulum (ER) forms a cup shaped phagophore which incorporates cytosolic components [16]. Enclosure of the expanding edges of the phagophore produces a double-

membraned autophagosome, which can then fuse with late endosomes and lysosomes to form degradative autolysosomes [17].

Intact and efficient autophagy is of critical importance to post-mitotic cells, which cannot overcome proteotoxic burden through cellular division [18]. Neurons may be exceptionally susceptible to defects in autophagy due to their extreme architecture, particularly the axon which can extend for distances up to a meter from the soma [19,20]. Autophagosomes are constitutively generated in the axon, predominantly at its most distal extremities [21,22]. In order to maintain this localized biogenesis, machineries necessary for autophagosome generation must be delivered to the distal axon; and once completed, *de novo* generated autophagosomes retrogradely trafficked toward the soma for their clearance by resident lysosomes. The sole mammalian transmembrane ATG protein, ATG9A is thus of particular interest, as it relies upon vesicular sorting and trafficking mechanisms for its distribution. With its roles in phagophore extension and autophagosome maturation [23,24], effective sorting and delivery of ATG9A may be critical for the maintenance of constitutive generation of autophagosomes in the distal axon. Indeed, dysgenesis of the corpus callosum has recently been identified in a CNS-specific *atg9a* knockout-mouse model [25]. This defect in commissural axon crossing arising from loss of ATG9A is highly reminiscent of the thinning of the corpus callosum in AP-4 deficiency, raising the question of whether the recent identification of altered ATG9A sorting in cell lines lacking AP-4 function [26] is of relevance to the pathological features of AP-4 deficiency.

Here we identify neuroanatomical defects in an *ap4e1* knockout-mouse model mirroring those of AP-4 deficiency patients. We show that ATG9A is a neuronal AP-4 cargo, which is retained within the TGN *in vivo* and in culture as a consequence of the disruption of AP-4 assembly. TGN retention results in depletion of axonal ATG9A, reduction in the capacity of axonal autophagosome generation and aberrant accumulation of ER within swellings in the distal axon. This alteration in axonal autophagosome biogenesis likely underlies defective axonal extension and integrity when AP-4 function is lost, leading to axonal loss and the characteristic phenotypes of AP-4 deficiency syndrome.

Results

Ap4e1 *null mice recapitulate neuroanatomical features of AP-4 deficiency*

To elucidate the mechanisms underpinning the pathology in AP-4 deficiency, we first sought to characterize a mouse model developed by the International Mouse Phenotyping Consortium (IMPC) by targeting one of the 2 large subunits of the AP-4 complex [27]. Heterozygous mice carrying 1 copy of the targeting cassette (Figure 1(a)) were crossed, generating litter matched $Ap4e1^{+/+}$ (WT) and $ap4e1^{-/-}$ (KO) animals (Figure S1 (a)). The AP4E1 subunit was confirmed to be entirely absent at the protein level in KO animals (Figure 1(b)), and levels of the

AP4B1 subunit were reduced in tandem, indicating destabilization of the entire AP-4 complex [2–4], and thus loss of AP-4 complex assembly. Using a beta-galactosidase assay we showed the AP4E1 subunit to be expressed throughout all tissues during embryonic development (Figure S1(b,c)), and across regions in the adult brain (Figure S1(d)).

We next examined whether mice with loss of AP-4 function phenocopied the characteristic neuroanatomical features of AP-4 deficiency patients. To this end, we prepared sections from WT and KO mice and examined their brain morphology through staining of RBFOX3/NeuN and GFAP (Figure 1(c)). We found dramatic and specific enlargement of the lateral ventricles in KO animals by 1 month, and that this enlargement did not appear to progress in severity by 4 months (Figure 1(d), S1E; lateral ventricular area; 1 month: WT 52,216 ± 7,092 μm^2, KO 528,509 ± 130,084 μm^2, p = 0.0064; 4 month: WT 235,874 ± 67,610 μm^2, KO 650,456 ± 76,361 μm^2, p = 0.015; Figure S1(e); area of third ventricle: WT 297,649 ± 51,048 μm^2, KO 278,361 ± 34,709 μm^2, p = 0.78; area of fourth ventricle: WT 9,966 ± 2,333 μm^2, KO 9,793 ± 1815 μm^2, p = 0.96; t-test). Given this similarity to patients' ventriculomegaly, we next examined whether KO mice additionally exhibited the characteristic thinning of the corpus callosum by staining brain sections using FluoroMyelin to reveal axon tracts (Figure 1(e)). Robust thinning of the corpus callosum axonal tracts was evident at 1 month in KO animals, which did not progress in severity by 4 months (Figure 1(f); corpus callosum thickness FluoroMyelin; 1 month: WT 302.5 ± 8.26 μm, KO 197.4 ± 8.25, p = 0.0008; 4 month: WT 317.7 ± 5.74 μm, KO 225.4 ± 12.52, p = 0.0026; t-test). We confirmed that this was as a result of the loss of axons by staining sections against the axon-resident neurofilament, NEFH/NF200 (Figure 1(g,h); corpus callosum thickness NEFH/NF200: WT 300 ± 10.7 μm, KO 212 ± 12.7 μm, p = 0.0007; t-test). In addition to the corpus callosum, thinning of the apical anterior commissure and external capsule axonal tracts was evident at 1 month in KO animals (Figure S1(f, g); anterior commissure area: WT 80,200 ± 12,050 μm^2, KO 45,900 ± 4,950 μm^2, p = 0.0272; external capsule length: WT 142.3 ± 6.2 μm^2, KO 97.22 ± 4.29 μm^2, p < 0.0001; t-test), whereas no alteration was found in the lateral optic tract (Figure S1(h); lateral optic tract: WT 38,500 ± 2716 μm, KO 37,140 ± 3,890 μm; p = 0.78).

The thinning of commissural axon tracts and enlargement of lateral ventricles led us to question whether these defects arise due to defective axon development, or through extensive neuronal cell loss. To address this, we quantified neuronal cell numbers within regions of KO brain at 1 and 4 months. We found that cortical neuronal numbers in KO were indistinguishable from WT animals both at 1 and 4 months (Figure S1(i); relative cortical neuronal cell number; 1 month: WT 1 ± 0.053, KO 1.053 ± 0.033, p = 0.44; 4 month: WT 1 ± 0.09, KO 0.94 ± 0.057, p = 0.63; t-test). Neither was there a detectable reduction in neuronal cell number in major regions of the hippocampus at 1 month (Figure S1(j, k); relative neuronal cell number; CA1: WT 1 ± 0.11, KO 1.05 ± 0.031, p = 0.72; CA3: WT 1 ± 0.077, KO 0.99 ± 0.057, p = 0.92; DG: WT 1 ± 0.059, KO 0.97 ± 0.093, p = 0.78; t-test). We did note however a small decrease in cell number in the CA1
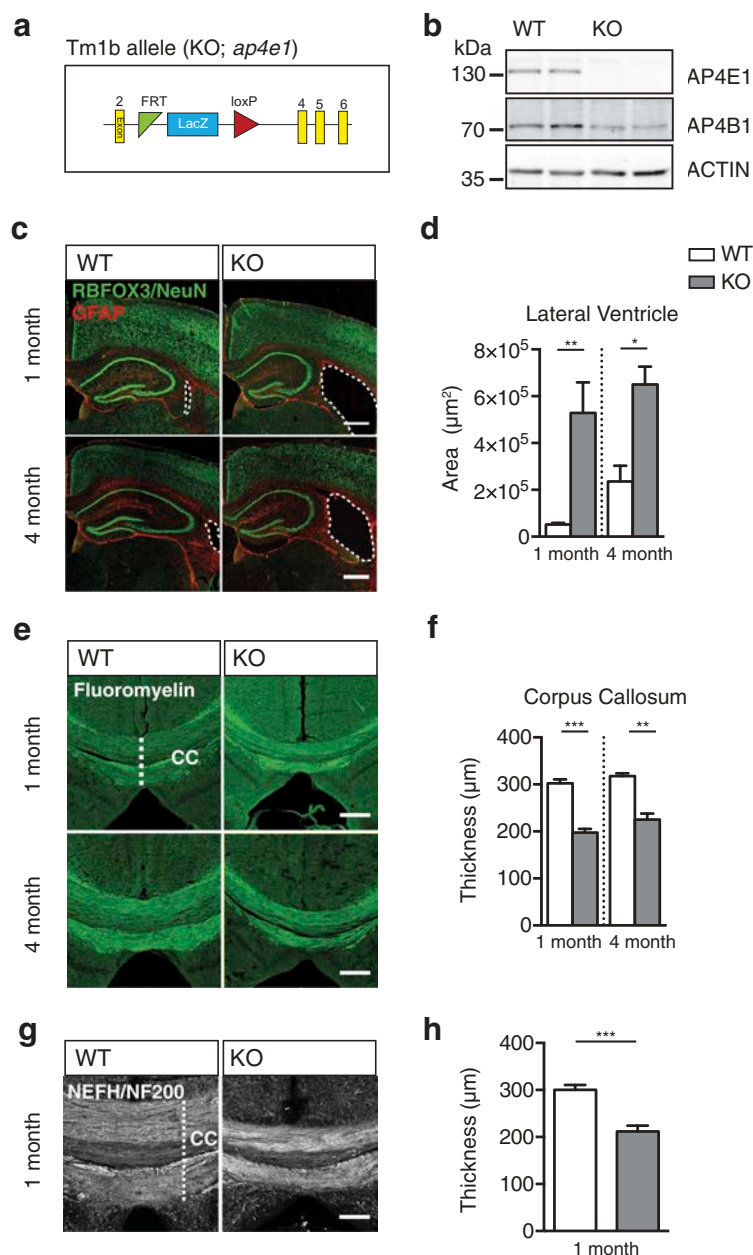
Figure 1. *ap4e1* null mice recapitulate neuroanatomical features of AP-4 deficiency. (**a**) Schematic of promoter driven *ap4e1* KO tm1b allele, showing removal of critical exon 3. (**b**) Western blot prepared from AP-4 line showing total loss of AP4E1 protein and concurrent loss of AP4B1 at protein level in *ap4e1* KO animals. (**c, d**) Sections prepared from animals at 1 and 4 month timepoints stained against RBFOX3/NeuN and GFAP showing lateral ventricular enlargement in KO. Scale bar: 200 µm. (D) Quantification of relative area of lateral ventricle (n = 3/5 animals 1 and 4 months). (**e, f**) Axons stained using FluoroMyelin at 1 month and 4 months showing thinning of corpus callosum tracts in KO. Scale bar: 200 µm. (**f**) Quantification of thickness of corpus callosum (n = 3 animals). (**g, h**) Commissural crossing axons at 1 month, stained against Neurofilament-200 (NEFH/NF200). Scale bar: 100 µm. (**h**) Quantification of thickness of corpus callosum (n = 5 animals). Quantified data expressed as mean ± SEM. Statistical analysis: Two-tailed unpaired Student's t-test, *p < 0.05, **p < 0.01 and ***p < 0.001. CC – corpus callosum.

region of the hippocampus at 4 months, whereas CA3 and DG regions were unaffected (Figure S1(j, l); relative neuronal cell number; CA1: WT 1 ± 0.037, KO 0.85 ± 0.031, p = 0.036; CA3: WT 1 ± 0.076, KO 0.79 ± 0.045, p = 0.082; DG: WT 1 ± 0.073, KO 0.91 ± 0.14, p = 0.59; t-test). To further examine whether there was evidence of neuronal cell death in KO brains, we investigated astrocytic proliferation in regions of the hippocampus. No increase in astrocyte resident GFAP immunoreactivity was evident at 1 month nor 4 months (Figure S1(j,m,n); relative GFAP immunoreactivity; 1 month CA1: WT 1 ± 0.11, KO 0.93 ± 0.098, p = 0.66; 1 month CA3: WT 1 ± 0.086, KO 1.02 ± 0.15, p = 0.91;

1 month DG: WT 1 ± 0.18, KO 0.94 ± 0.068, p = 0.77; 4 month CA1: WT 1 ± 0.055, KO 0.82 ± 0.086, p = 0.15; 4 month CA3: WT 1 ± 0.15, KO 0.97 ± 0.11, p = 0.9; 4 month DG: WT 1 ± 0.083, KO 0.82 ± 0.095, p = 0.22; t-test), indicating that there was no astrogliosis and thus no evidence of neurodegenerative cell death in KO animals. The identification of enlarged lateral ventricles and concurrent thinning of the corpus callosum are highly reminiscent of the characteristic features of AP-4 deficiency patients [7], supporting *ap4e1* KO mice as a model of AP-4 deficiency. We show that these anatomical defects are evident at 1 month and have no progressive element in our model by 4 months of age.

ATG9A trafficking is affected in vivo in *ap4e1* KO mice

We next questioned what essential functions of AP-4 or its cargoes are lost that leads to the specific and severe axonal pathology evident in AP-4 deficiency. Intriguingly, the trans-membrane protein ATG9A has been identified as a putative AP-4 interactor by mass spectroscopy [28] and recent work has highlighted that ATG9A has altered distribution in cell lines lacking AP-4 [26,29]. Given the localization of AP-4 to the TGN, and the necessity of sorting transmembrane ATG9A from the TGN to the distal axonal for local autophagosome generation; we sought to elucidate whether this alteration of ATG9A handling was evident *in vivo*, and thus potentially the mechanism underpinning the pathology in AP-4 deficiency.

Confirming the interaction between ATG9A and the AP-4 complex by Co-IP of ATG9A and AP4E1 from adult mouse brain (Figure 2(a)), we showed that ATG9A is an AP-4 cargo in the brain. Interestingly, in these immunoprecipitation experiments we also noticed that the protein level of ATG9A was robustly increased in our input samples. Preparing lysates from KO hippocampus at 1 month we confirmed the increase in ATG9A protein in KO brain (Figure 2(b,c); relative ATG9A protein: WT 1 ± 0.23, KO 2.33 ± 0.05, $p = 0.0046$; t-test), indicating that not only did ATG9A interact with AP-4, but its protein levels were affected by loss of AP4E1. Indeed, ATG9A was increased at protein level in all regions of the brain investigated (Figure S2(a)), and throughout other tissues including the heart, liver and lung in KO animals (Figure S2(b)). Investigating brain sections from mice at 1 month, we found not only a marked increase in the immunoreactivity of ATG9A in KO brain (Figure 2(d)), but notably that ATG9A appeared to accumulate within distinct structures in neuronal cell layers of the cortex and CA1 regions of KO brain (Figure 2(e,f)). Thus, it is evident that loss of AP-4 function dramatically alters the amount and localization of ATG9A *in vivo* in *ap4e1* KO animals, suggesting that ATG9A function may be affected in AP-4 deficiency.
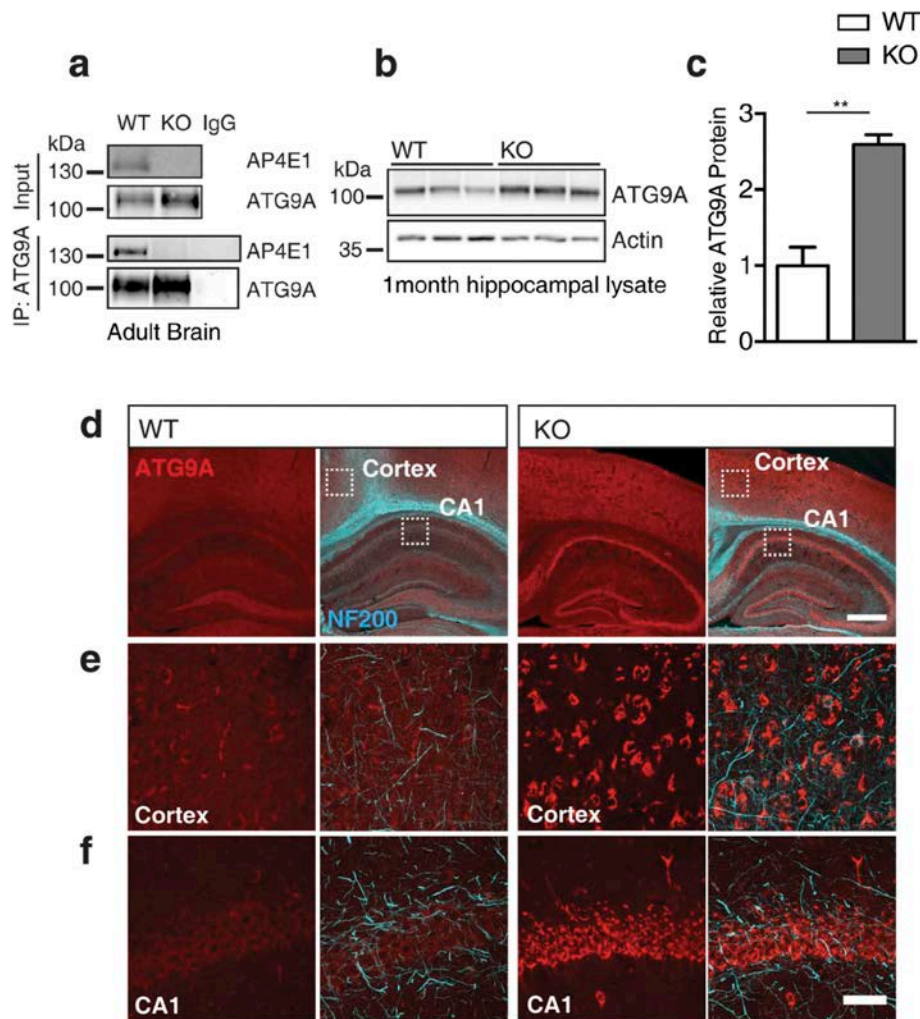

Figure 2. ATG9A handling is affected *in vivo* in *ap4e1* KO mice. (**a**) Endogenous co-immunoprecipitation of AP4E1 with ATG9A from mouse brain, showing interaction between AP-4 and ATG9A (n = 3 independent experiments). (**b**) Western blot of ATG9A in hippocampus at 1 month showing increase in KO animals. (**c**) Quantification of relative ATG9A protein (n = 3 animals). (**d**) Sections prepared from AP-4 line at 1 month stained against ATG9A and NEFH/NF200, showing increased immunoreactivity and accumulation of ATG9A within neuronal cell layers. Scale bars: 200 and 50 µm (**e**) High magnification showing accumulation of ATG9A within cortex and (**f**) CA1 of hippocampus. Scale bar: 20 µm (n = 5 animals). Quantified data is expressed as mean ± SEM. Statistical analysis: Two-tailed unpaired Student's t-test, **p < 0.01.

ATG9A accumulates within the TGN in ap4e1 *KO neurons*

Given the accumulation of ATG9A in KO neurons *in vivo*, we sought to identify the compartment within which ATG9A was retained. To address this, we examined cultured hippocampal neurons, staining against ATG9A and the neuron specific dendritic marker, MAP2 (Figure 3(a)).

Similar to our *in vivo* findings, endogenous ATG9A was increased in KO neurons (Figure 3(a,b)); relative neuronal ATG9A signal: WT 1 ± 0.06, KO 2.8 ± 0.2, $p < 0.0001$; t-test), and other cell types including astrocytes (Figure S3 (a); relative astrocytic ATG9A signal: WT 1 ± 0.11 KO 2.42 ± 0.27, $p < 0.0001$; t-test).
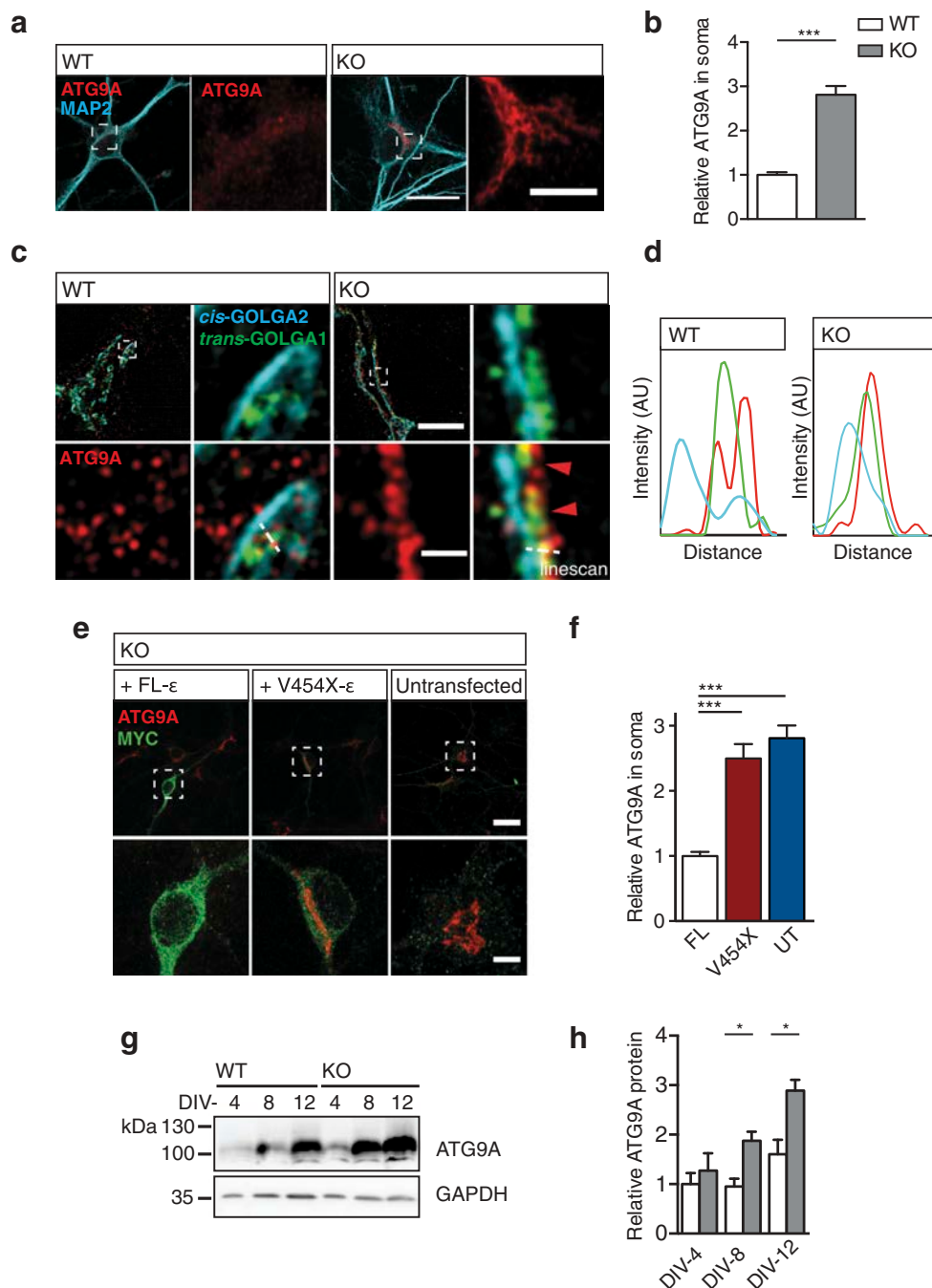

Figure 3. ATG9A accumulates within the TGN in *ap4e1* KO neurons. (**a**) DIV-8 cultured hippocampal neurons stained against ATG9A and MAP2. Inset panels show zoomed regions indicated by dashed boxes of cell body and accumulation of ATG9A. Scale bars: 20 µm; crop: 5 µm. (**b**) Quantification of relative ATG9A in neuronal soma (n = 40/20 neurons WT/KO). (**c**) SIM of DIV-8 cultured hippocampal neurons stained against ATG9A, *cis*-Golgi marker GOLGA2/GM130 and *trans*-Golgi marker GOLGA1/GOLG97. Dashed boxes indicate region in magnified panels, showing ATG9A overlapping GOLGA1/GOLG97 in KO. (**d**) Intensity linescans demonstrate ATG9A retention within the TGN in KO neurons. Scale bars: 5 µm; crop: 0.5 µm (n = 3 experimental repeats). (**e**) Reconstitution of AP-4 complex with expression of MYC-tagged FL AP4E1 and AP-4 deficiency associated AP4E1[V454X] *Ap4e1* constructs (refer to Fig S3B). Dashed boxes indicate region in magnified panels. Scale bars: 5 µm; crop: 2 µm. (**f**) Quantification of relative ATG9A in soma of KO neurons in rescue conditions (n = 26/26/23 neurons FL AP4E1/AP4E1[V454X]/UT). (**g**) Western blot of lysates prepared from cortical neurons after 4, 8 and 12 days in culture probed against ATG9A. (**h**) Quantification of relative levels of ATG9A (n = 3/4 embryos WT/KO). Quantified data is expressed as mean ± SEM. Statistical analysis: (b, h) Two-tailed unpaired Student's t-test, (f) Kruskall-Wallis test, *p < 0.05 and ***p < 0.001.

Given the known localization of AP-4 to the TGN in cell lines, we hypothesized that the sorting of ATG9A may be dependent on AP-4, and thus ATG9A may be retained within the TGN in neurons [26,29,30]. We firstly confirmed neuronal AP-4 localization at the TGN, through staining of endogenous AP4E1 and the TGN resident marker, GOLGA1/Golgin-97/GOLG97 (Figure S3(b)). Following this, we used a super-resolution approach (structured illumination microscopy, SIM) to clarify the ATG9A compartment in KO neurons. Staining the *cis* and *trans* faces of the Golgi network (GOLGA2, and GOLGA1 respectively), we found that ATG9A was specifically retained in the TGN of KO neurons (Figure 3(c,d)). In contrast, ATG9A exhibited a vesicular localization in WT neurons, highlighting the dramatic alteration in ATG9A sorting and localization when AP-4 function is lost.

To confirm that TGN retention of ATG9A arose as a result of failure of AP-4 dependent sorting, we opted to reconstitute the AP-4 complex through exogenous expression of the AP4E1 in KO neurons. We cloned N-terminally tagged AP4E1 (Figure S3(b)), and through transient transfection examined the effect upon ATG9A retention (Figure 3(e)). Reconstitution of the AP-4 complex with a full-length (FL) AP4E1 was able to entirely rescue ATG9A retention, and its levels in KO neurons. However, an AP4E1^{V454X} construct carrying a premature termination mutation identified in an AP-4 deficiency cohort [10], failed to restore ATG9A retention and levels in KO neurons (Figure 3(e,f); relative ATG9A in soma: FL 1 ± 0.06, AP4E1^{V454X} 2.48 ± 0.22, untransfected [UT] 2.81 ± 0.19, p < 0.0001 AP4E1^{V454X}/UT to FL, NS between AP4E1^{V454X} and UT; Kruskall-Wallis). Thus, functional AP-4 assembly is necessary for the TGN exit of ATG9A both *in vivo* and in cultured neurons. Does this retention lead to the increased levels of ATG9A evident in KO animals? Preparing lysates from neurons at DIV-4, DIV-8 and DIV-12 we identify that the level of ATG9A increased progressively over time (Figure 3(g,h); relative ATG9A protein; DIV-4: WT 1 ± 0.22, KO 1.27 ± 0.35, p = 0.55; DIV-8: WT 0.95 ± 0.16, KO 1.88 ± 0.18, p = 0.014; DIV-12: WT 1.6 ± 0.29, KO 2.89 ± 0.22, p = 0.012; t-test), confirming that retention within the TGN results in the accumulation of ATG9A protein.

Defective autophagosome maturation in ap4e1 *KO neurons*

Having elucidated the necessity of AP-4 for the sorting of ATG9A from the TGN, we next sought to understand what effect this retention had on the distribution and function of ATG9A in AP-4-deficient neurons. Staining dendritic and axonal compartments using MAP2 and NEFH/NF200 respectively, we found a specific reduction in the axonal pool of ATG9A (Figure 4(a,b); ATG9A vesicles per 10 μm^2; axonal: WT 5.42 ± 0.32, KO 3.49 ± 0.39, p = 0.0009; dendritic: WT 4.47 ± 0.25, KO 4.18 ± 0.26, p = 0.43; t-test). Notably, dendritic ATG9A in KO was at parity with WT levels, whereas axonal ATG9A was reduced despite the near 3-fold increase in ATG9A within neuronal somas (Figure 3(b)). Together these results identify a clear reduction in the axonal pool of ATG9A, whereas dendritic ATG9A appears unaffected.

Given the known functions of ATG9A, what does this reduction in its axonal distribution mean for the capacity of autophagosome biogenesis within this compartment? To address this we examined nascent autophagosome maturation within the distal-most portions of the axon. Transient transfection of RFP-LC3 (MAP1LC3B), which associates with autophagosomes from early through to late maturation states, provided a robust marker for tracking autophagosomes throughout their lifespan [15]. Maturing autophagosomes initially exhibit bidirectional movement [21] prior to switching to robust dynein driven retrograde movement mediated by MAPK8IP1/JIP1 [31,32]. We found nascent autophagosomes in the distal WT axon to exhibit classical bidirectional motility with net retrograde displacement towards the neuronal soma (Figure 4(c), movies S1 and S2) [21]. In KO axons however, we found a reduction in the number of motile LC3-positive structures (Figure 4(c,d); RFP-LC3 structures; Total: WT 0.88 ± 0.35, KO 1 ± 0.47, p = 0.51; motile: WT 0.43 ± 0.2, KO 0.32 ± 0.16, p = 0.044; Mann-Whitney U), and that these nascent autophagosomes exhibited a reduced propensity to move retrogradely toward the soma, both in absolute retrograde displacement (Figure 4(c,e); absolute retrograde displacement: WT 10.43 ± 1.99 μm, KO 1.139 ± 1.42 μm, p < 0.0001; Mann-Whitney U test) and in individual retrograde runs, whereas anterograde movements were unaltered (Figure 4(f); anterograde run length: WT 15.89 ± 1.28 μm, KO 11.96 ± 1.16 μm, p = 0.686; retrograde run length: WT 25.75 ± 1.59 μm, KO 12.58 ± 1.055 μm, p < 0.0001; Mann-Whitney U). Autophagosomes in KO axons were less motile, with reduced total run length (Figure 4(g); total run length per autophagosome: WT 41.64 ± 2.11 μm, KO 24.54 ± 1.72 μm, p < 0.0001; Mann-Whitney U test), spent more time stationary (Figure 4(h): proportion time stationary: WT 58.75 ± 1.6%, KO 65.82 ± 2.077%, p = 0.0055; Mann-Whitney U) and less time moving retrogradely than in the WT axon (Figure 4(h); time moving anterogradely: WT 17.80 ± 1.17%, KO 18.66 ± 1.55%, p = 0.45; time moving retrogradely: WT 23.45 ± 1.29%, KO 15.52 ± 1.13%, p = 0.0003; Mann-Whitney U test). Importantly, anterograde motility and trafficking of RFP-LC3 structures in KO axons was entirely indistinguishable from that of WT in run lengths, in their proportion of time moving and velocity of individual runs (Figure 4(h); anterograde velocity; WT 0.29 ± 0.026 μm/s, KO 0.27 ± 0.035 μm/s, p = 0.38; mean retrograde velocity; WT 0.42 ± 0.02 μm/s, KO 0.31 ± 0.032 μm/s, p < 0.0001; Mann-Whitney U test). Given that anterograde movements were normal, we conclude that trafficking is not affected *per se*, but that there is a specific defect in retrograde movements of nascent autophagosomes that depends on LC3-lipidation state. Collectively these parameters identify a critical alteration in the maturation state of nascent autophagosomes in KO axons, owing to the reduced provision of axonal ATG9A as a result of the loss of AP-4 function.

We next examined whether alteration to autophagosome maturation impacted upon the autophagic capacity of KO neurons directly through investigation of autophagic flux in cultured neurons. DIV-8 neurons were treated in the presence of 100 nM bafilomycin A$_1$ (BafA$_1$) with 250 nM rapamycin (Rap) or starved in EBSS to induce autophagy (Figure 4(j)),
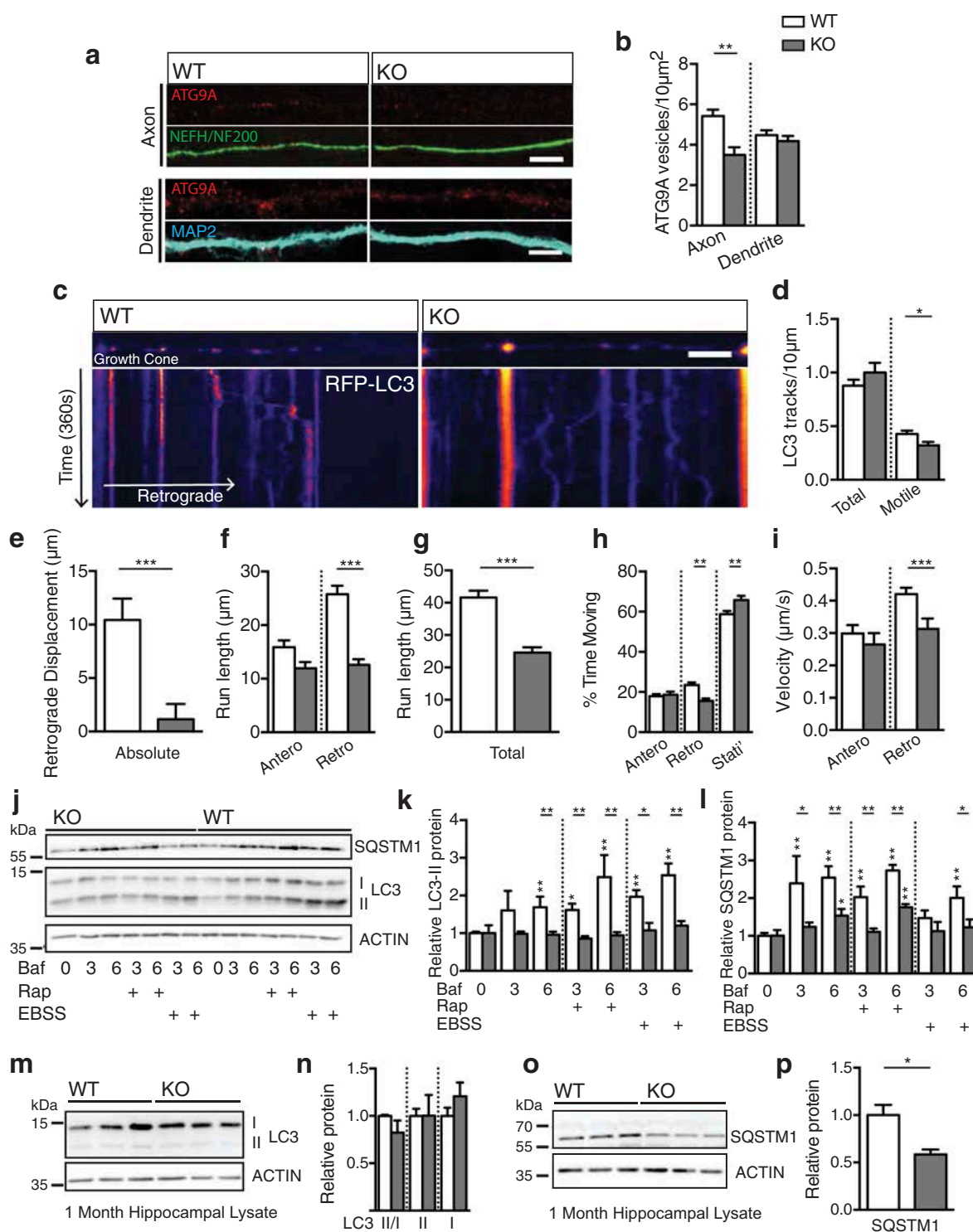
Figure 4. Defective autophagosome maturation in *ap4e1* KO neurons. (**a**) Endogenous ATG9A vesicles in axons and dendrites, stained using NEFH/NF200 and MAP2 markers respectively. (**b**) Quantification of ATG9A vesicles per 10 μm² in axons and dendrites. Scale bar: 5 μm. (Axon; n = 19/12 WT/KO, Dendrite; 28/24 WT/KO). (**c**) Live imaging of nascent autophagosome biogenesis in distal most 75 μm of axon, showing aberrant autophagosome maturation in KO axons. Movies generated over 6 min from cultured hippocampal neurons at DIV-6/7 transfected with RFP-LC3. First frames and kymographs shown with pseudo-coloring of RFP-LC3 signal. X-axis scale bar: 10 μm, Y-axis represents time (1 px/1.5 s). Quantification of; (**d**) Total and motile RFP-LC3 tracks (**e**) absolute retrograde displacement, (**f**) anterograde and retrograde run length per motile autophagosome, (**g**) total distance travelled per motile autophagosome, (**h**) proportion of time spent stationary, moving anterogradely or retrogradely per motile autophagosome and (**i**) velocity of motile autophagosomes. (n = 227/117 motile autophagosomes from 46/36 neurons WT/KO). (Refer to Movies S1 and S2). (**j**) Autophagic flux assay in DIV-8 cultured cortical cultures. Neurons were treated in the presence of 100 nM bafilomycin for durations (in hours) indicated with either EBSS or 250 nM rapamycin to induce autophagy (n = 6 embryos). (**k**) Quantification of relative LC3-II and (**l**) SQSTM1/p62 levels relative to own 0 h control. (**m**) Western blot of lysates prepared from KO hippocampus at 1 month showing no alteration in endogenous LC3 levels nor processing. (**n**) Quantification of LC3-II:I ratio, LC3-II and LC3-I (n = 3 animals). (**o**) Blot of endogenous SQSTM1/p62 in KO hippocampus at 1 month showing reduction in AP-4 KO. (**p**) Quantification of relative protein level of SQSTM1/p62 (n = 3 animals). Quantified data is expressed as mean ± SEM. Statistical analysis: (**b, n and p**) Two-tailed unpaired Student's t-test, (**d – i, k and l**) Mann-Whitney test, *p < 0.05, **p < 0.01 and ***p < 0.001.

and lipidated LC3 and SQSTM1/p62 levels examined by western blotting. A significantly reduced rate of LC3 lipidation was revealed in KO neurons, both basally, and with the induction of autophagy with rapamycin or EBSS (Figure 4(j, k); Table S1). Further, we found slowed SQSTM1/p62 accumulation in KO neurons during these treatments (Figure 4(j, l); Table S1). Interestingly, steady state levels of LC3 were unaffected in cultured KO neurons (Figure 4(j,k)), but also in hippocampal lysates prepared from animals at 1 month (Figure 4(m,n); relative LC3-II:I ratio: WT 1 ± 0.012, KO 0.82 ± 0.13, p = 0.24; relative LC3-II: WT 1 ± 0.077, KO 1 ± 0.22, p = 0.99; relative LC3-I: WT 1 ± 0.089, KO 1.21 ± 0.14, p = 0.29; t-test), in agreement with data recently reported [30]. Further, we found a robust decrease in SQSTM1/p62 in KO animals at 1 month (Figure 4(o,p); relative SQSTM1/p62 protein: WT 1 ± 0.11, KO 0.59 ± 0.05, p = 0.025; t-test), similar to that reported in *ap4b1* null mice [13]. The level of WIPI2 in the KO was at parity with WT animals (Figure S4(a,b); relative WIPI2 protein: WT 1 ± 0.066, KO 1.16 ± 0.12, p = 0.32; t-test) and we found no accumulation of ubiquitinated proteins in KO brain (Figure S4(c,d); relative ubiquitin protein: WT 1 ± 0.14 KO 1.11 ± 0.05, p = 0.49; t-test). Together these results indicate that AP-4 dependent ATG9A sorting is required for proper induction of autophagy in neurons, and to maintain autophagosome generation in the distal axon.

Using endogenous WIPI2 as a marker of early sites of autophagosome generation [33], we investigated autophagosome generation within neuronal somas. We identified a reduction of WIPI2 sites in KO somas (Figure S4(e,f); relative number of WIPI2 puncta: WT 1 ± 0.075, KO 0.74 ± 0.094, p = 0.031; Mann-Whitney U) and a reduction in the number of autophagosomes in KO neuronal somas, as evidenced by a reduction in the number of LC3 puncta (Figure S4(e,f); relative number LC3 puncta: WT 1 ± 0.097, KO 0.71 ± 0.12, p = 0.011; Mann-Whitney U). Indeed, despite this reduction in the numbers of puncta of both WIPI2 and LC3 in the soma, neither exhibited alteration in their size (Figure S4(e,g); size of LC3 puncta: WT 0.084 ± 0.0044 μm², KO 0.078 ± 0.006 μm², p = 0.17; size of WIPI2 puncta: WT 0.084 ± 0.0049 μm², KO 0.094 ± 0.0085 μm², p = 0.42; Mann-Whitney U), and LC3 associated with WIPI2 in KO somas indistinguishably from WT (Figure S4(e,h); proportion LC3 associated with WIPI2: WT 13.5 ± 2.3%, KO 15.3 ± 3.77, p = 0.96; Mann-Whitney U). Thus, sites of biogenesis in the soma as marked by WIPI2 appear functional but are reduced in number leading to a reduction in *de novo* autophagosome generation and thus flux. Together, these results indicate a slowing of autophagosome biogenesis through altered ATG9A sorting in *ap4e1* KO, resulting in fewer autophagosome being generated. However, once generated autophagic degradation in KO neurons appears to be normal.

Axon specific defects in ap4e1 *KO neurons*

Does the reduction in the capacity of autophagosome generation underlie the overt axonal pathology evident in AP-4 deficiency? To answer this, we investigated the integrity of hippocampal neurons in our AP-4 deficiency model. Through transient transfection of GFP we revealed the entire morphology of cultured hippocampal neurons (Figure 5(a)) and examined their integrity after 14 days in culture. We identifed no alteration in dendritic complexity (Figure 5(b); number of intersections per 10 μm sholl: NS; two-way ANOVA), total dendritic length (Figure 5(a,c); total dendritic length: WT 2807 ± 326.1 μm, KO 2730 ± 324.2 μm, p = 0.87; t-test) nor branch number (Figure 5(a,d); total dendritic branches: WT 55.6 ± 4.9, KO 51.3 ± 5.1, p = 0.56; t-test). Using Golgi silver staining of slices prepared from our model at 4 months, we reconstructed entire dendritic arbors of CA1 hippocampal neurons (Figure S5(a)). Similarly to our findings in culture, we found no significant alteration in the complexity of apical (Figure S5(b); apical dendritic length per 10 μm; NS; two way ANOVA) nor basal dendrites (Figure S5(c); basal dendritic length per 10 μm; NS; two way ANOVA), total lengths of both apical and basal dendrites (Figure S5(d); total dendritic length; apical: WT 1529 ± 206 μm, KO 1732 ± 312 μm, p = 0.6; basal: WT 1037 ± 125 μm, KO 1058 ± 133 μm, p = 0.91; t-test), nor numbers of dendritic branches in KO neurons (Figure S5(e); total dendritic branches; apical: WT 15.9 ± 2.1, KO 15.2 ± 2.7, p = 0.85; basal: WT 12.4 ± 1.4, KO 11.3 ± 1.5; p = 0.6; t-test). Together we show that dendritic morphology is unaffected by the loss of AP-4 function both *in vivo* and cultured neurons.

We next examined whether the reduced capacity of axonal autophagosome maturation gives rise to a specific alteration to axonal integrity and thus the axonal pathology of AP-4 deficiency. Investigating cultured neurons at DIV-4, after the specification of the axonal process, we were able to examine the entirety of the axonal extension of an individual neuron. We identified decreased axon length in KO neurons (Figure 5 (e,f): total axonal length; WT 963.5 ± 76.2 μm, KO 679.2 ± 51.9 μm, p = 0.0055; t-test), and in axon branching (Figure 5(e,g): number of axonal branches: WT 5.6 ± 3.2, KO 3.7 ± 1.9, p = 0.023; Mann-Whitney U test). Despite this, at this age in culture nascent dendritic processes of KO neurons were unaltered in their length (Figure 5(e,h); nascent dendritic length: WT 412 ± 37.6 μm, KO 385 ± 19.1 μm, p = 0.5; t-test) and branching (Figure 5(i): nascent dendritic branches: WT 10.4 ± 1.1, KO 10.0 ± 0.77, p = 0.772; t-test), highlighting that axonal extension is specifically affected. This reduction in axonal extension and branching may underpin the ventriculomegaly and thinning of the corpus callosum characteristic of AP-4 deficiency.

Distal generation of axonal swelling, comprised of ER accumulations in AP-4 deficiency

In examining axonal extension in culture, we noted that KO axons exhibited dramatic distal swellings (Figure 5(e,j,k); axonal swellings: WT 1.5 ± 0.61, KO 7.2 ± 1, p < 0.0001; Mann-Whitney U test), that were not seen in dendritic processes. These swellings were also evident in more mature cultures (Figure S5(f,g); axonal swellings per 100 μm: WT 0.23 ± 0.04, KO 1.1 ± 0.2, p = 0.005; t-test). Do these arise directly as a result of reduced axonal ATG9A (Figure 4(a)), or is there contribution from other AP-4 cargoes? To address this, we attempted to artificially drive increased axonal ATG9A through transient exogenous expression of HA-ATG9A (Figure S5(h)). We found that expression of HA-ATG9A for
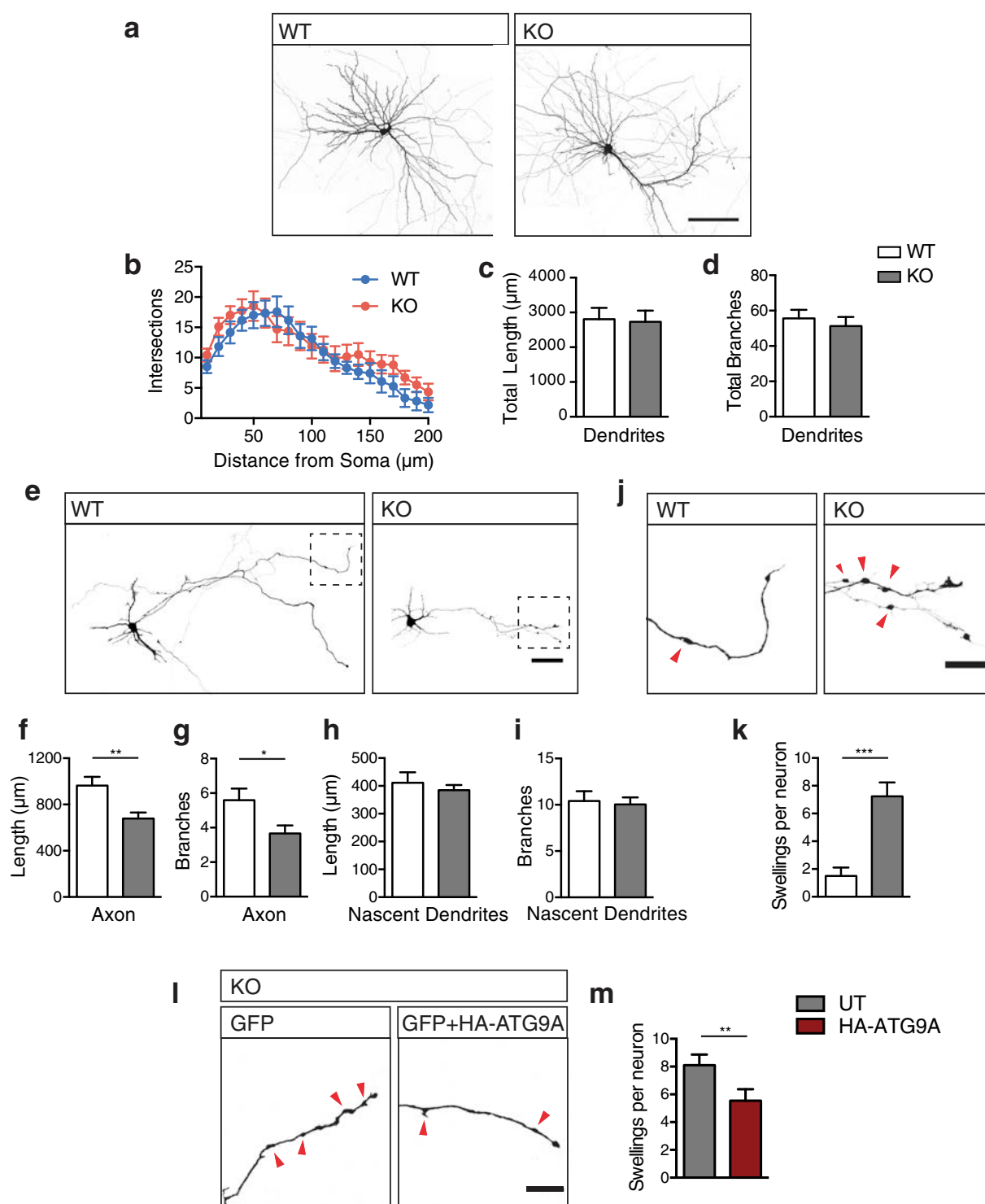
Figure 5. Axon specific defects in *ap4e1* KO neurons. (a) Cultured GFP-filled DIV-14 hippocampal neurons stained against GFP showing neuronal morphology. Scale bar: 100 μm. (b) Analysis of dendritic complexity using 10 μm concentric sholl intersections. Quantification of (c) total dendritic length and (d) total branches per neuron (n = 12/17 neurons WT/KO). (e) Cultured GFP-filled DIV-4 hippocampal neurons stained against GFP revealing neuronal morphology and entire axonal extension from individual neurons. Scale bar: 50 μm. (f) Quantification of total axonal length and (g) axonal branches. (n = 22/18 neurons WT/KO). (h) Quantification of nascent dendritic processes in total length and, (i) total branches (n = 22/27 neurons WT/KO). (j) Inset magnified panel from (e) of distal axonal regions, red arrows indicating axonal swellings. Scale bar: 20 μm. (k) Quantification of number of swellings per neuron (n = 20/17 neurons WT/KO). (l) Distal axonal regions of KO neurons transfected with GFP alone, or in combination with HA-ATG9A, showing a reduction in the number of axonal swellings upon expression of ATG9A, scale bar: 20 μm, (m) Quantification of number of swellings per neuron (n = 29/26 neurons WT/KO). Quantified data is expressed as mean ± SEM. Statistical analysis: (b) Two-way ANOVA with Bonferroni post-hoc test, (c, d, f, h and i) Two-tailed unpaired Student's t-test, (g, k and m) Two-tailed Mann-Whitney U test, *p < 0.05, **p < 0.01 and ***p < 0.001.

2 days was sufficient to increase axonal delivery of ATG9A in KO axons, presumably through inclusion of exogenous ATG9A into other axonally-targeted vesicles (Figure S5(h,i); relative axonal ATG9A: untransfected (UT) 1 ± 0.19 HA-ATG9 4.8 ± 0.68, p < 0.0001; Mann-Whitney U test). As a result of this transient increase in axonal ATG9A, we found a significant reduction in the number of axonal swellings in KO axons (Figure 5(l,m)); swellings per neuron: UT 8.1 ± 0.76,

HA-ATG9 5.5 ± 0.83, p = 0.0075; Mann-Whitney U test), supporting ATG9A as the primary contributor to axonal swelling in KO neurons. Intriguingly, distal axonal swellings have previously been identified in mouse models ablated of ATG5 and ATG7 function [34,35]; ATG5, ATG7 and ATG9A have roles in autophagosome biogenesis post the initiation machinery [14,36], suggesting that axonal swelling may arise where autophagosome biogenesis has been initiated, but is stalled at this stage. To elucidate the nature of axonal swelling in KO neurons, we examined growing axons using long-term imaging of neurons transiently transfected with GFP for durations of 6 h (Figure 6(a), movies S3, S4).

Strikingly, this revealed that swellings are generated *de novo* in *ap4e1* KO axons, emerging either directly from, or in close proximity to the advancing growth cone. These generated swellings were non-motile and persisted for durations in the range of hours (Figure 6(a), movies S3, S4). Interestingly, we found that growing WT axons also have the propensity to generate smaller, more transient swellings (Figure 6(b), S6A movies S5, S6, S7, S8), which disassembled rapidly when compared to those of KO axons.

We next addressed what these *de novo* generated distal swellings comprised of using a correlative light and electron microscopy (CLEM) approach. Identifying individual
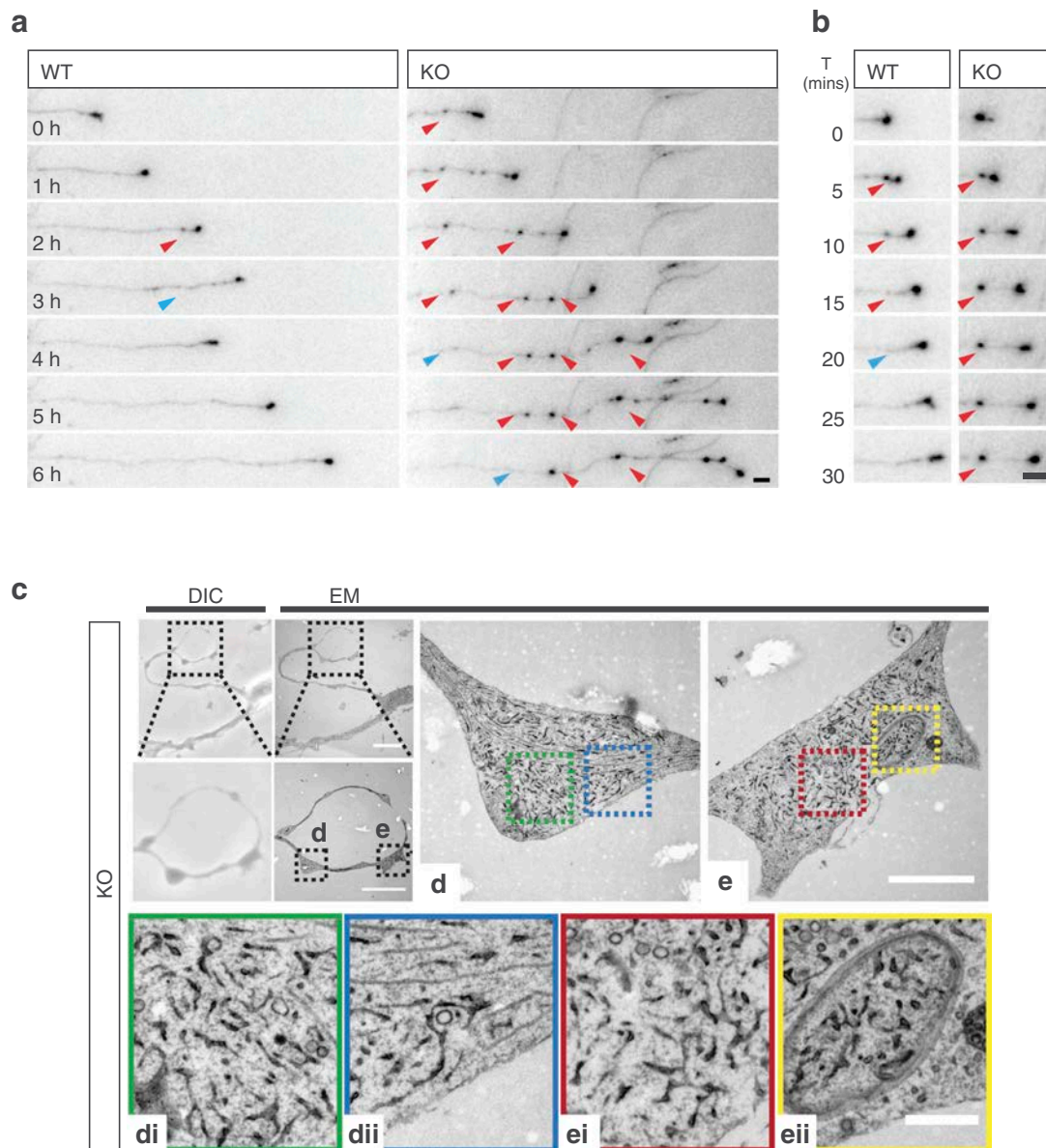

Figure 6. Distal generation of axonal swelling comprised of ER accumulations in AP-4 deficiency. (**a**) Long-term imaging of DIV-6 hippocampal neurons transfected with GFP enabling tracking of growing axons. Axonal swellings are *de novo* generated distally in close proximity to the growth cone in KO axons, indicated by red arrows. Swellings disassemble over time, as indicated by blue arrows (Refer to Movies S3 and S4). Scale bar: 5 μm. (**b**) Swellings formed in WT axons disassemble rapidly, whereas KO swellings persist at their site of deposition for dramatically longer durations (formation indicated by red arrow, disassembly by blue arrow) (Refer to movies S5 to S8). Scale bar: 5 μm. (**c**) Cultured DIV-4 hippocampal neurons were identified by DIC (b) for CLEM, showing correlation of axonal region with swellings, scale bars: 20 μm, 10 μm. Please refer to Fig S6B for WT example. Individual swellings (**d**) and (**e**) shown at higher magnification, scale bar: 2 μm. Cropped regions of (**d**) indicated by blue and green dashed boxes, (**di**) and (**dii**) respectively, showing accumulation of ER within axonal swelling. (**e**) Swelling showing incorporation of ER into double membraned autophagosome within axonal swelling, cropped regions indicated by red and yellow dashed boxes, (**ei**) and (**eii**). Scale bar: 0.5 μm. (n = 3 experimental repeats).

swellings in cultured neurons (Figure 6(c), S6(b)), we found that swellings in KO axons contained aberrantly accumulated ER (Figure 6(b-d)); whereas expanded portions of distal WT axons were largely devoid of ER (Figure S6(b)). Intriguingly, we also identified that these accumulations were incorporated into autophagosomes in KO axons (Figure 6(e), 6Eii, S6(e)). These findings, in combination with our data showing impaired autophagosome generation and autophagic flux, suggest that the accumulation of ER membranes in the axonal swellings of *ap4e1* KO axons is due to the reduced capacity of autophagosome generation where AP-4 dependent axonal ATG9A provision is reduced.

Discussion

Despite mounting evidence implicating impaired autophagy in neurodevelopmental and neurodegenerative disease [37–42], autophagy remains poorly understood mechanistically in the neuron. The post-mitotic nature of the neuron, its extreme architecture, and limited capacity to upregulate autophagy [43] underlies its increased vulnerability to impaired autophagic flux. Here we show that failure of AP-4 mediated ATG9A sorting from the TGN depleted axonal ATG9A, impairing axonal autophagosome biogenesis. This resulted in aberrant accumulation of ER in *de novo* generated distal axonal swellings, likely underpinning the reduction in axonal extension, and neuroanatomical defects evident in our AP-4 deficiency mouse model. We provide evidence toward pathology in AP-4 deficiency arising through this specific reduction in the capacity of autophagic clearance in the axon.

In the present study, we identified neuroanatomical defects mirroring those of AP-4 deficiency patients. We show that these arose developmentally in our *ap4e1* KO mouse; thinning of the corpus callosum and lateral ventricular enlargement were evident by 1 month of age, and did not progress in severity by 4 months. Further, we show that these features did not result from neurodegenerative cell loss, as evidenced by the distinct lack of astrogliosis in KO animals at 4 months. Indeed, gross anatomy of KO mice was normal throughout development and into adulthood, despite their prominent neuroanatomical defects. We find that the thinning of axonal tracts *in vivo* arose as a result of the loss of axonal density; hippocampal neuron cultures revealed reduced axonal extension and branching at the level of the individual neuron. Strikingly however, the complexity and integrity of the dendritic arbors of hippocampal neurons were entirely indistinguishable from WT. The overt axonal pathology in AP-4 deficiency likely results from the specific depletion of axonal ATG9A in KO neurons; ATG9A being dramatically TGN retained where AP-4 is lost. We clarify that this is a feature of AP-4 deficiency by showing that functional AP-4 is required for the exit and sorting of ATG9A in neurons. Reconstitution of the AP-4 complex through exogenous expression of AP4E1 in KO neurons rescued ATG9A retention, whereas a pathological mutation carrying subunit was unable to do so [10]. Together, our findings reveal a critical role for AP-4 in ATG9A sorting in the neuron, highlighting the importance of axonal distribution of ATG9A for the maintenance of axonal integrity.

Maintenance of constitutive distal autophagosome biogenesis in the axon requires that the delivery of newly synthesized cargoes from the soma is tightly balanced with efficient clearance from this compartment. We show here that where the provision of ATG9A to the axon is reduced, the resulting slowing of autophagosome maturation lead to *de novo* generation of distal axonal swellings. These swellings comprised of expanded portions of ER are transient in their nature, being consumed through incorporation into autophagosomes. Swellings are immobile, persisting at their sites of formation for their duration. Thus, their collapse is not accounted for by re-distribution of constituent ER to more distally generated swellings, but likely through incorporation into autophagosomes. Together these results implicate a potential reduction in the capacity of axonal clearance of ER (reticulophagy), in the pathology of our model through the failure of AP-4 mediated ATG9A sorting. During the preparation of this manuscript we became aware of a study also identifying similar neuroanatomical defects in *ap4e1* KO mice [30]. Interestingly, the authors identify that over-expression of aggregate prone n-terminal fragments of huntingtin leads to its accumulation within axonal swellings. The identification herein of the dynamic nature of axonal swelling formation through slowing of autophagosome maturation as a result of reduced provision of axonal ATG9A provides the mechanism for this accumulation, and further adds to the evidence of a reduced capacity of autophagic clearance from the axon.

Distal axonal swellings are emerging as a hallmark in mouse models ablated of proteins critical for early stages of autophagosome biogenesis: *atg5, atg7, atg9a* [25,34,35], and are reported in multiple models of HSP [44–46]. Aberrant accumulation of ER is also found within the axonal swellings *of atg5* null mice [34], and ER expansion is evident where ATG5 or BECN1 are silenced [47]. Moreover, factors critical for ER shaping and remodeling including ATL1, REEP1, SPAST, RTN2 are implicated in over 60% of all HSP cases [48–51], and evidence is emerging that ATL1-dependent remodeling is necessary for selective autophagosomal incorporation of ER [52]. Given that autophagosomes form from ER sites [15,16], and ER resident proteins modulate autophagosome biogenesis [53] it remains to be ascertained in our model whether ER accumulated due to the reduction in the capacity to consume it [47,54,55]; or whether the reduced capacity of autophagosome biogenesis leads to reduced incorporation of ER into the autophagosomal membrane itself. Together, our model adds to the evidence implicating ER shaping, remodeling and additionally reticulophagy in the maintenance of axonal integrity in HSP [51,56–60].

70% of complex HSP patients presenting with progressive spasticity, intellectual impairment and thin corpus callosum are accounted for by mutations in SPG11/spatacsin and ZFYVE26/spastizin [6], both having roles in autophagosome maturation and endolysosomal function [57]. Thin corpus callosum has also been identified in autophagy-related CNS specific KO mouse models including *ulk1 ulk2* double knockout and *atg9a* [25,61], and axonal extension is concomitantly reduced in neurons cultured from these lines [25,56,62,63]. Given this striking similarity to *ap4e1* KO mice, we provide evidence towards thinning of the corpus

callosum in AP-4 deficiency arising developmentally through defective axonal extension as a result of reduced axonal autophagosome biogenesis. Constitutive knockout of *atg5, atg7, atg9a* and *ulk1/2* double knockout leads to peri-natal lethality [64–68], whereas AP-4-deficient mice, and indeed patients, survive into adulthood. Importantly, in the present study we show that autophagosome biogenesis was slowed, but not entirely blocked. Sites of autophagosome maturation as marked by WIPI2 were reduced in the soma, but appear functional, giving rise to fewer autophagosomes. This remaining autophagic capacity was able to sustain dendritic integrity even by 4 months *in vivo*, whereas axonal defects manifested by 4 days in culture. Given the progressive nature of ATG9A accumulation in KO neurons, we speculate that increased ATG9A resident within the TGN membrane leads to its stochastic incorporation into vesicles mediated by other carriers. As a result, sufficient vesicular ATG9A is delivered somatodendritically in KO neurons to maintain effective autophagy within this compartment, whereas axonally destined vesicular delivery is reduced. Indeed, in *C. elegans* where AP-4 is not evolutionarily conserved [69], axonal delivery of ATG9A is also critical for autophagosome biogenesis and axon outgrowth [70].

Interestingly, we were able to partially rescue axonal swelling in KO neurons through overexpression of exogenous ATG9A, which increased axonal delivery presumably through inclusion of ATG9A into other axonally targeted vesicles at the TGN. Thus, promoting axonal ATG9A delivery from the TGN represents an intriguing therapeutic possibility either through increased ATG9A biosynthesis or manipulation of the recently identified AP-4 cargo adaptor RUSC2 [29]. Whilst we cannot entirely rule out whether other unidentified AP-4 cargoes contribute to the alterations in autophagosome generation evident in the axon, the limited AP-4 cargo repertoire emerging in recent studies [29] and the known roles of ATG9A make it the prime candidate in our AP-4-deficiency model.

In sum, we reveal a critical role of AP-4 in sorting ATG9A from the TGN in neurons. Impairment of this function as evident in the AP-4 deficiency model leads to accumulation of ATG9A within the TGN *in vivo* and in culture, leading to a specific reduction to the axonal delivery of ATG9A. As a result, axonal autophagosome biogenesis is defective, likely underlying the axonal defects evident in *ap4e1* KO mice. Together, our findings provide evidence towards a mechanism of pathology in AP-4 deficiency.

Materials and methods

Animals

ap4e1 knockout (*ap4e1*^{−/−}, C57BL/6J-*Ap4e1*[tm1b{KOMP}Wtsi], KO) were generated using the knockout-first tm1b allele system [71] by the International Mouse Phenotyping Consortium (IMPC) MRC Harwell. Animals were maintained under controlled 12:12 h light-dark cycles at a temperature of 20 ± 2°C with food and water ad libitum. Genotyping was carried out using the following primers; AP4E1-5arm-WTF: GCCTCTGTTTAGTTTGCGATG, AP4E1-Crit-WTR: CGTGCACAGACAGGTTTGAT and 5mut-R1: GAACTTCGGAATAGGAACTTCG. Littermate matched

controls were used for primary neuronal cultures and immunocytochemistry experiments. All experimental procedures were in accordance with UCL institutional animal welfare guidelines, and under the UK Home Office licence in accordance with the Animals (Scientific Procedures) Act 1986.

Antibodies and DNA constructs

Antibodies: For immunocytochemistry (ICC), Immunohistochemistry (IHC) and western blotting (WB) antibodies were used with the following dilutions; ACTB/actin (Sigma, A2066; WB: 1:1,000), AP4B1 (Atlas Antibodies, HPA028652; WB: 1:200), AP4E1 (BD Biosciences, 612,018; WB: 1:300, ICC: 1:250), ATG9A (rabbit, STO-219; WB: 1:2000, IF: 1:2000 [72]) and rabbit ATG9A; (Abcam ab108338; WB: 1:1000, IF: 1:1000), ATG9A (Hamster 14F2 8B1; IF: 1:500 [72]), GAPDH (Abcam ab8245; WB: 1:10,000), GFAP (Dako, Z0334; ICC: 1:300), GFP (Nescalai Tesque 04404–84; ICC: 1:1000), GOLGA2/GM130 (BD Biosciences 610,822; ICC: 1:1000), GOLGA1/Golgin-97 (Cell Signaling Technology, 13,193; ICC: 1:250), HA (12CA5 hybridoma; WB: 1:200, ICC: 1:100), LC3B (Abgent AP1802a; WB: 1:250), LC3B (Cell Signaling Technology D-11 3868S; IF: 1:250), MAP2 (Synaptic Systems 188–004, ICC: 1:500), RBFOX3/NeuN (Chemicon International MAB377; IHC: 1:300), NEFH/NF200 (Abcam ab4680; IF: 1/500 IHC: 1/500), MYC (NeuroMab 9E10; WB: 1:100, ICC: 1:100), ubiquitin (Enzo Biosciences FK2; WB: 1/500) and WIPI2 (Ms Monoclonal; WB: 1:250, ICC: 1:250 [73]). HRP-conjugated anti-mouse/rabbit antibodies were used for western blotting at 1:10,000 (Jackson Laboratories, 1,706,516/1,706,515). Alexa Fluor-conjugated secondary antibodies for ICC, IHC and super-resolution imaging were used as follows; anti-chicken 405 and 647 (Abcam, ab175675 and ab150175) anti-guinea pig 405 and 647 (Abcam, ab175678 and ab150187 anti-mouse 488 and 647 (Jackson immunoresearch, 715–545-151-JIR and 715–605-151), anti-rabbit 555 and 647 (Abcam, ab1500074 and ab150063). Anti-Armenian hamster conjugated to Cy3 was used for super-resolution imaging (Jackson immunoresearch, 127–165-160).

DNA Constructs: CAG-GFP (Addgene, 16,664; deposited by F Gage), pmRFP-LC3 [74] (Addgene, 21,075; deposited by T Yoshimori). Full-length N-terminally MYC-tagged AP4E1 was generated by cloning the coding sequence of *Ap4e1* (Cusabio; CSB-CL890772HU, cDNA clone MGC: 163,338) into pRK5-Myc [75]. AP4E1^{V454X}-ε was then generated by reverse mutagenesis methods replicating the reported 2 nucleotide insertion leading to frameshift induced premature stop at V454 [10]. HA-ATG9A was kindly gifted by the Tooze laboratory [72].

Brain lysate preparation for co-immunoprecipitation

Lysate Preparation: Brains to be used for co-immunoprecipitation were removed from animals and homogenized in ice cold HEPES buffer (50 mM HEPES [GIBCO, 15,630–056], 0.5% Triton X-100 [Sigma Aldrich T-8787], 150 mM NaCl [Fisher Scientific, 11,904,061], 1 mM EDTA [Sigma Aldrich E5134], 1 mM PMSF [Panreac AppliChem,

A0999,0025], 50 μl antipain, pepstatin and leupeptin [Peptide Institute, 4062, 4367, 4041] in ddH$_2$O). Lysate was solubilized by rotation for 2 h at 4°C prior to ultracentrifugation at 80,000 g for 40 min. Protein content determined using a BCA assay kit (Promega, PI-23,225).

Co-Immunoprecipitation: Brain lysate (5 mg) was incubated with 1 μg of antibody in HEPES buffer for 12 h at 4°C with rotation, and 1 μg IgG control (rabbit; Thermo Fisher, 02–6102) was incubated with WT brain lysate in tandem. Input samples were incubated in the same manner at all steps as immunoprecipitation samples. Protein A agarose beads (Generon, PC-A25) were added for 4 h to IP samples, beads washed in HEPES buffer and suspended in protein sample buffer (150 mM Tris, pH 8 [Sigma Aldrich, 93,352], 6% SDS [Fisher Scientific, 10,090,490], 300 mM DTT [Melford, MB1015], 30% glycerol [Fisher scientific, 10,021,083], 0.3% bromophenol blue [Sigma Aldrich, B0126]) and heated to 95°C for 7 min prior to SDS-Page and western blotting.

Brain and tissue lysate preparation; SDS-PAGE and western blotting

Lysate Preparation: Brains and tissues to be used for western blotting were removed from animals and snap frozen at −80°C. For preparation of lysates, brains and tissues were defrosted, relevant regions dissected and kept on ice throughout. Tissue was homogenized by sonication in lysis buffer (50 mM HEPES, pH 7.5, 0.5% Triton X-100, 150 mM NaCl, 1 mM EDTA, 1 mM PMSF, antipain/pepstatin/leupeptin as above), and debris pelleted at 38,000 x g for 10 min at 4°C. Lysate protein content was determined using a commercial BCA assay kit (Promega, PI-23,225) and samples denatured for 7 min at 95°C in protein sample buffer. Samples were stored at −80°C.

SDS-PAGE and western blotting: Protein lysate (20–40 μg) was separated by SDS-PAGE using Xcell Minicell II systems (Invitrogen, EI0002) and transferred onto nitrocellulose (GE healthcare, 10,600,003) or 0.45-μm pore PVDF (for LC3; GE Healthcare, 11,330,744). Membranes were blocked in milk (4% non-fat milk powder [Marvel, S0942], 0.05% Tween-20 [National Diagnostics, EC-607]) in PBS (137 mM NaCl [Fisher Scientific, 10,428,420], 2.7 mM KCl [Merck, 104,936], 10 mM Na$_2$HPO$_4$ [Merck, 106,586], 1.8 mM KH$_2$PO$_4$ [Merck, 529,568]), pH 7.4, 3% BSA [Sigma Aldrich, 05482-100G] for LC3 and AP4E1 for 1 h and incubated with primary antibodies at empirically determined dilutions as above overnight with agitation at 4°C. Membranes were then washed, secondary HRP-conjugated antibodies applied in milk at 1:10,000 and after a final washing steps bands visualized by application of ECL substrate (Millipore Luminata Crescendo, WBLUR0500) and imaging using a CCD based system (Quant LAS 4000, GE Healthcare). Densitometric analysis was performed using FIJI software (NIH).

Beta-galactosidase staining of embryos, brains and sections

Embryos and embryonic brains: Embryos to be stained with X-gal were removed at developmental stages E12.5, E13.5 and E15.5. Due to impermeability of embryos at E15.5, brains were removed from animals and stained similarly to whole embryos. Embryos and brains were washed in PBS briefly, fixed in 4% PFA (Sigma-Aldrich, P6148-500G) for 90 min and stained at room temperature (RT) for 18 h (5 mM EGTA [Sigma-Aldrich, E4378], 2 mM MgCl$_2$ [Melford, M0535], 0.2% gluteraldehyde [Sigma-Aldrich, G5882], 0.4% PFA, 0.01% DOC [Sigma-Aldrich, D6750], 0.02% NP40 [Millipore Calbiochem, 492,018] in PBS). Subsequently, embryos and brains were washed in PBS and serially dehydrated in increasing concentrations of EtOH (50–100%), and stored at 4°C in 100% EtOH.

Adult brain X-Gal staining: Brains were removed from adult mice and fixed similarly to embryos. Fixed brains were washed, and 100-μm sections prepared using a vibratome (Leica). Sections were mounted onto glass slides, stained, washed and dehydrated similarly to embryonic brains. Sections were mounted with cover glass using Mowiol (Calbiochem, 475,904) medium and stored at 4°C.

Golgi-cox silver staining and neuronal reconstruction

Golgi staining: Neurons in intact brains were stained using the Rapid GolgiStain Kit [FD Neurotechnologies, PK401]. Staining was carried out as per manufacturer's protocols, briefly; removed brains were impregnated with solution in darkness, stained for 2 weeks, and sectioned using a vibratome (Leica) at a thickness of 100 μm. Slices were transferred to gelatin coated slides (0.3% gelatin [Sigma-Aldrich, G9391], 0.05% chromium potassium sulfate [Acros Organics, 222,521,000] in H$_2$O) and dried. Dried slices were stained using kit working solutions, dehydrated using increasing concentrations of EtOH and cleared using xylene (Fisher scientific, 10,385,910) prior to mounting with per mount (Fischer scientific, 15,832,544) and covering with coverglass.

Neuronal reconstruction: Prepared sections were imaged, traced and analyzed using Neurolucida software (MBF Bioscience). Neurons were traced live in X, Y and Z dimensions using and reconstructed and analyzed using inbuilt sholl-analysis tools within Neurolucida.

Hippocampal and cortical neuronal culture and transient transfection

Hippocampal/Cortical neuronal cultures: Hippocampal/Cortical cultures from crosses of heterozygous *Ap4e1* animals were prepared from embryos at E16 as described previously [76–78]. Briefly, hippocampi and cortices were dissected in ice-cold HBSS [Gibco, 14,180–046] supplemented with 10 mM HEPES, pH 7.5 and incubated in 0.25% trypsin (Sigma-Aldrich, T4799) for 15 min prior to trituration. Dissociated neurons were seeded onto poly-L-lysine (Sigma-Aldrich, P2636; 0.5 mg/ml in 0.1 M borate buffer, pH 8)-coated coverslips at a density of 30–50,000/cm^2 in attachment medium (10% horse serum [Gibco, 26,050,088], 10 mM sodium pyruvate [Gibco, 11,360,070], 0.6% glucose in MEM [Gibco, 31,095,029]). Attachment media was replaced the next day with Maintenance medium (2% B27 [Gibco, 17,504–044], 2 mM glutamax [Gibco, 35,050,061], 100 μg/ml Penicillin/Streptomycin [Gibco, 15,140–163] in Neurobasal

[Gibco, 21,103,049]). Fifty percent of the maintenance medium was replaced every 4 days after the first week in culture to maintain cell health.

Transient transfection: Neurons were transfected using lipofectamine 2000 (Invitrogen, 1,168,019) according to manufacturer's protocols, at an empirically determined ratio of lipofectamine to DNA per construct used (GFP 0.25 μg, RFP-LC3 0.25 μg, HA-ATG9A 1 μg and *Ap4e1* constructs 1 μg per 2 coverslips, 1 μl lipofectamine per coverslip). Neurons were left to express constructs for 2–3 days prior to further experimentation.

Immunocytochemistry, immunohistochemistry and fluorescent dyes

Immunocytochemistry (ICC): Hippocampal cultures on coverslips were fixed prior to staining with 4% PFA with 4% sucrose (Sigma-Aldrich, S9378) in PBS for 7 min at RT. Post-fixation coverslips were washed in PBS and permeabilized for 10 min in blocking solution (1% BSA, 10% horse serum, 0.1% Triton X-100 in PBS). Primary antibodies were diluted in blocking solution at empirically determined dilutions and applied for 1 h at RT in a dark humidified chamber. Coverslips were washed in PBS and fluorescent-conjugated secondary antibodies as listed above were used at a concentration of 1:1000 and applied for 1 h at RT in a humidified chamber. Coverslips were mounted in ProLong Gold mounting medium (Invitrogen, P36930) and allowed to dry overnight at RT prior to imaging.

Immunohistochemistry (IHC): Brains were removed from animals and fixed by immersion in 4% PFA for 24 h at 4°C, cryoprotected in 30% Sucrose-PBS for 24 h and frozen and stored at −80°C. Frozen brains were embedded into OCT compound (Tissue-Tek, 4583) and serially cryosectioned into 30-μm sections in a Bright OTF-AS Cryostat (Bright Instruments) and stored at −20°C prior to staining in cryoprotective solution (30% glycerol, 30% PEG in PBS). IHC staining was performed with free-floating sections at RT with gentle agitation. Sections were washed and permeabilized in PBS-Tx (0.5% Triton X-100 in PBS) for 30 min prior to blocking in IHC blocking solution (3% BSA, 10% FBS, 0.2 M glycine [Fisher scientific, 10,080,160] in PBS-Tx) for 3 h. A second block was applied for 3 h as prior but with the addition of goat anti-mouse Fab-fragment (Jackson Immunoresearch, 115–007-003) at 50 μg/ml to reduce endogenous background when using antibodies raised in mouse. Sections were washed for 30 min and primary antibodies applied at concentrations as listed above in IHC blocking solution for 4 h. Sections were washed for 30 min and fluorescent antibodies applied for 4 h prior to a final wash and mounting onto glass slides with Mowiol medium. Slides were allowed to dry at RT overnight prior to imaging.

Fluorescent dyes: Free-floating sections as prepared for IHC were washed in PBS-Tx, and incubated at RT with gentle agitation for 4 h with FluoroMyelin Green (Invitrogen, F34651; 1:400) in blocking solution. Sections were washed for 3 × 30 min prior to mounting onto glass slides with Mowiol. Slides were allowed to dry at RT overnight prior to imaging.

Autophagic flux assays

Cortical neurons were cultured onto 6-well dishes at a density of 80,000 per well and maintained in neuronal maintenance media as described. At DIV-8, cells were treated with 100 nM bafilomycin A_1 (VWR, 196,000), in conditioned maintenance media, or additionally with 250 nM rapamycin (Cayman Biotech, 53,123–88-9) for durations as indicated. EBSS conditions were first washed once with EBSS (to remove excess serum form maintenance media) followed by addition of EBSS + bafilomycin A_1. After treatment, cells were washed once in EBSS and collected directly by addition of sample buffer. Samples were sonicated, boiled and subjected to SDS-PAGE and western blotting as described.

Correlative light and electron microscopy

Cells were cultured on gridded coverslip-bottomed dishes (MatTek, P35G-1.5–14-CGRD) to facilitate correlation between light and electron microscopy and processed for the latter as described in [79]. Brightfield images of regions of interest were acquired using an Olympus BX50WI upright microscope and TEM images acquired using an FEI tecnai G2 Spirit transmission electron microscope and an Olympus SIS Morada CCD camera.

Live imaging, autophagosome motility analysis and long-term live imaging

Live Imaging of autophagosome maturation: For autophagosome maturation and motility experiments, cultured hippocampal neurons were transfected at DIV-4 with RFP-LC3 as described, to be imaged at DIV 6–7. Imaging was carried out under perfusion with ACSF (124 mM $NaCl_2$, 2.5 mM $CaCl_2$ [VWR, 190464k], 2.5 mM KCl [Sigma-Aldrich, P9541], 1 mM $MgCl_2$ [Melfords, M0535], 10 mM D-glucose [Fisher scientific, G/0500/53], 25 mM $NaHCO_3$ [Sigma-Aldrich, S5761], 1 mM Na_2HPO_4, pH 7.4) at 37°C with a flow-rate of 1–2 ml/min and aerated (5% CO_2, 95% O_2) throughout. Growth-cones were identified and the RFP-LC3 signal in the distal most 75 μm of axon captured using a EM-CCD camera system (iXon, Andor technology) mounted to an Olympus microscope (BX60M) with a 60x objective, as described previously [75]. A mercury arc lamp with filtering provided excitation of the RFP fluorophore (Cairn Research). Images were acquired using MicroManager (Opensource, Micro-manager.org) [80] for 6 min at 1 frame every 1.5 s.

Autophagosome motility analysis: Movies generated from distal axons used to generate kymographs using the 'Multiple Kymograph' plugin. Resulting kymographs represent autophagosome motion as time on the Y axis (1.5 s/px) and distance on the X (0.1333 μm/px). Trajectories were manually tracked and analyzed using an in-house MATLAB script. Briefly, the motion of an autophagosome is possible to define precisely by the positional change from co-ordinates x^1/y^1 to x^2/y^2. Calculating all of the individual trajectory changes for an individual autophagosome's track we were able to ascertain; velocity, proportion of time spent moving, directionality

etc. Per track, portions of time spent moving at less than 0.05 μm/s were classed as stationary.

Long-term live imaging: Neurons were seeded onto Poly-L-Lysine coated 96-well plates (Ibidi, 89,626), transfected with CAG-GFP at DIV-3/4 as described and imaged 2 days later using an ImageXpress Micro XLS imaging system (MolecularDevices) with environmental control. Timelapse movies were taken from up to 16 different fields per well at a rate of 1 frame every 5 min for 6 h (72 frames). Eight-bit images were recorded, movies generated using a custom ImageJ plugin, and regions with growing axons cropped for analysis.

Structured illumination imaging (SIM)

SIM was performed on a commercially developed Zeiss Elyra PS.1 inverted microscope using a Zeiss 63x oil objective lens (NA: 1.4) and pco.edge CMOS camera and ZEN Black software (Zeiss) as described previously [78,79]. Images were captured using SIM paradigms (34-μm grating, 3 rotations and 5 lateral shifts) and processed using the SIM reconstruction module within ZEN Black with default theoretical PSF and other settings. Shifts between acquired channels were corrected for using 100-nm Tetraspeck fluorescent microspheres (Invitrogen, T7279).

Image analysis

All imaging and image analysis techniques were performed blinded. All WT and KO embryos generated per genotype were used, and cell numbers kept consistent between embryos rather than genotypes (as a result of blinding at acquisition stage). Between 3 and 6 images were taken per condition and samples sizes kept consistent across experimental techniques. All microscopic imaging unless stated otherwise was using an upright Zeiss LSM700 confocal microscope. Images were digitally captured using Zen 2010 Software (Zeiss), using oil immersion objectives: 63x; 1.4 NA, 40 × 1.3 NA and air objectives; 10 × 0.3 NA, 5 × 0.16 NA.

Brain measurements: Quantification of the thickness and lengths of axonal tracts was performed manually using Fiji. At least 2 brain sections per animal were analyzed and the mean measurement used as the representative value.

Axonal Length, Branching and swellings: GFP-filled neurons at DIV-4 were fixed and imaged using a 40x objective, and images stitched using 'MosaicJ' or 'Pairwise stitching' [81] plugins in FIJI as required. Entire lengths of axons including all branches was measured manually using FIJI, and branches quantified excluding any process below 20 μm. Axonal swellings were defined as a compartment > 2x the width of the axon shaft, and numbers counted manually. For DIV-14 swellings quantification, fields of view were captured, total axonal length and numbers of swellings present within the field captured were counted to determine swellings per 100 μm of axon.

Dendritic morphology and complexity: DIV-14 GFP-filled neurons were fixed and imaged, and images stitched as previously described where necessary. Dendritic morphology was reconstructed using Neuronstudio (CNIC) and inbuilt analysis tools used to ascertain total dendritic length and branches

as described previously [75,82]. Sholl analysis of intersections was performed using the 'Simple Neurite Tracer' plugin in FIJI, with a sholl radius of 10 μm. Images were stitched where necessary.

Nascent dendritic length and branching: DIV-4 GFP filled neurons were reconstructed using Neuronstudio and total length and branches of nascent dendritic processes per neuron quantified using inbuilt tools.

ICC quantification of total fluorescent signal: For quantification of dendritic and axonal vesicle numbers, regions positive for compartment markers (MAP2 and NEFH/NF200 respectively) were outlined manually per image, and values normalized to area. Total fluorescence of ATG9A was quantified by outlining the cell soma and measuring total fluorescence using inbuilt FIJI tools. GFAP immunoreactivity was quantified using total fluorescence per hippocampal region.

Neuronal cell number quantification: For neuronal cell number measurements, sections stained against RBFOX3/ NeuN were imaged and RBFOX3/NeuN-positive cells counted. For relative cortical neuronal density, 100-μm wide columns of the cortex were cropped and counted (2 sections per animal); for regions of the hippocampus, 30 μm regions were cropped and counted (2 sections per animal).

Puncta size, number and association: For quantification of sizes and numbers of puncta, DIV-8 hippocampal neurons were stained using relevant antibodies and processed and imaged as described. Puncta size and number were analyzed using in-built tools within Metamorph software (Molecular Devices). Signals for LC3 and WIPI2 were blindly thresholded over entire sample sets, puncta manually segmented where required (when overlapping or in indiscernible proximity when threshold applied) and puncta number and area quantified with an exclusion cut-off set at 0.05 μm^2. Puncta association (WIPI2 and LC3) was quantified using inbuilt integrated co-localization tool.

Statistical analysis

Results were analyzed using Graphpad Prism 6 (Graphpad Software Inc). Data is presented as mean ± SEM. Where normalized, values are presented relative to the average of control values unless stated otherwise. Data was tested for normality prior to statistical testing, and appropriate statistical tests used. For differences between 2 groups statistical significance was determined using unpaired two-tailed Student's t-tests when parametric. Two groups were tested using two-tailed Mann-Whitney U tests where at least one group was non-parametric. For 3 or more groups, statistical significance was determined by two-way ANOVAs with Bonferroni post-hoc testing where data was parametric. Kruskall-Wallis H tests were used for comparison of three or more groups where at least 1 group was non-parametric. Significance is represented as; p* < 0.05, p** < 0.01 and p*** < 0.001.

Acknowledgments

ORCID

Davor Ivankovic ⓘ http://orcid.org/0000-0002-4881-9096
James Drew ⓘ http://orcid.org/0000-0002-2864-7987
Flavie Lesept ⓘ http://orcid.org/0000-0002-7398-9652
Guillermo López Doménech ⓘ http://orcid.org/0000-0002-3114-2082
Sharon A. Tooze ⓘ http://orcid.org/0000-0002-2182-3116
Josef T. Kittler ⓘ http://orcid.org/0000-0002-3437-9456

References

[1] Robinson MS. Adaptable adaptors for coated vesicles. Trends Cell Biol. 2004;14:167–174.
[2] Dell'Angelica EC, Klumperman J, Stoorvogel W, et al. Science. 1998;280:431–434.
[3] Mitsunari T, NakatsuF, ShiodaN, et al. Clathrin adaptor AP-2 is essential for early embryonal development. Mol Cell Biol. 2005;25:9318–9323.
[4] Hardies K, May P, Djémié T, et al. . . Hirst, J Hum Mol Genet. 2015;24:2218–2227.
[5] Abou Jamra R, Philippe O, Raas-Rothschild A, et al. Adaptor Protein Complex 4 Deficiency Causes Severe Autosomal-Recessive Intellectual Disability, Progressive Spastic Paraplegia, Shy Character, and Short Stature. Am J Hum Genet. 2011;88:788–795.
[6] Tesson C, Koht J, Stevanin G. Hum Genet. 2015;134:511–538.
[7] Abdollahpour H, Alawi M, Kortüm F, et al. Eur J Hum Genet. 2015;23:256–259.
[8] Verkerk AJMH, Schot R, Dumee B, et al. Mutation in the AP4M1 Gene Provides a Model for Neuroaxonal Injury in Cerebral Palsy. Am J Hum Genet. 2009;85:40–52.
[9] Moreno-De-Luca A, Helmers SL, Mao H, et al. Adaptor protein complex-4 (AP-4) deficiency causes a novel autosomal recessive cerebral palsy syndrome with microcephaly and intellectual disability. J Med Genet. 2011;48:141–144.
[10] Najmabadi H, Hu H, Garshasbi M, et al. Nature. 2011;478:57–63.
[11] Hirst J, Bright NA, Rous B, et al. Mol Biol Cell. 1999;10:2787–2802.
[12] Dell'Angelica EC, Mullins C, Bonifacino JS. J Biol Chem. 1999;274:7278–7285.
[13] Matsuda S, Miura E, Matsuda K, et al. Accumulation of AMPA receptors in autophagosomes in neuronal axons lacking adaptor protein AP-4. Neuron. 2008;57:730–745.
[14] Mizushima N, Yoshimori T, Ohsumi Y. Annu Rev Cell Dev Biol. 2011;27:107–132.

[15] Maday S, Holzbaur ELF. Autophagosome biogenesis in primary neurons follows an ordered and spatially regulated pathway. Dev Cell. 2014;30:71–85.
[16] Ktistakis NT, Tooze SA. Digesting the expanding mechanisms of autophagy. Trends Cell Biol. 2016;26:624–635.
[17] Galluzzi L, Baehrecke EH, Ballabio A, et al. Embo J. 2017;36:1811–1836.
[18] Vijayan V, Verstreken P. J Cell Biol. 2017;216:1895–1906.
[19] Ariosa AR, Klionsky DJ. Autophagy. 2015;11:193–194.
[20] Cai Q, Lu L, Tian J-H, et al. Snapin-regulated late endosomal transport is critical for efficient autophagy-lysosomal function in neurons. Neuron. 2010;68:73–86.
[21] Maday S, Wallace KE, Holzbaur ELF. J Cell Biol. 2012;196:407–417.
[22] Okerlund ND, Schneider K, Leal-Ortiz S, et al. Neuron. Vol. 93. Maryland Heights (MO): Publisher name: Cell Press; 2017. p. 897–913.e7.
[23] Webber JL, Tooze SA. New insights into the function of Atg9. FEBS Lett. 2010;584:1319–1326.
[24] Karanasios E, Walker SA, Okkenhaug H, et al. Nat Commun. 2016;7:12420.
[25] Yamaguchi J, Suzuki C, NanaoT, et al. Autophagy. 2018;14:764–777.
[26] Mattera R, Park SY, De Pace R, et al. Proc Natl Acad Sci USA. 2017;114:E10697–E10706.
[27] Dickinson ME, Flenniken AM, Ji X, et al. International Mouse Phenotyping Consortium; Jackson Laboratory; Infrastructure Nationale PHENOMIN, Institut Clinique de la Souris (ICS); Charles River Laboratories; MRC Harwell; Toronto Centre for Phenogenomics; Wellcome Trust Sanger Institute; RIKEN BioResource Center; MacArthur, D. G.; Tocchini-Valentini, G. P.; Gao, X.; Flicek, P.; Bradley, A.; Skarnes, W. C.; Justice, M. J.; Parkinson, H. E.; Moore, M.; Wells, S.; Braun, R. E.; Svenson, K. L.; de Angelis, M. H.; Herault, Y.; Mohun, T.; Mallon, A.-M.; Henkelman, R. M.; Brown, S. D. M.; Adams, D. J.; Lloyd, K. C. K.; McKerlie, C.; Beaudet, A. L.; Bućan, M.; Murray, S. A. Nature. 2016;537:508–514.
[28] Mattera R, Guardia CM, Sidhu SS, et al. J Biol Chem. 2015;290:30736–30749.
[29] Davies AK, ItzhakDN, Edgar JR, et al. Nat Commun. 2018;9:3958.
[30] De Pace R, Skirzewski M, Damme M, et al. Altered distribution of ATG9A and accumulation of axonal aggregates in neurons from a mouse model of AP-4 deficiency syndrome. PLoS Genet. 2018;14: e1007363.
[31] Fu -M-M, Nirschl JJ, Holzbaur ELF. LC3 binding to the scaffolding protein JIP1 regulates processive dynein-driven transport of autophagosomes. Dev Cell. 2014;29:577–590.
[32] Cheng X-T, Zhou B, Lin M-Y, et al. Autophagy. 2015;11:1434–1436.
[33] Dooley HC, Razi M, Polson HEJ, et al. Mol. Cell. 2014; (55):238–252.
[34] Nishiyama J, Miura E, MizushimaN, et al. Aberrant Membranes and Double-Membrane Structures Accumulate in the Axons of Atg5-Null Purkinje Cells before Neuronal Death. Autophagy. 2007;3:591–596.
[35] Komatsu M, Wang QJ, Holstein GR, et al. Proc Natl Acad Sci USA. 2007;104:14489–14494.
[36] Orsi A, Razi M, Dooley HC, et al. Mol Biol Cell. 2012;23:1860–1873.
[37] Nixon RA, Wegiel J, Kumar A, et al. J Neuropathol Exp Neurol. 2005;64:113–122.
[38] Lee S, Sato Y, Nixon RA. J Neurosci. 2011;31:7817–7830.
[39] Alvarez-Erviti L, Rodriguez-Oroz MC, Cooper JM, et al. Chaperone-mediated autophagy markers in Parkinson disease brains. Arch Neurol. 2010;67:1464–1472.
[40] Shibata M, Lu T, Furuya T, et al. JBiol Chem. 2006;281:14474–14485.
[41] Winslow AR, Chen C-W, Corrochano S, et al. J Cell Biol. 2010;190:1023–1037.

[42] Xie Y, Zhou B, Lin M-Y, et al. Endolysosomal Deficits Augment Mitochondria Pathology in Spinal Motor Neurons of Asymptomatic fALS Mice. Neuron. 2015;87:355–370.

[43] Maday S, Holzbaur ELF. Compartment-specific regulation of autophagy in primary neurons. J Neurosci. 2016;36:5933–5945.

[44] Fassier C, Tarrade A, Peris L, et al. Dis Model Mech. 2013;6:72–83.

[45] Tarrade A, Fassier C, Courageot S, et al. Hum Mol Genet. 2006;15:3544–3558.

[46] Watanabe F, Arnold WD, Hammer RE, et al. J Neuropathol Exp Neurol. 2013;72:1016–1028.

[47] Khaminets A, Heinrich T, Mari M, et al. Nature. 2015;522:354–358.

[48] Botzolakis EJ, Zhao J, Gurba KN, et al. The effect of HSP-causing mutations in SPG3A and NIPA1 on the assembly, trafficking, and interaction between atlastin-1 and NIPA1. Mol Cell Neurosci. 2011;46:122–135.

[49] Montenegro G, Rebelo AP, Connell J, et al. Mutations in the ER-shaping protein reticulon 2 cause the axon-degenerative disorder hereditary spastic paraplegia type 12. J Clin Invest. 2012;122:538–544.

[50] Park SH, Zhu -P-P, Parker RL, et al. Hereditary spastic paraplegia proteins REEP1, spastin, and atlastin-1 coordinate microtubule interactions with the tubular ER network. J Clin Invest. 2010;120:1097–1110.

[51] Renvoisé B, Blackstone C. Emerging themes of ER organization in the development and maintenance of axons. Curr Opin Neurobiol. 2010;20:531–537.

[52] Liang A, Lingeman E, Ahmed S, et al. BioRxiv. Rockefeller University (NY): Rockefeller University Press; 2018.

[53] Zhao YG, Liu N, Miao G, et al. Curr. Biol. Vol. 28. Maryland Heights (MO): Cell Press; 2018. p. 1234–1245.e4.

[54] Grumati P, Morozzi G, Hölper S, et al. Elife. 2017;6.

[55] Mochida K, Oikawa Y, Kimura Y, et al. Nature. 2015;522:359–362.

[56] Khundadze M, Kollmann K, Koch N, et al. PLoS Genet. 2013;9: e1003988.

[57] Vantaggiato C, Crimella C, Airoldi G, et al. Brain. 2013;136:3119–3139.

[58] Varga R-E, Khundadze M, Damme M, et al. PLoS Genet. 2015;11: e1005454.

[59] Oz-Levi D, Ben-Zeev B, Ruzzo EK, et al. Mutation in TECPR2 reveals a role for autophagy in hereditary spastic paraparesis. Am J Hum Genet. 2012;91:1065–1072.

[60] Chang J, Lee S, Blackstone C. Spastic paraplegia proteins spastizin and spatacsin mediate autophagic lysosome reformation. J Clin Invest. 2014;124:5249–5262.

[61] Wang B, Iyengar R, Li-Harms X, et al. The autophagy-inducing kinases, ULK1 and ULK2, regulate axon guidance in the developing mouse forebrain via a noncanonical pathway. Autophagy. 2017;14.

[62] Pérez-Brangulí F, Mishra HK, Prots I, et al. Hum Mol Genet. 2014;23:4859–4874.

[63] Zhou X, Babu JR, Da Silva S, et al. Unc-51-like kinase 1/2-mediated endocytic processes regulate filopodia extension and branching of sensory axons. Proc Nat Acad Sci. 2007;104:5842–5847.

[64] Saitoh T, Fujita N, Hayashi T, et al. Proc Natl Acad Sci USA. 2009;106:20842–20846.

[65] Kojima T, Yamada T, AkaishiR, et al. Role of the Atg9a gene in intrauterine growth and survival of fetal mice. Reprod Biol. 2015;15:131–138.

[66] Komatsu M, Waguri S, Ueno T, et al. J Cell Biol. 2005;169:425–434.

[67] McAlpine F, Williamson LE, Tooze SA, et al. Regulation of nutrient-sensitive autophagy by uncoordinated 51-like kinases 1 and 2. Autophagy. 2013;9:361–373.

[68] Cheong H, Lindsten T, Wu J, et al. Proc Natl Acad Sci USA. 2011;108:11121–11126.

[69] Boehm M, Bonifacino JS. Genetic analyses of adaptin function from yeast to mammals. Gene. 2002;286:175–186.

[70] Stavoe AKH, Hill SE, Hall DH, et al. KIF1A/UNC-104 transports ATG-9 to regulate neurodevelopment and autophagy at synapses. Dev Cell. 2016;38:171–185.

[71] Skarnes WC, Rosen B, West AP, et al. Nature. 2011;474:337–342.

[72] Young ARJ, Chan EYW, Hu XW, et al. Starvation and ULK1-dependent cycling of mammalian Atg9 between the TGN and endosomes. J Cell Sci. 2006;119:3888–3900.

[73] Polson HEJ, de Lartigue J, Rigden DJ, et al. Autophagy. 2010;6:506–522.

[74] Atkin TA, Brandon NJ, Kittler JT. Disrupted in Schizophrenia 1 forms pathological aggresomes that disrupt its function in intracellular transport. Hum Mol Genet. 2012;21:2017– 2028.

[75] Norkett R, Modi S, Birsa N, et al. DISC1-dependent Regulation of Mitochondrial Dynamics Controls the Morphogenesis of Complex Neuronal Dendrites. J Biol Chem. 2016;291:613–629.

[76] López-Doménech G, Higgs NF, Vaccaro V, et al. Loss of Dendritic Complexity Precedes Neurodegeneration in a Mouse Model with Disrupted Mitochondrial Distribution in Mature Dendrites. Cell Rep. 2016;17:317–327.

[77] Vaccaro V, Devine MJ, Higgs NF, et al. EMBO Rep. 2017;18:231–240.

[78] Davenport EC, Pendolino V, Kontou G, et al. An essential role for the tetraspanin LHFPL4 in the cell-type-specific targeting and clustering of synaptic GABAA receptors. Cell Rep. 2017;21:70–83.

[79] Vitureira N, Letellier M, White IJ, et al. Nat Neurosci. 2012;15:81–89.

[80] Edelstein AD, Tsuchida MA, Amodaj N, et al. The autism and schizophrenia associated gene CYFIP1 is critical for the maintenance of dendritic complexity and the stabilization of mature spines. J Biol Methods. 2014;4(3):e374.

[81] Preibisch S, Saalfeld S, Tomancak P. Bioinformatics. 2009;25:1463–1465.

[82] Pathania M, Davenport EC, Muir J, et al. The autism and schizophrenia associated gene CYFIP1 is critical for the maintenance of dendritic complexity and the stabilization of mature spines. Transl Psychiatry. 2014;4:e374.

LOCAL AND RETROGRADE GENE TRANSFER INTO PRIMATE NEURONAL PATHWAYS VIA ADENO-ASSOCIATED VIRUS SEROTYPE 8 AND 9

Y. MASAMIZU,[a1] T. OKADA,[b] K. KAWASAKI,[c]
H. ISHIBASHI,[a] S. YUASA,[d] S. TAKEDA,[b]
I. HASEGAWA[c] AND K. NAKAHARA[a*]

[a]*Department of Neurophysiology, National Institute of Neuroscience, NCNP, 4-1-1 Ogawa-Higashi, Kodaira, Tokyo 187–8502, Japan*

[b]*Department of Molecular Therapy, National Institute of Neuroscience, NCNP, 4-1-1 Ogawa-Higashi, Kodaira, Tokyo 187–8502, Japan*

[c]*Department of Physiology, Niigata University School of Medicine, 1 Asahimachi-dori, Niigata, Niigata 951-8510, Japan*

[d]*Department of Ultrastructural Research, National Institute of Neuroscience, NCNP, 4-1-1 Ogawa-Higashi, Kodaira, Tokyo 187–8502, Japan*

Abstract—Viral vector-mediated gene transfer has become increasingly valuable for primate brain research, in particular for application of genetic methods (e.g. optogenetics) to study neuronal circuit functions. Neuronal cell tropisms and infection patterns are viable options for obtaining viral vector-mediated transgene delivery that is selective for particular neuronal pathways. For example, several types of viral vectors can infect axon terminals (retrograde infections), which enables targeted transgene delivery to neurons that directly project to a particular viral injection region. Although recent studies in rodents have demonstrated that adeno-associated virus serotype 8 (AAV8) and 9 (AAV9) efficiently transduce neurons, the tropisms and infection patterns remain poorly understood in primate brains. Here, we constructed recombinant AAV8 or AAV9, which expressed an enhanced green fluorescent protein (EGFP) gene driven by a ubiquitous promoter (AAV8-EGFP and AAV9-EGFP, respectively), and stereotaxically injected it into several brain regions in marmosets and macaque monkeys. Immunohistochemical analyses revealed almost exclusive colocalization of EGFP fluorescence via AAV9-mediated gene transfer with a neuron-specific marker, indicating endogenous neuronal tropism of AAV9, which was consistent with our previous results utilizing AAV8. Injections of either AAV8-EGFP or AAV9-EGFP into the marmoset striatum resulted in EGFP expression in local striatal neurons as a result of local infection, as well as expression in dopaminergic neurons of the substantia nigra via retrograde transport along nigrostriatal axonal projections. Retrograde infections were also observed in the frontal cortex and thalamus, which are known to have direct projections to the striatum. These local and retrograde gene transfers were further demonstrated in the geniculocortical pathway of the marmoset visual system. These findings indicate promising capabilities of AAV8 and AAV9 to deliver molecular tools into a range of primate neural systems in pathway-specific manners through their neuronal tropisms and infection patterns. © 2011 IBRO. Published by Elsevier Ltd. All rights reserved.

Key words: AAV8, AAV9, common marmoset, gene transfer, macaque monkey, neuronal pathway.

The utilization of nonhuman primates as animal models for neuroscience research has provided a better understanding of mechanisms of high-level brain functions (Felleman and Van Essen, 1991; Nakahara et al., 2007; Passingham, 2009). Although lesion, anatomical and electrophysiological studies have revealed neural substrates and activities in primate brains, the lack of effective methods has hampered efforts to correlate detailed neural circuits with functions. Recently developed genetic methods provide promise for facilitating such studies, especially by the use of genetically encoded modulators, which have the ability to turn neuronal activity on or off with high spatiotemporal precision (Tan et al., 2006; Zhang et al., 2007; Han et al., 2009). A major hurdle for the application of genetic methods has been the specific *in vivo* expression of transgenes encoding relevant molecules in neurons of the central nervous system (CNS). In primates, although a few cases have proven successful (Chan et al., 2001; Sasaki et al., 2009), the use of generations of transgenic animals remains impractical. Therefore, gene transfer vectors could serve as a useful method for delivering transgenes into the primate CNS.

Adeno-associated viruses (AAV) are used as transgene vectors within the CNS, because they can readily infect postmitotic cells (Kaplitt et al., 1994; Kaspar et al., 2002; Hollis et al., 2008; Towne et al., 2010). Diverse AAV serotypes exist because of variations of capsid proteins, which also act as tropism determinants. Although the AAV serotype 2 (AAV2) has been most frequently used, recent attempts have sought to determine suitable AAV serotypes for target cell types, tissues, and species (Gao et al., 2002, 2004; Tan et al., 2006). Rodent studies have demonstrated that AAV8 and AAV9 are suitable for transgene deliveries into neuronal cells (Broekman et al., 2006; Taymans et al., 2007; Foust et al., 2009, 2010), and recently, we and

[1] Present address: Division of Brain Circuits, National Institute for Basic Biology, Nishigonaka 38, Myodaiji, Okazaki, Aichi 444-8585, Japan.
*Corresponding author. Tel: +81-42-346-1724; fax: +81-42-346-1754.
E-mail address: nakahara@ncnp.go.jp (K. Nakahara).
Abbreviations: AAV8, adeno-associated virus serotype 8; AAV9, adeno-associated virus serotype 9; CAG, modified chicken β-actin promoter with a cytomegalovirus immediate early enhancer; CNS, central nervous system; DA, dopamine; EGFP, enhanced green fluorescent protein; GFAP, glial fibrillary acidic protein; LGN, lateral geniculate nucleus; NeuN, neuron-specific nuclear protein; Olig2, oligodendrocyte transcription factor 2; PBS, phosphate-buffered saline; PCR, polymerase chain reaction; SNc, substantia nigra pars compacta; SNr, substantia nigra pars reticulata; TH, tyrosine hydroxylase; WPRE, woodchuck hepatitis virus post-transcriptional regulatory element.

others showed that AAV8 exhibits strong tropism for neurons in marmoset (Masamizu et al., 2010) and macaque monkey (Dodiya et al., 2010) brains. However, AAV9, another promising neurotropic serotype, has not yet been tested on primate brains.

Several AAV serotypes can transfer genes into neurons via local and retrograde infection. Although local infections from neuronal somata and/or dendrites allow for gene transfer into neurons surrounding the virus administration sites, retrograde infections from axon terminals provide axonal transport of viral genomes. This results in transgene expression in neuronal somata of distal regions that project to the virus administration sites, which could provide strategies for transgene delivery targeted to specific neuronal pathways. For instance, AAV-mediated retrograde gene transfers have been successful in the substantia nigra and in spinal cord motoneurons (Yasuda et al., 2007; Towne et al., 2010). Exploring the infection patterns of AAV8 and AAV9 in primate brains is, therefore, a prerequisite for utilizing these serotypes in a neuronal pathway-specific manner.

The present study initially analyzed the cell tropism of AAV9 in common marmoset and macaque monkey brains. Subsequently, we explored the infection patterns of either AAV8 or AAV9 in the marmoset brain after injection into the striatum to determine the ability of retrograde infection. Moreover, the utilization of this gene transfer strategy was demonstrated by successful application of AAV8 and AAV9 to the geniculocortical pathway of the visual system.

EXPERIMENTAL PROCEDURES

Animals

Five adult, male, common marmosets (*Callithrix jacchus*) and two adult, male, macaque monkeys (*Macaca mulatta* and *Macaca fuscata*) were used for the present study (Table 1). The marmosets were 20–59 months old (230–325 g), and the macaques were 8 years old (9.2 kg) and 7 years old (6.2 kg) at the start of the experiment. All experiments were conducted in accordance with protocols approved by the ethics committee for primate research at the National Center of Neurology and Psychiatry, Japan.

Virus production

Recombinant AAV8 and AAV9 expressing enhanced green fluorescent protein (EGFP) were produced (AAV8-EGFP and AAV9-EGFP, respectively) as previously described (Okada et al., 2005,

2009). The vector plasmid (pAAV-EGFP) contained EGFP cDNA and the woodchuck hepatitis virus post-transcriptional regulatory element (WPRE), which was expressed under control of the CAG promoter, a modified chicken β-actin promoter with a cytomegalovirus immediate early enhancer. AAV8-EGFP and AAV9-EGFP viruses were produced following triple-transfection of HEK293 cells with pAAV-EGFP, an adenoviral helper plasmid pAdeno (Matsushita et al., 1998), and a chimeric helper plasmid encoding either AAV2 rep/AAV8 cap genes or AAV2 rep/AAV9 cap genes (pAAV2-8, pAAV2-9, respectively, gifts from Dr. James M. Wilson) (Gao et al., 2002, 2004), which was mediated by calcium phosphate co-precipitation with active gassing (Okada et al., 2005). At 72 h after transfection, cell suspensions were collected, centrifuged at $300 \times g$ for 10 min, and resuspended in 30 ml Tris-buffered saline (100 mM Tris–HCl [pH 8.0], 150 mM NaCl). AAV8-EGFP and AAV9-EGFP viruses were harvested by five-cycle freeze-thawing of the resuspended pellet. The crude viral lysate was initially concentrated by a brief two-tier CsCl gradient centrifugation for 3 h (Okada et al., 2002) and further purified by dual ion-exchange chromatography (Okada et al., 2009). Quantitative polymerase chain reaction of DNase I-treated stocks with plasmid standards determined the final number of AAV8-EGFP and AAV9-EGFP virus particles as 3.0×10^{13} and 9.27×10^{12} vector genomes (vg)/ml, respectively.

Virus injection

All surgical procedures and virus injections were conducted under aseptic conditions. Animals were initially i.m. anesthetized with 15–22 mg/kg of ketamine (for marmosets) or with 5 mg/kg of ketamine and 0.03 mg/kg of medetomidine (for macaques), followed by intubation and placement in a stereotaxic apparatus. Anesthesia was then maintained with inhalation of isoflurane (1.5–2.5% in oxygen). Saturation of pulse oxygen (SpO_2), heart rate, body temperature, end-tidal CO_2 ($ETCO_2$) and O_2 (ETO_2), isoflurane ($ETISO$), and fraction of inspired CO_2 ($FiCO_2$), O_2 (FiO_2), and isoflurane ($FiISO$) were continuously monitored. Following i.m. injection of the antibiotic cefovecin, a small craniotomy (2–3 mm in diameter) was made over the area of interest, and the underlying dura was slit to allow penetration of the virus-containing 10-μl Hamilton syringe connected to a 33 G (45° angle) needle. The viral solution (3 μl) was injected at a rate of 0.25 μl/min at each site. Injection sites were determined with a stereotaxic atlas of the marmoset brain (Yuasa et al., 2010) and the macaque brain (BrainMaps.org, http://brainmaps.org/), respectively. The marmoset injection sites were aimed at the striatum: 12.0 mm anterior from the interaural line, 3.0 mm lateral (L) from the midline and 6.0 mm ventral (V) from the brain surface (Eslamboli et al., 2005), as well as the primary visual cortex: 10.0 mm posterior from the interaural line, 5.0 mm L, and 2.5 mm V (Fritsches and Rosa, 1996). After each injection, the needle was maintained in place for an additional 5 min (striatum) or 15 min (primary visual cortex), and then slowly withdrawn (2 mm/min). The macaque injection sites were aimed at the primary visual cortex. After each injection, the needle was maintained in place for an additional 5 min, and then slowly withdrawn (2 mm/min).

Immunohistochemistry

Procedures were performed as previously described (Nakahira and Yuasa, 2005; Masamizu et al., 2010). At 4 weeks postinjection, animals were deeply anesthetized with a sodium pentobarbital overdose and transcardially perfused with 4% paraformaldehyde in 0.1 M phosphate-buffered saline (PBS, pH 7.4). Brains were removed from the skull and postfixed at 4 °C for 2–3 days using the same fresh fixative. The brains were embedded in 3% agar/PBS and sliced into 100-μm thick coronal sections using a Microslicer (DTK-3000, Dosaka EM, Kyoto, Japan). After 1 h of preincubation with 10% normal goat serum at 4 °C, floating sec-

Table 1. Injection sites and viral vectors in marmosets and macaques

	Striatum		Primary visual cortex	
Animal	Right	Left	Right	Left
Marmoset A		AAV9		
Marmoset B		AAV9		
Marmoset C		AAV8		
Marmoset D			AAV9	
Marmoset E			AAV9	AAV8
Macaque A				AAV9
Macaque B			AAV8	AAV9

tions were incubated with primary antibodies in PBS/2% Triton X-100 at 4 °C overnight. Antibodies against the following neuronal or glial marker proteins were used: neuron-specific nuclear protein (NeuN; mouse IgG, 1:500; Cat. No. MAB377, Millipore, Billerica, MA, USA), tyrosine hydroxylase (TH; mouse IgG, 1:1000; Cat. No. T2928, Sigma-Aldrich, St. Louis, MO, USA), glial fibrillary acidic protein (GFAP; rabbit IgG, 1:200; Cat. No. Z0334, Dako, Glostrup, Denmark), and oligodendrocyte transcription factor 2 (Olig2; rabbit IgG, 1:2000 Cat. No. AB9610, Millipore, Billerica, MA, USA). Following PBS rinses, the sections were incubated with secondary antibodies in PBS at 4 °C for 5 h. Secondary antibodies (Alexa goat anti-mouse 594 IgG [1:500; Cat. No. A11005, Molecular Probes, Eugene, OR, USA] or Alexa goat anti-rabbit 594 IgG [1:500; Cat. No. A11012, Molecular Probes, Eugene, OR, USA]), which were directed against the species in which the primary antibody was raised, were used in each case.

Imaging, cell quantification, and statistics

Brain sections were mounted on glass slides with Fluoromount-G (Beckman Coulter, Fullerton, CA, USA). Immunofluorescence and EGFP fluorescence were observed under a confocal laser-scanning microscope (LSM5 Pascal, Zeiss, Oberkochen, Germany) at a resolution of 1024×1024 pixels and one confocal plane. Co-expression of NeuN, GFAP, or Olig2 with EGFP-fluorescence was quantified using ImageJ software (National Institute of Health, Bethesda, MD, USA, http://rsb.info.nih.gov/ij/) with a 40× objective lens. For cell counting analyses, we examined 5–12 microscopic fields in two to four adjacent sections in each case. The number of EGFP-positive cells was statistically analyzed by the chi-square test using JMP8 (SAS Institute, Cary, NC, USA).

Viral transgene detection

Brain slices prepared as in the immunohistochemical analyses (see above) were used for the viral transgene detection assay. Small volumes of tissue were sampled from the injection sites and from regions that contained neuron populations expressing retrograde EGFP labels, under the guidance of EGFP fluorescence by microscopic observation. Extraction and polymerase chain reaction (PCR) amplification of total DNA were performed using the KAPA MG Kit (Cat. No. KK7153, Kapa Biosystems, Woburn, MA, USA). Viral transgenes were detected by PCR using the EGFP (5′-TATATCATGGCCGACAAGCA-3′) and WPRE (5′-CCA-CATAGCGTAAAAGGAGCA-3′) primers. For internal controls, β-actin DNA was amplified using the primers for β-actin 001 (5′-TCCTGACCCTGAAGTACCCC-3′) and β-actin 002 (5′-GTG-GTGGTGAAGCTGTAGCC-3′) (Sasaki et al., 2009).

Thirty-five cycles of PCR were performed (15 s each at 95, 62, and 72 °C) in between an initial denaturation at 95 °C for 3 min and a final elongation at 72 °C for 10 min. PCR products were analyzed by electrophoresis on a 1.2% agarose gel.

RESULTS

Preferential neuronal tropism of AAV9 in marmoset and macaque brains

We have previously shown that AAV8 exhibits a strong tropism for neurons, but not for glia, in the marmoset brain (Masamizu et al., 2010). The present study aimed to determine the tropism of AAV9, which is another promising neurotropic serotype, in the marmoset brain. Recombinant AAV9 expressing the EGFP gene under the CAG promoter (AAV9-EGFP) was generated and stereotaxically injected into the striatum of two marmoset monkeys (Fig. 1A). Four weeks after injection, striatal sections were observed with

a confocal microscope. EGFP fluorescence was visible in numerous cell bodies and processes around the injection site (Fig. 1B). Immunohistochemistry revealed that almost all EGFP-positive cells also expressed NeuN (Fig. 1D). Computer-aided cell counting revealed that 99% of EGFP-positive cells also expressed NeuN (Table 2). In contrast, co-expression of EGFP-positive cells with the astrocyte marker GFAP or the oligodendrocyte marker Olig2 was rarely detected (Fig. 1E, F, Table 2). Frequencies of co-localization of cell type-specific markers with EGFP signals were significantly different across cell types ($P<0.0001$, chi-square test; Table 2). Because CAG promoter activity was expected to be ubiquitous across neuronal and glial cell types, these results indicate strong endogenous neuronal tropism of AAV9.

AAV9 neurotropism was also observed in the macaque monkey, the most widely used primate model animal in neuroscience research. AAV9-EGFP was injected into the primary visual cortex of two macaque monkeys. EGFP fluorescence was coexpressed almost exclusively with NeuN, but rarely with glial markers (Fig. 2).

Viral gene transfers to neuronal pathways after the striatum infection

To date, AAV8 and AAV9 infection patterns (local infection from cell bodies/dendrites or retrograde infection from axon terminals) in primate brains have not been elucidated; however, the reciprocal projections between the striatum and substantia nigra offer an appropriate model system for analyzing this. GABAergic neurons in the striatum project to the substantia nigra pars reticulata (SNr), and dopaminergic neurons in the substantia nigra pars compacta (SNc) project to the striatum (Albin et al., 1989; Alexander and Crutcher, 1990; Minamimoto et al., 2009) (Fig. 3B). Therefore, either AAV8-EGFP or AAV9-EGFP was injected into the marmoset striatum, followed by analysis of EGFP expression in the SNr and SNc, ipsilateral to the injection side (Fig. 3A). For both vectors, strong EGFP fluorescence was directly observed in axon terminals in the SNr, as well as in cell bodies of the SNc (Fig. 3C, F). Almost all EGFP-positive cells in the SNc were dopaminergic neurons, as revealed by co-expression of TH (Fig. 3D, G), indicating retrograde EGFP gene transfers after the viral infection in the striatum. We counted the number of EGFP-positive cells among TH-positive neurons to estimate efficacy of retrograde gene transfers. Proportions of EGFP-positive cells among TH-positive neurons were 38% for AAV8 (EGFP-positive/TH-positive: 81/216), and 49% for AAV9 (EGFP-positive/TH-positive: 102/208). In the SNr, high-power confocal images revealed EGFP-positive fibers and varicosities surrounding NeuN-positive cell bodies (Fig. 3E, H). These results suggested that an AAV8-EGFP or AAV9-EGFP injection into the striatum resulted in anterograde transport of transgene products to nerve terminals in the SNr via the striatonigral pathway, as well as retrograde transport of the transgene to cell bodies in the SNc via the nigrostriatal dopaminergic pathway (Fig. 3B).

The striatum receives major projections from the thalamus and the cerebral cortex (Alexander and Crutcher,
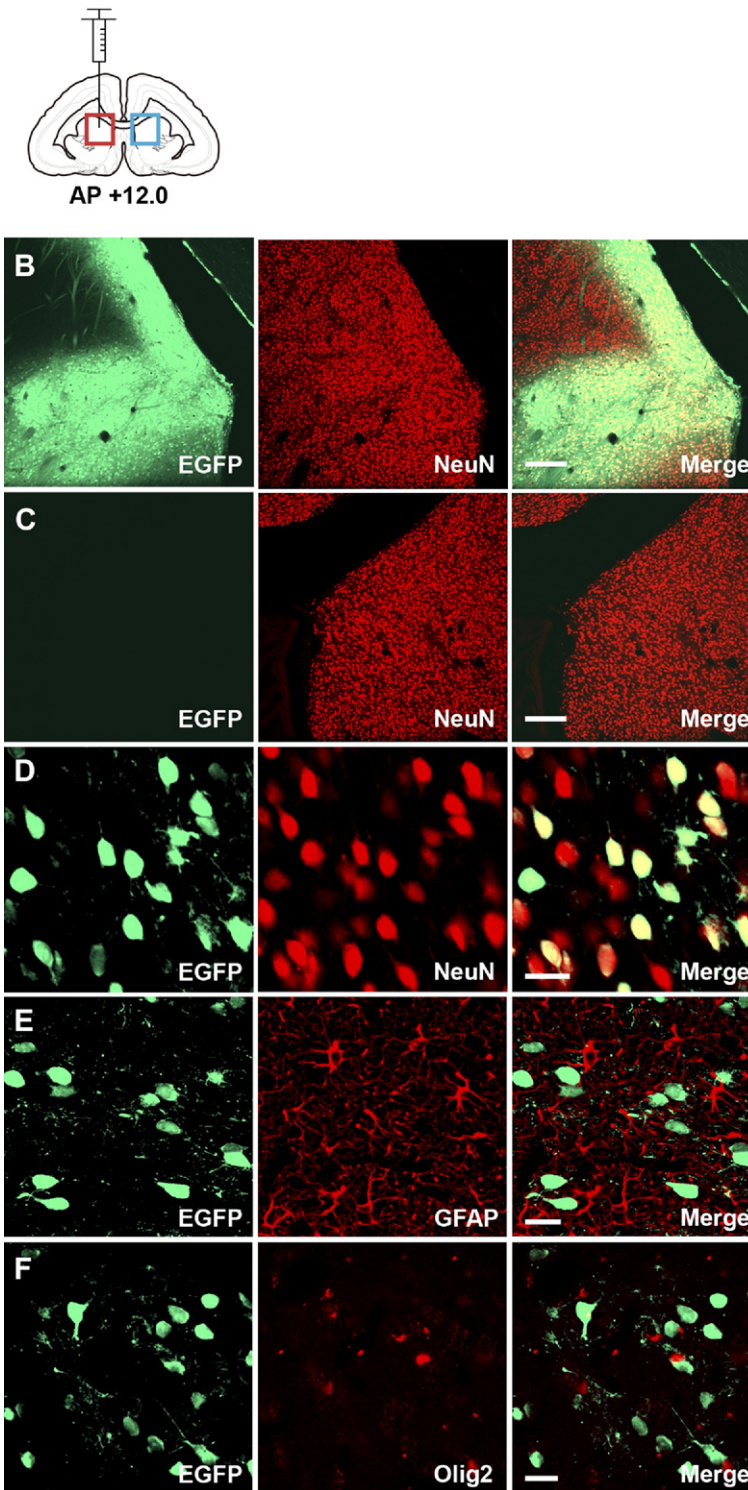
Fig. 1. Efficient gene transfer into neurons of the marmoset striatum using AAV9. (A) The striatal injection site is indicated on a coronal section of the marmoset brain, approximately 12 mm anterior to the interaural line. (B) Low power confocal images corresponding to the red box on the coronal marmoset brain map in (A). Native EGFP fluorescence (left, green), NeuN immunofluorescence signal (center, red), and the merged image (right) are shown. (C) Images of the noninjected control side corresponding to the light-blue box in (A). (D) Confocal images of high-power fields reveal that EGFP-positive cells (green) co-express NeuN (red), as shown by the merged image (yellow). (E, F) EGFP-positive cells (green) rarely co-express GFAP (E; red) or Olig2 (F; red). Bars=200 μm in (B, C) and 20 μm in (D–F). AAV9, adeno-associated virus serotype 9; AP, anteroposterior; EGFP, enhanced green fluorescent protein; GFAP, glial fibrillary acidic protein; NeuN, neuron-specific nuclear protein; Olig2, oligodendrocyte transcription factor 2.

Table 2. Proportion of cells expressing NeuN, GFAP, or Olig2 in EGFP-positive cells in the striatum and primary visual cortex of marmosets following AAV8-EGFP or AAV9-EGFP viral injection

Injection site	Neuron (NeuN$^+$/EGFP$^+$ cells)	Astrocyte (GFAP$^+$/EGFP$^+$ cells)	Oligodendrocyte (Olig2$^+$/EGFP$^+$ cells)
Striatum (AAV8)	98% (484/494)	0% (0/497)	1% (5/500)
Striatum (AAV9)	99% (492/495)	0% (0/500)	1% (3/497)
Primary visual cortex (AAV8)	99% (490/497)	0% (0/502)	1% (3/498)
Primary visual cortex (AAV9)	98% (494/505)	0% (0/493)	1% (5/502)

In all cases, the frequencies of colocalization of cell type-specific markers with EGFP signals are significantly different across cell types ($P < 0.0001$, chi-square-test).

1990; Minamimoto et al., 2009). Thus, we also sought retrogradely infected neurons in these regions. We found EGFP expressing neuronal somata in the thalamus probably corresponding to the parafascicular thalamic nucleus (Fig. 4B) (Minamimoto et al., 2009; Yuasa et al., 2010). Neurons expressing EGFP were also found in the frontal and insular cortices at almost the same anterior–posterior level as the striatal injection site (Fig. 4C, D) (Yuasa et al., 2010).

To further confirm retrograde neuronal infections by AAV8 and AAV9, we aimed to detect AAV transgenes in neurons with retrograde EGFP labels. We extracted total DNA from small areas of the frontal/insular cortices and the thalamus where retrograde EGFP labels were observed, and performed PCR using the primers complimentary to a sequence within the AAV construct. For both AAV8 and AAV9, we detected the presence of viral transgenes in the frontal/insular cortices and in the thalamus (Fig. 4E), indicating the viral transgene itself was transported to remote somata after retrograde infections with AAV8 or AAV9.

Local and retrograde gene transfer to the geniculocortical pathway

Gene transfer capabilities of AAV8 and AAV9 were subsequently analyzed in the marmoset visual system. The primary visual cortex (V1) and lateral geniculate nucleus (LGN) constitute reciprocal loops typical for corticothalamic pathways: feedforward projections from the LGN to V1 and feedback projections from the V1 to LGN (Felleman and Van Essen, 1991; Murphy and Sillito, 1996). Either AAV8-EGFP or AAV9-EGFP were injected into the marmoset V1, aiming at the region representing foveal retinotopy, according to previously described electrophysiological mappings (Fritsches and Rosa, 1996). Following injection, EGFP signals were observed across cortical layers at the injection site, and AAV8 and AAV9 neuronal tropisms were confirmed by nearly complete co-expression with NeuN (Table 2). EGFP fluorescence was then detected in the ipsilateral LGN (Fig. 5 for AAV9-EGFP; data not shown for AAV8-EGFP), demonstrating that V1 injection of either AAV8-EGFP or AAV9-EGFP resulted in EGFP expression in the LGN, which was in apparent retinotopic correspondence with the V1 injection site (White et al., 1998) (Fig. 5B). The EGFP labels were apparently restricted to the parvocellular layer (White et al., 1998). In confocal images with high-power magnification, EGFP-positive axons and varicosities were clearly identified (Fig. 5D), suggesting anterograde transport of the transgene

products (EGFP) via projections from the V1 to LGN. Neuronal somata also expressed EGFP in the LGN, suggesting retrograde axonal transport of the transgene from the V1 injection site (Fig. 5D). Efficacy of retrograde infections in the LGN were relatively low compared with that in the SNc. Proportions of EGFP-positive cells among NeuN-positive neurons were 15% for AAV8 (EGFP-positive/NeuN-positive: 26/170) and 22% for AAV9 (EGFP-positive/NeuN-positive: 38/173).

DISCUSSION

The present study demonstrated that AAV9 efficiently and selectively infected neurons *in vivo* in the marmoset brain (Fig. 1). This neuronal tropism was similar to that of AAV8, which was shown in our previous study (Masamizu et al., 2010). Results from the present study, in combination with our preliminary results, demonstrate strong AAV8 and AAV9 neurotropism in the brains of macaque monkeys, the most widely used primate animal model in neuroscience research (Fig. 2 for AAV9, data not shown for AAV8). These results suggest that AAV8 and AAV9 exhibit a wide range of neuronal infection across primate species, possibly including humans. To obtain selective transgene expression in neurons, neuron-specific promoters, such as the CaMKII promoter, are used typically. However, neuron-specific promoter activity is often weak and insufficient for effective transgene expression. Endogenous AAV8 and AAV9 tropisms permit efficient and almost exclusive neuronal transgene expression through the use of ubiquitous, strong promoters, such as the CAG promoter, rather than specific, weak promoters.

Recently, Foust et al. (2009, 2010) reported that intravascular injection of AAV9 allows transduction of neurons throughout the brain in newborn mice, as well as in spinal motoneurons of newborn cynomolgus monkeys. In adult mice, however, i.v. delivery of AAV9 results in preferential transduction of astrocytes, rather than neurons. In the present study, AAV9 infected, almost exclusively, neurons in the adult marmoset and macaque brain via direct virus injection into the parenchyma. The discrepancy in cell tropism may be attributed to species differences and/or differences in brain entry: i.v. vs. parenchyma injection. The structure of genomes and the purification procedure of viral particles may also affect cell tropism of AAV vectors. Here, we used conventional single-stranded AAV9 purified with ion-exchange chromatography, whereas Foust et al. used double-stranded, self-complementary AAV9 purified
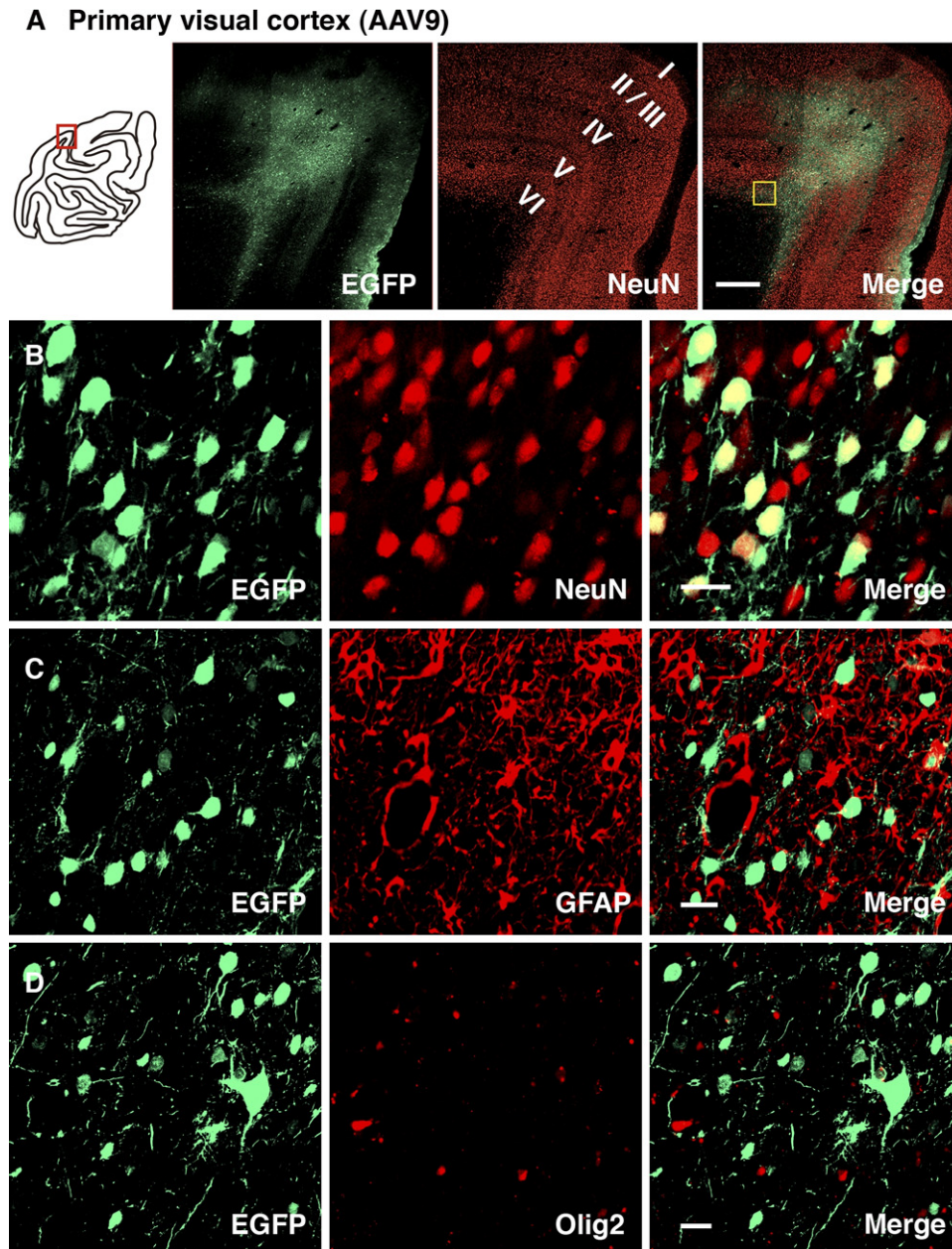
A Primary visual cortex (AAV9)

Fig. 2. Gene transfer into neurons of the primary visual cortex of macaque monkeys with AAV9. (A) Low power confocal images at the injection site, approximately corresponding to the red box on a coronal section of the macaque brain map (left). The confocal images reveal prominent EGFP fluorescence around the injection site (green) and NeuN signals (red). (B) Confocal images reveal co-expression of EGFP (green) and NeuN (red), as shown by the merged image (yellow). The view field approximately corresponds to the yellow box on the right panel of (A). (C, D) EGFP-positive cells rarely co-express GFAP (red) or Olig2 (red), as shown by the merged images. Bars=500 μm in (A) and 20 μm in (B–D). The abbreviations are as listed in Fig. 1.

without the use of ion-exchange chromatography. More importantly, results from Foust et al. demonstrated that AAV9 crossed the blood–brain barrier in mice and cyno-molgus monkeys, which offers a method for brain-wide gene delivery with less invasiveness, especially for gene therapy applications.

The present study revealed, for the first time, neuronal infection patterns of AAV8 and AAV9 in the primate brain. AAV8, as well as AAV9, exhibited both local and retro-grade infection patterns in nigrostriatal, corticostriatal,

thalamostriatal and geniculocortical pathways. In the LGN, EGFP labeling was apparently restricted to the parvocel-lular layers. This observation, together with the observa-tion of a lack of retrograde labeling in other brain regions, which are known to have connections with V1, may sug-gest that retrograde gene transfer after injection of AAV8 or AAV9 into the V1 are limited to the parvocellular layers of the LGN, although future experiments are required to obtain concrete evidence. For both AAV8 and AAV9, the number of neurons expressing EGFP by retrograde trans-
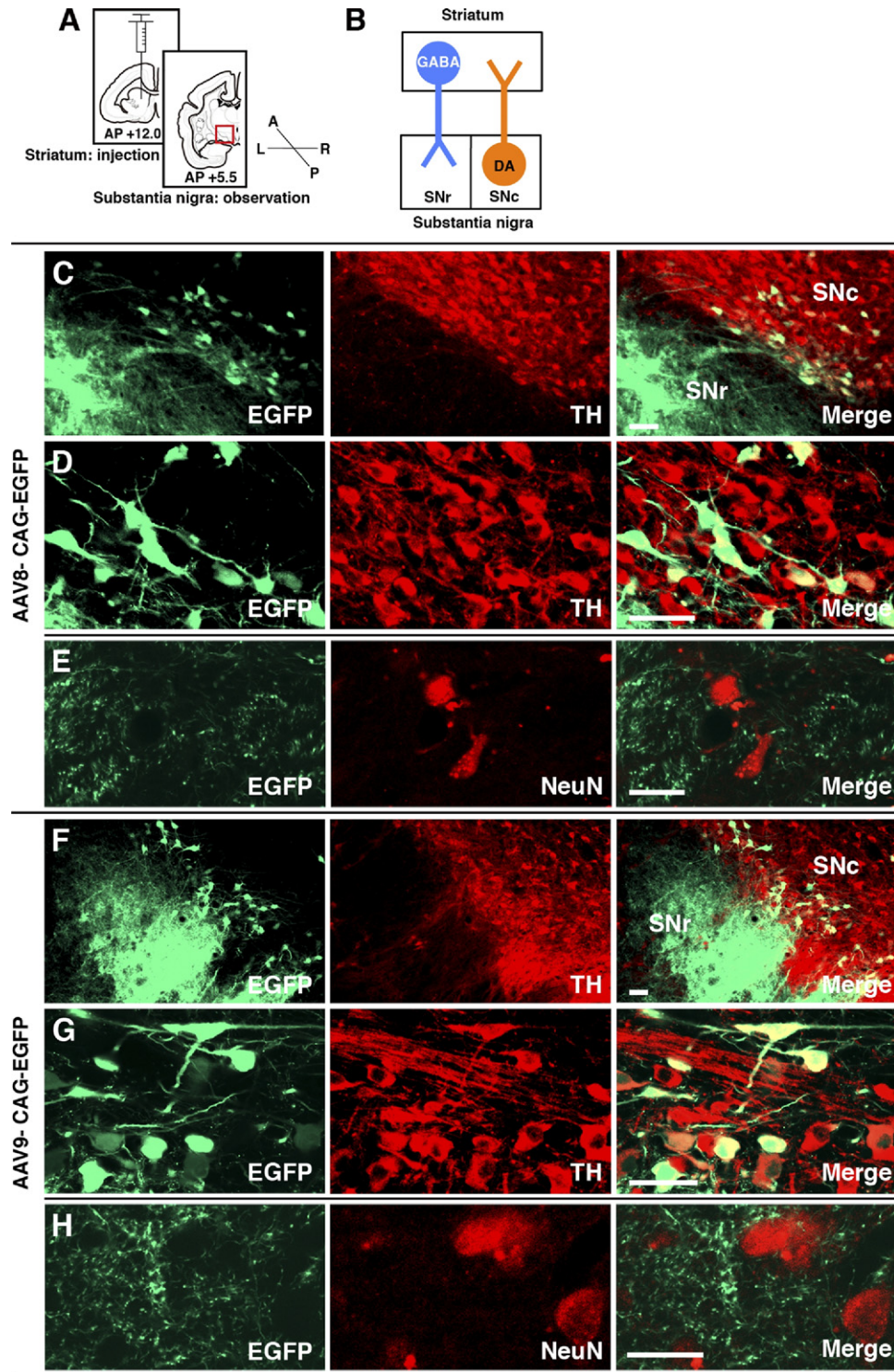
Fig. 3. Local and retrograde gene transfer into the marmoset nigrostriatal pathway with AAV8 and AAV9. (A) Experimental design. EGFP fluorescence is detected in the substantia nigra (red box) following AAV8-EGFP or AAV9-EGFP injection into the striatum. A, anterior; P, posterior; R, right; L, left. (B) Schematic diagram of the nigrostriatal pathway. GABAergic neurons in the striatum (GABA, blue) project to the SNr, and dopaminergic neurons (DA, orange) in the SNc project to the striatum. (C, F) EGFP fluorescence is observed in axon terminals in the SNr, as well as in cell bodies of the SNc following AAV8 (C) or AAV9 (F) injection. (D, G) High-power images of the SNc. EGFP-positive cell bodies (green) co-express TH (red), as shown by the merged images (yellow). (E, H) High-power images of the SNr. EGFP-positive fibers and varicosities (green) are evident around NeuN-positive cell bodies (red). Bars=50 μm in (C, D, F, G) and 20 μm in (E, H). AAV8, adeno-associated virus serotype 8; DA, dopamine; GABA, gamma-aminobutyric acid; SNc, substantia nigra pars compacta; SNr, substantia nigra pars reticulata; TH, tyrosine hydroxylase. Other abbreviations are as listed in Fig. 1.
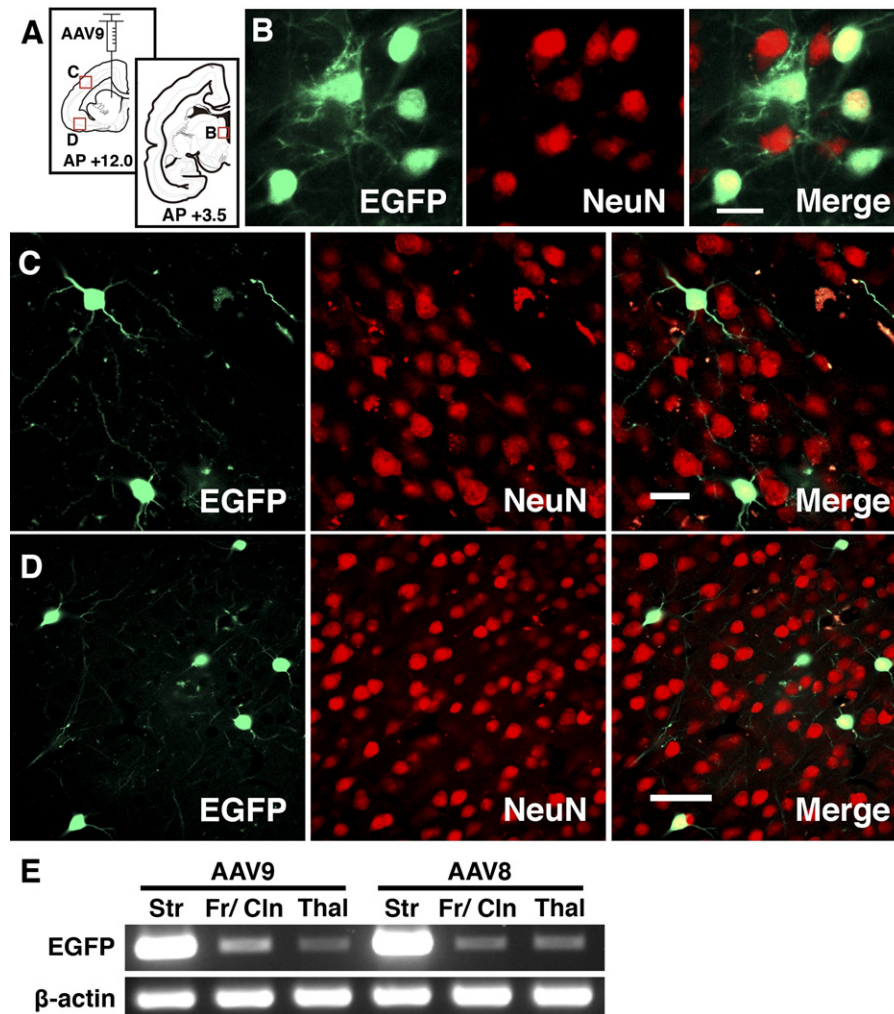
Fig. 4. Retrograde gene transfer into neurons of the frontal/insular cortices and thalamus following AAV9 injection into the striatum. (A) AAV9-EGFP was injected into the striatum at anteroposterior (AP) +12 mm. Retrograde EGFP labels were detected in the thalamus, probably corresponding to the parafascicular thalamic nucleus (B), the frontal cortex (C), and the insular cortex (D). (B–D) Confocal images indicate co-expression of EGFP (green) and NeuN (red) in the thalamus (B), the frontal cortex (C), and the insular cortex (D), as shown in the merged images (yellow). (E) Polymerase chain reaction (PCR) analyses reveal the presence of viral transgene (EGFP) not only in the striatal local infection site (Str), but also in the frontal/insular cortices (Fr/Cln) and the thalamus (Thal) in which cell bodies with retrograde EGFP fluorescence were observed. Bars=20 μm in (B, C) and 50 μm in (D). PCR, polymerase chain reaction. Other abbreviations are as listed in Fig. 1.

fer was modest in the substantia nigra and relatively small in the LGN. Transgene expression was examined at 4 weeks after viral injection; however, the time frame may be insufficient for acquiring full transgene expression in the somata via retrograde transport. In general, AAV-mediated transgene expression persists for long periods (more than a year), and long-term expression would allow for improved efficiency of neuronal transgene expression via retrograde AAV transport.

In the present study, we conducted PCR analyses and confirmed the presence of viral transgenes in the neuronal somata following retrograde infections of either AAV8 or AAV9. These results prove that the genome of AAV8 or AAV9 itself is transported to the soma after retrograde infection at the axon terminal in the brain. This probable mechanism has been demonstrated in several other AAV serotypes, such as AAV1, AAV2, and AAV6 (Kaspar et al., 2002; Hollis et al., 2008; Towne et al., 2010).

A number of neuroscience studies have demonstrated the roles of hierarchical and interconnected structures of the brain in terms of information processing for cognition and behavior (Felleman and Van Essen, 1991; Murphy and Sillito, 1996; Nishimura et al., 2007; Bostan et al., 2010). Retrograde neuronal delivery of molecular tools through the use of AAV8 or AAV9 vectors could provide methods for analyzing hierarchical information processing in the brain. For example, injection of recombinant AAV8 or AAV9 expressing transgenes encoding optogenetic tools into a given brain region could lead to transgene neuronal delivery with direct projections to the injected site, thereby allowing for experimental *in vivo* manipulation of neuronal inputs to the injected brain area. Therefore, transgene
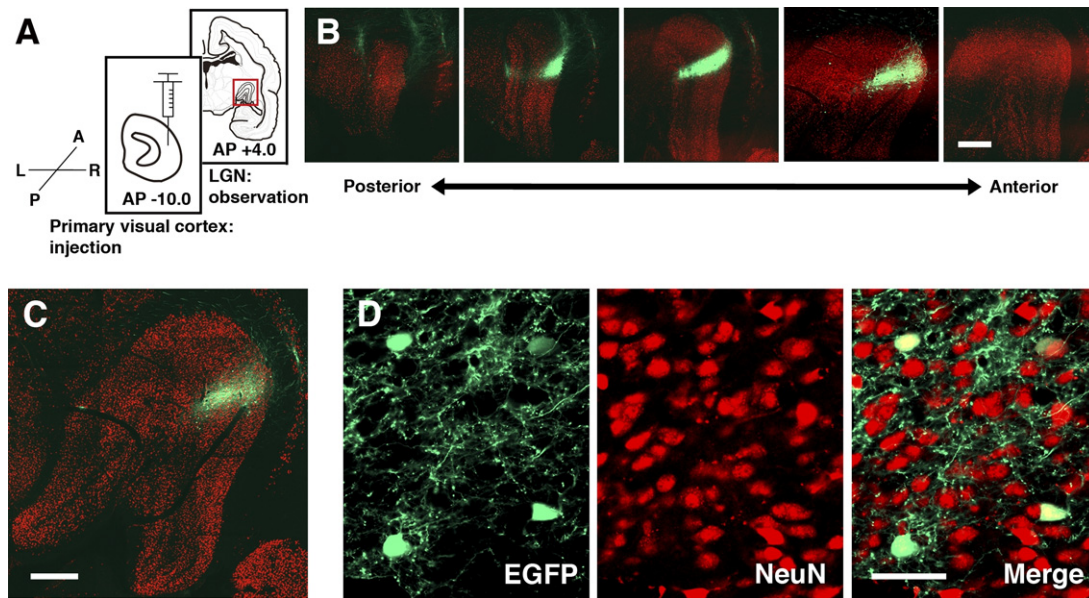
Fig. 5. Local and retrograde gene transfer into the marmoset geniculocortical pathway with AAV9. (A) Experimental design. EGFP expression is visible in the LGN (red box) following injection of AAV9-EGFP into the primary visual cortex. (B) Confocal images of EGFP fluorescence (green) and NeuN expression (red) in coronal sections of the LGN, approximately 3.4–4.2 mm anterior to the interaural line. (C) Representative coronal section of the LGN around the center of EGFP expression (green) overlaid on NeuN signals (red). Approximately 4.0 mm anterior to the interaural line. (D) High-power confocal images show EGFP-positive cell bodies, axons and varicosities (green) in the LGN. EGFP-positive cell bodies co-express NeuN (red), as shown by the merged image (yellow). Bars=500 μm in (B, C) and 50 μm in (D). LGN, lateral geniculate nucleus. Remaining abbreviations are as listed in Fig. 1.

delivery into primate brains via AAV8 and AAV9 vectors could facilitate studies focused on circuit-based principles of brain function by utilizing high-infection efficiencies, as well as neuronal infection patterns.

CONCLUSIONS

Results from the present study, in combination with our previous study, revealed that AAV8 and AAV9 exhibited strong endogenous tropism for neurons in primate brains. The present results further demonstrated that these AAV serotypes can infect neurons both locally and retrogradely. These infection patterns allow transgene delivery to local neurons surrounding virus-injection sites via local infection from somata/dendrites, as well as to distal neurons that project to virus-injection sites via retrograde infections from axon terminals.

REFERENCES

Albin RL, Young AB, Penney JB (1989) The functional anatomy of basal ganglia disorders. Trends Neurosci 12:366–375.

Alexander GE, Crutcher MD (1990) Functional architecture of basal ganglia circuits: neural substrates of parallel processing. Trends Neurosci 13:266–271.

Bostan AC, Dum RP, Strick PL (2010) The basal ganglia communicate with the cerebellum. Proc Natl Acad Sci U S A 107:8452–8456.

Broekman ML, Comer LA, Hyman BT, Sena-Esteves M (2006) Adeno-associated virus vectors serotyped with AAV8 capsid are more efficient than AAV-1 or -2 serotypes for widespread gene delivery to the neonatal mouse brain. Neuroscience 138:501–510.

Chan AW, Chong KY, Martinovich C, Simerly C, Schatten G (2001) Transgenic monkeys produced by retroviral gene transfer into mature oocytes. Science 291:309–312.

Dodiya HB, Bjorklund T, Stansell J, III, Mandel RJ, Kirik D, Kordower JH (2010) Differential transduction following basal ganglia administration of distinct pseudotyped AAV capsid serotypes in nonhuman primates. Mol Ther 18:579–587.

Eslamboli A, Georgievska B, Ridley RM, Baker HF, Muzyczka N, Burger C, Mandel RJ, Annett L, Kirik D (2005) Continuous low-level glial cell line-derived neurotrophic factor delivery using recombinant adeno-associated viral vectors provides neuroprotection and induces behavioral recovery in a primate model of Parkinson's disease. J Neurosci 25:769–777.

Felleman DJ, Van Essen DC (1991) Distributed hierarchical processing in the primate cerebral cortex. Cereb Cortex 1:1–47.

Foust KD, Nurre E, Montgomery CL, Hernandez A, Chan CM, Kaspar BK (2009) Intravascular AAV9 preferentially targets neonatal neurons and adult astrocytes. Nat Biotechnol 27:59–65.

Foust KD, Wang X, McGovern VL, Braun L, Bevan AK, Haidet AM, Le TT, Morales PR, Rich MM Burghes AH, Kaspar BK (2010) Rescue of the spinal muscular atrophy phenotype in a mouse model by early postnatal delivery of SMN. Nat Biotechnol 28:271–274.

Fritsches KA, Rosa MG (1996) Visuotopic organisation of striate cortex in the marmoset monkey (Callithrix jacchus). J Comp Neurol 372:264–282.

Gao G, Vandenberghe LH, Alvira MR, Lu Y, Calcedo R, Zhou X, Wilson JM (2004) Clades of Adeno-associated viruses are widely disseminated in human tissues. J Virol 78:6381–6388.

Gao GP, Alvira MR, Wang L, Calcedo R, Johnston J, Wilson JM (2002) Novel adeno-associated viruses from rhesus monkeys

as vectors for human gene therapy. Proc Natl Acad Sci U S A 99:11854–11859.

Han X, Qian X, Bernstein JG, Zhou HH, Franzesi GT, Stern P, Bronson RT, Graybiel AM, Desimone R, Boyden ES (2009) Millisecond-timescale optical control of neural dynamics in the nonhuman primate brain. Neuron 62:191–198.

Hollis ER, II, Kadoya K, Hirsch M, Samulski RJ, Tuszynski MH (2008) Efficient retrograde neuronal transduction utilizing self-complementary AAV1. Mol Ther 16:296–301.

Kaplitt MG, Leone P, Samulski RJ, Xiao X, Pfaff DW, O'Malley KL, During MJ (1994) Long-term gene expression and phenotypic correction using adeno-associated virus vectors in the mammalian brain. Nat Genet 8:148–154.

Kaspar BK, Erickson D, Schaffer D, Hinh L, Gage FH, Peterson DA (2002) Targeted retrograde gene delivery for neuronal protection. Mol Ther 5:50–56.

Masamizu Y, Okada T, Ishibashi H, Takeda S, Yuasa S, Nakahara K (2010) Efficient gene transfer into neurons in monkey brain by adeno-associated virus 8. Neuroreport 21:447–451.

Matsushita T, Elliger S, Elliger C, Podsakoff G, Villarreal L, Kurtzman GJ, Iwaki Y, Colosi P (1998) Adeno-associated virus vectors can be efficiently produced without helper virus. Gene Ther 5:938–945.

Minamimoto T, Hori Y, Kimura M (2009) Roles of the thalamic CM-PF complex-Basal ganglia circuit in externally driven rebias of action. Brain Res Bull 78:75–79.

Murphy PC, Sillito AM (1996) Functional morphology of the feedback pathway from area 17 of the cat visual cortex to the lateral geniculate nucleus. J Neurosci 16:1180–1192.

Nakahara K, Adachi Y, Osada T, Miyashita Y (2007) Exploring the neural basis of cognition: multi-modal links between human fMRI and macaque neurophysiology. Trends Cogn Sci 11:84–92.

Nakahira E, Yuasa S (2005) Neuronal generation, migration, and differentiation in the mouse hippocampal primoridium as revealed by enhanced green fluorescent protein gene transfer by means of in utero electroporation. J Comp Neurol 483:329–340.

Nishimura Y, Onoe H, Morichika Y, Perfiliev S, Tsukada H, Isa T (2007) Time-dependent central compensatory mechanisms of finger dexterity after spinal cord injury. Science 318:1150–1155.

Okada T, Nomoto T, Yoshioka T, Nonaka-Sarukawa M, Ito T, Ogura T, Iwata-Okada M, Uchibori R, Shimazaki K, Mizukami H, Kume A, Ozawa K (2005) Large-scale production of recombinant viruses by use of a large culture vessel with active gassing. Hum Gene Ther 16:1212–1218.

Okada T, Nonaka-Sarukawa M, Uchibori R, Kinoshita K, Hayashita-Kinoh H, Nitahara-Kasahara Y, Takeda S, Ozawa K (2009) Scal-able purification of adeno-associated virus serotype 1 (AAV1) and AAV8 vectors, using dual ion-exchange adsorptive membranes. Hum Gene Ther 20:1013–1021.

Okada T, Shimazaki K, Nomoto T, Matsushita T, Mizukami H, Urabe M, Hanazono Y, Kume A, Tobita K, Ozawa K, Kawai N (2002) Adeno-associated viral vector-mediated gene therapy of ischemia-induced neuronal death. Methods Enzymol 346:378–393.

Passingham R (2009) How good is the macaque monkey model of the human brain? Curr Opin Neurobiol 19:6–11.

Sasaki E, Suemizu H, Shimada A, Hanazawa K, Oiwa R, Kamioka M, Tomioka I, Sotomaru Y, Hirakawa R, Eto T, Shiozawa S, Maeda T, Ito M, Ito R, Kito C, Yagihashi C, Kawai K, Miyoshi H, Tanioka Y, Tamaoki N, Habu S, Okano H, Nomura T (2009) Generation of transgenic non-human primates with germline transmission. Nature 459:523–527.

Tan EM, Yamaguchi Y, Horwitz GD, Gosgnach S, Lein ES, Goulding M, Albright TD, Callaway EM (2006) Selective and quickly reversible inactivation of mammalian neurons in vivo using the Drosophila allatostatin receptor. Neuron 51:157–170.

Taymans JM, Vandenberghe LH, Haute CV, Thiry I, Deroose CM, Mortelmans L, Wilson JM, Debyser Z, Baekelandt V (2007) Comparative analysis of adeno-associated viral vector serotypes 1, 2, 5, 7, and 8 in mouse brain. Hum Gene Ther 18:195–206.

Towne C, Schneider BL, Kieran D, Redmond DE, Jr, Aebischer P (2010) Efficient transduction of non-human primate motor neurons after intramuscular delivery of recombinant AAV serotype 6. Gene Ther 17:141–146.

White AJ, Wilder HD, Goodchild AK, Sefton AJ, Martin PR (1998) Segregation of receptive field properties in the lateral geniculate nucleus of a New-World monkey, the marmoset Callithrix jacchus. J Neurophysiol 80:2063–2076.

Yasuda T, Miyachi S, Kitagawa R, Wada K, Nihira T, Ren YR, Hirai Y, Ageyama N, Terao K, Shimada T, Takada M, Mizuno Y, Mochizuki H (2007) Neuronal specificity of alpha-synuclein toxicity and effect of Parkin co-expression in primates. Neuroscience 144:743–753.

Yuasa S, Nakamura K, Kohsaka S (2010) Stereotaxic atlas of the marmoset brain with immunohistochemical architecture and MRI Images. National Institute of Neuroscience, National Center of Neurology and Psychiatry, Tokyo, Japan.

Zhang F, Wang LP, Brauner M, Liewald JF, Kay K, Watzke N, Wood PG, Bamberg E, Nagel G, Gottschalk A, Deisseroth K (2007) Multimodal fast optical interrogation of neural circuitry. Nature 446:633–639.